Computational Modelling and Simulation of Ductile Damage in Metals

von der Fakultät Maschinenbau
der Technischen Universität Dortmund
zur Erlangung des akademischen Grades

Doktor-Ingenieur (Dr.-Ing.)

genehmigte Dissertation

von

Leon Sprave

aus Hagen

Referent:	Prof. Dr.-Ing. habil. A. Menzel
Korreferenten:	Prof. Dr. M. Ekh
	Prof. Dr.-Ing. habil. F.-J. Barthold
Tag der Einreichung:	03.09.2024
Tag der mündlichen Prüfung:	20.02.2025

Bibliografische Information Der Deutschen Bibliothek
Die Deutsche Bibliothek verzeichnet diese Publikation in der Deutschen Nationalbibliografie; detaillierte bibliografische Daten sind im Internet über **http://dnb.dnb.de** abrufbar.

Bibliographic information published by Die Deutsche Bibliothek
Die Deutsche Bibliothek lists this publication in the Deutsche Nationalbibliografie; detailed bibliographic data is available in the Internet at **http://dnb.dnb.de**.

Schriftenreihe des Instituts für Mechanik

Herausgeber: Institut für Mechanik
Fakultät Maschinenbau
Technische Universität Dortmund
Leonhard-Euler-Str. 5
D-44227 Dortmund

Druck: Koffler DruckManagement GmbH

Als Manuskript gedruckt. Printed in Germany.

ISSN 2191-0022
ISBN 978-3-947323-54-8

Acknowledgements

The research of this thesis was conducted during my time as a PhD student at the Institute of Mechanics at TU Dortmund University. I would like to thank my supervisor Andreas Menzel for the opportunity to continue researching at the Institute of Mechanics after finishing my master studies by offering me a PhD-Student position in 2016, for all the scientific guidance, hints and discussions during supervision of my thesis and for (implicitly) pushing me to continue digging until the root of a problem was found.

I greatly appreciate the time and effort spent by the co-referees Magnus Ekh and Franz-Joseph Barthold.

Working at the institute has always been very pleasant and productive, especially due to the philosophy of 'open doors' — enabling, even encouraging, discussions with colleagues whenever one was in need of another perspective. I appreciated the welcoming atmosphere of the whole team. Special thanks go out to Tobias, Robin, Markus and Lars who I enjoyed working with already during my bachelor studies. Further thanks go out to Tina, Kerstin and Matthias who, each in their own way, make sure the institute functions efficiently.

Part of this work was supported by the German Research Foundation (DFG) via Collaborative Research Centre/Transregio 188 (project number 278868966). The financial support as well as the countless opportunities for scientific discussion with project partners from the same but also from different scientific fields were greatly acknowledged.

Last but not least, I must express sincere gratitude to my family. They patiently understood when I had less time for them and I needed more time for research, they encouraged me when my motivation was lacking and they supported me however necessary.

Once again, thanks to everyone for their support without which I would not have been able to finish this thesis.

Dortmund, May 2025 Leon Sprave

Zusammenfassung

In der vorliegenden Arbeit wird eine neuartige Modellierungsumgebung für Kontinuumsschädigung entwickelt, durch die es möglich wird, phänomenologische Effekte duktiler Schädigung auf mechanische Eigenschaften von Metallen akkurat vorherzusagen. Dabei stellt die vorgeschlagene Modellierungsumgebung, im Rahmen einer Implementierung mittels der mit dem mikromorphen Ansatz regularisierten Finite Elemente Methode, eine Beziehung zwischen dem makroskopischen Dehnungs- und Spannungszustand her. Dadurch wird die Simulation von (Kalt-)Umformprozessen möglich, die die sich ergebenden mechanischen Eigenschaften und insbesondere die Sicherheitsreserve des hergestellten Bauteils akkurat vorhersagt.

Die Modellierungsumgebung wird im Rahmen von drei separaten, aufeinander aufbauenden Modellen mit steigender Komplexität entwickelt. Als erstes wird ein regularisiertes, isotropes, dreidimensionales, duktiles Schädigungsmodell für finite Verzerrungen etabliert. Im Fokus stehen die Kopplung von Schädigung und Plastizität mittels eines Mehrflächenansatzes sowie die Fähigkeit des Materialmodells das Verhalten des Dualphasenstahls DP800 widerzuspiegeln, d.h. es werden Versuche durchgeführt und Parameter anhand von ortsaufgelösten Verschiebungsfeldern identifiziert.

Als nächstes wird ein regularisiertes anisotropes Schädigungsmodell implementiert, bei der die Schädigung durch eine Abbildung mit Verbindung zur fiktiven ungeschädigten Konfiguration beschrieben wird. Die Kopplung zwischen Schädigung und Plastizität wird weiterentwickelt indem effektive Triebkräfte eingeführt werden, die verantwortlich für das Einsetzen von Schädigungs- beziehungsweise Plastizitätsentwicklung sind. Verschiedene Möglichkeiten der Regularisierung werden untersucht und die Ergebnisse durch anschauliche Beispiele dargestellt.

Die finale Entwicklungsstufe der Modellierungsumgebung fügt den Mikroriss Schließ- und Öffnungseffekt hinzu. Motiviert durch mikromechanische Zusammenhänge, bei denen sich die mechanische Steifigkeit unter Zug- und unter Druckbelastung unterschiedlich entwickelt, werden zwei separate Schädigungsvariablen eingeführt. In vorherigen Stufen des Materialmodells wurden thermodynamisch konsistente assoziierte Evolutionsgleichungen verwendet. Im Gegensatz dazu wird die Rückgewinnung von Steifigkeit bei Verschliessen eines Mikrorisses mit einem nicht-assoziierten Ansatz modelliert und der Erfüllung der Dissipationsungleichung besondere Beachtung geschenkt.

Bei allen betrachteten Modellen werden die dazugehörigen Gleichungen in der algorithmischen Implementierung implizit und monolithisch gelöst. Des Weiteren wird das charakteristische Verhalten der entwickelten Modelle anhand von anschaulichen Beispielen dargelegt.

Abstract

This thesis deals with the development of a novel continuum damage modelling framework which enables the accurate prediction of the phenomenological effects of ductile damage on the mechanical properties of metals. The proposed modelling framework establishes a relation between the macroscopic strain and stress states and is embedded into a finite element method regularised by adopting the micromorphic approach. Thereby, the simulation of (cold) forming processes with more accurate predictions of the resulting mechanical properties and, especially, of the safety margin of the produced part becomes possible.

The process of developing the modelling framework is set forth by means of three separate models which increase in complexity. At first, a regularised, isotropic, three-dimensional, ductile damage model is established at finite strains. The analysis focuses on the coupling of damage and plasticity by means of a multisurface approach as well as on the applicability of the material model to resemble the behaviour of the dual-phase steel DP800, i.e. experiments are performed and parameters are identified by using full-field displacement data.

Secondly, a regularised anisotropic ductile damage model is implemented by adopting the fictitious configuration concept, where damage is described by a mapping related to a fictitiously undamaged configuration. The coupling of damage and plasticity is further enriched by introducing effective driving forces controlling onset and evolution of damage and plasticity, respectively. Different possibilities of regularisation are analysed and the results are underlined by illustrative examples.

The final stage of material model development incorporates the micro-crack closure and reopening effect. Motivated from micro-mechanical considerations where mechanical stiffness in tension and in compression may evolve differently, two separate damage variables are introduced. Previous stages of the material model are formulated with thermodynamically consistent associated evolution equations. In contrast, the recovery of stiffness on crack closure is modelled in terms of a non-associated approach where special attention is paid towards fulfilling the dissipation inequality.

For all discussed models, the algorithmic implementation encompasses an implicit and monolithic solution of the model equations. Furthermore, the characteristic behaviour of the developed models is demonstrated in terms of illustrative examples.

Publications

Some essential scientific findings of this thesis have already been published in peer-reviewed journal articles.

[161] L. Sprave, A. Menzel: *A large strain gradient-enhanced ductile damage model: finite element formulation, experiment and parameter identification*, Acta Mechanica, 231:5159–5192, 2020.

[163] L. Sprave, A. Schowtjak, R. Meya, T. Clausmeyer, A. E. Tekkaya, A. Menzel: *On mesh dependencies in finite-element-based damage prediction: application to sheet metal bending*, Production Engineering, 14:123–134, 2020.

[76] F. Guhr, L. Sprave, F.-J. Barthold, A. Menzel: *Computational shape optimisation for a gradient-enhanced continuum damage model*, Computational Mechanics, 65:1105–1124, 2020.

[122] A. Menzel, L. Sprave: *Continuum Damage Mechanics — Modelling and Simulation* in: J. Merodio, R. Ogden (Eds.) Constitutive Modelling of Solid Continua, Springer, 231–256, 2020.

[162] L. Sprave, A. Menzel: *A large strain anisotropic ductile damage model — Effective driving forces and gradient-enhancement of damage vs. plasticity*, Computer Methods in Applied Mechanics and Engineering, 416:116284, 2023.

The articles [161] and [162] are works of only the author of this thesis and his supervisor. The author of this thesis worked on the conceptualisation of the articles, on the theory and on the implementation of the models. He performed simulations and experiments and wrote the articles.
The joint work [163] was mainly written by the author of this thesis. He also contributed to theoretical aspects, to the implementation and to the simulations.
For the joint work [76], the author of this thesis was involved in the conceptualisation of the published article. He was responsible for the theory of the finite element implementation as well as for the experiments and he took part in the writing of the article.
For [122], the author of this thesis provided the literature overview and some examples.

Contents

Notation **xiii**

1 Introduction **1**
1.1 Interpretation of the term 'damage' . . . 1
1.2 Experimental analysis of (ductile) damage . . . 3
1.3 Damage in continuum mechanics . . . 4
1.3.1 Ductile damage in continuum mechanics . . . 4
1.3.2 Influence of stress triaxiality and Lode-angle . . . 5
1.3.3 Microcrack-closure reopening effect . . . 6
1.4 Regularisation . . . 8
1.5 Parameter identification . . . 10
1.6 Objective and outline of this work . . . 10

2 A Finite Element framework for regularised damage **13**
2.1 Essential kinematics . . . 13
2.2 Micromorphic approach . . . 14
2.2.1 Formulation of the governing equations . . . 15
2.2.2 Discretisation . . . 15
2.2.3 Linearisation . . . 17
2.3 Direct approach using complementarity functions — a short summary . . . 18
2.3.1 Nonlocality residual and non-local driving force . . . 18
2.3.2 Finite Element formulation and discretisation . . . 20
2.4 Linear constraints and arc-length methods . . . 21
2.4.1 Linear constraints . . . 21
2.4.2 Arc-length methods . . . 23
2.4.3 Combining linear constraints with arc-length methods . . . 24

3 A regularised framework for isotropic damage coupled to finite plasticity **27**
3.1 Continuous formulation of the constitutive model . . . 28
3.1.1 Helmholtz energy and dissipation . . . 28
3.1.2 Multi-surface formulation . . . 30
3.2 Algorithmic treatment . . . 32
3.2.1 Time discretisation and radial return scheme . . . 32
3.2.2 Update of Lagrange multipliers in principal stress space . . . 34
3.2.3 Jacobian for local Newton scheme . . . 35

3.2.4 Determination of stresses and stiffness contributions 37
3.2.5 Derivatives in principal space 40
3.3 Parameter study 41
3.4 Parameter identification and validation 43
3.4.1 Experimental data 47
3.4.2 Simulation setup 48
3.4.3 Objective function 49
3.4.4 Identified parameters 52
3.4.5 Validation 55
3.5 Application to air bending 62
3.6 Update of the parametrisation 66
3.6.1 Updated parameter identification 67

4 A regularised framework for anisotropic damage coupled to finite plasticity 73
4.1 Fictitious configuration framework 74
4.2 Modelling framework 76
4.3 Coupling of damage and plasticity — effective driving forces 79
4.4 Choice of constitutive relations 82
4.5 Algorithmic treatment 87
4.5.1 Discretisation of the evolution equations 87
4.5.2 Local tangent contributions 90
4.6 Specific choice of non-local energy 95
4.7 Stresses and driving forces for the Finite Element formulation 96
4.8 Global tangent contributions for the Finite Element formulation 96
4.9 Response under homogeneous deformation 99
4.9.1 Homogeneous uniaxial tension — local parameter identification . 99
4.9.2 Homogeneous uniaxial tension — parameter variation 100
4.9.3 Homogeneous simple shear 105
4.9.4 Homogeneous simple shear combined with uniaxial tension 105
4.10 Analysis of regularisation behaviour 107
4.10.1 Setup of the numerical examples 107
4.10.2 Elasticity with damage 109
4.10.3 Elastoplasticity 110
4.10.4 Elastoplasticity with damage 111
4.10.5 Elastoplasticity with damage and activated deterioration function 115
4.11 Formulation in terms of Haigh-Westergaard coordinates 121
4.11.1 Parametrisation of the damage initiation surface 123
4.11.2 Convexity condition of the parametrised damage initiation surface 125

5 Microcrack closure and reopening for ductile damage 131
5.1 Micromechanical motivation 131
5.2 Modelling framework 132

5.3 A prototype model 139
5.4 Reduction to scalar-valued damage variables 143
5.4.1 Algorithmic implementation 144
5.4.2 Proof of non-negative dissipation 146
5.5 Response under homogeneous deformation 148

6 Summary and outlook **155**

A Exponent of a second order tensor **163**

B Some implementation details of abraxas++ **165**
B.1 Load curve functionality 165
B.2 Automatic time stepping and convergence control 167

Bibliography **171**

Notation

Although the notation used in this thesis should be self-explanatory, a brief overview of the most important relations used throughout the whole work is provided in the following.

Tensors Let the three-dimensional Euclidean space be spanned by the (orthonormal) Cartesian basis vectors $\boldsymbol{e}_i$, with $i = 1, 2, 3$. Tensors of first, second and fourth order can then be expressed in terms of their coefficients with respect to these basis vectors following Einstein's summation convention, i.e.

$$\begin{aligned}
\boldsymbol{a} &= a_i \, \boldsymbol{e}_i \,, \\
\boldsymbol{A} &= A_{ij} \, \boldsymbol{e}_i \otimes \boldsymbol{e}_j \,, \\
\mathsf{A} &= \mathsf{A}_{ijkl} \, \boldsymbol{e}_i \otimes \boldsymbol{e}_j \otimes \boldsymbol{e}_k \otimes \boldsymbol{e}_l \,.
\end{aligned}$$

In this work, non-bold (italic) letters indicate scalars while bold-face (italic) letters are used for tensors. In general, bold-face lower-case letters are primarily used for tensors of first order and bold-face upper-case letters for tensors of second order. Within this work, however, bold-face lower-case letters often represent tensors of second order referred to the current configuration and bold-face upper-case letters represent tensors of second order referred to the reference configuration. Furthermore, tensors referred to the intermediate configuration are marked with a hat, i.e. $\widehat{\boldsymbol{A}}$, and tensors referred to the fictitious configuration are marked with an overline, i.e. $\overline{\boldsymbol{A}}$. Tensors of fourth order are represented by bold-face sans-serif letters.

Inner tensor products Each contraction of an inner tensor product is characterised by a dot, i.e. single and double contractions are defined as

$$\begin{aligned} c = \boldsymbol{a} \cdot \boldsymbol{b} &= a_i\, b_i\,, \\ \boldsymbol{c} = \boldsymbol{A} \cdot \boldsymbol{b} &= A_{ij}\, b_j\, \boldsymbol{e}_i\,, \\ \boldsymbol{C} = \boldsymbol{A} \cdot \boldsymbol{B} &= A_{ij}\, B_{jk}\, \boldsymbol{e}_i \otimes \boldsymbol{e}_k\,, \\ c = \boldsymbol{A} : \boldsymbol{B} &= A_{ij}\, B_{ij}\,, \\ \boldsymbol{C} = \mathsf{A} : \boldsymbol{B} &= \mathsf{A}_{ijkl}\, B_{kl}\, \boldsymbol{e}_i \otimes \boldsymbol{e}_j\,, \\ \mathsf{C} = \mathsf{A} : \mathsf{B} &= \mathsf{A}_{ijkl}\, \mathsf{B}_{klmn}\, \boldsymbol{e}_i \otimes \boldsymbol{e}_j \otimes \boldsymbol{e}_m \otimes \boldsymbol{e}_n\,, \end{aligned}$$

Double contractions are defined as a contraction of two indices at once rather than as a sequence of two single contractions, i.e. $\boldsymbol{C} = \mathsf{A} : \boldsymbol{B} \neq A_{ijkl}\, B_{lk}$ (unless $\boldsymbol{B}$ is symmetric).

Outer tensor products In addition to the standard outer tensor product (or dyadic product) represented by the classical symbol $\otimes$, the non-standard symbols $\overline{\otimes}$, $\underline{\otimes}$ and $\underline{\overline{\otimes}}$ are introduced as they represent standard results of derivatives. One has the definitions

$$\begin{aligned} \boldsymbol{C} = \boldsymbol{a} \otimes \boldsymbol{b} &= a_i\, b_i\, \boldsymbol{e}_i \otimes \boldsymbol{e}_j\,, \\ \mathsf{C} = \boldsymbol{A} \otimes \boldsymbol{B} &= A_{ij}\, B_{kl}\, \boldsymbol{e}_i \otimes \boldsymbol{e}_j \otimes \boldsymbol{e}_k \otimes \boldsymbol{e}_l\,, \\ \mathsf{C} = \boldsymbol{A} \,\overline{\otimes}\, \boldsymbol{B} &= A_{ik}\, B_{jl}\, \boldsymbol{e}_i \otimes \boldsymbol{e}_j \otimes \boldsymbol{e}_k \otimes \boldsymbol{e}_l\,, \\ \mathsf{C} = \boldsymbol{A} \,\underline{\otimes}\, \boldsymbol{B} &= A_{il}\, B_{jk}\, \boldsymbol{e}_i \otimes \boldsymbol{e}_j \otimes \boldsymbol{e}_k \otimes \boldsymbol{e}_l\,, \\ \mathsf{C} = \boldsymbol{A} \,\underline{\overline{\otimes}}\, \boldsymbol{B} &= \tfrac{1}{2}\left[\boldsymbol{A} \,\overline{\otimes}\, \boldsymbol{B} + \boldsymbol{A} \,\underline{\otimes}\, \boldsymbol{B}\right]. \end{aligned}$$

Identity tensors The second-order identity tensor $\boldsymbol{I}$ as well as the fourth-order identity tensor I and the fourth-order symmetric identity tensor $\mathsf{I}^{\mathrm{sym}}$ are defined as

$$\begin{aligned} \boldsymbol{I} &= \delta_{ij}\, \boldsymbol{e}_i \otimes \boldsymbol{e}_j\,, \\ \mathsf{I} &= \boldsymbol{I} \,\overline{\otimes}\, \boldsymbol{I}\,, \\ \mathsf{I}^{\mathrm{sym}} &= \boldsymbol{I} \,\underline{\overline{\otimes}}\, \boldsymbol{I}\,, \end{aligned}$$

where the Kronecker delta symbol is given as $\delta_{ij} = \boldsymbol{e}_i \cdot \boldsymbol{e}_j$.

1 Introduction

In today's world, resources are becoming more and more precious and the effort spent on efficiently utilising these resources rises more and more. One possibility of increasing the efficiency of resource utilisation is to improve the production process of a product. In this regard, (cold) forming processes are of special interest with respect to this thesis.

The idea is, that by recognising damage (as a precursor to failure) as an important influence during the forming process and by setting up an accurate model for the prediction of damage and plasticity during the forming process, the production process can be optimised. On the one hand, the forming capability of the material may be utilised more efficiently and on the other hand the safety margin may be determined more accurately as the prediction by means of simulations with an improved material model becomes more precise, ultimately saving costs and energy.

To this end, the goal of this thesis is to develop an accurate material model for the prediction of ductile damage and plasticity in metals. The introduction starts by discussing the term 'damage' and its various subcategories. Thereafter, focus is placed on ductile damage — a summary of experimental findings and of continuum damage modelling in the literature is provided. A literature overview of advanced modelling techniques, e.g. regularisation, is given. At the end of the introduction, the objective and scope of this thesis are laid out.

1.1 Interpretation of the term 'damage'

The term 'damage' is widely used in different scientific communities, in the industry and even in everyday language. Coincidentally, the exact meaning of the term 'damage' differs significantly between the communities. A common ground for the delineation of 'damage' is that it describes the degradation or even the complete loss of functional properties or other desired properties like e.g. appearance. In everyday language, damage may be used for e.g. a scratch in a floor tile (degradation of appearance), a damaged car after an accident (potentially loss of functional properties) or a hole in the roof of a building (degradation of functional property). In the producing industry, damage is used for e.g. a shattered bearing in a machine, a fire in a production facility, the loss of reputation or the loss of data from a damaged file. Damage is also used in the context of

finances. In materials science, damage is used to describe the state on the micro-scale — e.g. pores, cracks and other defects on the micro-scale. On the macro-scale, damage may, amongst other effects, induce degradation of stiffness or reduction of the yield stress. Clearly, damage is a term which is omnipresent, but with different meanings.

An important aspect in the following work is the delimitation of damage and failure. While in many communities the terms 'damage' and 'failure' can be used synonymously, damage precedes failure in material modelling and in materials science. In these communities, the term damage describes mechanisms which occur locally on the microscale — mostly by means of the creation of new surfaces — and, in addition, it describes their effects on the macro-scale. One may further divide damage into the following subcategories:

- Ductile damage is concerned with damage in connection with large plastic deformation. On the micro-mechanical level, ductile damage can be observed in the form of micro-cracks and micro-voids. Ductile damage is the primary damage type discussed as this work proceeds and an extensive list of references is provided in Section 1.3.1.

- Brittle damage commonly develops without plastic deformations and is exhibited in e.g. rocks, concrete, ceramics and glass. Continuum damage models of Lemaitre-type, without the incorporation of plasticity related effects, are capable of modelling effects related to brittle damage. For damage models specifically designed to capture brittle damage effects, see e.g. [132] or the monographs [51, 95]. An extension to finite deformations can be found in e.g. [44].

- Polycrystalline materials may experience creep damage effects, which originate from the nucleation of microcracks on grain boundaries under elevated temperatures and constant stress levels. The damage models of Kachanov, [89], and Rabotnov [146], already included the description of such creep damage phenomena. Since the publication of these pioneering works, the theory of creep damage has been further extended, see e.g. [27, 45], the review contribution [80] or for creep damage combined with finite strains see [181].

- In the case where a material degrades under cyclic loading conditions, related damage effects are classified as fatigue damage. One may further classify fatigue damage based on the number of cycles before final failure occurs. Fatigue damage constitutes a wide field of research; for more detailed information the reader is referred to, e.g., [107]. Further damage classifications have been established, such as creep fatigue damage and spall damage, which are discussed in the monographs cited above.

- Moreover, damage in composite materials has intensively been studied since the early nineties, see e.g. [99, 176]. In this context, Ladevèze, [100], focused on the

modelling of debonding effects of the fibre matrix interface and microcracking of the matrix itself, while Voyiadjis and Kattan proposed a generalised model incorporating damage and plasticity in composites, [176]. For more detailed information on damage modelling of composites, the reader is referred to e.g. [177].

- Another active field of research in continuum damage is the modelling of damage effects in biological materials. Biological materials typically possess complex (micro-) structures, such as layered vessel walls which can be considered as a composite with layers of different fibre reinforcements, see e.g. [15, 35, 142, 143].

1.2 Experimental analysis of (ductile) damage

Damage can be analysed experimentally either geometrically, e.g. by imaging the microstructure by means of (electron) microscopy, or mechanically by measuring properties which are influenced by damage, e.g. mechanical stiffness, cf. [170] wherein geometric approaches are reported to be more precise but contain large systemic errors. Both approaches provide very different results, and it is not straight-forward to deduce the influence of the (geometrically) observed damage on the overall properties or, vice versa, to deduce which microstructural changes are present due to a change in the mechanical properties.

Ductile damage in dual-phase steel sheets (ferrite-martensite) is analysed geometrically in [82]. They identify the primary damage mechanism to be martensite-cracking triggered by high plastic strains in the surrounding ferrite matrix. Subsequently, further damage sites in the ferrite nucleate at the crack in the martensite. Furthermore, they observe a microstructure with finer grains resulting in a more dispersed damage state as well as necking occurring later, at higher strains.

The work [73] analyses damage in DP1000 dual-phase steel by means of in-situ microtensile tests. With the help of DIC the authors are able to quantify the local strain state and report a heterogeneous strain distribution with strains accumulating in bands orientated at 45 degrees loading direction. The damage mechanisms they observe are void nucleation and growth in the ferrite and crack initiation on the interface between ferrite and martensite.

Another dual-phase steel is DP800, which is also used in this work, see Section 3.4.1. Damage mechanisms in DP800 were recently identified in [96] by means of algorithmic detection and categorisation of voids in large panorama images obtained by electron microscopy — a novel methodology validated against established methods in [97]. The authors primarily observed (brittle) martensite cracking at small plastic strains and a shift towards ductile mechanisms as the plastic strains increase. The dominating ductile mechanisms are void nucleation, e.g. in form of phase boundary decohesion, and void plasticity. Analysis of the martensite crack orientation in DP800 sheets, as carried out in [120], revealed cracks to be primarily oriented perpendicular to the loading direction for

uniaxial tension loading and an isotropic distribution of crack-angles for biaxial tension loading.

A combination of geometrical and mechanical damage measurement of DP800 sheets is approached in [98]. Their analysis concludes that the local stress state influences void nucleation and that the global stress state influences void growth. Furthermore, they found a correlation between plastic strains and the number of voids, i.e. plastic strains influence void nucleation. Stress triaxiality correlates with median void size and thus influences void growth. Lastly, they observed void coalescence to occur mainly along shear bands.

Similarly, in [33], the influence of the stress-state on damage (and fracture) mechanisms is analysed for a biaxially loaded aluminium alloy. They use a fitted anistropic continuum damage model to obtain the stress state for each material point based on strain measurement by means of DIC.

1.3 Damage in continuum mechanics

The description of damage from the perspective of continuum mechanics — often called continuum damage mechanics (CDM) — focuses on the change of mechanical properties of a sample material by means of degradation processes — starting with the initiation of micro-cracks and ending with the beginning formation of a macro-crack. The field of damage mechanics dates back to the original findings from Kachanov [89] and further development by Rabotnov [146], who proposed a single scalar damage variable to model the effects of creep damage. A review of the early research can be found in [40]. It took until the late seventies for continuum damage mechanics to become a highly active research topic, [85], and several monographs on continuum damage mechanics have been published since, see e.g. [90, 106, 131]. While initially only creep damage was considered, the term damage has since been extended to many different physical mechanisms and phenomenological effects. Similar to the distinction of damage types described in the previous section, continuum damage can be divided into several subcategories dependent on the material studied, on the acting physical mechanisms and on the applied loading conditions. In the following, this work focuses on ductile damage in metallic materials.

1.3.1 Ductile damage in continuum mechanics

Modelling of ductile damage in the sense of continuum damage mechanics can be divided into micromechanically motivated models and phenomenological damage models. On the one hand, micro-mechanically motivated Gurson-type approaches model damage as the evolution of void-volume fraction influencing the evolution of plasticity without affecting the elastic properties, see [77, 133, 173]. On the other hand, Lemaitre-type models introduce a phenomenologically motivated damage variable which deteriorates the elastic properties of the material, see [95, 105, 106]. The probably most prominent

candidate from the first category is the model based on void volume fractions proposed by Gurson [77] and their extensions by Tvergaard and Needleman [173] as well as by Rousselier [152]. Many researchers have worked on and with these models, see e.g. the recent contributions [36, 190] and references cited therein. Phenomenological models are typically referred back to the $1 - d$ approach established by Lemaitre [105, 106] and Krajcinovic [95] and are continuously further developed, see e.g. [14, 31, 32, 94, 179]. A detailed literature review on ductile damage and fracture can be found in [10, 25].

Damage is intrinsically of anisotropic nature. Early contributions, however, considered damage isotropically by means of a scalar damage variable. Anisotropic damage is typically represented by a tensor of at least second order [104] and many different approaches have been proposed with tensors of either second or fourth order, see e.g. [26, 42, 93]. The preferred directions of anisotropy may either be fixed or, as is typical for ductile damage in metals, they evolve dependent on the applied load. One of the approaches dealing with evolving anisotropy is the introduction of a fictitious configuration, see [28, 34, 61, 123, 125, 130, 157] amongst others.

Many recent contributions focus on anisotropic ductile damage. Most contributions use a second order tensor as damage variable. A fourth order damage tensor evolving dependent on the applied load is proposed in [16] for application in ceramic matrix-composites. Multiple scalar damage variables, each attached to a different mode of a decomposed stress tensor and its evolution governed by its own surface, are proposed in e.g. [1] to model ductile damage in concrete. Examples for material models using the fictitious configuration are the model proposed in [14] where the evolution of damage and plasticity is governed by separate potentials in a two-surface setting or, the model proposed in [102] where a single-surface setting for small strains is used. A ductile damage model based on visco-plasticity with its principal damage directions being aligned with its principal stress directions is applied to semi-crystalline polymers in [9]. In the contribution [83] a two-surface approach governs evolution of damage and plasticity for a model using logarithmic strains with an additive split. An approach where structural tensors are used for damage is proposed in [148].

1.3.2 Influence of stress triaxiality and Lode-angle

Although most of the following references are concerned with ductile failure — as opposed to ductile damage which lies in the focus of this work — it may be inferred that stress-triaxiality and Lode-angle also influence ductile damage as ductile damage finally results in ductile failure. The importance of stress triaxiality on ductile failure was first observed experimentally by Hancock and Mackenzie, cf. [79]. It took until many years later for the Lode-angle to be recognised as another important factor influencing ductile failure, see [183]. Thereafter, it has been shown that stress-triaxiality is an important factor for driving pore growth, whereas the Lode-angle is connected to micro-crack elongation, see e.g. [119, 191].

As ductile failure is often determined in terms of quantities stemming from plasticity, the dependency on the Lode-angle was incorporated into the formulation of the yield surface as a kind of interpolation between the Tresca yield surface and the von Mises yield surface, see [11, 12]. In [129], initiation of ductile failure is analysed and experiments with different levels of stress-triaxiality and Lode-angle are compared with each other. The authors conclude that the direct influence of the Lode-angle on failure is less pronounced, but that the Lode-angle has a significant influence on the evolution of the yield surface instead. Consequently, they propose a new yield surface dependent on the Lode angle which was geometrically constructed and which lies in between the yield surfaces of Tresca and von Mises. However, the resulting yield surface is non-convex and the impact on thermodynamics is not discussed in their contribution. A generalised yield surface in the form of $f(p) + f(\theta)\, q^2 - 1 = 0$, with pressure p, Lode-angle θ and deviatoric stress q is proposed in [137] and the conditions for convexity of the proposed surface are determined by the methodology based on differential geometry proposed in [169].

A micro-mechanical investigation using periodic boundary conditions on a representative volume element containing a spherical void is reported in [19]. Therein, the authors have found out that the influence of the Lode-angle on void shape and on void coalescence decreases as stress-triaxiality rises. Similarly, in [58] a unit-cell analysis of a single pore is performed and the computed failure strain is plotted over stress-triaxiality and Lode-angle.

Experimentally, the influence of triaxiality and Lode-angle on ductile failure is analysed, e.g., by means of butterfly tests in [4]. On the contrary, the theoretical and numerical study by Mattiello and Desmorat, cf. [118], analyses the dependence of various previously proposed failure loci on triaxiality and Lode-angle and compares them to existing non-associated damage evolution equations in the literature.

Stress-triaxiality and Lode-angle have been explicitly taken into account for damage evolution in the modelling of ductile fracture in [191]. An empiric continuum damage model for aluminium — explicitly taking stress-triaxiality and Lode-angle in the damage surface into account — is proposed in [72]. The proposed model is calibrated with biaxial experiments by using proportional and non-proportional load paths by means of full-field displacement measurements obtained from DIC (digital image correlation). Similarly, a non-associated single-surface model is developed in [189]. They propose effective quantities wherein the influence of damage is more pronounced for positive stress-triaxiality. Furthermore, damage evolution is influenced by a function of the Lode-angle.

1.3.3 Microcrack-closure reopening effect

The microcrack-closure reopening (MCR) effect — often synonymously denoted unilateral damage effect — describes a different material response whether the local material state is tension or compression. To this end, a model where (scalar) damage affected neg-

atively signed stresses differently than positively signed stresses was proposed in [109], see also [131].

A more general format for discerning tensile and compressive contributions was published shortly afterwards, see [138]. Therein, the author has proposed the use of projection tensors to extract positive and negative strains or stresses. In the following years, several other projection operators were proposed — each with different characteristics, but also with different deficiencies, especially problems with spurious energy dissipation as pointed out in the review [185]. Consequently, they propose a projection operator without spurious energy dissipation.

Damage models with a single damage variable differently affecting tensile and compressive contributions were soon extended by multiple damage variables. The (brittle-elastic) damage model for concrete proposed in [24] introduced a tensile and a compressive damage variable. Each variable is represented by a tensor of second order and describes microcracks. They affect the positive, respectively negative, strain in the Helmholtz energy. In addition, a scalar damage variable — describing the effect of pores — is introduced which affects the volumetric strain contribution. In the same work, the authors propose a very similar second model, but which is formulated in terms of the Gibbs enthalpy. The damage variables are all reduced to scalar quantities and instead of splitting strains, the stresses are split into positive and negative contributions.

Many of the damage models proposed in the earlier stages, which take the unilateral damage effect into account, suffer from a discontinuous stress/strain response and lack major symmetry of the stiffness tensor under certain loading conditions, as explained in the review contribution [41]. The same author then proposes a damage model free of these deficiencies, cf. [42].

Another model is the so-called 'd+/d- damage model', originally proposed in [38] as a formulation directly in state laws. Therein, two damage variables — 'd+' referred to as tensile damage and 'd-' referred to as compressive damage — are introduced. Many years later the model was reformulated by using projection operators and a formulation in the Helmholtz energy with internal variables, see [37]. The two damage variables d+/d- may each evolve independently, but conceptually follow identical evolution equations. All described models up until now, were concerned with brittle-elastic material behaviour, typical for rocks or concrete. However, the contribution [39] incorporated permanent strains (e.g. plastic strains) into the model formulation. Lastly, the work [184] contains another reformulation of the d+/d- damage model. The model is formulated with variationally interpreted positive/negative projection tensors which results in a formulation with a stiffness tensor possessing major symmetry.

In [61], the scalar damage model including the MCR effect, proposed in [62], is extended to anisotropic damage formulated in terms of the fictitious configuration concept, cf. [126]. Damage is described by a single integrity tensor of second order and affects the stiffness only under tensile loading.

Further models including the MCR effect are e.g. the model from [74] wherein the MCR effect is incorporated but without making use of projection operators and instead

the elastic stiffness is specified dependent on different crack directions for an orthotropic material; the model described in [55] where damage evolves only with the positive part of effective strains; or the model proposed in [2] which introduced two separate damage variables for tension and for compression — each governed by their own damage growth function.

Lastly, in [64] an efficient approach to incorporate the MCR effect into an already existing damage model with only minor modifications has been proposed. The authors demonstrate their approach by means of a brittle-elastic, small strain, gradient-extended damage model where the strains in the Helmholtz energy are split into positive and negative contributions and where the negative contribution is only partially affected by damage.

1.4 Regularisation

A well-known deficiency of damage models, respectively all continuum models including softening or degradation effects, is the possible loss of ellipticity of the governing equations, see e.g. [110], and references cited therein, where the underlying acoustic tensor is investigated. In the context of Finite Element formulations, the loss of ellipticity may lead to mesh dependent results. To remedy mesh dependency, multiple non-local damage theories have been proposed. The contributions by Bažant et al. [22, 23] introduce a non-local damage variable which is defined as the integral value of an only pointwise defined, local damage variable. However, non-local formulations based on gradients are more commonly used. Theories incorporating strain gradients were established at an earlier stage, see e.g. [48, 141, 172], but theories based on gradients of other variables, such as damage, were thereafter proposed [165, 166]. If gradients are explicitly taken into account, the underlying Karush-Kuhn-Tucker conditions may need to be dealt with on a global (Finite Element) level. Thereto, an active-set algorithm may be used, see e.g. [110, 111], or non-linear complementarity functions my be used, see e.g. [76]. An approach using a direct damage gradient in combination with an operator split is proposed in [175]. Implicitly taking gradients into account by means of gradient-enhancement [56] or the micromorphic approach [67] allows the treatment of the Karush-Kuhn-Tucker conditions on the local (integration point) level. This approach has been adopted throughout many contributions in the literature, see [31, 136, 142, 178, 188] amongst others. Effort has been made to explore efficient implementations of gradient-enhancement into commercial Finite Element tools [139, 155]. A different approach to efficiently include gradients has been published, see [88]. The gradient-enhanced theory has been extended to incorporate non-constant regularisation parameters in e.g. [135, 174, 188], i.e. the gradient contribution in the free Helmholtz energy is weighted by a term dependent on history variables, e.g. the damage state itself.

Regularisation of anisotropic damage was first achieved by the incorporation of non-local strain measures, cf. e.g. [52, 53] which used a second order tensor as damage

variable. The contribution [145] used a viscous regularisation to regularise a model formulated in terms of an orthotropic damage variable, which was later expanded in [87] to the regularisation by means of four non-local equivalent strains. Similarly, integral averaging of strain measures was used to regularise an orthotropic intra-laminar damage model for fibre-reinforced composites in [69].

Anisotropic brittle damage was successfully regularised with the help of the gradient-extension of the scalar damage hardening variable, even though the actual damage variable was a tensor of second order, cf. [63]. Regularisation of anisotropic damage specified in terms of multiple scalar damage variables was efficiently achieved by gradient-extension of a scalar averaged damage variable in [156] by using a (fast Fourier transform) FFT-solver. The contribution [43] proposed a non-local Gurson-type model for fibre-reinforced composites where regularisation was achieved by gradient-extension of the isotropic hardening variable. Anisotropic damage in a single crystal, in analogy to crystal plasticity, was regularised by gradient-extension of a scalar accumulated damage variable in [7]. A crystal plasticity formulation including a scalar micromorphic variable for strain-like micro-damage is proposed in [113]. In [102] the full second order tensor is gradient-enhanced, resulting in six (due to symmetry) additional degrees of freedom. The contribution [83] achieved regularisation by gradient-extension of the three invariants of the second order damage tensor. A gradient-extended damage formulation for solid-shells was proposed and analysed in [17, 18].

Another mathematically involved regularisation approach is the Eikonal non-local damage model [54]. This approach uses an integral averaging of the damage variable where the integrated length depends on propagation time which is influenced by damage itself. The Eikonal non-local damage approach has since been developed further in [147] and [171].

In the modelling of ductile damage, localisation is not necessarily solely caused by damage itself but may also occur due to necking induced by plastic flow. Gradient-enhancement of damage as well as plasticity has been shown to regularise the overall response in [57]. In [83] the necessity of regularisation of plasticity to counteract localising shear bands is mentioned, and Friedlein et al. [70] analysed the regularisation of plasticity by using logarithmic strains in additive form. In a single-surface damage formulation where damage evolution is dependent on the (plastic) Lagrange multiplier, the contribution [71] demonstrated gradient-enhancement of plasticity to be sufficient for the regularisation of damage. For further literature and modelling approaches on gradient-enhanced plasticity see, e.g., [92], where a gradient-enhanced plasticity framework with additional degrees of freedom related to plastic deformation contributions and non-local (Mandel-type) stresses is proposed, and [91, 187] as well as references cited in these works.

A different approach of regularisation was proposed in [59]. Instead of regularisation contributions in space, a regularisation in time is proposed by introducing rate dependent damage evolution. This type of regularisation is often denoted as viscous regularisation and intrinsically introduces dependency of the underlying parameters related to, say,

relaxation time. The modelling approach has been further developed and used for several applications, see e.g. [3, 68, 103, 133].

1.5 Parameter identification

A major challenge for the simulation of production processes is the identification of suitable material parameters. A detailed description of the parameter identification process in combination with the Finite Element method is given in [116]. Parameter identification in combination with gradient damage models is first reported in [115], though without taking full-field measurements into account. Further information regarding parameter identification is summarised in the review contributions [8, 117]. In recent years, Roux and Bouchard [153] have been working on parameter identification for a local Lemaitre model including full-field data, but have tested the framework only with numerically perturbed simulation data. In [4] a GISSMO failure surface identification is performed by using full-field measurements obtained via DIC (digital image correlation). Direct determination of the change in the elastic modulus — already identified as a suitable measure to quantify damage in [108] — during loading/unloading of DP800 is reported in [5]. An approach for optimisation based parameter identification using full field measurement of displacements is proposed in [149] and extended to thermal full field data in [150]. Parameters of an anisotropic local continuum damage model are identified in [72] by means of biaxial loading tests using full field measurement of displacements.

1.6 Objective and outline of this work

The primary objective of this thesis is to develop a ductile damage model capable of accurately predicting the evolution of plasticity and of damage in a production process. Thereby, the many possibilities of modelling are reduced by adhering to several principles:

- The developed material models shall yield a response on the macro-scale, focusing on capturing the phenomena of the physical material. But, wherever possible, modelling choices should be micro-mechanically motivated, i.e. the physics of the micro-scale should be incorporated or, at least, taken into consideration.

- The proposed models shall be embedded in a computationally robust setting, i.e. they shall yield identical responses independent of the chosen discretisation.

- The material models shall be adaptable to many materials (in the group of ductile metals). Hence, focus is placed on developing a framework rather than on developing one (or multiple) specific material model(s). Consequently, a non-empiric

modelling approach is pursued which is guaranteed to fulfil the dissipation inequality for a large domain of parameters.

The thesis starts by introducing the implementation of the regularisation framework in **Chapter 2**. Due to the inherent softening of (ductile) damage, an implicit gradient-enhancement — the micromorphic approach — is used as numerically efficient regularisation framework. In addition, a summary of a direct gradient-enhanced approach is provided, highlighting key differences between the direct and implicit approaches.

An isotropic ductile damage model is proposed in **Chapter 3**. The main purpose of the isotropic model is to focus on and to analyse regularisation of ductile damage, coupling of damage and plasticity, and identification of parameters. Coupling of damage and plasticity is achieved by using effective driving forces in a multisurface approach, i.e. individual criteria for the onset of damage and plasticity are proposed. The proposed isotropic ductile damage model is regularised by means of the micromorphic approach described in Chapter 2. The parameters of the model are identified for the dual phase steel DP800 and an air-bending process is simulated.

Chapter 4 deals with the extension of isotropic damage to anisotropic damage. To this end, a fictitious (undamaged) configuration is utilised. Implications for the effective driving forces are discussed in detail, where the introduction of an effective damage driving force removes the sole dependence of damage evolution on elastic strains and thereby enables the possibility to predict the onset of failure. Furthermore, the anisotropic ductile damage model is extensively analysed in view of which fields require regularisation.

The last chapter, **Chapter 5**, integrates the micro-crack closure and reopening effect into the models established in the previous chapters. The already existing research, which mostly is concerned with brittle damage in the absence of plastic strains, is further developed in order to include plastic strains. Ultimately, two separate damage variables — one degrading elastic stiffness under tension and one under compression — are introduced. They represent the expected jump in stiffness from the reopening of previously compressed micro-cracks.

2 A Finite Element framework for regularised damage

This chapter summarises details regarding the Finite Element implementation. The basis of the described topics can be found in relevant textbooks regarding continuum mechanics and Finite Element analysis, see e.g. [21, 30, 84] amongst many contributions.

The first topic, after a brief introduction of the essential kinematics in Section 2.1, is concerned with the micromorphic approach [67] — or the implicit gradient-enhanced framework [56, 166] — see Section 2.2. In a generalised format, the governing equations are derived and discretised by means of finite elements. The resulting non-linear equations are solved with an iterative Newton-Raphson scheme. To this end, the system of linear equations which needs to be solved in each iteration is obtained from linearisation.

Contrary to the (implicit) micromorphic approach, Section 2.3 summarises the regularisation approach using gradients directly which was published in the joint work [76]. A brief description of the material model — including the nonlocality residual [144] — is given, since formulation of the material model and implementation of the Finite Element method are strongly interconnected in the direct regularisation approach. The inequalities from the local Karush-Kuhn-Tucker problem need to be solved globally, e.g. by means of complementarity functions, resulting in a different structure compared to standard Finite Element implementations.

Lastly, Section 2.4 is concerned with implementation details regarding application and control of loading and of boundary conditions. It includes a brief summary of linear constraints [180] and of arc-length methods [46] as well as a combination of both methods.

2.1 Essential kinematics

In order to describe the Finite Element formulation, some essential kinematic relations need to be introduced. Let the reference (or material) configuration be denoted by $\mathcal{B}_0$ and let $\boldsymbol{X}$ be the related placement vector, see Figure 2.1. Furthermore, let $\mathcal{B}_t$ denote the current (or spatial) configuration with placement vector $\boldsymbol{x}$. A deformation

map $\boldsymbol{\varphi}(\boldsymbol{X}, t)$ is introduced mapping placements from the reference configuration to the spatial configuration, i.e. $\boldsymbol{x} = \boldsymbol{\varphi}(\boldsymbol{X}, t)$ with t denoting time. The mapping between the tangent spaces of both configurations is introduced as the deformation gradient

$$\boldsymbol{F} := \nabla_{\boldsymbol{X}} \boldsymbol{\varphi} = \frac{\mathrm{d}\boldsymbol{\varphi}}{\mathrm{d}\boldsymbol{X}} = \frac{\mathrm{d}\boldsymbol{x}}{\mathrm{d}\boldsymbol{X}} \,. \tag{2.1}$$

Line elements in the reference configuration $\mathrm{d}\boldsymbol{X}$ are transformed to the current configuration as $\mathrm{d}\boldsymbol{x} = \boldsymbol{F} \cdot \mathrm{d}\boldsymbol{X}$. Referential volume elements $\mathrm{d}V$ transform according to $\mathrm{d}v = J \, \mathrm{d}V$, with $J := \det(\boldsymbol{F})$. Surface elements in reference configuration $\mathrm{d}\boldsymbol{A}$ can be transformed to the current configuration via $\mathrm{d}\boldsymbol{a} = \mathrm{cof}(\boldsymbol{F}) \cdot \mathrm{d}\boldsymbol{A} = J \, \boldsymbol{F}^{-\mathrm{t}} \cdot \mathrm{d}\boldsymbol{A}$.

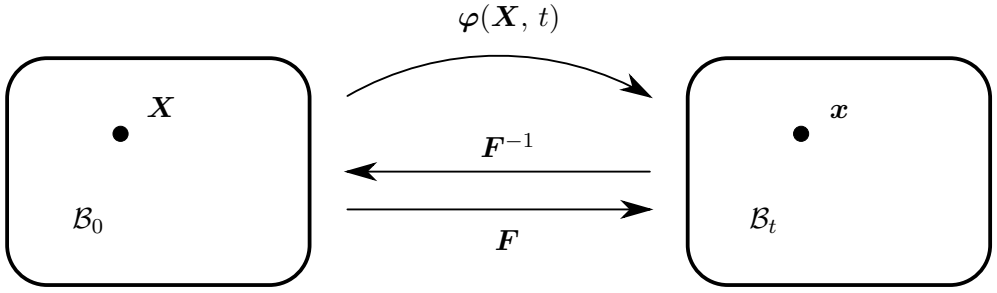

Figure 2.1: Sketch of the reference and current configuration.

2.2 Micromorphic approach

The idea of the gradient-enhanced framework, cf. [56, 67, 166], is to introduce additional (global) field variables which are coupled to (local) material point variables in the context of a micromorphic formulation. By only incorporating the gradients of the introduced non-local (global) field variables — and not the gradients of the (local) material point variables — the ensuing Karush-Kuhn-Tucker problem can still be solved on a (local) material point level. Let the vector of aggregated non-local (global) field variables be denoted by $\boldsymbol{\phi}(\boldsymbol{X}, t)$. The Helmholtz energy Ψ can be additively split into a local part Ψ^{loc}, containing e.g. the elastic part of the energy, a gradient part Ψ^{grd} and a coupling part Ψ^{cpl}, i.e.

$$\Psi = \Psi^{\mathrm{loc}}(\boldsymbol{F}, \boldsymbol{\mathcal{I}}) + \Psi^{\mathrm{grd}}(\nabla_{\boldsymbol{X}} \boldsymbol{\phi}) + \Psi^{\mathrm{cpl}}(\boldsymbol{F}, \boldsymbol{\phi}, \boldsymbol{\mathcal{I}}) \,. \tag{2.2}$$

The gradient contribution to the Helmholtz energy Ψ^{grd} may additionally depend on other local variables, compare e.g. the approach in [174, 188]. In this framework it is assumed to remain independent of further local variables and, notably, it is independent of the non-local field variables $\boldsymbol{\phi}$. Contrary, the coupling contribution Ψ^{cpl} is assumed to remain independent of the gradient of the non-local field variables $\nabla_{\boldsymbol{X}} \boldsymbol{\phi}$. Since localisation is more pronounced under tensile loading, the referential gradient $\nabla_{\boldsymbol{X}} \boldsymbol{\phi}$ is chosen as it should provide stronger regularisation (under tensile loading).

2.2.1 Formulation of the governing equations

The governing system of equations is derived by following the postulate of minimum potential energy. Let the total potential energy of the quasi-static system be given by

$$\Pi = \int_{\mathcal{B}_0} \Psi \, \mathrm{d}V - \int_{\mathcal{B}_0} \boldsymbol{B} \cdot \boldsymbol{\varphi} \, \mathrm{d}V - \int_{\partial\mathcal{B}_0} \boldsymbol{T} \cdot \boldsymbol{\varphi} \, \mathrm{d}A \,, \tag{2.3}$$

where deformation independent (dead) loads in the form of the (dead) body forces $\boldsymbol{B}$ act in the body $\mathcal{B}_0$ and the (dead) traction forces $\boldsymbol{T}$ act on the surface $\partial\mathcal{B}_0$. Tractions and additional body forces for the non-local field variables $\boldsymbol{\phi}$ are assumed to vanish, i.e. homogeneous Neumann boundary conditions are assumed. From the extremal conditions for the minimum of the total potential energy one obtains the governing system of equations in weak form as

$$\int_{\mathcal{B}_0} \frac{\partial \Psi}{\partial \boldsymbol{F}} : \nabla_{\boldsymbol{X}} \delta\boldsymbol{\varphi} \, \mathrm{d}V - \int_{\mathcal{B}_0} \boldsymbol{B} \cdot \delta\boldsymbol{\varphi} \, \mathrm{d}V - \int_{\partial\mathcal{B}_0} \boldsymbol{T} \cdot \delta\boldsymbol{\varphi} \, \mathrm{d}A \stackrel{!}{=} 0 \,, \tag{2.4}$$

$$\int_{\mathcal{B}_0} \frac{\partial \Psi}{\partial \nabla_{\boldsymbol{X}} \boldsymbol{\phi}} \bullet \nabla_{\boldsymbol{X}} \delta\boldsymbol{\phi} + \frac{\partial \Psi}{\partial \boldsymbol{\phi}} \bullet \delta\boldsymbol{\phi} \, \mathrm{d}V \stackrel{!}{=} 0 \,, \tag{2.5}$$

with $\bullet$ denoting the appropriate scalar product and where $\delta\boldsymbol{\varphi}$ as well as $\delta\boldsymbol{\phi}$ are appropriate test-functions. The occurring derivatives can be identified as the Piola stress tensor $\boldsymbol{P}$ and the non-local driving forces related to the non-local field variables and its gradients, i.e.

$$\boldsymbol{P} := \frac{\partial \Psi}{\partial \boldsymbol{F}} \,, \qquad \boldsymbol{Y}_{\mathrm{grd}} := \frac{\partial \Psi}{\partial \nabla_{\boldsymbol{X}} \boldsymbol{\phi}} \,, \qquad \boldsymbol{Y} := \frac{\partial \Psi}{\partial \boldsymbol{\phi}} \,. \tag{2.6}$$

The set of equations (2.4) and (2.5) shall be solved with the Finite Element method. To this end, relevant quantities are discretised in the following section.

In addition, by using Gauss's divergence theorem as well as some algebra on (2.4) and (2.5) the Euler-Lagrange equations in local form are obtained, i.e.

$$\begin{aligned} \nabla_{\boldsymbol{X}} \cdot \boldsymbol{P} - \boldsymbol{B} &= \boldsymbol{0} \quad \text{in} \quad \mathcal{B}_0 \,, \\ \boldsymbol{P} \cdot \boldsymbol{N} &= \boldsymbol{T} \quad \text{on} \quad \partial\mathcal{B}_0 \,, \end{aligned} \tag{2.7}$$

$$\begin{aligned} \nabla_{\boldsymbol{X}} \cdot \boldsymbol{Y}_{\mathrm{grd}} - \boldsymbol{Y} &= \boldsymbol{0} \quad \text{in} \quad \mathcal{B}_0 \,, \\ \boldsymbol{Y}_{\mathrm{grd}} \cdot \boldsymbol{N} &= \boldsymbol{0} \quad \text{on} \quad \partial\mathcal{B}_0 \,. \end{aligned} \tag{2.8}$$

2.2.2 Discretisation

The boundary value problem is discretised in time and space. Since the quasi-static problem shall not explicitly depend on time, the simulated time is only used to incrementally apply external loads. The actual time step is obtained as $t_{n+1} = t_n + \Delta t_n$,

where the time increment Δt_n is not necessarily constant. In view of the discretisation in space, configuration $\mathcal{B}_0$ is subdivided into n_{el} finite elements so that

$$\mathcal{B}_0 \approx \mathcal{B}_0^h = \bigcup_{e=1}^{n_{\text{el}}} \mathcal{B}_0^e \,. \tag{2.9}$$

To each element e there are n_{en}^u nodes attached which are referred to the deformation $\boldsymbol{\varphi}$ and, respectively, n_{en}^ϕ nodes which are referred to the non-local field variables $\boldsymbol{\phi}$. The referential placements $\boldsymbol{X}$ are interpolated with shape functions $N_A^{\boldsymbol{X}}$ resulting in

$$\boldsymbol{X} \approx \boldsymbol{X}^h = \sum_{A=1}^{n_{\text{en}}^u} N_A^{\boldsymbol{X}}\, \boldsymbol{X}_A \,, \tag{2.10}$$

where $\boldsymbol{X}_A$ is the referential placement at node A. Following a (partial) isoparametric concept ($N^{\boldsymbol{X}} = N^{\boldsymbol{\varphi}} \neq N^{\boldsymbol{\phi}}$) together with the Bubnov-Galerkin method, one obtains

$$\begin{aligned}
\boldsymbol{\varphi} &\approx \boldsymbol{\varphi}^h = \sum_{C=1}^{n_{\text{en}}^u} N_C^{\boldsymbol{\varphi}}\, \boldsymbol{\varphi}_C \,, & \delta\boldsymbol{\varphi} &\approx \delta\boldsymbol{\varphi}^h = \sum_{A=1}^{n_{\text{en}}^u} N_A^{\boldsymbol{\varphi}}\, \delta\boldsymbol{\varphi}_A \,, \\
\boldsymbol{F} &\approx \boldsymbol{F}^h = \sum_{C=1}^{n_{\text{en}}^u} \boldsymbol{\varphi}_C \otimes \nabla_{\boldsymbol{X}} N_C^{\boldsymbol{\varphi}} \,, & \nabla_{\boldsymbol{X}}\delta\boldsymbol{\varphi} &\approx \nabla_{\boldsymbol{X}}\delta\boldsymbol{\varphi}^h = \sum_{A=1}^{n_{\text{en}}^u} \delta\boldsymbol{\varphi}_A \otimes \nabla_{\boldsymbol{X}} N_A^{\boldsymbol{\varphi}} \,, \\
\boldsymbol{\phi} &\approx \boldsymbol{\phi}^h = \sum_{D=1}^{n_{\text{en}}^\phi} N_D^{\boldsymbol{\phi}}\, \boldsymbol{\phi}_D \,, & \delta\boldsymbol{\phi} &\approx \delta\boldsymbol{\phi}^h = \sum_{B=1}^{n_{\text{en}}^\phi} N_B^{\boldsymbol{\phi}}\, \delta\boldsymbol{\phi}_B \,, \\
\nabla_{\boldsymbol{X}}\boldsymbol{\phi} &\approx \nabla_{\boldsymbol{X}}\boldsymbol{\phi}^h = \sum_{D=1}^{n_{\text{en}}^\phi} \boldsymbol{\phi}_D \otimes \nabla_{\boldsymbol{X}} N_D^{\boldsymbol{\phi}} \,, & \nabla_{\boldsymbol{X}}\delta\boldsymbol{\phi} &\approx \nabla_{\boldsymbol{X}}\delta\boldsymbol{\phi}^h = \sum_{B=1}^{n_{\text{en}}^\phi} \delta\boldsymbol{\phi}_B \otimes \nabla_{\boldsymbol{X}} N_B^{\boldsymbol{\phi}} \,.
\end{aligned} \tag{2.11}$$

Inserting the discretisation (2.11) into the weak forms (2.4) and (2.5) allows us to separate the nodal values from the test-functions and, together with the definitions of the internal and external forces

$$\boldsymbol{f}_{eA}^{\text{int},\boldsymbol{\varphi}} = \int_{\mathcal{B}_0^e} \boldsymbol{P} \cdot \nabla_{\boldsymbol{X}} N_A^{\boldsymbol{\varphi}} \,\mathrm{d}V \,, \tag{2.12}$$

$$\boldsymbol{f}_{eA}^{\text{ext},\boldsymbol{\varphi}} = \int_{\mathcal{B}_0^e} \boldsymbol{B}\, N_A^{\boldsymbol{\varphi}} \,\mathrm{d}V + \int_{\partial\mathcal{B}_0^e} \boldsymbol{T}\, N_A^{\boldsymbol{\varphi}} \,\mathrm{d}A \,, \tag{2.13}$$

$$\boldsymbol{f}_{eB}^{\text{int},\boldsymbol{\phi}} = \int_{\mathcal{B}_0^e} \boldsymbol{Y}_{\text{grd}} \cdot \nabla_{\boldsymbol{X}} N_B^{\boldsymbol{\phi}} + \boldsymbol{Y}\, N_B^{\boldsymbol{\phi}} \,\mathrm{d}V \,, \tag{2.14}$$

the discretised weak forms are obtained by multiplication of the internal and external forces with the (element independent) test-functions $\delta\boldsymbol{\varphi}_A$ and $\delta\boldsymbol{\phi}_B$, i.e.

$$\begin{aligned}
\delta\boldsymbol{\varphi}_A \cdot \boldsymbol{f}_{eA}^{\text{int},\boldsymbol{\varphi}} - \boldsymbol{f}_{eA}^{\text{ext},\boldsymbol{\varphi}} &= 0 \,, \\
\delta\boldsymbol{\phi}_B \cdot \boldsymbol{f}_{eB}^{\text{int},\boldsymbol{\phi}} &= 0 \,.
\end{aligned} \tag{2.15}$$

Since the equations (2.15) need to hold for arbitrary values of the test-functions $\delta\boldsymbol{\varphi}_A$ and $\delta\boldsymbol{\phi}_B$, the sum of the forces needs to vanish. Hence, the residuals concerned with element e and node A, respectively node B, are introduced as

$$\begin{aligned} \boldsymbol{r}^{\boldsymbol{\varphi}}_{eA} &= \boldsymbol{f}^{\mathrm{int},\boldsymbol{\varphi}}_{eA} - \boldsymbol{f}^{\mathrm{ext},\boldsymbol{\varphi}}_{eA} = \boldsymbol{0}\,, \\ \boldsymbol{r}^{\boldsymbol{\phi}}_{eB} &= \boldsymbol{f}^{\mathrm{int},\boldsymbol{\phi}}_{eB} = \boldsymbol{0}\,. \end{aligned} \tag{2.16}$$

2.2.3 Linearisation

The non-linear residuals (2.16) are, after assembly, solved with an iterative Newton-Raphson scheme. A Taylor series expansion of these residuals at iteration step $i+1$, neglecting further higher-order terms, yields

$$\boldsymbol{r}^{\boldsymbol{\varphi}}_{eA\,i+1} = \boldsymbol{r}^{\boldsymbol{\varphi}}_{eA\,i} + \sum_{C=1}^{n^{u}_{\mathrm{en}}} \frac{\mathrm{d}\boldsymbol{r}^{\boldsymbol{\varphi}}_{eA\,i}}{\mathrm{d}\boldsymbol{\varphi}_C} \cdot \Delta\boldsymbol{\varphi}_C + \sum_{D=1}^{n^{\phi}_{\mathrm{en}}} \frac{\mathrm{d}\boldsymbol{r}^{\boldsymbol{\varphi}}_{eA\,i}}{\mathrm{d}\boldsymbol{\phi}_D} \bullet \Delta\boldsymbol{\phi}_D\,, \tag{2.17}$$

$$\boldsymbol{r}^{\boldsymbol{\phi}}_{eB\,i+1} = \boldsymbol{r}^{\boldsymbol{\phi}}_{eB\,i} + \sum_{C=1}^{n^{u}_{\mathrm{en}}} \frac{\mathrm{d}\boldsymbol{r}^{\boldsymbol{\phi}}_{eB\,i}}{\mathrm{d}\boldsymbol{\varphi}_C} \cdot \Delta\boldsymbol{\varphi}_C + \sum_{D=1}^{n^{\phi}_{\mathrm{en}}} \frac{\mathrm{d}\boldsymbol{r}^{\boldsymbol{\phi}}_{eB\,i}}{\mathrm{d}\boldsymbol{\phi}_D} \bullet \Delta\boldsymbol{\phi}_D\,, \tag{2.18}$$

where $\Delta\boldsymbol{\varphi}_C$ and $\Delta\boldsymbol{\phi}_D$ are the increments of the respective field. The total derivatives of the residuals are computed element-wise and the stiffness contributions are introduced as

$$\boldsymbol{K}^{\boldsymbol{\varphi}\boldsymbol{\varphi}}_{eAC} := \frac{\mathrm{d}\boldsymbol{r}^{\boldsymbol{\varphi}}_{eA\,i}}{\mathrm{d}\boldsymbol{\varphi}_C} = \int_{\mathcal{B}^e_0} [\boldsymbol{I} \otimes \nabla_{\boldsymbol{X}} N^{\boldsymbol{\varphi}}_A] : \frac{\mathrm{d}\boldsymbol{P}}{\mathrm{d}\boldsymbol{F}} \cdot \nabla_{\boldsymbol{X}} N^{\boldsymbol{\varphi}}_C \,\mathrm{d}V\,, \tag{2.19}$$

$$\boldsymbol{K}^{\boldsymbol{\varphi}\boldsymbol{\phi}}_{eAD} := \frac{\mathrm{d}\boldsymbol{r}^{\boldsymbol{\varphi}}_{eA\,i}}{\mathrm{d}\boldsymbol{\phi}_D} = \int_{\mathcal{B}^e_0} [\boldsymbol{I} \otimes \nabla_{\boldsymbol{X}} N^{\boldsymbol{\varphi}}_A] : \frac{\mathrm{d}\boldsymbol{P}}{\mathrm{d}\boldsymbol{\phi}} \, N^{\boldsymbol{\phi}}_D \,\mathrm{d}V\,, \tag{2.20}$$

$$\boldsymbol{K}^{\boldsymbol{\phi}\boldsymbol{\varphi}}_{eBC} := \frac{\mathrm{d}\boldsymbol{r}^{\boldsymbol{\phi}}_{eB\,i}}{\mathrm{d}\boldsymbol{\varphi}_C} = \int_{\mathcal{B}^e_0} N^{\boldsymbol{\phi}}_B \, \frac{\mathrm{d}\boldsymbol{Y}}{\mathrm{d}\boldsymbol{F}} \cdot \nabla_{\boldsymbol{X}} N^{\boldsymbol{\varphi}}_C \,\mathrm{d}V\,, \tag{2.21}$$

$$\boldsymbol{K}^{\boldsymbol{\phi}\boldsymbol{\phi}}_{eBD} := \frac{\mathrm{d}\boldsymbol{r}^{\boldsymbol{\phi}}_{eB\,i}}{\mathrm{d}\boldsymbol{\phi}_D} = \int_{\mathcal{B}^e_0} N^{\boldsymbol{\phi}}_B \, \frac{\mathrm{d}\boldsymbol{Y}}{\mathrm{d}\boldsymbol{\phi}} \, N^{\boldsymbol{\phi}}_D + [\boldsymbol{I} \otimes \nabla_{\boldsymbol{X}} N^{\boldsymbol{\phi}}_B] : \frac{\mathrm{d}\boldsymbol{Y}_{\mathrm{grd}}}{\mathrm{d}\nabla_{\boldsymbol{X}}\boldsymbol{\phi}} \cdot \nabla_{\boldsymbol{X}} N^{\boldsymbol{\phi}}_D \,\mathrm{d}V\,, \tag{2.22}$$

where the notation assumes the field $\boldsymbol{\phi}$ to be a tensor of second order. All nodal quantities can now be aggregated in the element quantities

$$\boldsymbol{r}_e = \begin{bmatrix} \boldsymbol{r}^{\boldsymbol{\varphi}}_{eA} \\ \boldsymbol{r}^{\boldsymbol{\phi}}_{eB} \end{bmatrix}, \qquad \boldsymbol{K}_e = \begin{bmatrix} \boldsymbol{K}^{\boldsymbol{\varphi}\boldsymbol{\varphi}}_{eAC} & \boldsymbol{K}^{\boldsymbol{\varphi}\boldsymbol{\phi}}_{eAD} \\ \boldsymbol{K}^{\boldsymbol{\phi}\boldsymbol{\varphi}}_{eBC} & \boldsymbol{K}^{\boldsymbol{\phi}\boldsymbol{\phi}}_{eBD} \end{bmatrix}, \qquad \Delta\boldsymbol{z}_e = \begin{bmatrix} \Delta\boldsymbol{\varphi}_C \\ \Delta\boldsymbol{\phi}_D \end{bmatrix}, \tag{2.23}$$

which allows the assembly of the global residual, stiffness matrix and increments as

$$\boldsymbol{r} := \mathop{\mathsf{A}}_{e=1}^{n_{\mathrm{el}}} \boldsymbol{r}_e\,, \qquad \boldsymbol{K} := \mathop{\mathsf{A}}_{e=1}^{n_{\mathrm{el}}} \boldsymbol{K}_e\,, \qquad \Delta\boldsymbol{z} := \mathop{\mathsf{A}}_{e=1}^{n_{\mathrm{el}}} \Delta\boldsymbol{z}_e\,. \tag{2.24}$$

Aggregating all test-function values in the global test-function vector $\boldsymbol{\eta}$, one obtains

$$\boldsymbol{\eta} \cdot \boldsymbol{K} \cdot \Delta \boldsymbol{z} = -\boldsymbol{\eta} \cdot \boldsymbol{r} \,. \tag{2.25}$$

Obviously, (2.25) needs to hold for admissible but otherwise arbitrary values of the test-function vector $\boldsymbol{\eta}$ and one may equivalently solve the system of linear equations

$$\boldsymbol{K} \cdot \Delta \boldsymbol{z} = -\boldsymbol{r} \,. \tag{2.26}$$

2.3 Direct approach using complementarity functions — a short summary

The direct approach summarised in the following was published in the joint work [76] where the author of this thesis contributed the idea and theoretical outline of the Finite Element approach and the material model. Due to the strong interconnection of the direct approach with the material model a brief description of the material model is necessary even though this chapter is concerned with the finite element method.

2.3.1 Nonlocality residual and non-local driving force

For the sake of simplicity, assume an (unspecified) damage model with isotropic damage variable d. Let the Helmholtz energy be given by

$$\Psi = \Psi^{\mathrm{loc}}(\boldsymbol{F},\, d) + \Psi^{\mathrm{grd}}(\nabla_{\boldsymbol{X}} d) \,, \tag{2.27}$$

where the gradient of the damage variable $\nabla_{\boldsymbol{X}} d$ is taken into account directly. Following [60, 110, 144] the (pointwise) dissipation,

$$\mathcal{D} = \boldsymbol{P} : \dot{\boldsymbol{F}} - \dot{\Psi} + \mathcal{P} \geq 0 \,, \tag{2.28}$$

includes the nonlocality residual $\mathcal{P}$ which takes into account dissipation from the surrounding area. With the definition of the stresses and driving forces

$$\boldsymbol{P} = \frac{\partial \Psi}{\partial \boldsymbol{F}} \,, \qquad q = -\frac{\partial \Psi}{\partial d} \,, \qquad \boldsymbol{q} = -\frac{\partial \Psi}{\partial \nabla_{\boldsymbol{X}} d} \,, \tag{2.29}$$

one obtains the reduced dissipation inequality

$$\mathcal{D}^{\mathrm{red}} = q\, \dot{d} + \boldsymbol{q} \cdot \dot{\overline{\nabla_{\boldsymbol{X}} d}} + \mathcal{P} \geq 0 \,. \tag{2.30}$$

The reduced dissipation inequality shall take the form

$$\mathcal{D}^{\mathrm{red}} \doteq \overline{q}\, \dot{d} \geq 0 \,, \tag{2.31}$$

where $\overline{q}$ takes the function of a non-local effective driving force. Combining (2.30) with (2.31) yields an expression for the nonlocality residual, i.e.

$$\mathcal{P} = \overline{q}\,\dot{d} - q\,\dot{d} - \boldsymbol{q} \cdot \dot{\overline{\nabla_{\boldsymbol{X}} d}}\,. \tag{2.32}$$

Since the nonlocality residual does not add any dissipation to the body in total, the condition

$$\int_{\mathcal{B}_0} \mathcal{P}\,\mathrm{d}V = 0 \tag{2.33}$$

holds. Applying some algebra to (2.33) yields

$$\int_{\mathcal{B}_0} \left[\overline{q} + \nabla_{\boldsymbol{X}} \cdot \boldsymbol{q} - q\right]\,\dot{d}\,\mathrm{d}V - \int_{\partial\mathcal{B}_0} \left[\boldsymbol{q} \cdot \boldsymbol{N}\right]\,\dot{d}\,\mathrm{d}A = 0\,, \tag{2.34}$$

which needs to hold for any damage rate $\dot{d} \geq 0$ and one obtains

$$\begin{aligned} &\boldsymbol{q} \cdot \boldsymbol{N} = 0 \qquad &&\text{on} \quad \partial\mathcal{B}_0\,, \\ &\overline{q} = q - \nabla_{\boldsymbol{X}} \cdot \boldsymbol{q} \qquad &&\text{in} \quad \mathcal{B}_0\,, \end{aligned} \tag{2.35}$$

i.e. an expression for the non-local effective driving force $\overline{q}$. Homogeneous Neumann boundary conditions are assumed over the whole boundary $\partial\mathcal{B}_0$ for the damage field. This driving force shall be the determining quantity for onset and evolution of damage, since it incorporates local and non-local effects. Let the onset of damage evolution be governed by the potential

$$\Phi = \overline{q} - q_{\max}\,, \tag{2.36}$$

with damage initiation threshold $q_{\max}$. The evolution equation for damage is then (in quasi-associated form) obtained as

$$\dot{d} = \lambda\,, \tag{2.37}$$

together with typical loading and unloading conditions

$$\Phi \leq 0\,, \qquad \lambda \geq 0\,, \qquad \lambda\,\Phi = 0\,. \tag{2.38}$$

In view of a Finite Element implementation, cf. Section 2.3.2, the damage variable d is a field variable meaning it cannot be solved for at material point level and the loading and unloading conditions need to be taken into account on (global) finite element level.

2.3.2 Finite Element formulation and discretisation

The Finite Element formulation for the mechanical part of the problem at hand stays identical to the one described previously, cf. Section 2.2. The governing equation for the damage variable d, which in this direct approach is a field variable, is obtained from the loading and unloading conditions (2.38). To this end, the damage potential Φ, see (2.36), and the Lagrange multiplier λ are integrated over the body $\mathcal{B}_0$ and multiplied with test functions $\delta\Phi$ and $\delta\lambda$, respectively, i.e.

$$\begin{aligned} \overline{\Phi} &= \int_{\mathcal{B}_0} \boldsymbol{q} \cdot \nabla_{\boldsymbol{X}} \delta\Phi + \delta\Phi \, [q - q_{\max}] \, \mathrm{d}V - \int_{\partial\mathcal{B}_0} \delta\Phi \, \boldsymbol{q} \cdot \boldsymbol{N} \, \mathrm{d}A \,, \\ \overline{\lambda} &= \int_{\mathcal{B}_0} \delta\lambda \, \lambda \, \mathrm{d}V \,, \end{aligned} \tag{2.39}$$

where integration by parts and the Gauss-theorem have been applied already. Classically, evolution of inelasticity governed by some initiation criterion is often solved by means of a predictor-corrector-type scheme. In [110], the loading and unloading conditions are solved on (global) finite element level by means of an active set formulation. The drawback of this formulation, however, is that the size of the system to be solved changes depending on the number of elements where damage evolution is active.

Alternatively, one might solve the loading and unloading conditions — a set of inequalities and equations — by means of a complementarity function, which yields a single equation to be solved, regardless of damage evolution being active or not. One of the complementarity functions is the Fischer-Burmeister function, cf. [66] — more details and a comparison of different implementations can be found in e.g. [20]. Hence, the loading and unloading conditions (2.38) are equivalently fulfilled by

$$r_{\mathrm{d}} = \sqrt{[\Phi]^2 + [\lambda]^2} + \Phi - \lambda \doteq 0 \,. \tag{2.40}$$

Discretisation follows in standard fashion, where all quantities referred to this damage problem use the shape functions N^d, and one obtains

$$\begin{aligned} d \approx d^h &= \sum_{D=1}^{n_{\mathrm{en}}^d} N_D^d \, d_D \,, & \nabla_{\boldsymbol{X}} d \approx \nabla_{\boldsymbol{X}} d^h &= \sum_{D=1}^{n_{\mathrm{en}}^d} d_D \, \nabla_{\boldsymbol{X}} N_D^d \,, \\ \delta\Phi \approx \delta\Phi^h &= \sum_{B=1}^{n_{\mathrm{en}}^d} N_B^d \, \delta\Phi_B \,, & \nabla_{\boldsymbol{X}} \delta\Phi \approx \nabla_{\boldsymbol{X}} \delta\Phi^h &= \sum_{B=1}^{n_{\mathrm{en}}^d} \delta\Phi_B \, \nabla_{\boldsymbol{X}} N_B^d \,, \\ \delta\lambda \approx \delta\lambda^h &= \sum_{B=1}^{n_{\mathrm{en}}^d} N_B^d \, \delta\lambda_B \,, & \nabla_{\boldsymbol{X}} \delta\lambda \approx \nabla_{\boldsymbol{X}} \delta\lambda^h &= \sum_{B=1}^{n_{\mathrm{en}}^d} \delta\lambda_B \, \nabla_{\boldsymbol{X}} N_B^d \,. \end{aligned} \tag{2.41}$$

Inserting these discretisations into (2.42) yields the discretised elementwise quantities referred to node B

$$\begin{aligned} \overline{\Phi}_{eB} &= \int_{\mathcal{B}_0^e} q\, N_B^d + \boldsymbol{q} \cdot \nabla_{\boldsymbol{X}} N_B^d - q_{\max}\, N_B^d \,\mathrm{d}V\,, \\ \overline{\lambda}_{eB} &= \int_{\mathcal{B}_0^e} \lambda\, N_B^d \,\mathrm{d}V\,, \end{aligned} \tag{2.42}$$

which can be assembled into the global nodal quantities

$$\overline{\boldsymbol{\Phi}} := \mathop{\mathsf{A}}_{e=1}^{n_{\mathrm{el}}} \overline{\Phi}_{eB}\,, \qquad \overline{\boldsymbol{\lambda}} := \mathop{\mathsf{A}}_{e=1}^{n_{\mathrm{el}}} \overline{\lambda}_{eB}\,. \tag{2.43}$$

Finally, the Fischer-Burmeister function is applied to each damage degree of freedom A,

$$r_{\mathrm{d},A} = \sqrt{\left[\overline{\Phi}_A\right]^2 + \left[\overline{\lambda}_A\right]^2} + \overline{\Phi}_A - \overline{\lambda}_A \doteq 0\,, \tag{2.44}$$

which yields the final residual referred to the damage field variable $\boldsymbol{r}_{\mathrm{d}}$. Atypically, additional computations are necessary to complete the residual after the assembly process. Hence, the implementation of this direct approach cannot be achieved by only modifying or implementing an element formulation. This leads to a very challenging if not impossible implementation in view of commercial Finite Element tools.

2.4 Linear constraints and arc-length methods

This section is concerned with the combination of arc-length methods and linear constraints, which is provided after short summaries of the individual methods in the first two subsections. All finite element examples in this work are computed using the (custom) Finite Element framework abraxas++. Therein, Dirichlet boundary conditions are applied by means of linear constraints as described in Section 2.4.1, since the resulting structure of the system matrix is beneficial for the iterative parallelised solver package PETSc [13], which is used within abraxas++. A description of further implementation details of abraxas++, i.e. load curves and time stepping control, can be found in Appendix B.

2.4.1 Linear constraints

Following the description in [180], assume a boundary value problem solved with the Finite Element method additionally has to fulfil the linear constraints

$$\boldsymbol{z} = \widetilde{\boldsymbol{c}} + \boldsymbol{P} \cdot \boldsymbol{z}\,, \tag{2.45}$$

where $\boldsymbol{z}$ is the vector of degrees of freedom of the discretised boundary value problem and the vector $\widetilde{\boldsymbol{c}}$ as well as the (unsymmetric) matrix $\boldsymbol{P}$ may depend on time t. In each iteration step of the Finite Element method a system of equations is solved for the increments of the degrees of freedom $\Delta\boldsymbol{z}$. Writing equation (2.45) in incremental form yields

$$\Delta\boldsymbol{z} = \boldsymbol{c} + \boldsymbol{P} \cdot \Delta\boldsymbol{z}\,, \tag{2.46}$$

where the vector $\boldsymbol{c}$ has to be computed from

$$\boldsymbol{c} = \widetilde{\boldsymbol{c}} - \widetilde{\boldsymbol{c}}_n = \widetilde{\boldsymbol{c}} - \boldsymbol{z}_n + \boldsymbol{P}_n \cdot \boldsymbol{z}_n\,, \tag{2.47}$$

with $\boldsymbol{z}_n$ being the degrees of freedom of the previous time step. Direct insertion into the linearised system of equations of the FE-method (2.25) yields

$$\boldsymbol{\eta}^{\mathrm{t}} \cdot \boldsymbol{P}^{\mathrm{t}} \cdot \Big[\boldsymbol{K} \cdot [\boldsymbol{c} + \boldsymbol{P} \cdot \Delta\boldsymbol{z}] - \boldsymbol{b}\Big] = 0\,, \tag{2.48}$$

which already considers that the test functions $\boldsymbol{\eta}$ have to fulfil $\boldsymbol{\eta} = \boldsymbol{P} \cdot \boldsymbol{\eta}$. This system of equations can be rewritten as a system of linear equations in the form

$$\boldsymbol{\eta}^{\mathrm{t}} \cdot \Big[\boldsymbol{K}' \cdot \Delta\boldsymbol{z} - \boldsymbol{b}'\Big] = 0\,, \tag{2.49}$$

with $\boldsymbol{K}' = \boldsymbol{P}^{\mathrm{t}} \cdot \boldsymbol{K} \cdot \boldsymbol{P}$ and $\boldsymbol{b}' = \boldsymbol{P}^{\mathrm{t}} \cdot [\boldsymbol{b} - \boldsymbol{K} \cdot \boldsymbol{c}]$. However, the matrix of this system, $\boldsymbol{K}'$, is rank-deficient, i.e. the rows corresponding to the degrees of freedom with Dirichlet boundary conditions are zero ($z_i = c_i(t)$, i.e. $P_{ij} = 0$). These rows can be used to update the degrees of freedom according to the linear constraint equations. Symmetrising and scaling the linear constraints by multiplying with $\alpha\,[\boldsymbol{I} - \boldsymbol{P}]^{\mathrm{t}}$ allows rewriting equation (2.46) as

$$\alpha\,[\boldsymbol{I} - \boldsymbol{P}]^{\mathrm{t}} \cdot [\boldsymbol{I} - \boldsymbol{P}] \cdot \Delta\boldsymbol{z} - \alpha\,[\boldsymbol{I} - \boldsymbol{P}]^{\mathrm{t}} \cdot \boldsymbol{c} = \boldsymbol{0}\,, \tag{2.50}$$

where $\boldsymbol{I}$ is the identity matrix and $\alpha \in \mathbb{R}^+$. Adding the symmetrised linear constraint equations to the system of equations (2.49) yields a system of equations of, in general, full rank

$$\boldsymbol{\eta}^{\mathrm{t}} \cdot [\widehat{\boldsymbol{K}} \cdot \Delta\boldsymbol{z} - \widehat{\boldsymbol{b}}] = 0\,, \tag{2.51}$$

with the modified system matrix $\widehat{\boldsymbol{K}}$ and right-hand-side vector $\widehat{\boldsymbol{b}}$ given by

$$\widehat{\boldsymbol{K}} = \boldsymbol{P}^{\mathrm{t}} \cdot \boldsymbol{K} \cdot \boldsymbol{P} + \alpha\,[\boldsymbol{I} - \boldsymbol{P}]^{\mathrm{t}} \cdot [\boldsymbol{I} - \boldsymbol{P}] \quad \text{and} \quad \widehat{\boldsymbol{b}} = \boldsymbol{P}^{\mathrm{t}} \cdot [\boldsymbol{b} - \boldsymbol{K} \cdot \boldsymbol{c}] + \alpha\,[\boldsymbol{I} - \boldsymbol{P}]^{\mathrm{t}} \cdot \boldsymbol{c}\,. \tag{2.52}$$

Using this method, Dirichlet boundary conditions can be handled by means of linear constraints (with the corresponding line in $\boldsymbol{P}$ being zero) and additional effort to discern degrees of freedom with associated Dirichlet boundary conditions from degrees of freedom without Dirichlet boundary conditions is no longer necessary. Due to the structure of system matrix $\widehat{\boldsymbol{K}}$ solvers are able to solve the larger system similarly fast.

2.4.2 Arc-length methods

The idea of arc-length methods is to flexibly vary the load level so as to capture non-monotonous load paths, i.e. snap-back or snap-through behaviour. To this end, a loading parameter λ is introduced, which controls the level of external loading. In the context of the Finite Element method the residual form is obtained as

$$\boldsymbol{r}(\boldsymbol{z}) = \boldsymbol{f}_{\text{int}}(\boldsymbol{z}) - \lambda\, \boldsymbol{f}_{\text{ext}} = \boldsymbol{0}\,. \tag{2.53}$$

The loading parameter λ is determined implicitly by a constraint $f^{\text{arc}}(\boldsymbol{z},\, \lambda) = 0$. Various constraint functions have been proposed, from which we will focus on the so called spherical arc-length method proposed in [46], i.e.

$$f^{\text{arc}}(\boldsymbol{z},\, \lambda) = \|\boldsymbol{z} - \boldsymbol{z}_n\|^2 + [\lambda - \lambda_n]^2\, \psi^2\, \|\boldsymbol{f}_{\text{ext}}\|^2 - \Delta s^2 = 0\,, \tag{2.54}$$

wherein typically $\psi = 1/\|\boldsymbol{f}_{\text{ext}}\|$ is chosen and Δs is the chosen radius of the sphere — proportional to the level of loading per step. Linearisation of this system of equations leads to

$$\begin{bmatrix} \boldsymbol{K} & -\boldsymbol{f}_{\text{ext}} \\ \partial_{\boldsymbol{z}} f^{\text{arc}} & \partial_\lambda f^{\text{arc}} \end{bmatrix} \cdot \begin{bmatrix} \Delta\boldsymbol{z} \\ \Delta\lambda \end{bmatrix} = - \begin{bmatrix} \boldsymbol{r} \\ f^{\text{arc}} \end{bmatrix}\,. \tag{2.55}$$

One may explicitly write the solution for the increment of the degrees of freedom $\Delta\boldsymbol{z}$ as

$$\Delta\boldsymbol{z} = -\boldsymbol{K}^{-1} \cdot \boldsymbol{r} + \Delta\lambda\, \boldsymbol{K}^{-1} \cdot \boldsymbol{f}_{\text{ext}} = \Delta\boldsymbol{z}_z + \Delta\lambda\, \Delta\boldsymbol{z}_\lambda\,, \tag{2.56}$$

which enables an explicit solution for the loading parameter. The total current degrees of freedom $\boldsymbol{z}$ as well as the loading parameter can be split into three parts, i.e.

$$\boldsymbol{z} = \boldsymbol{z}_n + \boldsymbol{z}^k + \Delta\boldsymbol{z} \qquad \text{and} \qquad \lambda = \lambda_n + \lambda^k + \Delta\lambda\,, \tag{2.57}$$

where $\bullet^k$ represents the sum of increments of the respective quantity for the first k iterations of the global Newton-Raphson scheme of the current time step. Insertion into the constraint function (2.54) results in

$$\|\boldsymbol{z}^k + \Delta\boldsymbol{z}_z + \Delta\lambda\, \Delta\boldsymbol{z}_\lambda\|^2 + [\lambda^k + \Delta\lambda]^2 - \Delta s^2 = 0\,, \tag{2.58}$$

which is a quadratic equation in $\Delta\lambda$ with the two solutions

$$\Delta\lambda_{1,2} = -\frac{a_2}{a_1} \pm \sqrt{\frac{a_2^2}{a_1^2} + \frac{a_3}{a_1}}\,. \tag{2.59}$$

The constants a_i are given by

$$a_1 = 1 + \|\Delta\boldsymbol{z}_\lambda\|^2\,, \tag{2.60}$$

$$a_2 = \Delta\boldsymbol{z}_\lambda \cdot [\boldsymbol{z}^k + \Delta\boldsymbol{z}_z] + \lambda^k\,, \tag{2.61}$$

$$a_3 = \|\boldsymbol{z}^k + \Delta\boldsymbol{z}_z\|^2 + \left[\lambda^k\right]^2 - \Delta s^2\,. \tag{2.62}$$

From the two possible solutions $\Delta\lambda_{1,2}$ a suitable one has to be chosen. An elegant way is to employ a minimum angle criterion — the increment which results in the smallest angle $\theta_{1,2}$ between the previous solution and the solution with the current increment, i.e.

$$\Delta s^2 \cos(\theta_i) = \boldsymbol{z}^k \cdot [\boldsymbol{z}^k + \Delta\boldsymbol{z}_z + \Delta\lambda_i \, \Delta\boldsymbol{z}_\lambda] + \lambda^k [\lambda^k + \Delta\lambda_i], \quad i = 1, 2\,. \tag{2.63}$$

This requires a predictor in the first iteration step, since $\boldsymbol{z}^k = \boldsymbol{0}$ and $\lambda^k = 0$ in the first iteration. One may choose

$$\lambda^{k=1} = \begin{cases} +\Delta s \, \|\Delta\boldsymbol{z}_\lambda\|^{-1} & \text{if} \quad \Delta\boldsymbol{z}_\lambda \cdot \boldsymbol{f}_{\text{ext}} > 0 \\ -\Delta s \, \|\Delta\boldsymbol{z}_\lambda\|^{-1} & \text{if} \quad \Delta\boldsymbol{z}_\lambda \cdot \boldsymbol{f}_{\text{ext}} < 0 \end{cases} . \tag{2.64}$$

2.4.3 Combining linear constraints with arc-length methods

The previously described methods are now combined. Thus, arc-length methods are able to be applied to inhomogeneous Dirichlet boundary conditions. The linear constraints (2.45) are extended by a term dependent on the load parameter λ,

$$\boldsymbol{z} = \widetilde{\boldsymbol{c}} + \lambda \, \boldsymbol{c}_\lambda + \boldsymbol{P} \cdot \boldsymbol{z}\,, \tag{2.65}$$

where $\boldsymbol{c}_\lambda$ is a constant aggregating the inhomogeneous Dirichlet boundary conditions (which shall be applied by means of an arc-length method). Transforming (2.65) into incremental form yields

$$\Delta\boldsymbol{z} = \boldsymbol{c} + \Delta\lambda \, \boldsymbol{c}_\lambda + \boldsymbol{P} \cdot \Delta\boldsymbol{z}\,. \tag{2.66}$$

Repeating the same steps as for the standard linear constraints problem, one first obtains

$$\boldsymbol{\eta}^{\text{t}} \cdot \boldsymbol{P}^{\text{t}} \cdot \Big[\boldsymbol{K} \cdot [\boldsymbol{c} + \Delta\lambda \, \boldsymbol{c}_\lambda + \boldsymbol{P} \cdot \Delta\boldsymbol{z}] - \boldsymbol{b}^\star\Big] = 0\,, \tag{2.67}$$

with $\boldsymbol{b}^\star = \boldsymbol{f}_{\text{int}} + \lambda \, \boldsymbol{f}_{\text{ext}}$ and with the constraint for the arc-length method $f^{\text{arc}}(\boldsymbol{z}, \lambda)$. After symmetrisation and scaling, the equation may be written as

$$\boldsymbol{\eta}^{\text{t}} \cdot \Big[\widehat{\boldsymbol{K}} \cdot \Delta\boldsymbol{z} - \widehat{\boldsymbol{b}} - \lambda \, \widehat{\boldsymbol{b}}_\lambda\Big] = 0\,, \tag{2.68}$$

where the quantities $\hat{\bullet}$ are given by

$$\widehat{\boldsymbol{K}} = \boldsymbol{P}^{\text{t}} \cdot [\boldsymbol{K} + \alpha \, \boldsymbol{I}] \cdot \boldsymbol{P} + \alpha \, [\boldsymbol{I} - \boldsymbol{P} - \boldsymbol{P}^{\text{t}}]\,, \tag{2.69}$$

$$\widehat{\boldsymbol{b}} = \boldsymbol{P}^{\text{t}} \cdot [\boldsymbol{f}_{\text{int}} - [\boldsymbol{K} + \alpha \, \boldsymbol{I}] \cdot \boldsymbol{c}] + \alpha \, \boldsymbol{c}\,, \tag{2.70}$$

$$\widehat{\boldsymbol{b}}_\lambda = \boldsymbol{P}^{\text{t}} \cdot [\boldsymbol{f}_{\text{ext}} - [\boldsymbol{K} + \alpha \, \boldsymbol{I}] \cdot \boldsymbol{c}_\lambda] + \alpha \, \boldsymbol{c}_\lambda\,. \tag{2.71}$$

The solution of the increment of the load parameter λ is nearly identical to before — instead of $\boldsymbol{f}_{\text{ext}}$ the vector $\widehat{\boldsymbol{b}}_\lambda$ is used, i.e. (2.53) can now be stated as

$$\boldsymbol{r}(\boldsymbol{z}) = \boldsymbol{f}_{\text{int}}(\boldsymbol{z}) - \lambda \, \widehat{\boldsymbol{b}}_\lambda = \boldsymbol{0}\,. \tag{2.72}$$

3 A regularised framework for isotropic damage coupled to finite plasticity

In the following chapter, a finite strain formulation of gradient-enhanced ductile damage, conceptually following the small-strain contribution [94], is adopted. Much of the model formulation and some of the results have already been published in [161] as well as [163]. However, relevant sections have received updates with recognitions from further research. Two aspects are in the focus of the following chapter.

First, the multi-surface approach is established at finite strains. Therefore, the approach pursued herein couples damage to plasticity in a typical manner by using an effective stress in the yield function, see e.g. [101]. Thereby, plasticity can evolve even in highly damaged material states. Analogous to the effective stress, a novel effective damage driving force is proposed. In order to facilitate damage evolution under high plastic strains — especially for low levels of hardening or already saturated hardening — the effective damage driving force increases with increasing plastic strains.

Second, the applicability of the proposed material model to DP800 is shown by means of microtensile experiments on two geometrically different specimens from DP800 steel sheets. In order to be able to capture the degradation affecting the elastic stiffness, the monotonous tensile loading of the specimens is interrupted multiple times for a full unloading. The experiment is observed by a camera, so that the full displacement field can be obtained from DIC. Experiments on one specimen geometry are used for parameter identification. The parameter identification approach incorporating full-field measurements chosen in this work is directly based on [149] and uses an objective function formulated in terms of the force and the displacement field. The experiments on the other specimen geometry are used to validate the identified parameter set.

The chapter is organised as follows. Section 3.1 describes the continuous formulation of the constitutive material model and an algorithmic implementation is given thereafter. The basic properties of the material model are discussed in Section 3.3. The next section deals with parameter identification. It is split into the description of experiments, the corresponding set up of the simulation, the choice of the objective function and

the presentation of the identified material parameters as well as their validation. The application of the model to an industrial process is exemplified by means of the air bending process in Section 3.5. Lastly, in Section 3.6, an updated parametrisation of the proposed model is discussed.

3.1 Continuous formulation of the constitutive model

This section deals with the formulation of the material model. Adopting an additive split of the elasticity related parts of the Helmholtz energy into volumetric and isochoric contributions entails, in combination with different damage functions, an implicit influence of stress triaxiality and Lode parameter on damage evolution. A multi-surface formulation shall be established including plastic and damage dissipation potentials which are based on effective driving forces. The damage driving force is thereby influenced by the plasticity related state and vice versa. Moreover, associated evolution equations are derived and thereafter discretised in time. The algorithmic formulation of the material model is then presented. The Lagrange multiplier associated to plasticity can be obtained from a radial return scheme in principal stress space. Together with the Lagrange multiplier connected to damage, a two-surface problem arises which may be solved with an active-set algorithm.

3.1.1 Helmholtz energy and dissipation

Assuming a multiplicative split of the deformation gradient $\boldsymbol{F} = \boldsymbol{F}^{\mathrm{e}} \cdot \boldsymbol{F}^{\mathrm{p}}$, the elastic Finger tensor and its spectral decomposition are given by

$$\boldsymbol{b}^{\mathrm{e}} = \boldsymbol{F}^{\mathrm{e}} \cdot [\boldsymbol{F}^{\mathrm{e}}]^{\mathrm{t}} = \sum_{i=1}^{3} [\lambda_i^{\mathrm{e}}]^2 \, \boldsymbol{n}_i \otimes \boldsymbol{n}_i \,, \tag{3.1}$$

Logarithmic strains $\boldsymbol{\varepsilon}^{\mathrm{e}}$ are defined as

$$\boldsymbol{\varepsilon}^{\mathrm{e}} = \sum_{i=1}^{3} \varepsilon_i^{\mathrm{e}} \, \boldsymbol{n}_i \otimes \boldsymbol{n}_i \quad \text{with} \quad \varepsilon_i^{\mathrm{e}} := \ln(\lambda_i^{\mathrm{e}}) \,, \tag{3.2}$$

and the volumetric and isochoric logarithmic strains are obtained as

$$\varepsilon^{\mathrm{e,vol}} := \sum_{i=1}^{3} \varepsilon_i^{\mathrm{e}} \,, \qquad \boldsymbol{\varepsilon}^{\mathrm{e,iso}} = \sum_{i=1}^{3} \left[\varepsilon_i^{\mathrm{e}} - \tfrac{1}{3} \, \varepsilon^{\mathrm{e,vol}}\right] \, \boldsymbol{n}_i \otimes \boldsymbol{n}_i \,. \tag{3.3}$$

The local part of the Helmholtz energy is split into a volumetric, an isochoric and a plastic contribution, to be specific

$$\begin{aligned} \Psi^{\mathrm{loc}}(\boldsymbol{\varepsilon}^{\mathrm{e}}, \, d, \, \alpha_{\mathrm{p}}) &= \Psi^{\mathrm{vol}}(\boldsymbol{\varepsilon}^{\mathrm{e}}, \, d) + \Psi^{\mathrm{iso}}(\boldsymbol{\varepsilon}^{\mathrm{e}}, \, d) + \Psi^{\mathrm{p}}(\alpha) \\ &= \frac{K}{2} \, f^{\mathrm{vol}}(d) \, [\mathrm{tr}(\boldsymbol{\varepsilon}^{\mathrm{e}})]^2 + G \, f^{\mathrm{iso}}(d) \, \boldsymbol{\varepsilon}^{\mathrm{e,iso}} : \boldsymbol{\varepsilon}^{\mathrm{e,iso}} + \frac{h_{\mathrm{p}}}{n_{\mathrm{p}} + 1} \, {\alpha_{\mathrm{p}}}^{n_{\mathrm{p}}+1} \,, \end{aligned} \tag{3.4}$$

with compression and shear moduli K and G. The hardening parameters are h_p and $n_\mathrm{p} \leq 1$, see also Remark 1, and an additional internal variable α_p represents the effects of proportional hardening. The so-called damage functions $f^\bullet$ degrade the effective elastic properties of the material for increasing values of the local damage variable d, i.e.

$$f^\bullet : \mathbb{R}_0^+ \to]0, 1] \qquad \text{with} \qquad f^\bullet(d) = \exp(-\eta\, \xi_\bullet\, d)\,, \tag{3.5}$$

where the parameter η influences the rate of degradation and where $\xi_\bullet$ weights the influence on the different terms. Local damage variable d is only constrained to be non-negative, but not constrained from above which is in contrast to classic $[1-d]$ approaches and also advantageous for the algorithmic treatment as this work proceeds.

Remark 1 *The specific form of the plastic contribution in the Helmholtz energy* (3.4) *is a generalisation of linear isotropic hardening through the parameter* n_p*, with* $n_\mathrm{p} = 1$ *corresponding to linear hardening. For* $n_\mathrm{p} < 1$ *the transition between the elastic and plastic stages (in the load-displacement diagram) becomes smooth, as is observed in dual-phase steels such as DP800 for which a parameter identification is carried out later on in Section 3.4. Other forms of non-linear hardening, such as saturation type hardening, can lead to quasi perfect plasticity in the saturated region of hardening. This also means that no further damage evolves, since damage evolves only with increasing elastic strains in this model.*

Regularisation of this isotropic damage model is achieved by coupling the local damage variable d to a non-local field variable, see Section 2.2, i.e. $\boldsymbol{\phi}$ solely contains the non-local damage variable ϕ_d. Hence, the gradient and coupling contributions to the Helmholtz energy, cf. (2.2), are specified by

$$\Psi^\mathrm{grd}(\nabla_{\boldsymbol{X}} \phi_\mathrm{d}) = \frac{c_\mathrm{d}}{2} \left\| \nabla_{\boldsymbol{X}} \phi_\mathrm{d} \right\|^2 , \tag{3.6}$$

$$\Psi^\mathrm{cpl}(\phi_\mathrm{d},\, d) = \frac{b_\mathrm{d}}{2} \left[\phi_\mathrm{d} - d\right]^2 , \tag{3.7}$$

where b_d is denoted as penalty parameter and where c_d is herein denoted as regularisation parameter. As this work proceeds, c_d shall be considered to be constant.

The dissipation inequality in local form — contributions from the gradient-enhancement vanish, cf. [67] — is given by

$$\mathcal{D} = \boldsymbol{m}^\mathrm{t} : \boldsymbol{l} - \dot{\Psi} \geq 0\,, \tag{3.8}$$

with the material time derivative $\dot{\bullet} := \frac{\mathrm{d}\bullet}{\mathrm{d}t}$ and the spatial velocity gradient $\boldsymbol{l} := \nabla_{\boldsymbol{x}} \dot{\boldsymbol{\varphi}}$. Following the framework of standard dissipative materials, the driving forces $\boldsymbol{\mathcal{F}} = \{\boldsymbol{m}^\mathrm{t},\, \beta_\mathrm{p},\, q\}$

include the (spatial) Mandel stresses, an isotropic hardening stress and a damage driving force, to be specific

$$\boldsymbol{m}^{\mathrm{t}} := 2\,\frac{\partial \Psi}{\partial \boldsymbol{b}^{\mathrm{e}}} \cdot \boldsymbol{b}^{\mathrm{e}}\,, \tag{3.9}$$

$$\beta_{\mathrm{p}} := -\frac{\partial \Psi}{\partial \alpha_{\mathrm{p}}}\,, \tag{3.10}$$

$$q := -\frac{\partial \Psi}{\partial d}\,. \tag{3.11}$$

The representation (3.9) requires isotropic elastic properties so that $\boldsymbol{m}$ turns out to be symmetric. By inserting the driving forces into the dissipation inequality (3.8) and with the split of the spatial velocity gradient into an elastic and plastic part, $\boldsymbol{l} = \boldsymbol{l}^{\mathrm{e}} + \boldsymbol{l}^{\mathrm{p}}$ with $\boldsymbol{l}^{\mathrm{p}} = \boldsymbol{F}^{\mathrm{e}} \cdot \dot{\boldsymbol{F}}^{\mathrm{p}} \cdot \boldsymbol{F}^{-1}$, one obtains the reduced dissipation inequality

$$\mathcal{D}^{\mathrm{red}} = \boldsymbol{m}^{\mathrm{t}} : \boldsymbol{l}^{\mathrm{p}} + \beta_{\mathrm{p}}\,\dot{\alpha_{\mathrm{p}}} + q\,\dot{d} \geq 0\,. \tag{3.12}$$

3.1.2 Multi-surface formulation

A multi-surface formulation is proposed in order to determine the evolution of damage and plasticity. Thereby, damage can evolve independently from plasticity which is important for the regularisation framework, see [94]. Furthermore, it offers excellent flexibility in terms of obtaining a ductile or brittle response. The admissible domain for the driving forces $\boldsymbol{\mathcal{F}}$ is the union of the admissible plastic and admissible damage domain, i.e.

$$\mathbb{E} := \{\boldsymbol{\mathcal{F}} \in \mathbb{R}^{6+1+1} \,|\, \mathbb{E}^{\mathrm{p}} \cup \mathbb{E}^{\mathrm{d}}\}\,. \tag{3.13}$$

The admissible damage and plasticity domains are each governed by dissipation potentials Φ^{d} and Φ^{p} respectively, such that

$$\mathbb{E}^{\mathrm{d}} = \{q \in \mathbb{R} \,|\, \Phi^{\mathrm{d}} \leq 0\}\,, \tag{3.14}$$

$$\mathbb{E}^{\mathrm{p}} = \{\{\boldsymbol{m}^{\mathrm{t}},\, \beta_{\mathrm{p}}\} \in \mathbb{R}^{6+1} \,|\, \Phi^{\mathrm{p}} \leq 0\}\,. \tag{3.15}$$

The dissipation potentials are formulated in terms of effective driving forces $\boldsymbol{m}^{\mathrm{t}}_{\mathrm{eff}}$ and q_{eff} in the form of

$$\boldsymbol{m}^{\mathrm{t}}_{\mathrm{eff}} := \frac{\boldsymbol{m}^{\mathrm{t}}}{f^{\boldsymbol{m}}(d)}\,, \quad \text{and} \quad q_{\mathrm{eff}} := \frac{q}{f^{\alpha_{\mathrm{p}}}(\alpha_{\mathrm{p}})}\,. \tag{3.16}$$

The effective Mandel stresses $\boldsymbol{m}^{\mathrm{t}}_{\mathrm{eff}}$ can be motivated by the postulate of strain equivalence, where the load-bearing cross section is reduced by the factor $f^{\boldsymbol{m}}$ in the damaged state. In analogy to the effective Mandel stresses, the damage driving force q is divided

by a function dependent on the proportional hardening variable α_p. For the plastic dissipation potential Φ^p a von Mises yield surface with isotropic hardening is assumed, i.e.

$$\Phi^\mathrm{p}(\boldsymbol{m}^\mathrm{t}_\mathrm{eff},\, \beta_\mathrm{p}) = \| \operatorname{dev}(\boldsymbol{m}^\mathrm{t}_\mathrm{eff})\| - \sqrt{\tfrac{2}{3}}\, [\sigma_{\mathrm{y}0} - \beta_\mathrm{p}] \;, \tag{3.17}$$

with the initial yield stress $\sigma_{\mathrm{y}0}$. The damage dissipation potential, given by

$$\Phi^\mathrm{d}(q,\, d) = q_\mathrm{eff} - q_\mathrm{max}\, [1 - f^q(d)]^{n_\mathrm{d}} \;, \tag{3.18}$$

compares the effective damage driving force q_eff to a threshold value q_max multiplied by a term that increases from zero to one with increasing local damage variable d and that additionally depends on the parameter $n_\mathrm{d} < 1$. The effects of this additional term are elaborated on in Remark 2. Straight forward calculation of damage driving force q result in an expression dependent on the elastic logarithmic strains. However, it is possible to transform q into an expression dependent on stress-triaxiality and equivalent stress, see Remark 4. Stress-triaxiality (and Lode parameter) have been identified as important factors driving damage evolution, see e.g. [191] amongst others.

Associative evolution equations are obtained as

$$\boldsymbol{l}^\mathrm{p} = \lambda_\mathrm{p}\, \frac{\partial \Phi^\mathrm{p}}{\partial \boldsymbol{m}^\mathrm{t}} = \lambda_\mathrm{p}\, \frac{\boldsymbol{\nu}}{f^{\boldsymbol{m}}(d)} \,, \tag{3.19}$$

$$\dot{\alpha_\mathrm{p}} = \lambda_\mathrm{p}\, \frac{\partial \Phi^\mathrm{p}}{\partial \beta_\mathrm{p}} = \lambda_\mathrm{p}\, \sqrt{\tfrac{2}{3}} \,, \tag{3.20}$$

$$\dot{d} = \lambda_\mathrm{d}\, \frac{\partial \Phi^\mathrm{d}}{\partial q} = \frac{\lambda_\mathrm{d}}{f^{\alpha_\mathrm{p}}(\alpha_\mathrm{p})} \,, \tag{3.21}$$

with two Lagrange multipliers λ_p and λ_d. The underlying Karush-Kuhn-Tucker (KKT) conditions result in two sets of loading and unloading conditions,

$$\begin{aligned} &\Phi^\mathrm{p} \le 0 \qquad \lambda_\mathrm{p} \ge 0 \qquad \Phi^\mathrm{p}\, \lambda_\mathrm{p} = 0 \,, \\ &\Phi^\mathrm{d} \le 0 \qquad \lambda_\mathrm{d} \ge 0 \qquad \Phi^\mathrm{d}\, \lambda_\mathrm{d} = 0 \,. \end{aligned} \tag{3.22}$$

Based on (3.17), the flow direction of plastic deformation in (3.19) specifies to $\boldsymbol{\nu} = \operatorname{dev}(\boldsymbol{m}^\mathrm{t})/\| \operatorname{dev}(\boldsymbol{m}^\mathrm{t}\|$.

Remark 2 *In the damage dissipation potential* (3.18) *the threshold value is weighted by the term* $[1 - f^q(d)]^{n_\mathrm{d}}$*, which results in an initial* ($d = 0$) *threshold value of zero. However, due to the exponential type of the term, the threshold value quickly increases. In the overall response, this results in a smooth transition into the damage region. Thereby, the numerical robustness is improved and a more controlled interplay of damage and plasticity is possible. Consequently, a response with higher ductility can be obtained. The effect of this term is similar to so-called damage hardening, cf. [31].*

Remark 3 *An alternative formulation can be obtained by multiplying plastic potential Φ^{p} with damage function $f^{\boldsymbol{m}}(d)$. Instead of an effective stress measure entering the plastic potential, the current yield surface is shrunk with evolving damage. In a similar way, damage potential Φ^{d} can be multiplied with hardening dependent function $f^{\alpha_{\mathrm{p}}}(\alpha_{\mathrm{p}})$, such that the current damage threshold is decreased by plastic hardening.*

Remark 4 *The damage driving force, introduced in* (3.11)*, together with the particular choice of the free Helmholtz energy* (3.4)*, results in*

$$q(\boldsymbol{\varepsilon},\, \phi_{\mathrm{d}},\, d) = \tfrac{1}{2}\, K\, f^{\mathrm{vol}\,\prime}(d)[\varepsilon^{\mathrm{e,vol}}]^2 + G\, f^{\mathrm{iso}\,\prime}(d)\, \|\boldsymbol{\varepsilon}^{\mathrm{e,iso}}\|^2 + b_{\mathrm{d}}\,[\phi_{\mathrm{d}} - d]\,. \tag{3.23}$$

With the expressions for the volumetric and isochoric parts of the stresses

$$m^{\mathrm{vol}} = K\, f^{\mathrm{vol}}(d)\, \varepsilon^{\mathrm{e,vol}}\,, \qquad \boldsymbol{m}^{\mathrm{t,iso}} = 2\, G\, f^{\mathrm{iso}}(d)\, \boldsymbol{\varepsilon}^{\mathrm{e,iso}}\,, \tag{3.24}$$

and with the definition of the stress-triaxiality

$$\eta_{\mathrm{triax}} = \frac{\mathrm{tr}(\boldsymbol{m}^{\mathrm{t}})}{3\,\sqrt{3\, J_2^{\boldsymbol{m}}}} = \frac{\sqrt{2}\, m^{\mathrm{vol}}}{\sqrt{27}\, \|\boldsymbol{m}^{\mathrm{t,iso}}\|} \quad \textit{with} \quad J_2^{\boldsymbol{m}} = \tfrac{1}{2}\, \|\boldsymbol{m}^{\mathrm{t,iso}}\|^2\,, \tag{3.25}$$

the damage driving force q can be expressed in terms of stress triaxiality η_{triax} and $J_2^{\boldsymbol{m}}$. Making use of $f^{\bullet\prime} = -\eta\, \xi_{\bullet}\, f^{\bullet}$ — only valid for the specific choice of the damage function (3.5) *— one obtains*

$$q(\eta_{\mathrm{triax}},\, J_2^{\boldsymbol{m}},\, \phi_{\mathrm{d}},\, d) = \left[\eta_{\mathrm{triax}}^2 + \xi_{\mathrm{iso}}\, \exp(-\eta\, d\,[1 - \xi_{\mathrm{iso}}])\, \frac{K}{27\, G}\right]\, \frac{27\, \eta\, J_2^{\boldsymbol{m}}}{2\, K\, f^{\mathrm{vol}}(d)} + b_{\mathrm{d}}\,[\phi_{\mathrm{d}} - d]\,, \tag{3.26}$$

where $\xi_{\mathrm{vol}} = 1$ is assumed, see Section 3.4. This reformulation of damage driving force q reveals the importance of the influence factor ξ_{iso}. It controls how much influence stress-triaxiality has on damage evolution.

3.2 Algorithmic treatment

3.2.1 Time discretisation and radial return scheme

The algorithmic treatment of the evolution equations requires a discretisation in time. The evolution equations for isotropic hardening (3.20) and isotropic damage (3.21) are discretised with an implicit backward-Euler scheme. In order to fulfil the plastic incompressibility condition, $\det(\boldsymbol{F}^{\mathrm{p}}) = 1$, an implicit exponential integration scheme is applied for the integration related to the evolution of plastic deformation contributions. For the particular model chosen this results in a radial return scheme. For better readability the index $n+1$, referring to the current time step $t_{n+1} = t_n + \Delta t$, is omitted as this

work proceeds and only quantities from the previous time step are indexed with n. With the incremental Lagrange multipliers $\Delta\lambda_\mathrm{p} := \Delta t\,\lambda_\mathrm{p}$ and $\Delta\lambda_\mathrm{d} := \Delta t\,\lambda_\mathrm{d}$, the discretised evolution equations result in

$$\boldsymbol{F}^\mathrm{p} = \exp\left(\Delta\lambda_\mathrm{p}\,\frac{\widehat{\boldsymbol{\nu}}}{f^{\boldsymbol{m}}(d)}\right)\cdot\boldsymbol{F}^\mathrm{p}_n\,, \tag{3.27}$$

$$\alpha_\mathrm{p} = \alpha_{\mathrm{p}_n} + \sqrt{\frac{2}{3}}\,\Delta\lambda_\mathrm{p}\,, \tag{3.28}$$

$$d = d_n + \frac{\Delta\lambda_\mathrm{d}}{f^{\alpha_\mathrm{p}}(\alpha_\mathrm{p})}\,. \tag{3.29}$$

The algorithmic update for the plastic deformation gradient $\boldsymbol{F}^\mathrm{p}$ requires the return direction in the intermediate configuration $\widehat{\boldsymbol{\nu}}$, defined with the Mandel stresses in the intermediate configuration $\widehat{\boldsymbol{M}}^\mathrm{t} = [\boldsymbol{F}^\mathrm{e}]^\mathrm{t}\cdot\boldsymbol{m}^\mathrm{t}\cdot[\boldsymbol{F}^\mathrm{e}]^{-\mathrm{t}}$. Computing the deviatoric spatial Mandel stresses $\mathrm{dev}(\boldsymbol{m}^\mathrm{t}) = 2\,\partial_{\boldsymbol{b}^\mathrm{e}}\Psi^\mathrm{iso}\cdot\boldsymbol{b}^\mathrm{e} = \boldsymbol{m}^{\mathrm{t,iso}}$ in spectral decomposition, i.e.

$$\boldsymbol{m}^{\mathrm{t,iso}} = \sum_{i=1}^{3} m_i^\mathrm{iso}\,\boldsymbol{n}_i\otimes\boldsymbol{n}_i\,,\quad m_i^\mathrm{iso} = 2\,G\,f^\mathrm{iso}(d)\,\varepsilon_i^{\mathrm{e,iso}}\,, \tag{3.30}$$

the spatial return direction can be identified as

$$\boldsymbol{\nu} = \sum_{i=1}^{3}\nu_i\,\boldsymbol{n}_i\otimes\boldsymbol{n}_i\,,\quad \nu_i = \frac{\varepsilon_i^{\mathrm{e,iso}}}{\sqrt{\sum_{k=1}^{3}\left[\varepsilon_k^{\mathrm{e,iso}}\right]^2}}\,, \tag{3.31}$$

where the principal directions $\boldsymbol{n}_i$ of the spatial stresses coincide with the principal directions of the elastic finger tensor due to isotropic elasticity. The return direction $\boldsymbol{\nu}$ transforms in the same manner as the plastic velocity gradient $\boldsymbol{l}^\mathrm{p}$, i.e. $\boldsymbol{\nu} = \boldsymbol{F}^\mathrm{e}\cdot\widehat{\boldsymbol{\nu}}\cdot\boldsymbol{F}^{\mathrm{e}-1}$.

Let $\boldsymbol{b}^{\mathrm{e,tr}}$ denote the trial elastic Finger tensor, computed with the current deformation gradient $\boldsymbol{F}$ and the plastic deformation gradient of the previous time step $\boldsymbol{F}^\mathrm{p}_n$ as

$$\boldsymbol{b}^{\mathrm{e,tr}} = \boldsymbol{F}\cdot\boldsymbol{F}_n^{\mathrm{p}-1}\cdot\boldsymbol{F}_n^{\mathrm{p}-\mathrm{t}}\cdot\boldsymbol{F}^\mathrm{t}\,. \tag{3.32}$$

For the particular model considered, the principal directions $\boldsymbol{n}_i$ coincide with the principal directions of the trial state $\boldsymbol{n}_i^\mathrm{tr}$. Consequently, the relation $\boldsymbol{\nu} = \boldsymbol{\nu}^\mathrm{tr}$ holds, such that the computation of the updated Lagrange multipliers can be performed in principal stress space, i.e. only two scalar equations need to be solved. The update of the elastic Finger tensor can be written as

$$\boldsymbol{b}^\mathrm{e} = \boldsymbol{F}^{\mathrm{e,tr}}\cdot\exp\left(-2\,\Delta\lambda_\mathrm{p}\,\frac{\widehat{\boldsymbol{\nu}}}{f^{\boldsymbol{m}}(d)}\right)\cdot\left[\boldsymbol{F}^{\mathrm{e,tr}}\right]^\mathrm{t}\,. \tag{3.33}$$

In order to improve the numerical stability of the strongly coupled problem, i.e. damage evolution depends on plasticity evolution and vice versa, a modified representation of the functions $f^{\boldsymbol{m}}(d)$ and $f^{\alpha_\mathrm{p}}(\alpha_\mathrm{p})$ in the form of

$$\widehat{f}^{\boldsymbol{m}}(d) = \frac{1+\epsilon}{f^{\boldsymbol{m}}(d)+\epsilon}\,, \tag{3.34}$$

$$\widehat{f}^{\alpha_\mathrm{p}}(\alpha_\mathrm{p}) = \frac{1+\epsilon}{f^{\alpha_\mathrm{p}}(\alpha_\mathrm{p})+\epsilon}\,, \tag{3.35}$$

is employed, where the stability parameter ϵ is in the order of 10^{-3} to 10^{-5}. The functions $f^\bullet$ and $\widehat{f}^\bullet$ relate inversely to each other.

3.2.2 Update of Lagrange multipliers in principal stress space

Several solution procedures exist in order to solve this multi-surface problem, cf. [94], the active-set strategy of which will be adopted here. To shorten the notation, $\bar{\bullet}$ is introduced as the n-tuple of eigenvalues of the tensor $\bullet$ and the derivative of the damage functions with respect to the damage variable is abbreviated as

$$f^{\bullet\prime} := \frac{\partial f^\bullet}{\partial d}\,. \tag{3.36}$$

Considering an elastic trial step, $\Delta\lambda_\mathrm{p} = \Delta\lambda_\mathrm{d} = 0$, both dissipation potentials are evaluated; see Table 3.2, step 4. If the KKT conditions (3.22) are fulfilled, the current step remains elastic and the update of internal variables as well as the computation of stresses and driving forces are straightforward. If any KKT condition is violated, the active-set algorithm starts. In fact, a simplistic algorithmic form of the active-set can be employed here since only two conditions need to be fulfilled. This reduces the maximum number of remaining cases to three: a) only plasticity evolves; b) only damage evolves; c) damage and plasticity evolve.

Let the active set $\mathcal{A}$ be a subset of the total set $\mathcal{T}$ composed of the plastic and damage part, $\mathcal{T} = \{\mathrm{p},\,\mathrm{d}\}$. The initial active set in iteration $k = 1$ is determined by the values of the inelastic potentials, i.e. $\mathcal{A}_1 = \{\mathrm{p}\}$ if $\Phi^{\mathrm{p,tr}} > \Phi^{\mathrm{d,tr}}$ and $\mathcal{A}_1 = \{\mathrm{d}\}$ otherwise. For the current active set $\mathcal{A}_k$ the corresponding Lagrange multipliers are solved subject to $\Phi^\mathrm{p} = 0$ and/or $\Phi^\mathrm{d} = 0$ using a Newton-Raphson scheme. Since the Newton-Raphson scheme for the cases where only damage or only plasticity is active requires the same quantities as in the case where both damage and plasticity evolve, only the latter case is detailed here. The Newton-Raphson scheme is set up with the unknowns $\boldsymbol{\xi}$, the residuum $\boldsymbol{r}$ and the Jacobian $\boldsymbol{J}$ given by

$$\boldsymbol{\xi} = \begin{bmatrix} \Delta\lambda_\mathrm{p} \\ \Delta\lambda_\mathrm{d} \end{bmatrix}, \qquad \boldsymbol{r} = \begin{bmatrix} \Phi^\mathrm{p} \\ \Phi^\mathrm{d} \end{bmatrix}, \qquad \boldsymbol{J} = \begin{bmatrix} \dfrac{\mathrm{d}\Phi^\mathrm{p}}{\mathrm{d}\Delta\lambda_\mathrm{p}} & \dfrac{\mathrm{d}\Phi^\mathrm{p}}{\mathrm{d}\Delta\lambda_\mathrm{d}} \\ \dfrac{\mathrm{d}\Phi^\mathrm{d}}{\mathrm{d}\Delta\lambda_\mathrm{p}} & \dfrac{\mathrm{d}\Phi^\mathrm{d}}{\mathrm{d}\Delta\lambda_\mathrm{d}} \end{bmatrix}. \tag{3.37}$$

In each iteration the update of variables depending on Lagrange multipliers $\boldsymbol{\xi}$ is computed and the entries of the new residuum are determined; see Table 3.1, step 3. The entries of Jacobian $\boldsymbol{J}$ are described in Section 3.2.3. Each iteration is completed by updating the unknown Lagrange multipliers as

$$\boldsymbol{\xi} = \boldsymbol{\xi} + \Delta\boldsymbol{\xi} \qquad \text{with} \qquad \Delta\boldsymbol{\xi} = -\boldsymbol{J}^{-1} \cdot \boldsymbol{r}\,. \tag{3.38}$$

The Newton-Raphson scheme is deemed converged once $\|\Delta\boldsymbol{\xi}\|$ is smaller than a chosen tolerance. The active set algorithm continues in the next iteration by updating the active set $\mathcal{A}_{k+1} = \mathcal{A}_k$. First, the set with the smallest (negative) incremental Lagrange multiplier is removed and the multiplier reset to zero, i.e.

$$\mathcal{A}_k = \mathcal{A}_k \backslash \{j\}\,, \quad \Delta\lambda^j = 0\,, \quad \text{with} \quad \Delta\lambda^j = \min\{\Delta\lambda^j \in \mathcal{A}_{k-1} \,|\, \Delta\lambda^j < 0\}\,. \tag{3.39}$$

Secondly, the largest inactive constraint is added to the active set, i.e.

$$\mathcal{A}_k = \mathcal{A}_k \cup \{j\}\,, \quad \text{with} \quad \Phi^j = \max\{\Phi^j \in \mathcal{T} \backslash \mathcal{A}_{k-1} \,|\, \Phi^j > 0\}\,. \tag{3.40}$$

If the active set did not change, i.e. $\mathcal{A}_{k+1}$ is identical to $\mathcal{A}_k$, the active set algorithm is finished, otherwise an update for the Lagrange multipliers of the new active set $\mathcal{A}_{k+1}$ has to be determined.

With the updated Lagrange multipliers at hand, the update for the internal variables as well as the stresses and driving forces can now be computed; see Table 3.2, steps 6 and 7.

3.2.3 Jacobian for local Newton scheme

The Newton-Raphson scheme to determine the update for the Lagrange multipliers within the active set algorithm, see Table 3.1, requires the entries

$$J_{\mathrm{pp}} := \frac{\partial \Phi^{\mathrm{p}}}{\partial \Delta\lambda_{\mathrm{p}}} = \frac{\partial \Phi^{\mathrm{p}}}{\partial d}\,\frac{\partial d}{\partial \Delta\lambda_{\mathrm{p}}} - 2\,G\,f^{\mathrm{iso}}[\widehat{f}^{\boldsymbol{m}}]^2 - \frac{2}{3}\,\frac{\partial \beta_{\mathrm{p}}}{\partial \alpha_{\mathrm{p}}}\,, \tag{3.41}$$

$$J_{\mathrm{pd}} := \frac{\partial \Phi^{\mathrm{p}}}{\partial \Delta\lambda_{\mathrm{d}}} = \frac{\partial \Phi^{\mathrm{p}}}{\partial d}\,\frac{\partial d}{\partial \Delta\lambda_{\mathrm{d}}}\,, \tag{3.42}$$

$$J_{\mathrm{dp}} := \frac{\partial \Phi^{\mathrm{d}}}{\partial \Delta\lambda_{\mathrm{p}}} = \left[2\,G\,f^{\mathrm{iso}\,\prime}\,\|\bar{\boldsymbol{\varepsilon}}^{\mathrm{e,iso}}\|\,\widehat{f}^{\boldsymbol{m}} + \frac{\partial q}{\partial d}\,\frac{\partial d}{\partial \Delta\lambda_{\mathrm{p}}}\right]\,\widehat{f}^{\alpha_{\mathrm{p}}} + q\,\widehat{f}^{\alpha_{\mathrm{p}}\,\prime}\,, \tag{3.43}$$

$$+\,q_{\max}\,n_{\mathrm{d}}\,[1 - f^q]^{n_{\mathrm{d}}-1}\,f^{q\,\prime}\,\frac{\partial d}{\partial \Delta\lambda_{\mathrm{p}}}\,, \tag{3.44}$$

$$J_{\mathrm{dd}} := \frac{\partial \Phi^{\mathrm{d}}}{\partial \Delta\lambda_{\mathrm{d}}} = \frac{\partial q}{\partial d}\,\frac{\partial d}{\partial \Delta\lambda_{\mathrm{d}}}\,\widehat{f}^{\alpha_{\mathrm{p}}} + q_{\max}\,n_{\mathrm{d}}\,[1 - f^q]^{n_{\mathrm{d}}-1}\,f^{q\,\prime}\,\frac{\partial d}{\partial \Delta\lambda_{\mathrm{d}}} \tag{3.45}$$

Table 3.1: Algorithmic update of the Lagrange multipliers.

1. initialise active-set algorithm $k = 0$, $\mathcal{A}_0 = \{\emptyset\}$, $\Phi^{\mathrm{p}} = \Phi^{\mathrm{p,tr}}$, $\Phi^{\mathrm{d}} = \Phi^{\mathrm{d,tr}}$
2. update active set $\mathcal{A}_{k+1} = \mathcal{A}_k$
   a) remove smallest active multiplier for which $\Phi^{\bullet} \leq 0$
   b) add largest inactive constraint with $\Phi^{\bullet} \geq 0$
   c) if $\mathcal{A}_{k+1} = \mathcal{A}_k \longrightarrow$ exit Box
   d) set $k = k + 1$
3. update active Lagrange multiplier by Newton-Raphson scheme
   a) compute Jacobian $\boldsymbol{J}$, see Section 3.2.3
   b) update multipliers $\Delta\boldsymbol{\xi} = -\boldsymbol{J}^{-1} \cdot \boldsymbol{r}$,
   $\Delta\lambda_{\mathrm{p}} = \Delta\lambda_{\mathrm{p}} + \Delta\xi_1$, $\Delta\lambda_{\mathrm{d}} = \Delta\lambda_{\mathrm{d}} + \Delta\xi_2$
   c) compute update for variables

$$
\begin{aligned}
\alpha_{\mathrm{p}} &= \alpha_{\mathrm{p}_n} + \sqrt{\tfrac{2}{3}}\,\Delta\lambda_{\mathrm{p}} \\
d &= d_n + \Delta\lambda_{\mathrm{d}} \widehat{f}^{\alpha_{\mathrm{p}}}(\alpha_{\mathrm{p}}) \\
\bar{\boldsymbol{\varepsilon}}^{\mathrm{e,iso}} &= \bar{\boldsymbol{\varepsilon}}^{\mathrm{e,iso,tr}} - \Delta\lambda_{\mathrm{p}}\, \bar{\boldsymbol{\nu}}^{\mathrm{tr}}\, \widehat{f}^{\boldsymbol{m}}(d) \\
q &= -\frac{K}{2}\, f^{\mathrm{vol}\,\prime}(d)\, [\varepsilon^{\mathrm{e,vol}}]^2 - G\, f^{\mathrm{iso}\,\prime}(d) \|\bar{\boldsymbol{\varepsilon}}^{\mathrm{e,iso}}\|^2 + b_{\mathrm{d}}\, [\phi_{\mathrm{d}} - d]
\end{aligned}
$$

   d) compute residuum

$$
\begin{aligned}
&\text{if p} \in \mathcal{A}_k : r_1 = \Phi^{\mathrm{p}} = 2\, G\, f^{\mathrm{iso}}(d)\, \widehat{f}^{\boldsymbol{m}}(d)\, \|\bar{\boldsymbol{\varepsilon}}^{\mathrm{e,iso}}\| - \sqrt{\tfrac{2}{3}}[\sigma_{\mathrm{y}0} + h_{\mathrm{p}}\, {\alpha_{\mathrm{p}}}^{n_{\mathrm{p}}}] \\
&\text{if d} \in \mathcal{A}_k : r_1 = \Phi^{\mathrm{d}} = q\, \widehat{f}^{\alpha_{\mathrm{p}}}(\alpha_{\mathrm{p}}) - q_{\max}\, [1 - f^q(d)]^{n_{\mathrm{d}}}
\end{aligned}
$$

   e) if $\|\Delta\boldsymbol{\xi}\| \geq \mathrm{tol} \longrightarrow$ goto 3. (a)

of Jacobian $\boldsymbol{J}$, cf. (3.37). The partial derivatives can be computed as

$$\frac{\partial d}{\partial \Delta\lambda_{\mathrm{p}}} = \Delta\lambda_{\mathrm{d}}\, \widehat{f}^{\alpha_{\mathrm{p}}\prime}\,, \tag{3.46}$$

$$\frac{\partial d}{\partial \Delta\lambda_{\mathrm{d}}} = \widehat{f}^{\alpha_{\mathrm{p}}}\,, \tag{3.47}$$

$$\frac{\partial \beta_{\mathrm{p}}}{\partial \alpha_{\mathrm{p}}} = h_{\mathrm{p}}\, n_{\mathrm{p}}\, {\alpha_{\mathrm{p}}}^{n_{\mathrm{p}}-1}\,, \tag{3.48}$$

$$\frac{\partial \Phi^{\mathrm{p}}}{\partial d} = 2\,G\,\|\bar{\boldsymbol{\varepsilon}}^{\mathrm{e,iso}}\|\left[f^{\mathrm{iso}\prime}\,\widehat{\boldsymbol{m}}^{\prime} + f^{\mathrm{iso}}\,\widehat{\boldsymbol{m}}^{\prime}\right] - 2\,G\,\Delta\lambda_{\mathrm{p}}\,f^{\mathrm{iso}}\,\widehat{\boldsymbol{m}}\,\widehat{\boldsymbol{m}}^{\prime}\,, \tag{3.49}$$

$$\frac{\partial q}{\partial d} = -\frac{K}{2}\,f^{\mathrm{vol}\prime\prime}\,[\varepsilon^{\mathrm{vol}}]^2 - G\,f^{\mathrm{iso}\prime\prime}\,\|\bar{\boldsymbol{\varepsilon}}^{\mathrm{e,iso}}\|^2 + b_{\mathrm{d}} + 2\,G\,f^{\mathrm{iso}\prime}\,\|\bar{\boldsymbol{\varepsilon}}^{\mathrm{e,iso}}\|\,\Delta\lambda_{\mathrm{p}}\,\widehat{f}^{\boldsymbol{m}\prime}\,. \tag{3.50}$$

3.2.4 Determination of stresses and stiffness contributions

The Piola stress tensor $\boldsymbol{P}$ (2.6) is required for the Finite Element implementation chosen here and can be obtained from a transformation of the Mandel stresses as

$$\boldsymbol{P} = \boldsymbol{m}^{\mathrm{t}} \cdot \boldsymbol{F}^{-\mathrm{t}}\,. \tag{3.51}$$

The aggregated non-local driving forces (2.6) used in the Finite Element implementation solely contain the non-local driving force Y_{d} and $\boldsymbol{Y}_{\mathrm{d}}$, i.e.

$$\boldsymbol{Y} = [Y_{\mathrm{d}}]\,, \qquad \boldsymbol{Y}_{\mathrm{grd}} = [\boldsymbol{Y}_{\mathrm{d}}]\,. \tag{3.52}$$

In the context of a Finite Element implementation the total derivatives of the driving forces with respect to the field variables are required to be computed, see (2.19)-(2.22). The aggregated stiffness contributions related to the aggregated non-local field variable $\boldsymbol{\phi}$ are given by

$$\frac{\mathrm{d}\boldsymbol{P}}{\mathrm{d}\boldsymbol{\phi}} = \left[\frac{\mathrm{d}\boldsymbol{P}}{\mathrm{d}\phi_{\mathrm{d}}}\right]\,, \qquad \frac{\mathrm{d}\boldsymbol{Y}}{\mathrm{d}\boldsymbol{F}} = \left[\frac{\mathrm{d}Y_{\mathrm{d}}}{\mathrm{d}\boldsymbol{F}}\right]\,. \tag{3.53}$$

Since a significant portion of the algorithm is computed in principal space, it is convenient to also split the derivatives into contributions computed in principal space and contributions computed in the Cartesian basis system. Following the algorithmic structure in [159], the spatial elasticity tensor $\mathbf{e}$ can be split into derivatives of the stress eigenvalues and derivatives of the eigenvectors; see Table 3.3, step 1. The derivatives of the stress eigenvalues with respect to the logarithmic strain eigenvalues are supplied in Section 3.2.5. A transformation of the tangent operator contribution $\mathbf{e}$ yields the derivative of the Piola stresses with respect to the deformation gradient; see Table 3.3, step 2. All derivatives of the stresses and driving forces which are required for the Finite Element implementation are summarised in Table 3.3.

Table 3.2: Algorithmic outline for the ductile damage model.

0. given: $\boldsymbol{F}$, ϕ_d, $\nabla_{\boldsymbol{X}}\phi_\mathrm{d}$ and internal variables of the previous time step $\boldsymbol{C}_n^{\mathrm{p}-1}$, α_{p_n}, d_n

1. compute trial elastic finger tensor and spectral decomposition

$$\boldsymbol{b}^{\mathrm{e,tr}} = \boldsymbol{F}\cdot\boldsymbol{C}_n^{\mathrm{p}-1}\cdot\boldsymbol{F}^{\mathrm{t}} = \sum_{i=1}^{3}[\lambda_i^{\mathrm{e,tr}}]^2\,\boldsymbol{n}_i\otimes\boldsymbol{n}_i\,, \qquad \varepsilon_i^{\mathrm{e,tr}} = \log(\lambda_i^{\mathrm{e,tr}})$$

2. compute return direction $\bar{\boldsymbol{\nu}} = \|\bar{\boldsymbol{\varepsilon}}^{\mathrm{e,iso,tr}}\|^{-1}\,\bar{\boldsymbol{\varepsilon}}^{\mathrm{e,iso,tr}}$

3. initialise $\Delta\lambda_\mathrm{p} = \Delta\lambda_\mathrm{d} = 0$

4. evaluate trial potentials

$$\begin{aligned}
\bar{\boldsymbol{m}}^{\mathrm{tr,iso}} &= 2\,G\,f^{\mathrm{iso}}(d)\,\bar{\boldsymbol{\varepsilon}}^{\mathrm{e,iso,tr}}\\
\Phi^{\mathrm{p,tr}} &= \|\bar{\boldsymbol{m}}^{\mathrm{tr,iso}}\|\,\widehat{f}^{m}(d_n) - \sqrt{\tfrac{2}{3}}\,[\sigma_{\mathrm{y}0} + h_\mathrm{p}\,\alpha_{\mathrm{p}_n}^{n_\mathrm{p}}]\\
q^{\mathrm{tr}} &= -\tfrac{1}{2}\,K\,f^{\mathrm{vol}\,\prime}(d_n)[\varepsilon^{\mathrm{e,vol}}]^2 - G\,f^{\mathrm{iso}\,\prime}(d_n)\,\|\bar{\boldsymbol{\varepsilon}}^{\mathrm{e,iso,tr}}\|^2 + b_\mathrm{d}\,[\phi_\mathrm{d} - d_n]\\
\Phi^{\mathrm{d,tr}} &= q^{\mathrm{tr}}\,\widehat{f}^{\alpha_\mathrm{p}}(\alpha_{\mathrm{p}_n}) - q_{\max}\,[1 - f^{q}(d_n)]^{n_\mathrm{d}}
\end{aligned}$$

5. if $\Phi^{\mathrm{p,tr}} > 0$ or $\Phi^{\mathrm{d,tr}} > 0$: update Lagrange multipliers $\longrightarrow$ Table 3.1

6. update internal variables

$$\begin{aligned}
\alpha_\mathrm{p} &= \alpha_{\mathrm{p}_n} + \sqrt{\tfrac{2}{3}}\,\Delta\lambda_\mathrm{p}\\
d &= d_n + \Delta\lambda_\mathrm{d}\widehat{f}^{\alpha_\mathrm{p}}(\alpha_\mathrm{p})
\end{aligned}$$

$$\boldsymbol{C}^{\mathrm{p}-1} = \boldsymbol{F}^{-1}\cdot\boldsymbol{b}^{\mathrm{e}}\cdot\boldsymbol{F}^{-\mathrm{t}}, \quad \text{with} \quad \boldsymbol{b}^{\mathrm{e}} = \sum_{i=1}^{3}\exp(2\,\varepsilon_i^{\mathrm{e,tr}} - 2\,\Delta\lambda_\mathrm{p}\,\widehat{f}^{\boldsymbol{m}}(d)\,\nu_i)\,\boldsymbol{n}_i\otimes\boldsymbol{n}_i$$

7. compute stresses and driving forces

$$\begin{aligned}
\boldsymbol{m}^{\mathrm{t}} &= \sum_{i=1}^{3} m_i\,\boldsymbol{n}_i\otimes\boldsymbol{n}_i\,, \qquad m_i = K\,f^{\mathrm{vol}}(d)\,\varepsilon^{\mathrm{e,vol}} + 2\,G\,f^{\mathrm{iso}}(d)\,\varepsilon_i^{\mathrm{e,iso}}\\
Y_\mathrm{d} &= b_\mathrm{d}\,[\phi_\mathrm{d} - d]\\
\boldsymbol{Y}_\mathrm{d} &= c_\mathrm{d}\,\nabla_{\boldsymbol{X}}\phi_\mathrm{d}
\end{aligned}$$

8. compute tangent moduli $\longrightarrow$ Table 3.3

Table 3.3: Algorithmic computation of tangent contributions.

1. computation of tangent operator contribution $\mathbf{e}$

$$g_{ij} = \begin{cases} -m_i & i = j \\ \dfrac{m_i\,[\lambda_j^{\mathrm{e}}]^2 - m_j\,[\lambda_i^{\mathrm{e}}]^2}{[\lambda_i^{\mathrm{e}}]^2 - [\lambda_j^{\mathrm{e}}]^2} & i \neq j \text{ and } \lambda_i \neq \lambda_j \\ \dfrac{[\lambda_j^{\mathrm{e}}]^2}{[\lambda_i^{\mathrm{e}}]^2}\left[\dfrac{1}{2}\dfrac{\mathrm{d}m_i}{\mathrm{d}\varepsilon_i} - m_i\right] - \dfrac{1}{2}\dfrac{\mathrm{d}m_j}{\mathrm{d}\varepsilon_i} & i \neq j \text{ and } \lambda_i = \lambda_j \end{cases}$$

$$\mathbf{e} = \sum_{i=1}^{3}\sum_{j=1}^{3}\left[\frac{\mathrm{d}m_i}{\mathrm{d}\varepsilon_j}\,\boldsymbol{n}_i \otimes \boldsymbol{n}_i \otimes \boldsymbol{n}_j \otimes \boldsymbol{n}_j + g_{ij}\left[\boldsymbol{n}_i \otimes \boldsymbol{n}_j \otimes \boldsymbol{n}_i \otimes \boldsymbol{n}_j + \boldsymbol{n}_i \otimes \boldsymbol{n}_j \otimes \boldsymbol{n}_j \otimes \boldsymbol{n}_i\right]\right]$$

2. compute derivatives of $\boldsymbol{P}$ with respect to $\boldsymbol{F}$ and ϕ_{d}

$$\frac{\mathrm{d}\boldsymbol{P}}{\mathrm{d}\boldsymbol{F}} = \left[\boldsymbol{I} \mathbin{\overline{\otimes}} \boldsymbol{F}^{-1}\right] : \mathbf{e} \cdot \boldsymbol{F}^{-\mathrm{t}} + \boldsymbol{I} \mathbin{\overline{\otimes}} \left[\boldsymbol{F}^{-1} \cdot \boldsymbol{P}\right]$$

$$\frac{\mathrm{d}\boldsymbol{P}}{\mathrm{d}\phi_{\mathrm{d}}} = \frac{\mathrm{d}\boldsymbol{m}^{\mathrm{t}}}{\mathrm{d}\phi_{\mathrm{d}}} \cdot \boldsymbol{F}^{-\mathrm{t}} = \left[\sum_{i=1}^{3}\frac{\mathrm{d}m_i}{\mathrm{d}\phi_{\mathrm{d}}}\,\boldsymbol{n}_i \otimes \boldsymbol{n}_i\right] \cdot \boldsymbol{F}^{-\mathrm{t}}$$

3. compute derivatives of Y_{d} with respect to $\boldsymbol{F}$ and ϕ_{d}

$$\frac{\mathrm{d}Y_{\mathrm{d}}}{\mathrm{d}\boldsymbol{F}} = \left[\sum_{i=1}^{3}\frac{\mathrm{d}Y_{\mathrm{d}}}{\mathrm{d}\varepsilon_i}\,\frac{1}{2\,[\lambda_i^{\mathrm{e}}]^2}\,\boldsymbol{n}_i \otimes \boldsymbol{n}_i\right] : \left[\boldsymbol{I} \mathbin{\overline{\otimes}} \boldsymbol{F} \cdot \boldsymbol{C}^{\mathrm{p}-1} + \boldsymbol{F} \cdot \boldsymbol{C}^{\mathrm{p}-1} \mathbin{\underline{\otimes}} \boldsymbol{I}\right]$$

$$\frac{\mathrm{d}Y_{\mathrm{d}}}{\mathrm{d}\phi_{\mathrm{d}}} = b_{\mathrm{d}}\left[1 - \frac{\mathrm{d}d}{\mathrm{d}\phi_{\mathrm{d}}}\right]$$

4. compute derivative of $\boldsymbol{Y}_{\mathrm{d}}$ with respect to $\nabla_{\boldsymbol{X}}\phi_{\mathrm{d}}$

$$\frac{\mathrm{d}\boldsymbol{Y}_{\mathrm{d}}}{\mathrm{d}\nabla_{\boldsymbol{X}}\phi_{\mathrm{d}}} = c_{\mathrm{d}}\,\boldsymbol{I}$$

3.2.5 Derivatives in principal space

In this section all derivatives which are required for the computation of the consistent algorithmic tangent operator, see Table 3.3, are given. The specific structure only requires the derivatives of the eigenvalues. The corresponding identity tensors are represented by $\bar{\boldsymbol{I}}$, an n-tuple with the value of all entries being identically 1, and by diag(1), a diagonal $n \times n$-matrix with all diagonal entries being identically 1.

The increments of the Mandel stress tensor and the non-local damage driving force, i.e.

$$\mathrm{d}\bar{\boldsymbol{m}} = [\bar{\mathbf{e}}^{\mathrm{e}} + \bar{\mathbf{e}}^{\mathrm{pp}}] \cdot \mathrm{d}\bar{\boldsymbol{\varepsilon}} + \bar{\boldsymbol{e}}^{\mathrm{pd}}\, \mathrm{d}\phi_{\mathrm{d}}\,, \tag{3.54}$$

$$\mathrm{d}Y_{\mathrm{d}} = \bar{\boldsymbol{e}}^{\mathrm{dp}} \cdot \mathrm{d}\bar{\boldsymbol{\varepsilon}} + \left[b_{\mathrm{d}} + e^{\mathrm{dd}}\right]\, \mathrm{d}\phi_{\mathrm{d}}\,, \tag{3.55}$$

requires the tangent contributions

$$\bar{\mathbf{e}}^{\mathrm{e}} = K\, f^{\mathrm{vol}}(d)\, \bar{\boldsymbol{I}} \otimes \bar{\boldsymbol{I}} + 2\,G\, f^{\mathrm{iso}}(d)\ \mathrm{diag}(1)\,, \tag{3.56}$$

$$\bar{\mathbf{e}}^{\mathrm{pp}} = \frac{\partial \bar{\boldsymbol{m}}}{\partial \bar{\boldsymbol{\varepsilon}}^{\mathrm{p}}} \cdot \frac{\mathrm{d}\bar{\boldsymbol{\varepsilon}}^{\mathrm{p}}}{\mathrm{d}\bar{\boldsymbol{\varepsilon}}} + \frac{\partial \bar{\boldsymbol{m}}}{\partial d} \otimes \frac{\mathrm{d}d}{\mathrm{d}\bar{\boldsymbol{\varepsilon}}}\,, \tag{3.57}$$

$$\bar{\boldsymbol{e}}^{\mathrm{pd}} = \frac{\partial \bar{\boldsymbol{m}}}{\partial \bar{\boldsymbol{\varepsilon}}^{\mathrm{p}}} \cdot \frac{\mathrm{d}\bar{\boldsymbol{\varepsilon}}^{\mathrm{p}}}{\mathrm{d}\phi_{\mathrm{d}}} + \frac{\partial \bar{\boldsymbol{m}}}{\partial d}\, \frac{\mathrm{d}d}{\mathrm{d}\phi_{\mathrm{d}}}\,, \tag{3.58}$$

$$\bar{\boldsymbol{e}}^{\mathrm{dp}} = \frac{\partial Y_{\mathrm{d}}}{\partial d}\, \frac{\mathrm{d}d}{\mathrm{d}\bar{\boldsymbol{\varepsilon}}}\,, \tag{3.59}$$

$$e^{\mathrm{dd}} = \frac{\partial Y_{\mathrm{d}}}{\partial d}\, \frac{\mathrm{d}d}{\mathrm{d}\phi_{\mathrm{d}}}\,. \tag{3.60}$$

where the partial derivatives of the driving forces result in

$$\frac{\partial \bar{\boldsymbol{m}}}{\partial \bar{\boldsymbol{\varepsilon}}^{\mathrm{p}}} = -\,\bar{\mathbf{e}}^{\mathrm{e}}\,, \tag{3.61}$$

$$\frac{\partial \bar{\boldsymbol{m}}}{\partial d} = K\, f^{\mathrm{vol}\prime}\, \varepsilon^{\mathrm{vol}}\, \bar{\boldsymbol{I}} + 2\,G\, f^{\mathrm{iso}\prime}\, \tilde{\varepsilon}\, \bar{\boldsymbol{\nu}}^{\mathrm{tr}}\,, \tag{3.62}$$

$$\frac{\partial Y_{\mathrm{d}}}{\partial d} = -\,b_{\mathrm{d}}\,. \tag{3.63}$$

Furthermore, the total derivatives of the internal variables — plastic strains $\bar{\boldsymbol{\varepsilon}}^{\mathrm{p}}$ and isotropic damage d — are specified by

$$\frac{\mathrm{d}d}{\mathrm{d}\bar{\boldsymbol{\varepsilon}}} = \widehat{f}^{\alpha_{\mathrm{p}}}\, \frac{\mathrm{d}\Delta\lambda_{\mathrm{d}}}{\mathrm{d}\bar{\boldsymbol{\varepsilon}}} + \Delta\lambda_{\mathrm{d}}\, \widehat{f}^{\alpha_{\mathrm{p}}\prime} \sqrt{\frac{2}{3}}\, \frac{\mathrm{d}\Delta\lambda_{\mathrm{p}}}{\mathrm{d}\bar{\boldsymbol{\varepsilon}}}\,, \tag{3.64}$$

$$\frac{\mathrm{d}d}{\mathrm{d}\phi_{\mathrm{d}}} = \widehat{f}^{\alpha_{\mathrm{p}}}\, \frac{\mathrm{d}\Delta\lambda_{\mathrm{d}}}{\mathrm{d}\phi_{\mathrm{d}}} + \Delta\lambda_{\mathrm{d}}\, \widehat{f}^{\alpha_{\mathrm{p}}\prime} \sqrt{\frac{2}{3}}\, \frac{\mathrm{d}\Delta\lambda_{\mathrm{p}}}{\mathrm{d}\phi_{\mathrm{d}}}\,, \tag{3.65}$$

$$\frac{\mathrm{d}\bar{\boldsymbol{\varepsilon}}^{\mathrm{p}}}{\mathrm{d}\bar{\boldsymbol{\varepsilon}}} = \bar{\boldsymbol{\nu}}^{\mathrm{tr}}\, \widehat{f}^{\boldsymbol{m}} \otimes \frac{\mathrm{d}\Delta\lambda_{\mathrm{p}}}{\mathrm{d}\bar{\boldsymbol{\varepsilon}}} + \Delta\lambda_{\mathrm{p}}\, \widehat{f}^{\boldsymbol{m}}\, \frac{\mathrm{d}\bar{\boldsymbol{\nu}}^{\mathrm{tr}}}{\mathrm{d}\bar{\boldsymbol{\varepsilon}}} + \Delta\lambda_{\mathrm{p}}\, \widehat{f}^{\boldsymbol{m}\prime}\, \bar{\boldsymbol{\nu}}^{\mathrm{tr}} \otimes \frac{\mathrm{d}d}{\mathrm{d}\bar{\boldsymbol{\varepsilon}}}\,, \tag{3.66}$$

$$\frac{\mathrm{d}\bar{\boldsymbol{\varepsilon}}^{\mathrm{p}}}{\mathrm{d}\phi_{\mathrm{d}}} = \bar{\boldsymbol{\nu}}^{\mathrm{tr}}\, \widehat{f}^{\boldsymbol{m}}\, \frac{\mathrm{d}\Delta\lambda_{\mathrm{p}}}{\mathrm{d}\phi_{\mathrm{d}}} + \Delta\lambda_{\mathrm{p}}\, \widehat{f}^{\boldsymbol{m}\prime}\, \bar{\boldsymbol{\nu}}^{\mathrm{tr}}\, \frac{\mathrm{d}d}{\mathrm{d}\phi_{\mathrm{d}}}\,. \tag{3.67}$$

The occurring total derivatives of the Lagrange multipliers are not straight-forward to determine. Utilisation of the implicit function theorem in the converged Newton-Raphson step leads to

$$\frac{\mathrm{d}\Delta\lambda_\mathrm{p}}{\mathrm{d}\bar{\boldsymbol{\varepsilon}}} = -\det(\boldsymbol{J}^{-1}) \left[J_\mathrm{pd}\, \widehat{f}^{\alpha_\mathrm{p}}\, \frac{\partial \bar{\boldsymbol{m}}}{\partial d} + 2\, J_\mathrm{dd}\, G\, f^\mathrm{iso} \widehat{f}^{\boldsymbol{m}}\, \bar{\boldsymbol{\nu}}^\mathrm{tr} \right], \tag{3.68}$$

$$\frac{\mathrm{d}\Delta\lambda_\mathrm{d}}{\mathrm{d}\bar{\boldsymbol{\varepsilon}}} = \det(\boldsymbol{J}^{-1}) \left[J_\mathrm{pp}\, \widehat{f}^{\alpha_\mathrm{p}}\, \frac{\partial \bar{\boldsymbol{m}}}{\partial d} + 2\, J_\mathrm{dp}\, G\, f^\mathrm{iso}\, \widehat{f}^{\boldsymbol{m}}\, \bar{\boldsymbol{\nu}}^\mathrm{tr} \right], \tag{3.69}$$

$$\frac{\mathrm{d}\Delta\lambda_\mathrm{p}}{\mathrm{d}\phi_\mathrm{d}} = \det(\boldsymbol{J}^{-1})\, J_\mathrm{pd}\, b_\mathrm{d}\, \widehat{f}^{\alpha_\mathrm{p}}, \tag{3.70}$$

$$\frac{\mathrm{d}\Delta\lambda_\mathrm{d}}{\mathrm{d}\phi_\mathrm{d}} = -\det(\boldsymbol{J}^{-1})\, J_\mathrm{pp}\, b_\mathrm{d}\, \widehat{f}^{\alpha_\mathrm{p}}. \tag{3.71}$$

3.3 Parameter study

This section illustrates the constitutive behaviour of the local ductile damage model by means of a homogeneous uniaxial deformation test. The influence of the material and model parameters is analysed in order to demonstrate basic model properties representing different material responses. An analysis of the implemented ductile damage model under homogeneous uniaxial tension loading is performed by prescribing a deformation in the form of

$$\boldsymbol{F} = \lambda_\parallel\, \boldsymbol{e} \otimes \boldsymbol{e} + \lambda_\perp \left[\boldsymbol{I} - \boldsymbol{e} \otimes \boldsymbol{e} \right], \tag{3.72}$$

with $\|\boldsymbol{e}\| = 1$ and where the stretch $\lambda_\perp$ develops such that the stress is uniaxial in the direction of $\boldsymbol{e}$, i.e. $\boldsymbol{P} = P_\parallel\, \boldsymbol{e} \otimes \boldsymbol{e}$. The applied deformation is not increasing monotonously but rather it is interrupted at stretch values of 1.1, 1.15 and 1.2 to simulate unloading behaviour. The exact load curve $\lambda_\parallel(t)$ is depicted in Figure 3.1. The gradient terms, and thus also the gradient related parameters c_d and b_d are not active, since a homogeneous deformation is applied.

The influence of individual parameters is demonstrated by comparing the simulation responses of a reference parameter set with responses where the studied parameter is increased and decreased. For the reference parameter set, the material parameters are adopted from an early stage of parameter identification, see Section 3.4, and resemble the typical response of a ductile steel, see Table 3.4.

The variations of two parameters each are grouped together and the response is illustrated in three figures (Figure 3.2-3.4), each depicting the stress-stretch response, the evolution of proportional hardening α_p and the evolution of the isotropic damage variable d. The stress-stretch response can be divided into three stages — the (very small) first stage shows an elastic response, the second stage is dominated by plastic behaviour and in the last stage deterioration of the material takes place. For all (apart from one) parameter combinations, plasticity and damage both continue to evolve throughout the

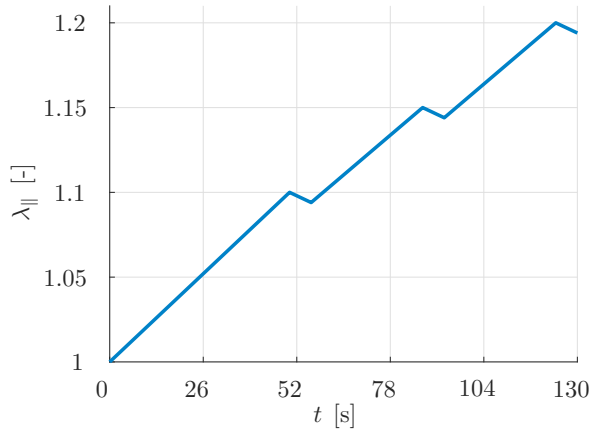

Figure 3.1: Evolution of the prescribed stretch $\lambda_{\parallel}$ over time t. The reduction of the stretch $\lambda_{\parallel}$ at values 1.1, 1.15 and 1.2 results in a deformation controlled unloading.

Table 3.4: List of material parameters for the homogeneous tension test. The third column contains the reference set, subsequent columns list the decreased and increased values of each parameter.

		Value			
Symbol	Description	reference	lower	higher	Unit
E	Young's modulus	208.0	—	—	GPa
ν	Poisson's ratio	0.3	—	—	–
σ_{y0}	yield stress	250.0	100.0	400.0	MPa
h_{p}	hardening modulus	1300.0	1000.0	2000.0	MPa
n_{p}	hardening exponent	0.25	0.15	0.35	–
$q_{\max}$	damage threshold	0.2	0.15	0.25	MPa
n_{d}	damage exponent	2/3	—	—	–
η	damage rate factor	0.1	0.05	0.15	–
ξ_{vol}	volumetric damage factor	1.0	—	—	–
ξ_{iso}	isochoric damage factor	1.0	0.5	1.5	–
ξ_q	threshold factor	10.0	5.0	20.0	–
ξ_m	effective stress factor	1.0	0.5	1.5	–
$\eta_{\alpha_{\mathrm{p}}}$	coupling factor	2.5	0.0	5.0	–

subsequent loading. Although the plastic parameters — yield stress σ_{y0}, hardening modulus h_p and hardening exponent n_p — are common in literature and have been extensively studied, the variation thereof is included here in order to demonstrate the non-intuitive influence upon the damage evolution. Increasing yield stress (Figure 3.2a, green line), hardening modulus (Figure 3.2b, green line) or decreasing the hardening exponent (Figure 3.3b, red line) all lead to slower evolution of plasticity and to a larger maximum of the elastic strains. Consequently, the stress is higher in the plasticity dominated stage. However, this also leads to an increased damage driving force and accelerates the evolution of damage — a smaller plasticity dominated stage is observed compared to the reference and a more pronounced decline in stress is observed in the last stage. The opposite effect, i.e. plasticity evolves more strongly and the decline in stress is less pronounced, is observed if these parameters are varied such that plasticity evolves more.

Variation of the damage threshold q_{max} (Figure 3.2a) and the damage rate factor η (Figure 3.2b) leads to expected results. A higher threshold value and/or lower damage rate factor yield stiffer responses with less evolution of damage and more evolution of plasticity. Vice versa, stresses are lower and less plasticity evolution is observed. The damage variable actually does not evolve more, compared to the reference set for a higher damage rate factor, but since the stiffness is influenced by a product of damage rate factor η and damage variable d, the overall deterioration of the elastic properties is higher. A much more diverse response is obtained by varying the damage influence factors $\xi_\bullet$ (Figure 3.3). While the influence factor on the isochoric elastic energy ξ_{iso} (Figure 3.3a) exhibits a similar behaviour to the damage rate factor η (Figure 3.2b), the influence factor for the effective stress ξ_m (Figure 3.3a) has a significant impact on the overall response. Increasing the factor leads to a slightly stiffer response (cyan line), a decrease however (orange line), leads to an abrupt loss of stress. At some point the yield limit is higher than the effective stress, and evolution of plasticity stops. Instead, damage evolution strongly increases reaching a value ten times above the reference parameter set. The reason lies in the lower influence factor ξ_m which results in an insufficient compensation of damage in the effective stress. The influence factor in the damage potential ξ_q (Figure 3.3b) mainly effects the transition from the plasticity dominated stage into the final stage. At some point the stress response as well as the accumulated damage coincide and the equivalent plastic strains only differ by a small amount.

3.4 Parameter identification and validation

The previously described ductile damage model shall now be employed to predict the behaviour of DP800 steel. To this end, a parameter identification is necessary, i.e. a numerical optimisation scheme. At this stage a simplex algorithm is carried out to determine (optimal) parameters in terms of an objective function which evaluates how well simulation results and experimental data match based on a least squares criterion. This

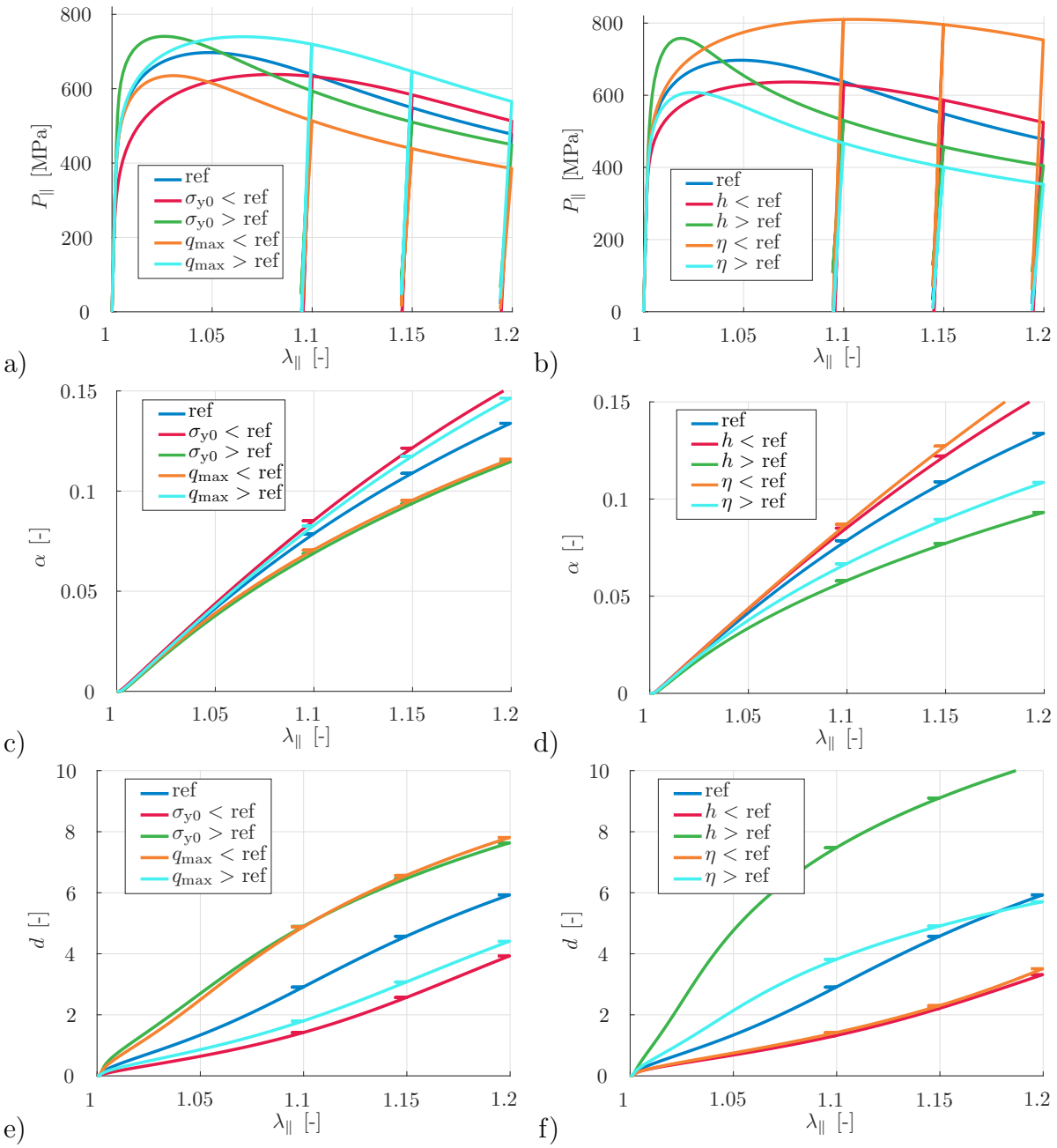

Figure 3.2: Stress-stretch-diagrams a) and b), proportional hardening-stretch-diagrams c) and d) and damage-stretch-diagrams e) and f). Influence of the initial yield limit σ_{y0} and the damage threshold q_{max} a), c) and e) as well as the hardening modulus h_p and the damage rate factor η b), d) and f) on the material response under homogeneous tension.

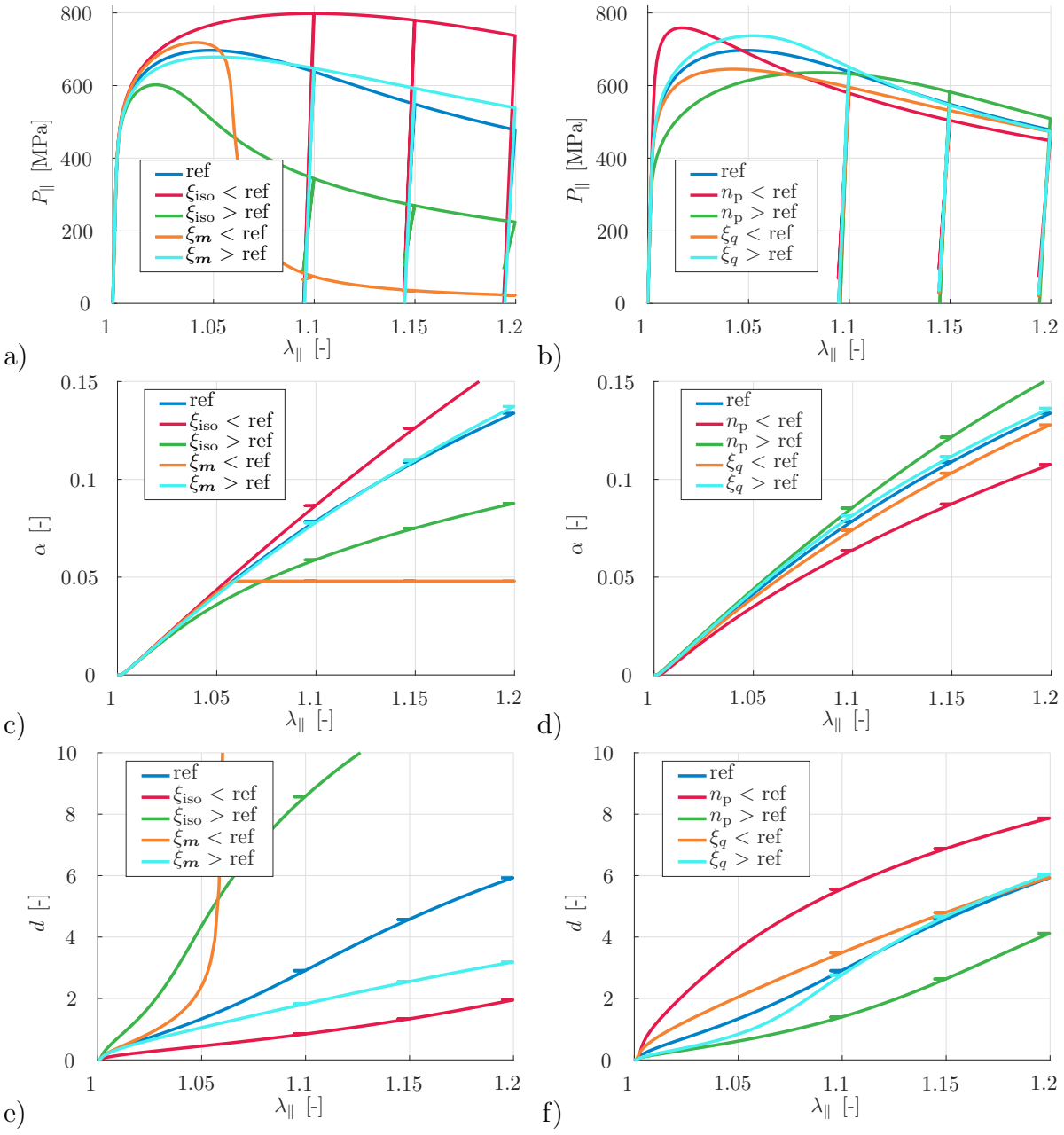

Figure 3.3: Stress-stretch-diagrams a) and b), proportional hardening-stretch-diagrams c) and d) and damage-stretch-diagrams e) and f). Influence of the isochoric damage factor ξ_{iso} and the effective stress factor ξ_m a), c) and e) as well as the hardening exponent n_{p} and the damage threshold factor ξ_q b), d) and f) on the material response under homogeneous tension.

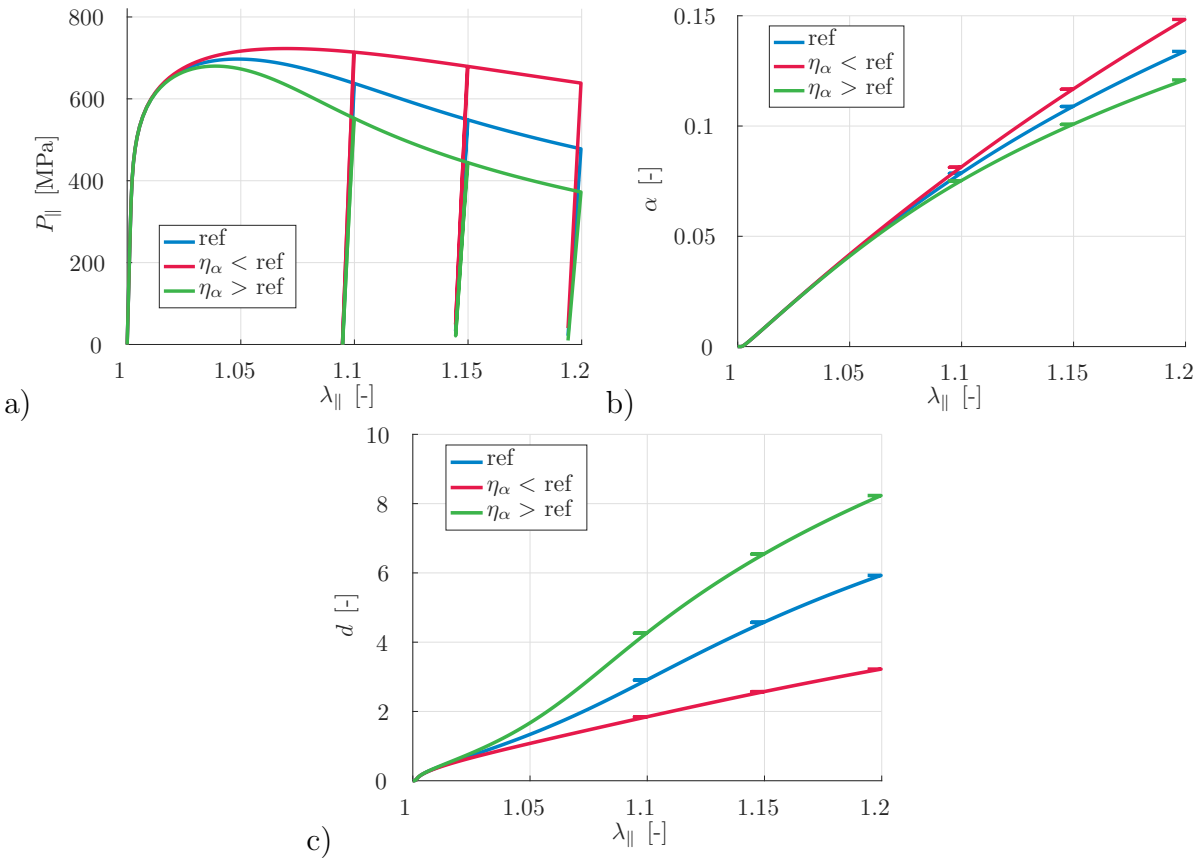

Figure 3.4: Stress-stretch-diagram a), proportional hardening-stretch-diagram b) and damage-stretch-diagram c). Influence of the coupling factor η_{α_p} on the material response under homogeneous tension.

section describes how the required experimental data is obtained, how simulation and objective function are set up and gives details on the parameter identification approach.

3.4.1 Experimental data

For the parameter identification process a tensile specimen of type A, see Figure 3.5a, is chosen and subjected to tensile loading with three unloading stages. The specimens are cut with a water jet from DP800 sheets with a thickness of 1.5 mm. In the tensile experiment, loading is applied by controlling the traverse displacement, see Figure 3.6a. The experiment is captured by a camera, see Figure 3.7a, which enables a determination of the inhomogeneous displacement field in a post-processing step. In addition, the camera is simultaneously used as an optical extensometer during the experiment which allows a real-time measurement of the displacements $u_\parallel$ in tensile direction and $u_\perp$ perpendicular to the tensile direction in the centre of the specimen. The optical extensometer measures the average displacement on the edges of a 10 mm by 2.6 mm rectangle which is centred at the centre of the specimen and which has its longer side aligned with the tensile direction. The force is measured by a 10 kN load cell. All experiments were carried out with a micro-tensile machine from Kammrath & Weiß supporting a maximum load of 10 kN. DIC (digital image correlation) is performed by means of the software Veddac 7.

Figure 3.6b exhibits the load displacement response of the tested specimens of type A. Overall, a response typical for dual phase steels can be observed. The initially elastic behaviour smoothly transitions into a regime dominated by plasticity, before damage effects lead to softening and finally to failure. For seven different tests the responses mostly coincide except that failure occurs at slightly different displacement load levels. The point of unloading occurs at different optically measured displacements $u_\parallel$ between the different specimens. The reason is that unloading is controlled by the traverse displacement u_T and that the optically measured displacements depend more strongly on the evolution of inelastic effects. The unloading response is important in order to be able to quantify the degradation of the elastic properties.

A degradation of elastic stiffness is measurable by using DIC. Consider only a narrow region in the center of the specimen with initial length $l_0 = 800\,\mu$m, see Figure 3.7b. Let l denote the current length, l_i the length of the region in fully unloaded state after i-th reloading, A the current cross-section and F the current force, then

$$\widetilde{E}_i := \frac{F}{A}\,\frac{l}{l - l_i}\,, \tag{3.73}$$

is a measure of the elastic stiffness during the i-th reloading step. Since elastic strains are small compared to the plastic strains at the points considered for stiffness determination, the current cross-section A is assumed to only depend on plastic strains. Thus, it is also reasonable to assume volume constancy which renders the current cross-section at the i-th unloading point to be $A_i = A_0\, l_0/l_i$. The result of the elastic stiffness analysis is depicted in Figure 3.8. Both, the average over all specimens and the values for specimen

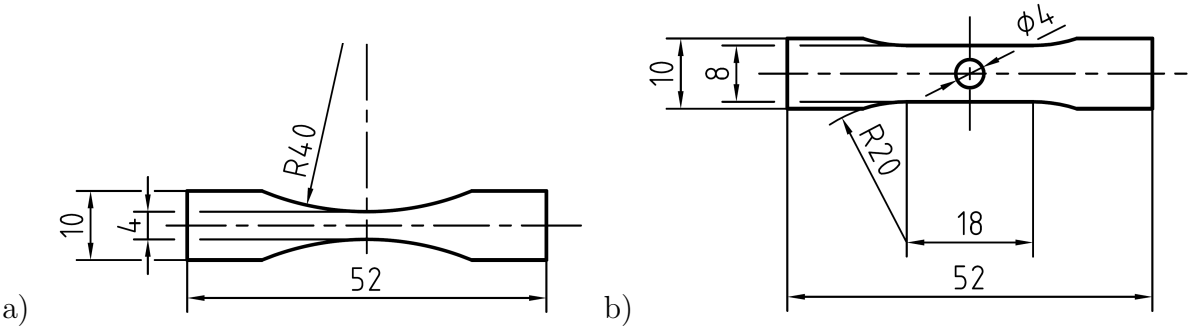

Figure 3.5: Geometries of specimens A and B with theoretical dimensions. The actual specimens are measured optically revealing an average minimum width of 3.85 mm instead of 4 mm and an average radius of 39.4 mm instead of 40 mm for specimens of type A. The optical measurement of specimens of type B yields 4.32 mm instead of 4 mm for the radius of the hole and 7.8 mm instead of 8 mm for the width.

A04, show a monotonous decline in elastic stiffness. However, the measurement is not very reliable, as the large error bars indicate, and may only be used for qualitative conclusions. The large deviations of the stiffness measurements between the different specimens may be explained by:

a) The initial state of damage may be different in each specimen, as it is manufactured from different regions of the same sheet.

b) Measurement of the displacement in the elastic regime is at the limit of the measuring capability. These displacements are in the order of 2 μm, while the resolution of the camera correlates 1 px to approximately 12 μm. Displacements smaller than 1 px rely on the sub-pixel recognition algorithm of the DIC system.

c) Loading and unloading of the specimens is displacement controlled. The points of reloading do not necessarily occur at similar states of internal damage.

d) Different errors may be multiplied and increase the overall error as, e.g., damage is computed based on the (measured) initial stiffness E_0.

3.4.2 Simulation setup

In order to successfully identify material parameters, it is vital to simulate the experiment as accurately as possible, whereby the specimen geometry and boundary conditions are of key importance. Boundary conditions can be applied most accurately by directly prescribing measured quantities, i.e. either the measured total reaction force or the displacement measured by the optical extensometer. Due to the underlying softening in the model, displacement controlled loading is advantageous in order to be able to compute a response for parameter combinations resulting in a too soft response. Since the optical extensometer measures over a length of 10 mm in the centre of specimen, it is most con-

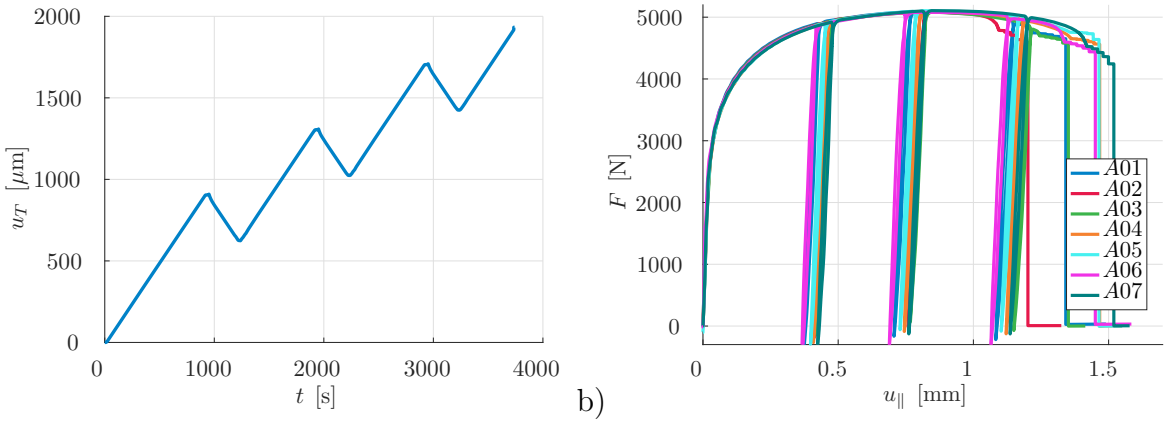

Figure 3.6: a) Loading path for testing of specimen A in terms of traverse displacement u_T. b) Load displacement diagram of the tensile tests of specimen A. Measured force F in N over optically measured displacement $u_\parallel$ in tensile direction in mm.

venient to restrict the simulation to this domain. Furthermore, to keep the numerical effort at a minimum, symmetry is used so that only a section measuring 5 mm needs to be discretised, see Figure 3.9a. This domain is discretised with 4000 8-noded brick elements, enhanced by the so-called F-bar method [49], with three displacement degrees of freedom and one non-local damage degree of freedom at each node. Displacement field and non-local damage field are linearly interpolated.

The specimens are measured optically revealing an average minimum width of 3.85 mm and an average radius of 39.4 mm resulting in an initial cross section of $A_0 = 5.755\,\mathrm{mm}^2$ instead of the theoretical dimensions given in Figure 3.5a. The deviations from these average dimensions between different specimens are small ($< 20\,\mu$m for the width). These measured dimensions are the basis for the discretised geometry.

3.4.3 Objective function

The implementation of the parameter identification closely follows the work in [149]. The goal of the objective function g is to quantify the difference between the response of the simulation and the physical specimen during the experiment. To this end, an objective function incorporating the reaction force and the displacement field is set up as

$$g = w_F\, g_F\big(F^{\mathrm{exp}}(t),\, F^{\mathrm{sim}}(t)\big) + w_{\Delta \boldsymbol{u}}\, g_{\Delta \boldsymbol{u}}\big(\Delta \boldsymbol{u}^{\mathrm{exp}}(\boldsymbol{X},\, t),\, \Delta \boldsymbol{u}^{\mathrm{sim}}(\boldsymbol{X},\, t)\big)\,, \tag{3.74}$$

with

$$g_F = \sum_t w_t \left[F^{\mathrm{exp}} - F^{\mathrm{sim}}\right]_t^2\,, \qquad g_{\Delta \boldsymbol{u}} = \sum_t \frac{w_t}{n_{\mathrm{np}}} \sum_i^{n_{\mathrm{np}}} \left\|\Delta \boldsymbol{u}_i^{\mathrm{exp}} - \Delta \boldsymbol{u}_i^{\mathrm{sim}}\right\|_t^2\,, \tag{3.75}$$

a) 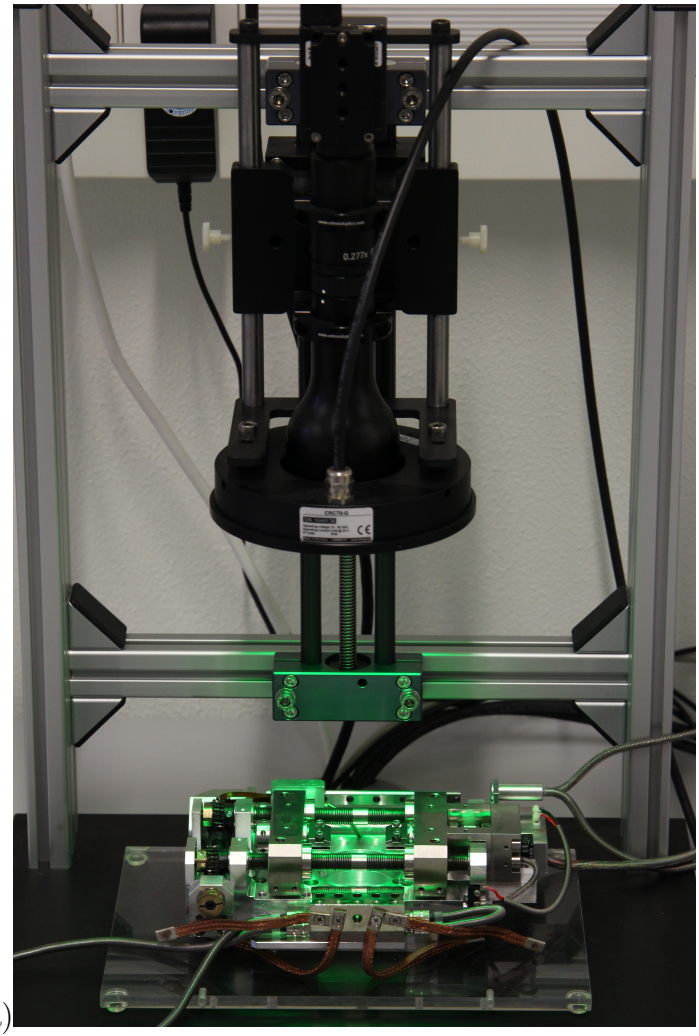 b) 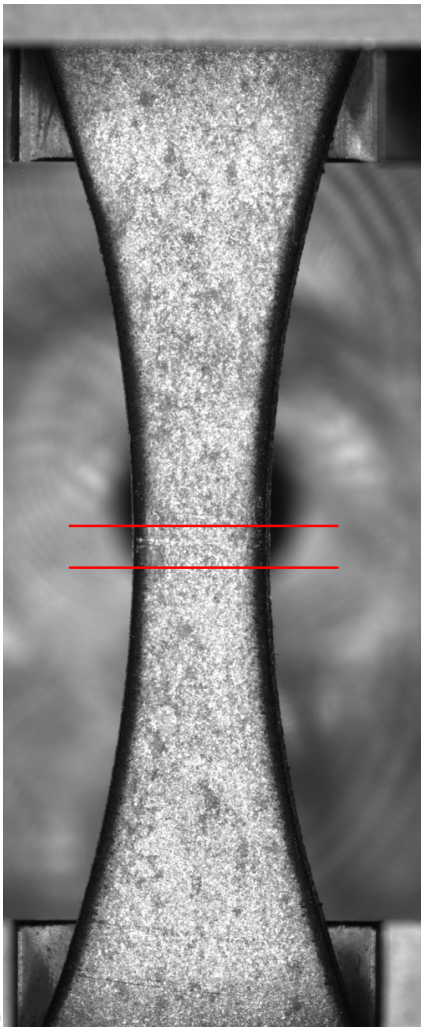

Figure 3.7: a) Image of the microtensile machine from Kammrath & Weiß placed beneath the DIC camera. b) Image of specimen A04 before testing taken from the DIC camera. Red lines indicate the 800 μm wide region for which the degradation of elastic stiffness is determined.

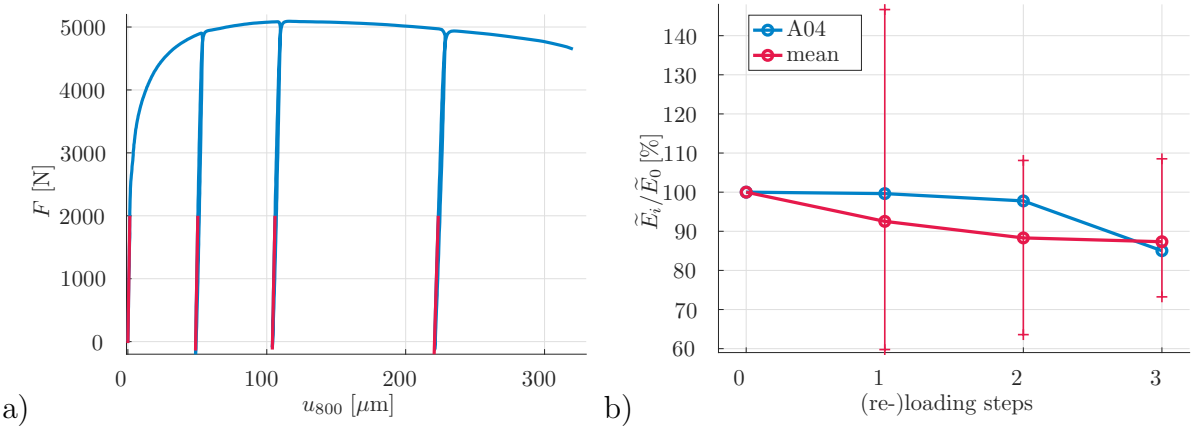

Figure 3.8: a) Load displacement diagram for specimen A04. Displacement u_{800} is determined from the 800 μm wide region marked in Figure 3.7b. The red lines indicate the determined stiffness. b) Degradation of stiffness over (re-)loading steps in terms of normalised stiffness. The blue line corresponds to the stiffness determined for specimen A04, while the red line (with error bars) is the average of specimens A01–A07.

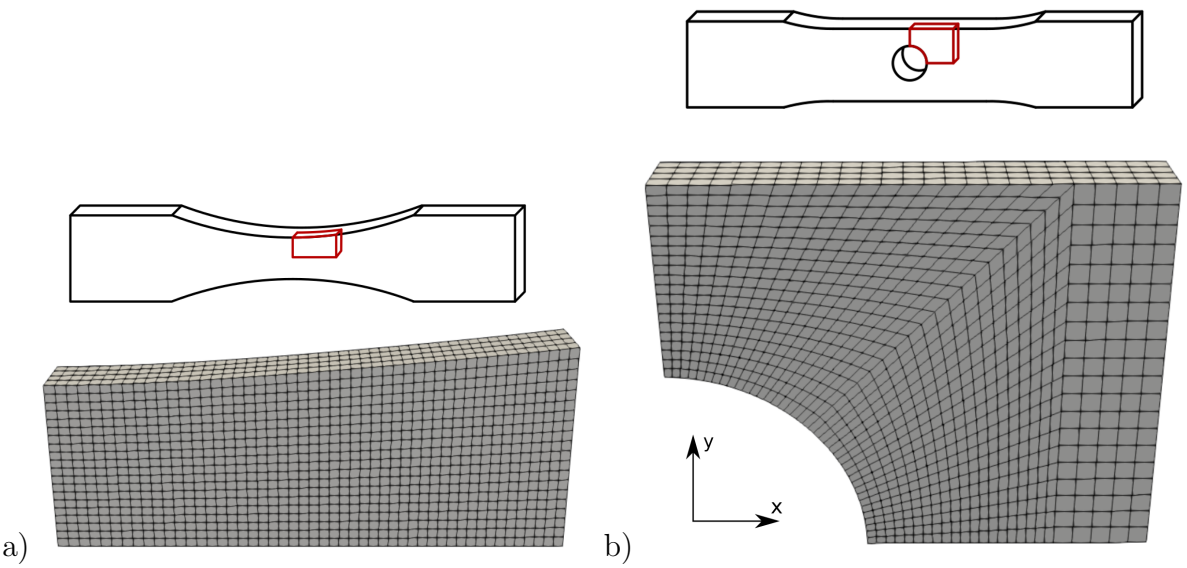

Figure 3.9: Discretised regions of specimens A and B.

where $w_\bullet$ are weighting factors and where $w_t = 1$ is chosen. The reaction force is taken into account by the difference between the total measured reaction force of the experiment F^{exp} and the total reaction force of the simulation F^{sim} in every time step. Directly comparing the displacement fields has the drawback of inherent rigid body motions in the measured displacement field. Thus, instead of using the displacement field directly, a strain-like quantity is employed for the evaluation of the objective function. By dividing the difference of the displacement of two neighbouring measurement points by their distance a simple strain-like quantity $\Delta\boldsymbol{u}$ is obtained which is free of rigid body motions, cf. [149]. The relative displacements $\Delta\boldsymbol{u}^i$ of measurement point i with coordinates $(x^i,\, y^i)$ and measured displacement $(u_x^i,\, u_y^i)$ can be computed by

$$\Delta\boldsymbol{u} = \begin{bmatrix} \Delta u_x \\ \Delta u_y \end{bmatrix}, \quad \text{with} \quad \Delta u_x = \frac{u_x^j - u_x^i}{x^j - x^i}, \qquad \Delta u_y = \frac{u_y^k - u_y^i}{y^k - y^i}, \tag{3.76}$$

with measurement point j being the next neighbour in x-direction (with $x^j > x^i$) and measurement point k being the next neighbour in y-direction (with $y^k > y^i$). Since the displacement field in the experiment is evaluated on different measurement points than the finite element nodes of the simulation, it is necessary to interpolate the measured displacement field to the finite element nodes — a linear interpolation in time and space is performed.

3.4.4 Identified parameters

Immediately starting with the identification of all 15 parameters in the model at once requires a high numerical effort, since even an educated guess for the starting parameters may be significantly far from a numerical optimum. In addition, with this amount of parameters the chosen experiment could possibly not yield enough information to uniquely identify all parameters. Before even beginning the identification process, some parameters can be excluded and can instead be arbitrarily set or determined manually. The penalty parameter b_{d} is kept constant as it just needs to be large enough in order to guarantee that the non-local damage variable ϕ_{d} matches the local damage variable d. If the penalty parameter b_{d} is chosen to be too large numerical instabilities may arise. Previous studies have shown $b_{\mathrm{d}} = 500\,\mathrm{MPa}$ to be sufficient, see also Figure 3.10b. The influence factor ξ_{vol} is chosen as $\xi_{\mathrm{vol}} = 1$ to prevent ambiguity between η and $\xi_\bullet$. The damage exponent n_{d} has a similar influence as does ξ_q, so that $n_{\mathrm{d}} = 0.6667$ is chosen. Further analysis of the model as well as the results of the following parameter identification motivated an update of the parametrisation of the model, see Section 3.6.

For the identification of the remaining 12 parameters the numerical effort can be considerably reduced by splitting the problem into smaller subproblems. In this case the elastic, plastic and damage stages can be distinguished in the response of the experiment in order to identify only the elastic, plastic or damage parameters, respectively. Since both plastic and damage stages are influenced by damage and plastic parameters, a final

Table 3.5: Determined elastic parameters for specimens A01–A07.

Specimen	$\widetilde{E}_0$ in GPa	ν	K in GPa	G in GPa
A01	221.41	0.194	120.59	92.72
A02	169.24	0.215	98.97	69.65
A03	234.02	0.255	159.20	93.24
A04	206.74	0.263	145.39	81.84
A05	199.40	0.258	137.33	79.25
A06	262.66	0.193	142.60	110.08
A07	244.05	0.304	207.53	93.58
average	219.65	0.240	140.95	88.55
literature	207.00	0.300	172.50	79.62
used for PI	207.00	0.210	118.97	85.54

optimisation identifying plastic and damage parameters at once is carried out, where the parameters identified in the subproblems are chosen as starting values.

The elastic properties E and ν can be determined directly from measurements. The Young's modulus E is calculated with the help of measured forces and optically measured displacements in tension direction as well as with geometry information, cf. (3.73), whereas the Poisson ratio ν is calculated with the (negative) ratio of the strains in the plane, i.e. $\nu = -\varepsilon^{\mathrm{e}}_{\perp}/\varepsilon^{\mathrm{e}}_{\parallel}$. The elastic parameters have been computed for each specimen from the gathered DIC-data in the $800\,\mu$m wide region (see Figure 3.7b) of the initial elastic loading — the elastic domain (of the first loading) is assumed to end after loading exceeds 1.5 kN, see Table 3.5. Additionally, relations $K = E/[3\,[1-2\,\nu]]$ and $G = E/[2\,[1+\nu]]$ have been used to add the parameters used in the model formulation. The last row shows the values actually used in the parameter identification process.

The plastic stage is assumed to end at $t = 900\,\mathrm{s}$ before the first unloading starts. At this early stage of loading the damage portion barely influences the response and it is possible to identify a very good estimate, as exhibited by Figure 3.10a, of the initial yield stress σ_{y0}, the hardening modulus h_{p} and the hardening exponent n_{p}, see Table 3.6. Since the plastic parameter identification includes a response free of softening, the loading in the underlying simulation can be controlled by force. By prescribing the experimentally measured force as boundary condition, only relative displacements in the objective function need to be taken into account, i.e. $w_F = 0$ and $w_{\Delta \boldsymbol{u}} = 1$. In other words, the force contribution in the goal function g_F is exactly satisfied.

On the basis of the identified plastic parameters, a parameter identification of only the most influential damage parameters (damage threshold $q_{\max}$, damage rate factor η, effective stress factor ξ_m and regularisation parameter c_{d}) is carried out, see Figure 3.10a for the corresponding load displacement responses. Simulating the damage regime entails the inclusion of softening effects, and it is therefore beneficial to run the simulation controlled by displacement. Consequently, the objective function needs to take the force into account. In order to similarly weight the influence of displacement and force,

both weights w_F and $w_{\Delta \boldsymbol{u}}$ are chosen such that the error in the objective function is scaled to have the unit of stress squared. To this end, the force is divided by cross-section squared, and the relative displacements (strain-like quantities) are multiplied by Young's modulus squared, i.e. $w_F = [4/A_0]^2$ and $w_{\Delta \boldsymbol{u}} = 0.7\, E^2$. The factor 4 in w_F is present due to symmetry and the factor 0.7 in $w_{\Delta \boldsymbol{u}}$ has been determined empirically as yielding a subjectively good balance between matching force and displacement response simultaneously. These weighting factors are used in all following identifications.

Using the preliminary parameters as starting values, an identification (PI1) where all 12 parameters are to be determined by the simplex algorithm yields, after some restarts of the simplex, a good match with the experimental response, see Figure 3.11. Based on this identification other identifications with perturbed starting values are set up (PI2, PI3, PI4). Since PI4 identified $\eta = 5.0$ and $\eta \leq 5.0$ was (arbitrarily) set as bound, restarts with a relaxed bound $\eta \leq 20.0$ are carried out with the same starting values (PI4a) and the parameters identified in PI4 as starting values (PI4b).

Out of these identifications, the PI4, PI4a and PI4b identifications stand out from the others; the total objective function value is slightly lower when compared to PI1 but the identified parameters differ considerably, see Tables 3.7 and 3.8. Especially the regularisation parameter c_d is magnitudes higher in PI4b than in PI1, and damage threshold q_max as well as damage rate factor η also have much higher values. However, the effective stiffness degradation of both parameter sets is in fact very similar since the maximum value of the damage variable in the last load increment is much higher for PI1 ($d_\mathrm{PI1} = 2.8$, $\exp(-\eta_\mathrm{PI1}\, d_\mathrm{PI1}) = 0.646$) than for PI4b ($d_\mathrm{PI4b} = 0.092$, $\exp(-\eta_\mathrm{PI4b}\, d_\mathrm{PI4b}) = 0.634$). In the load-displacement diagram, Figure 3.11, as well as in the contour plot of the damage function $f^\mathrm{vol}(d)$, Figure 3.14, the responses of parameter sets PI1 and PI4b are very similar, albeit distinguishable. A closer look at the error in relative displacement, as depicted in Figures 3.12 and 3.13, reveals no visible differences between both parameter sets. The relative displacements of the simulation matches the experimentally determined relative displacement quite well for roughly the first 2500 s of loading. Thereafter, relative displacements are higher in the simulation.

The other remarkable parameter set is PI3, which is the only set where the coupling factor η_{α_p} attains a significant value. Thereby, the response is able to capture the drop in force at the end of the loading stage much better compared to the other parameter sets, cf. Figure 3.11. However, the force response prior of the drop is captured worse, resulting in a higher objective function value.

From the identification point of view, i.e. by means of the objective function, the parameter sets of PI1 and PI4b seem to match the experimental response equally well. However, several problems arise. Even if both parameter sets resulted in identical responses for the current boundary value problem, they would not (necessarily) result in identical responses of the material model for arbitrary boundary value problems, i.e. further experimental data, ideally experiments which activate different deformations modes, need to be taken into account in the future. Another problem stems from the correlation between parameters, e.g. between the parameters η and c_d. Damage variable d always

Table 3.6: List of identified material parameters for DP800 steel sheets. Preliminary identification of a subset of parameters (plastic PI, damage PI) and first combined parameter identification results.

		plastic PI		damage PI		combined PI	
		start	identified	start	identified	start	identified
E	GPa	207.00		207.00		207.00	
ν	–	0.21		0.21		0.21	
σ_{y0}	MPa	243.00	50.00	50.00		50.00	50.48
h_p	MPa	1300.00	1306.94	1306.94		1306.94	1332.28
n_p	–	0.2500	0.1650	0.1650		0.1650	0.1564
q_{max}	MPa	15.5500		1.0000	2.6929	2.6929	3.2526
n_d	–	0.0000		0.6667		0.6667	
η	–	0.5000		0.2000	0.6353	0.6353	0.7388
ξ_{vol}	–	1.0000		1.0000		1.0000	
ξ_{iso}	–	1.0000		1.0000		1.0000	0.7475
ξ_q	–	10.0000		10.0000		10.0000	2.2926
ξ_m	–	1.0000		1.0000	0.2162	0.2162	0.2606
η_{α_p}	–	0.0000		0.0000	5.2768	5.2768	4.8702
c_d	N	11.0000		11.0000	24.4620	24.4620	69.0944
b_d	MPa	500.00		500.00		500.00	

appears in combination with the parameter η with the exception of the contribution of the gradient of non-local damage variable ϕ_d. In fact, the quotient c_d/η^2 yields approximately 22 for PI1 and 15 for PI4b — in contrast to the regularisation parameter c_d having the values 0.54 and 379, suggesting a high correlation between both parameters. This motivated an update of the parametrisation, see Section 3.6. Further problems lie in the consideration of damage during parameter identification. Damage can only be distinguished from plasticity by means of elastic stiffness degradation in this framework, e.g. by elastic unloading. In the herein considered experiment, damage is only implicitly taken into account via force and displacement measurements during unloading. It might be possible that different weighting of unloading and loading in the objective function — by choosing w_t accordingly — yields a parameter set which is able to predict the response of DP800 (or any other material) more precisely. An even more complex problem is the identifiability of the regularisation parameter c_d, since further experiments, especially with specimens of much larger or smaller dimensions, are required. In spite of these open problems, the next section is a first approach to the validation of the parameter sets identified in this section.

3.4.5 Validation

With two — apparently equally well fitting — parameter sets having been identified, cf. Tables 3.7 and 3.8, the validation reveals the prediction capability of the material model

Table 3.7: List of identified material parameters for DP800 steel sheets. Main parameter identification with different starting values — PI1: starting values from intermediate identification results, PI2 and PI3: arbitrarily, but moderately perturbed starting values.

		PI1		PI2		PI3	
		start	optimised	start	optimised	start	optimised
rel. tot. obj		100.00%		100.55%		110.38%	
% force obj.		31.29%		31.25%		43.13%	
E	GPa	207.00		207.00		207.00	
ν	–	0.21		0.21		0.21	
σ_{y0}	MPa	250.00	248.59	50.00	140.69	500.00	595.27
h_p	MPa	1700.00	1705.64	1300	1536.80	2500.00	1889.15
n_p	–	0.2500	0.2654	0.1500	0.2022	0.3500	0.5947
q_{max}	MPa	0.7500	0.6953	1.0000	1.9422	1.7500	2.3508
n_d	–	0.6667		0.6667		0.6667	
η	–	0.2000	0.1559	1.0000	0.2090	0.1000	0.1706
ξ_{vol}	–	1.0000		1.0000		1.0000	
ξ_{iso}	–	0.5000	0.5861	1.0000	2.5024	1.0000	1.9637
ξ_q	–	1.0000	0.8100	10.0000	6.3249	10.0000	7.0459
ξ_m	–	0.6000	0.6163	1.0000	1.6287	0.4000	0.9290
η_{α_p}	–	0.0000	0.0000	0.0000	0.0000	0.0000	7.4849
c_d	N	0.4000	0.5400	11.0000	33.2246	2.0000	2.7670
b_d	MPa	500.00		500.00		500.00	

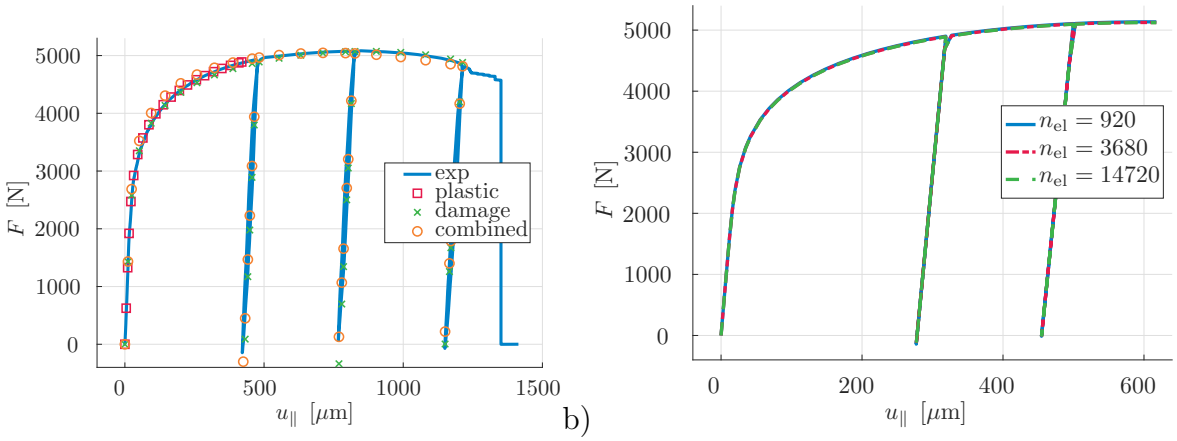

Figure 3.10: Load displacement diagram of the simulation response of selected parameter sets and experimental data. Force in N over optically measured displacement in tensile direction in mm. a) Responses of the preliminary identifications compared to experiment A03. The experimental response is displayed as a blue continuous line and the identifications by means of square, X and circle. b) The right load displacement diagram shows the mesh independence for parameter set PI1 by means of three different discretisations with 920, 3680 and 14720 elements for simulations with specimen geometry B01.

Table 3.8: List of identified material parameters for DP800 steel sheets. Main parameter identification with different starting values (continuation) — PI4: heavily perturbed starting parameters, PI4a and PI4b: restart with relaxed parameter bounds.

		PI4		PI4a		PI4b	
		start	optimised	start	optimised	start	optimised
rel. tot. obj		99.85%		104.07%		99.68%	
% force obj.		29.75%		37.88%		29.94%	
E	GPa	207.00		207.00		207.00	
ν	–	0.21		0.21		0.21	
σ_{y0}	MPa	450.00	424.76	450.00	731.64	425.00	478.71
h_p	MPa	8700.00	39896.53	8700.00	14432.08	39900.00	40771.87
n_p	–	1.0000	0.8814	1.0000	0.9983	0.8800	0.8920
q_{max}	MPa	6.7500	20.4152	6.7500	17.6545	20.4000	18.7378
n_d	–	0.6667		0.6667		0.6667	
η	–	2.0000	4.9991	2.0000	2.3509	5.0000	4.9551
ξ_{vol}	–	1.0000		1.0000		1.0000	
ξ_{iso}	–	1.5000	0.6023	1.5000	0.7806	0.6000	0.5545
ξ_q	–	100.0000	1.0431	100.0000	0.6443	1.0400	1.0031
ξ_m	–	1.6000	3.8737	1.6000	2.3145	3.8700	3.6116
η_{α_p}	–	3.0000	0.0442	3.0000	0.0188	0.0400	0.0026
c_d	N	50.0000	442.9782	50.0000	37.4659	443.0000	379.1240
b_d	MPa	500.00		500.00		500.00	

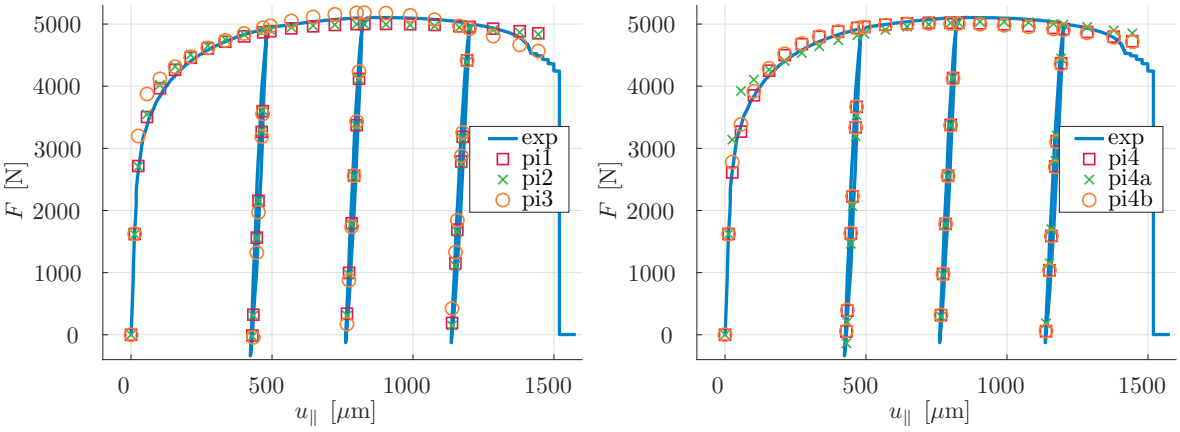

Figure 3.11: Load displacement diagram of the tensile test of specimen A07 and the simulation response with parameter sets PI1–PI4b. Force in N over optically measured displacement in tensile direction in mm. The experimental response is displayed as a blue continuous line and the identifications by means of square, x and circle.

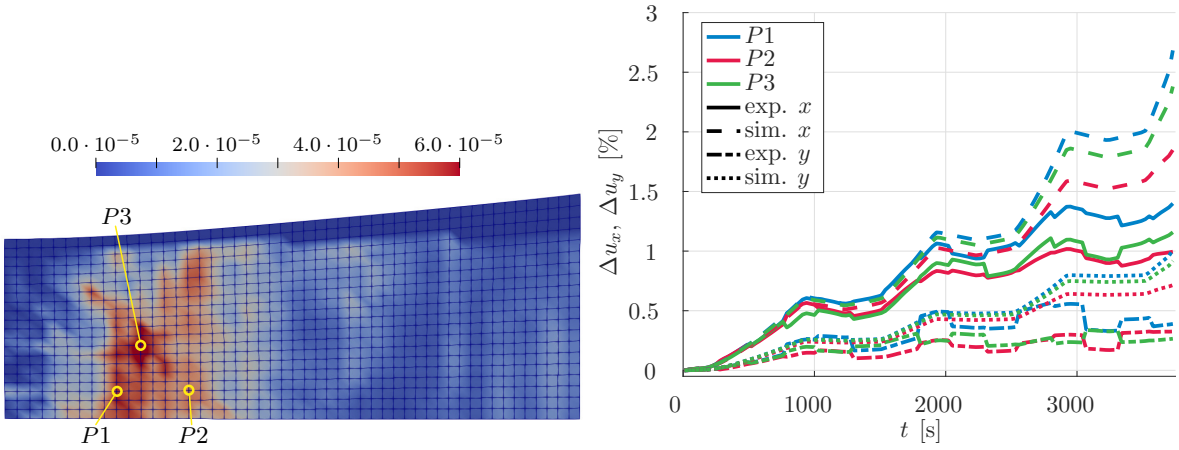

Figure 3.12: Depiction of the relative displacement $\Delta \boldsymbol{u}$ of the first identified parameter set PI1. Contour plot of the squared absolute error of the relative displacement, i.e. objective function $g_{\Delta \boldsymbol{u}}$, see (3.75), at each node at $t = 3520\,\mathrm{s}$ (left) and comparison of the evolution of the experimental and simulated relative displacements in x and y-direction over time (right) for nodes P1, P2 and P3.

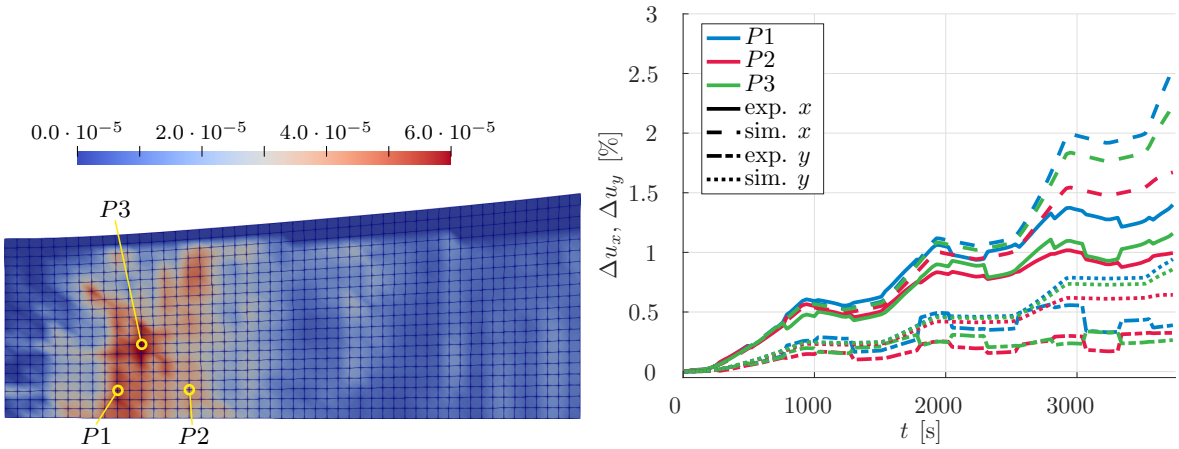

Figure 3.13: Depiction of the relative displacement $\Delta \boldsymbol{u}$ of the last identified parameter set PI4b. Contour plot of the squared absolute error of the relative displacement, i.e. objective function $g_{\Delta \boldsymbol{u}}$, see (3.75), at each node at $t = 3520\,\mathrm{s}$ (left) and comparison of the evolution of the experimental and simulated relative displacements in x and y-direction over time (right) for nodes P1, P2 and P3.

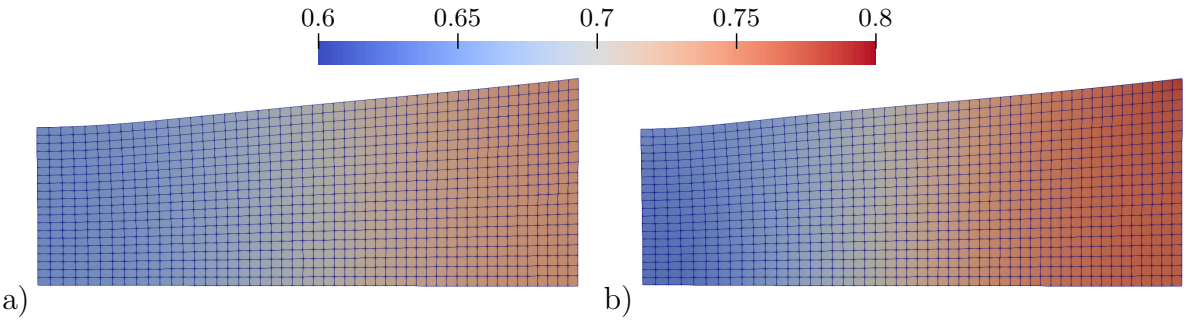

Figure 3.14: Contour plot of the damage function value $f^{\mathrm{vol}}(d)$ on the deformed configuration after the last load increment ($t = 3730\,\mathrm{s}$). Comparison between the two identified parameter sets: a) PI1, b) PI4b.

together with the identified parameters. To this end, a second experiment is considered, featuring a tensile specimen with a hole (specimen B, see Figure 3.5), see also Remark 5.

The tensile test is performed in the same way and with the same set up as the tensile test of the notched tensile specimen (type A), as described in Section 3.4.1. The comparison of the experimental response with the simulation response reveals clearly visible differences between the responses of the identified parameter sets in the load displacement diagram, see Figure 3.15. Parameter set PI1 (red squares, left side) shows overall good agreement with the experimental response, as the force is slightly underestimated in the beginning of the plastic stage. The parameter set PI4b (orange circles, right side), overestimates the force response in the inelastic stage but is able to predict the unloading behaviour as well as parameter set PI1. Despite the response with parameter set PI3 being able to predict a drop in force in the final stage of loading in the identification experiment, for the validation experiment no drop in force can be observed (orange circles, left side).

The comparison of the relative displacements confirms a better match between experimental and simulation response for parameter set PI1, see Figure 3.16, than for parameter set PI4b, see Figure 3.17. The contour plots showing the squared error of relative displacement indicate only very few spots with relevant error levels for PI1. The red region on the boundary of the hole can be ignored as relative displacements are not computed correctly at that edge. The two red patches on the upper edge can probably be attributed to measurement errors from DIC. In the necking region three points are marked and the evolution of relative displacements over time is plotted for these points in the right diagram of Figure 3.16. For point P1 a nearly perfectly matching simulation and experimental response can be observed, while points P2 and P3 show small offsets between experimental and simulation response. The offset for displacements in x-direction seems to slightly increase after each inelastic loading stage for both points. The displacements in y-direction match quite well in point P2, but for point P3 a constant offset is observed.

Qualitatively similar results are obtained for the second parameter set PI4b, see Fig-

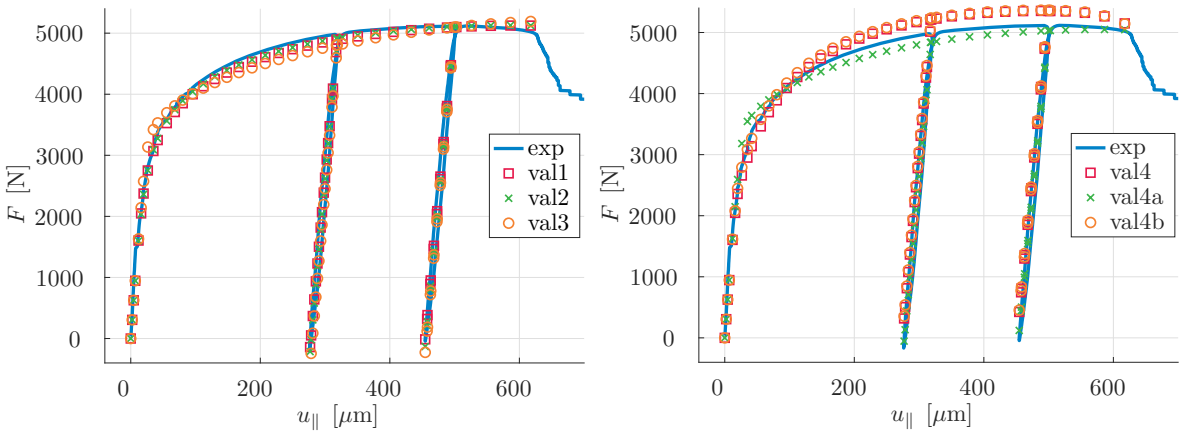

Figure 3.15: Load displacement diagrams with force in N over displacement in tensile direction in μm of the tensile test of specimen B01 and the validation simulation response with parameters of the parameter identifications PI1 through PI4b. The experimental response is displayed as a blue continuous line and the identifications by means of square, x and circle.

ure 3.17, but overall the error is higher. In the contour plot the red patches are larger and darker, especially around points P2 and P3 and to their right, indicating that probably the width of the localisation zone is predicted incorrectly in the simulation. This can be confirmed by looking at the evolution of relative displacements over time. Displacements at point P1 are underestimated in the first 1000 seconds, but in the end, after 2000 seconds, they are overestimated, whereas at points P2 and P3 the underestimation of displacements constantly increases. The comparison of the damage evolution, see Figure 3.18, reveals a higher localisation of damage evolution for the second parameter set.

Overall, the parameter set PI1 performs best and allows accurate predictions of the behaviour of DP800 steel. The mesh independence of this parameter set is proven in the left diagram of Figure 3.10. An identical response is obtained for three different discretisations.

Remark 5 *A proper validation requires a (sufficiently) distinct and more complex experiment in order to test a different deformation pattern than the one used for the identification. At the same time the experiment must lie within the region which the model is able to predict, e.g. a pressure dominated experiment can presumably not be correctly predicted with this model. The here chosen tensile tests with a notched specimen and a specimen with a hole both are tension dominated but exhibit different localisation patterns.*

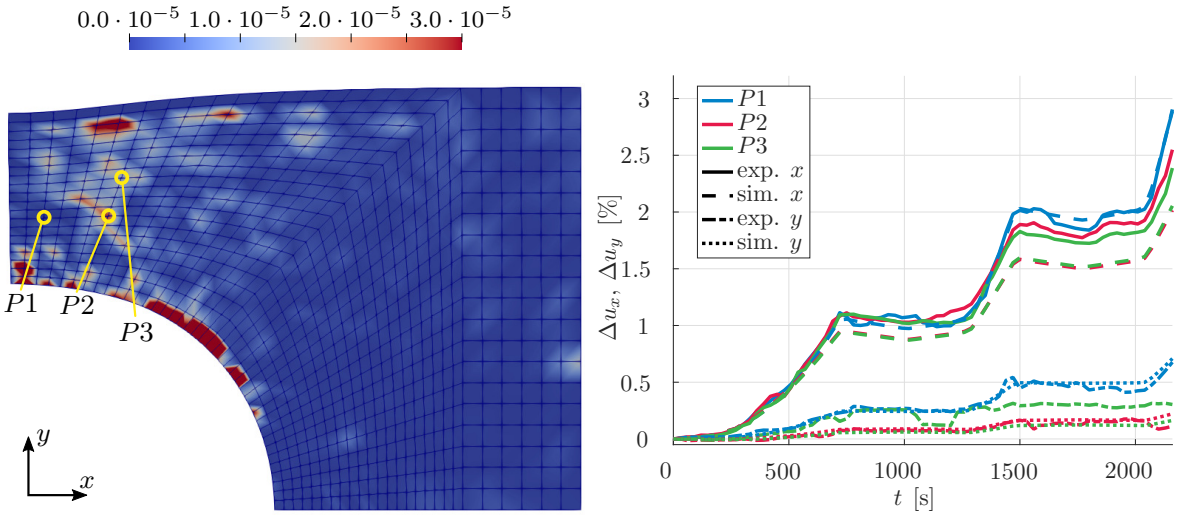

Figure 3.16: Illustration of the relative displacement $\Delta \boldsymbol{u}$ of the first identified parameter set PI1. Contour plot of the squared absolute error of the relative displacement, i.e. objective function $g_{\Delta \boldsymbol{u}}$, see (3.74), at each node at $t = 2160\,\mathrm{s}$ (left) and comparison of the evolution of the experimental and simulated relative displacements in x and y-direction over time (right) for nodes P1, P2 and P3.

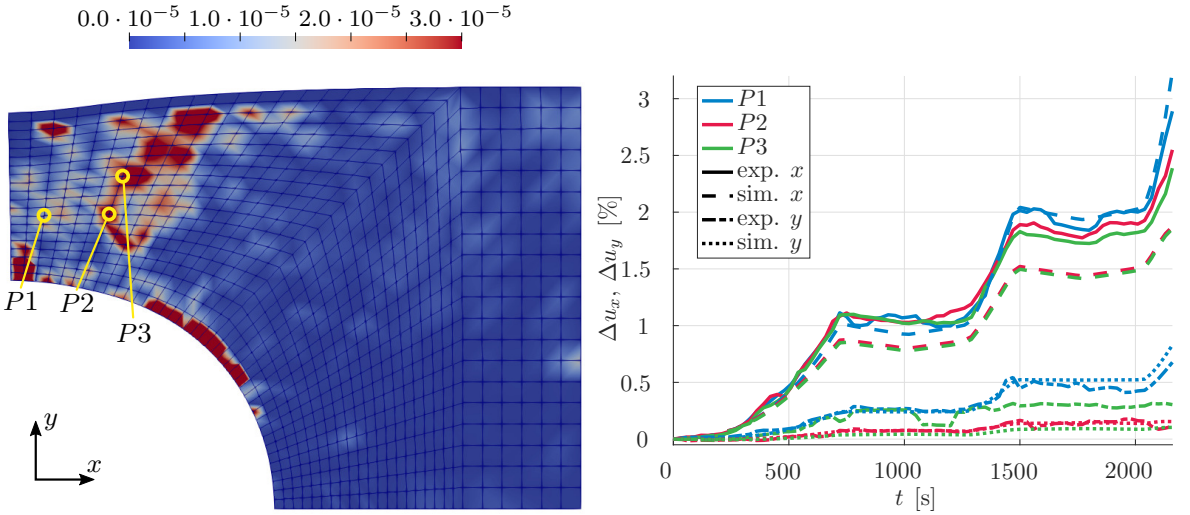

Figure 3.17: Illustration of the relative displacement $\Delta \boldsymbol{u}$ of the last identified parameter set PI4b. Contour plot of the squared absolute error of the relative displacement, i.e. objective function $g_{\Delta \boldsymbol{u}}$, see (3.74), at each node at $t = 2160\,\mathrm{s}$ (left) and comparison of the evolution of the experimental and simulated relative displacements in x and y-direction over time (right) for nodes P1, P2 and P3.

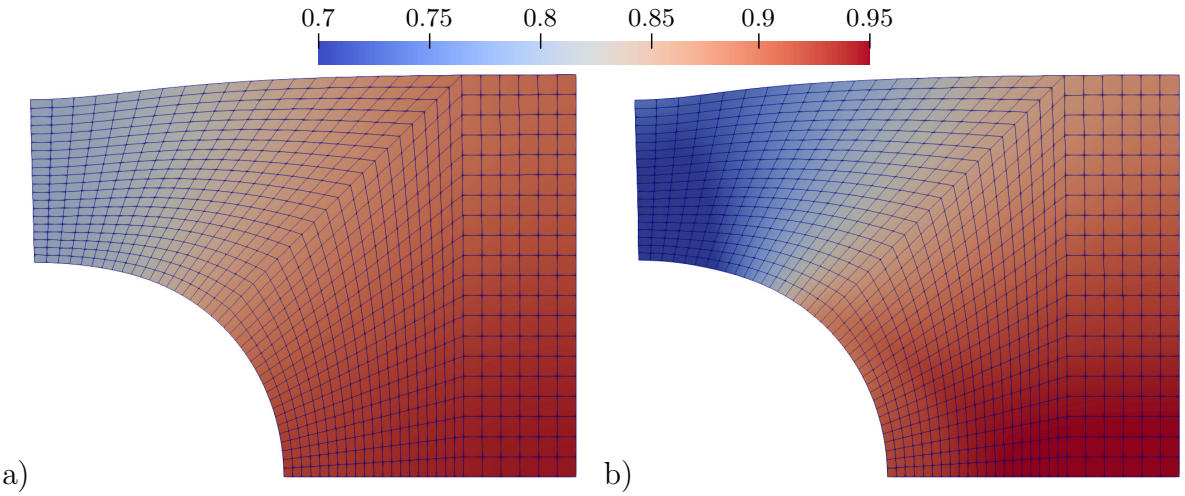

Figure 3.18: Contour plot of the damage function value $f^{\mathrm{vol}}(d)$ on the deformed configuration after the last load increment ($t = 2160\,\mathrm{s}$). Comparison between the two identified parameter sets: a) PI1, b) PI4b.

3.5 Application to air bending

In this section, the previously proposed regularised isotropic ductile damage model is used (in slightly modified form) to simulate an air bending process. The comparison of the regularised air bending simulation with a non-regularised air bending simulation can be found in [163].

An important aspect for the simulation of forming processes which is missing in the previously proposed model is, that damage does not evolve under fully compressive load states. A very simple and low-impact approach is to deactivate damage evolution if the volumetric elastic strain is negative. To this end, the damage initiation criterion is formulated in terms of the modified damage driving force $\widetilde{q}$ defined as

$$\widetilde{q} := \langle \mathrm{tr}(\boldsymbol{\varepsilon}^{\mathrm{e}}) \rangle^{0} \; q \,. \tag{3.77}$$

One of the biggest flaws of this approach is that for mixed strain states (i.e. one strain eigenvalue is positive and the other two are negative) with negative volumetric elastic strain damage evolution is disabled although in reality damage may evolve in the direction related to the positive strain eigenvalue. These strain states are typical for e.g. forward rod-extrusion, which limits the applicability of this approach. During the process of air bending, however, damage evolution mostly takes place where the volumetric elastic strain is positive.

The algorithmic impact of the modified driving force (3.77) is minimal, since the derivative of the modification with respect to the volumetric strain is (apart from the point of singularity) zero. Furthermore, the volumetric elastic strain is unaffected by damage evolution or plasticity evolution.

The regularised isotropic ductile damage model is implemented in Abaqus by means of user subroutines. Following the approach in [139], the implementation is achieved by supplying the subroutines "UMAT" and "UMATHT". The idea of the approach proposed in [139] (and of the similar approach in [155]) is to abuse the analogy of the non-local damage equation, cf. (2.8), with the steady state heat equation.

The Abaqus "UMAT" subroutine requires stresses and tangents to be given in a specific form. Abaqus expects to be given Cauchy stresses $\boldsymbol{\sigma}$, obtainable as

$$\boldsymbol{\sigma} = J^{-1}\, \boldsymbol{m}^{\mathrm{t}}\,, \tag{3.78}$$

and a tangent with correction for the Jaumann rate, herein denoted as T, i.e.

$$\mathsf{T} = J^{-1}\, \left[\mathsf{e} + \boldsymbol{I} \mathbin{\overline{\otimes}} \boldsymbol{m}^{\mathrm{t}} + \boldsymbol{m}^{\mathrm{t}} \mathbin{\overline{\otimes}} \boldsymbol{I}\right]\,. \tag{3.79}$$

The correction term is herein given in symmetrised form, see the discussion in [139] and references cited therein, although a non-symmetrised version is theoretically sufficient, see [160]. Similarly, the derivative of the stresses with respect to the non-local field variable ϕ_{d} is transformed by

$$\frac{\mathrm{d}\boldsymbol{\sigma}}{\mathrm{d}\phi_{\mathrm{d}}} = J^{-1}\, \frac{\mathrm{d}\boldsymbol{m}^{\mathrm{t}}}{\mathrm{d}\phi_{\mathrm{d}}}\,. \tag{3.80}$$

A schematic representation of the air bending process is given in Figure 3.19. The (metal) sheet is pushed into a die by means of a punch. The radii of the punch and the die are 1 mm each, i.e. $r_{\mathrm{punch}} = 1\,\mathrm{mm}$ and $r_{\mathrm{die}} = 1\,\mathrm{mm}$. Simulations are run with die widths $w = 24.5\,\mathrm{mm}$ and $w = 16\,\mathrm{mm}$. The tighter die width is used in order to amplify damage evolution and test the regularisation properties.

The set up of the air bending simulation in Abaqus uses rigid elements for the discretisation of punch and die. The die is fixed in space, whereas the punch displacement is completely prescribed. The sheet is discretised with linear quadrilateral plane strain elements. The numerical effort is reduced by considering symmetry conditions. The sheet is in contact with the punch and the die by means of a contact formulation using Lagrange multipliers. The element edge lengths of the two discretisations of the sheet are $l_e = 0.05\,\mathrm{mm}$ and $l_e = 0.025\,\mathrm{mm}$.

The successful regularisation of the air bending simulations is demonstrated by means of contour plots of damage evolution and plasticity evolution for a coarse and fine discretisation. Material parameters used in the simulation are given in Table 3.9. Damage evolution is portrayed by means of the stiffness degradation of the isochoric part of the energy, i.e. $d^{\mathrm{iso}} := 1 - f_{\mathrm{iso}}(d)$, see Figure 3.20. Plasticity evolution is plotted in terms of the isotropic hardening variable α_{p}, see Figure 3.21.

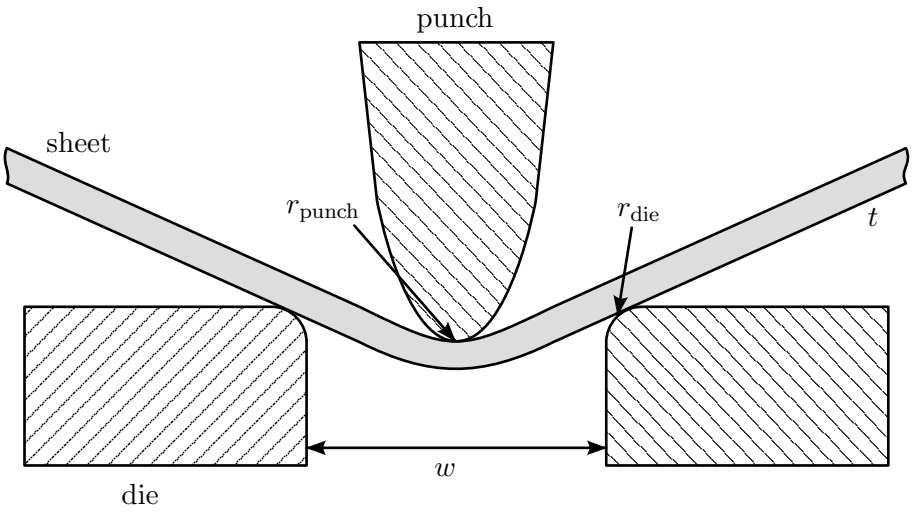

Figure 3.19: Schematic representation of the air bending process.

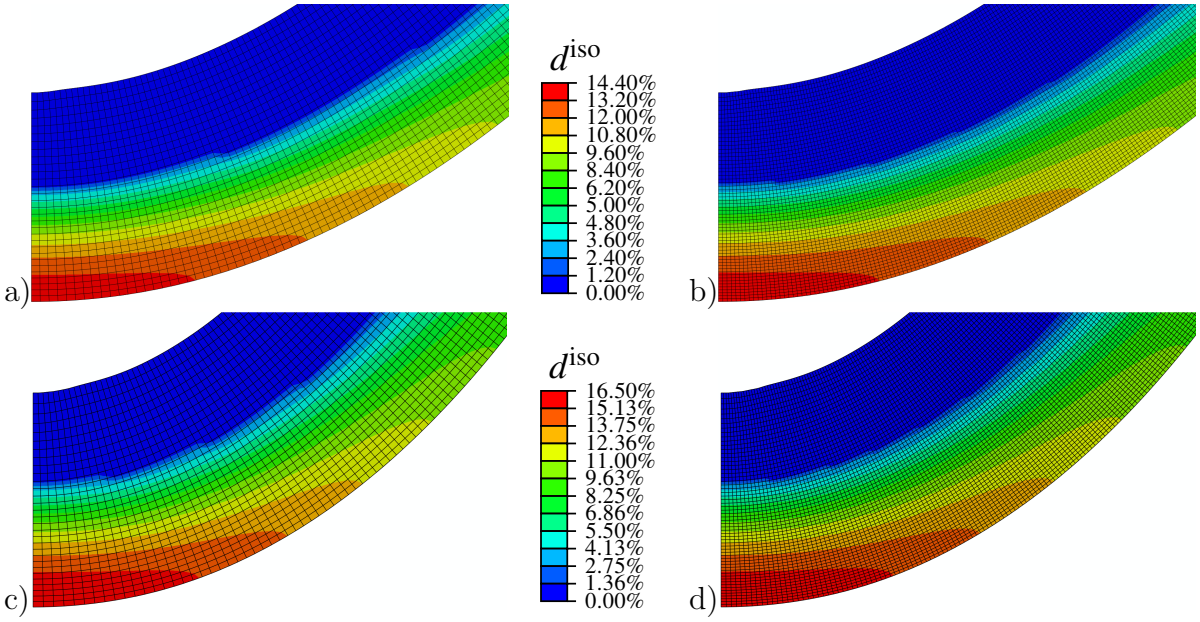

Figure 3.20: Contour plots of the damage variable d^{iso} for simulations with die width $w = 24.5\,\text{mm}$ in a) and b) and die width $w = 16\,\text{mm}$ in c) and d). On the left side, a) and c), the element edge length is $l_e = 0.05\,\text{mm}$ and on the right side, b) and d), it is $l_e = 0.025\,\text{mm}$. Reprinted from [163], Fig. 8 b)+d) and Fig. 10 b)+d).

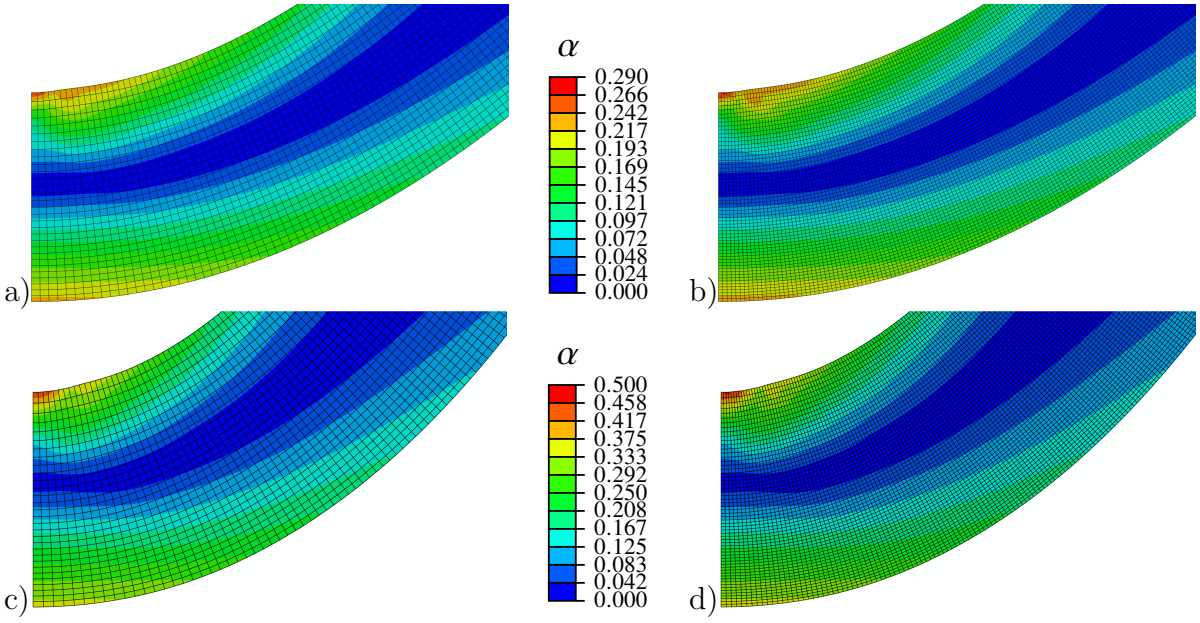

Figure 3.21: Contour plots of the isotropic hardening variable α_p for simulations with die width $w = 24.5\,\mathrm{mm}$ in a) and b) and with die width $w = 16\,\mathrm{mm}$ in c) and d). On the left side, a) and c), the element edge length is $l_e = 0.05\,\mathrm{mm}$ and on the right side, b) and d), it is $l_e = 0.025\,\mathrm{mm}$. Reprinted from [163], Fig. 9 b)+d) and Fig. 11 b)+d).

Table 3.9: List of material parameters for the air bending simulation. The third column contains the reference set, subsequent columns list the decreased and increased values of each parameter.

Symbol	Description	Value	Unit
E	Young's modulus	208.0	GPa
ν	Poisson's ratio	0.3	–
σ_{y0}	yield stress	165.66	MPa
h_p	hardening modulus	1611.24	MPa
n_p	hardening exponent	0.2436	–
q_max	damage threshold	1.5162	MPa
n_d	damage exponent	2/3	–
η	damage rate factor	0.5092	–
ξ_vol	volumetric damage factor	1.0	–
ξ_iso	isochoric damage factor	0.5	–
ξ_q	threshold factor	1.0	–
ξ_m	effective stress factor	0.3128	–
η_{α_p}	coupling factor	0.0	–
c_d	regularisation parameter	0.5	N
b_d	penalty parameter	100.0	MPa

3.6 Update of the parametrisation

Motivated by the identification of parameter sets PI1 and PI4b, see Section 3.4, with very different parameter values but very similar responses, a different parametrisation of the proposed isotropic ductile damage model is discussed. As already hinted at in Section 3.4, the damage variable d always appears in conjunction with damage rate factor η except for the coupling contribution Ψ^{cpl}. The idea is to remove η from the formulation completely.

To this end, a new damage variable $\widetilde{d}$ is introduced which is formally related to the previous damage variable d by

$$\widetilde{d} = \eta\, d\,. \tag{3.81}$$

The Helmholtz energy is now formulated in terms of $\widetilde{d}$ instead of d, i.e. $\widetilde{\Psi}(..., \widetilde{d})$. This influences the formulation threefold. The damage function $f^{\bullet}$ was previously formulated in terms of d and η, cf. (3.5). Now, it is given in terms of the new damage variable $\widetilde{d}$, i.e.

$$f^{\bullet} : \mathbb{R}_0^+ \to]0, 1] \qquad \text{with} \qquad f^{\bullet}(\widetilde{d}) = \exp(-\,\xi_{\bullet}\,\widetilde{d})\,, \tag{3.82}$$

whereby no parameters need to be changed. The driving force related to the damage variable q, is given as the negative derivative of the Helmholtz energy with respect to the damage variable d. With the new damage variable $\widetilde{d}$ the related driving force is denoted by $\widetilde{q}$. It is given by

$$\widetilde{q} = -\frac{\partial \widetilde{\Psi}}{\partial \widetilde{d}} = -\frac{\partial \Psi}{\partial d}\,\frac{\partial d}{\partial \widetilde{d}} = \frac{q}{\eta}\,, \tag{3.83}$$

and entering the damage initiation potential, cf. (3.18),

$$\widetilde{\Phi}_{\mathrm{d}}(\widetilde{q},\, \widetilde{d}) = \widetilde{q}_{\mathrm{eff}} - q_{\mathrm{min}} - q_{\mathrm{var}}\,\left[1 - f^{q}(\widetilde{d})\right]^{n_{\mathrm{d}}}\,, \tag{3.84}$$

where the damage threshold is modified. On the one hand, the constant threshold q_{min} is added (without affecting the algorithmic formulation or the derivatives; $q_{\mathrm{min}} = 0\,\mathrm{MPa}$ conforms to the previous formulation) and on the other hand the damage threshold value needs to be updated according to $q_{\mathrm{var}} = q_{\mathrm{max}}/\eta$ in order to match the response of the previous parametrisation. The function $\widehat{f}^{\alpha_{\mathrm{p}}}$ was originally defined with stability parameter ϵ ($\epsilon \approx 10^{-3}$ to 10^{-5}), compare (3.35), but, in view of the damage deterioration function defined in the anisotropic damage model, see (4.46), the stability parameter can be reinterpreted as a material parameter controlling at which point the plastic hardening begins to influence the damage driving force, i.e. the functions

$$f_{\mathrm{dp}}^{-1}(\alpha_{\mathrm{p}}) = \frac{e^{2\,h_{\mathrm{dp}}\,\alpha_{\mathrm{p}}} + e^{2\,h_{\mathrm{dp}}\,\alpha_{\mathrm{p,max}}}}{e^{2\,h_{\mathrm{dp}}\,\alpha_{\mathrm{p,max}}} + 1} \qquad \text{and} \qquad \widehat{f}^{\alpha_{\mathrm{p}}}(\alpha_{\mathrm{p}}) = \frac{e^{\eta_{\alpha_{\mathrm{p}}}\,\alpha_{\mathrm{p}}} + \epsilon\, e^{\eta_{\alpha_{\mathrm{p}}}\,\alpha_{\mathrm{p}}}}{1 + \epsilon\, e^{\eta_{\alpha_{\mathrm{p}}}\,\alpha_{\mathrm{p}}}}\,, \tag{3.85}$$

are very similar if the related parameters are chosen appropriately. Hence, $f_{\mathrm{dp}}^{-1}(\alpha_{\mathrm{p}})$ is used instead of $\widehat{f}^{\alpha_{\mathrm{p}}}(\alpha_{\mathrm{p}})$.

Lastly, the damage variable d enters the coupling contribution Ψ^{cpl}, but not in conjunction with η. Setting up the coupling contribution in analogy to (3.7) as

$$\widetilde{\Psi}^{\mathrm{cpl}} = \frac{\widetilde{b_{\mathrm{d}}}}{2} \left[\widetilde{\phi_{\mathrm{d}}} - \widetilde{d}\right]^2 , \tag{3.86}$$

where a comparison with the previous parametrisation yields the relations

$$\widetilde{\phi_{\mathrm{d}}} = \eta\, \phi_{\mathrm{d}} , \qquad \widetilde{b_{\mathrm{d}}} = \frac{b_{\mathrm{d}}}{\eta^2} . \tag{3.87}$$

Switching from ϕ_{d} to $\widetilde{\phi_{\mathrm{d}}}$ technically does not influence the gradient contribution to the Helmholtz energy Ψ^{grd}, cf. (3.7). The contribution is now given by

$$\widetilde{\Psi}^{\mathrm{grd}} = \frac{\widetilde{c_{\mathrm{d}}}}{2}\, \widetilde{b_{\mathrm{d}}}\, \nabla_{\boldsymbol{X}} \widetilde{\phi_{\mathrm{d}}} \cdot \nabla_{\boldsymbol{X}} \widetilde{\phi_{\mathrm{d}}} , \tag{3.88}$$

where the penalty parameter $\widetilde{b_{\mathrm{d}}}$ now appears in the gradient contribution. The idea behind this format derives from the governing equation, cf. (2.8), where the penalty parameter can be factored out of the equation such that solely the gradient parameter $\widetilde{c_{\mathrm{d}}}$ controls the width of the damage zone and solely the penalty parameter $\widetilde{b_{\mathrm{d}}}$ controls the coupling of local and non-local damage variable. The gradient parameter $\widetilde{c_{\mathrm{d}}}$ is correlated to the previous formulation by

$$\widetilde{c_{\mathrm{d}}} = \frac{c_{\mathrm{d}}}{b_{\mathrm{d}}} , \tag{3.89}$$

which means the unit of the gradient parameter is now mm^2.

3.6.1 Updated parameter identification

Based on this updated parametrisation, the parameters identified in the identifications PI1 and PI4b are converted to the new parametrisation, see Table 3.10. In the updated parameter sets, the damage factor ξ_{iso} is now fixed to 1.0 instead of ξ_{vol}. Thereby, solely the damage factor ξ_m influences the effective stress which was influenced previously by the difference of ξ_m and ξ_{iso}, cf. (3.16).

Using the updated parametrisation, parameter identifications PI1u and PI4u are set up with identical (converted) starting values as PI1 and PI4b, respectively. Additionally, PI5u is set up with arbitrarily perturbed starting values. The identified parameter sets as well as the values of the objective function relative to the objective value of PI1 are listed in Table 3.11. Redoing the parameter identification PI1 with the updated parameter set results in a better match (approximately 5% more accurate), but the identifications

Table 3.10: List of the conversion of the material parameters for identifications PI1 and PI4b, see Tables 3.7 and 3.8.

		PI1		PI4b	
		base	updated	base	updated
E	GPa	207.00		207.00	
ν	–	0.21		0.21	
σ_{y0}	MPa	248.59		478.71	
h_p	MPa	1705.64		40771.87	
n_p	–	0.2654		0.8920	
q_{min}	MPa	–	0.0	–	0.0
q_{var}	MPa	0.6953	7.609	18.7378	6.8197
n_d	–	0.6667		0.6667	
η	–	0.1559	–	4.9551	–
ξ_{vol}	–	1.0000	1.7062	1.0000	1.8034
ξ_{iso}	–	0.5861	1.0000	0.5545	1.0000
ξ_q	–	0.8100	1.3820	1.0031	1.8090
ξ_m	–	0.6163	1.0515	3.6116	6.5132
ϵ / $\alpha_{p,max}$	–	10^{-4}	-4.48	10^{-4}	-4.48
η_{α_p}	–	0.0000		0.0026	
c_d	N | mm^2	0.5400	0.0011	379.1240	0.7582
b_d	GPa	0.5000	59.8814	0.5000	0.0662

PI4u and PI5u yield worse matches compared to before. Most of the error for these two identifications stems from a mismatch in the force response ($\approx 65\%$).

The comparison of the load displacement response of the simulations with the updated identified parameter sets with the response of the experiment is shown in Figure 3.25. The response with parameter set PI1u matches the experimental response well and it is very similar to the response with parameter set PI1. The response with parameter set PI4u deviates from the experimental response in two areas. At the beginning of the plastic stage, the force response is overestimated because the plastic hardening exponent is identified to resemble linear behaviour. Towards the end of the prescribed loading, the response is too stiff. Remarkably, the response with parameter set PI4u is able to capture the characteristic drop in force leading up to failure of the specimen. The response with parameter set PI5u matches the experimental response well in the beginning, but starts to deviate more and more towards the end of the prescribed loading. The identified damage thresholds q_{min} and q_{var} are too large, such that no damage evolves during the simulation with this parameter set.

The depiction of the error in relative displacements, see Figures 3.22–3.24, is very similar to the version using the non-updated parametrisation. Notably, the relative displacements at the selected points $P1$–$P3$ increases much less after 3500 s for PI4u. Since the force drops and the deformation increases in this time frame the deformation is (likely) concentrated to the left of these points.

Table 3.11: List of identified material parameters for DP800 steel sheets. Rerun of the parameter identification using the updated parametrisation — PI1u: rerun of PI1, PI4u: rerun of PI4b and PI5u: perturbed starting parameters. The relative total objective is given in relation to the total objective value of PI1, cf. Table 3.7.

		PI1u		PI4u		PI5u	
		start	optimised	start	optimised	start	optimised
rel. tot. obj		94.47%		115.54%		113.10%	
% force obj.		33.53%		65.82%		64.86%	
E	GPa	207.0		207.0		207.0	
ν	–	0.21		0.21		0.21	
σ_{y0}	MPa	250.00	254.65	450.00	724.16	50.00	90.24
h_p	MPa	1700.00	1880.84	8700.00	4410.65	700.00	1369.85
n_p	–	0.2500	0.2976	1.0000	0.9934	0.1500	0.1763
q_{min}	MPa	0.5000	0.6806	0.5000	0.3943	3.5000	6.2561
q_{var}	MPa	3.7500	4.9146	2.2500	3.0710	13.7500	19.5411
n_d	–	0.6667		0.6667		0.6667	
ξ_{vol}	–	2.0000	2.2175	0.6700	0.6908	0.1000	0.1199
ξ_{iso}	–	1.0000		1.0000		1.0000	
ξ_q	–	2.0000	2.7311	66.0000	17.2168	5.0000	3.4211
ξ_m	–	1.0000	1.2958	1.1000	3.3473	1.0000	1.4082
η_{α_p}	–	0.0000	1.2175	0.0000	0.0703	0.5000	0.5839
$\alpha_{p,max}$	–	0.4000	0.5601	0.4000	0.4172	0.2000	0.1143
c_d	mm^2	0.0010	73.7023	0.1000	0.0176	1.0000	1.0685
b_d	MPa	10000.00		10000.00		10000.00	

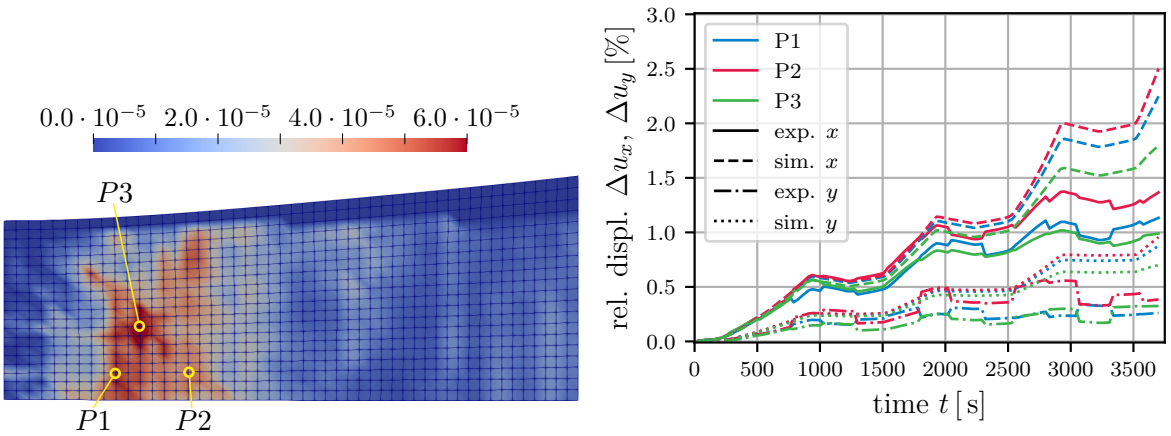

Figure 3.22: Depiction of the relative displacement $\Delta \boldsymbol{u}$ of the identified parameter set PI1u. Contour plot of the squared absolute error of the relative displacement, i.e. objective function $g_{\Delta \boldsymbol{u}}$, see (3.75), at each node at $t = 3520\,\mathrm{s}$ (left) and comparison of the evolution of the experimental and simulated relative displacements in x and y-direction over time (right) for nodes P1, P2 and P3.

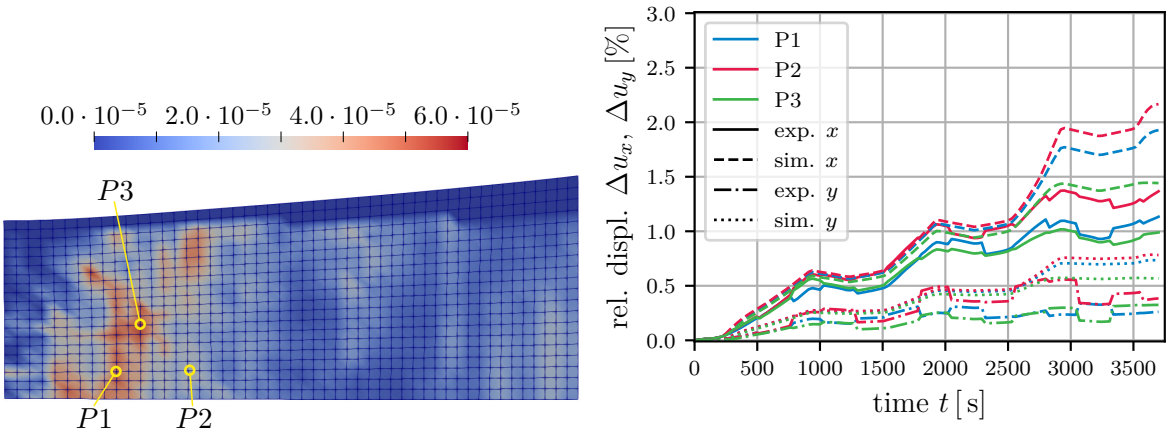

Figure 3.23: Depiction of the relative displacement $\Delta \boldsymbol{u}$ of the identified parameter set PI4u. Contour plot of the squared absolute error of the relative displacement, i.e. objective function $g_{\Delta \boldsymbol{u}}$, see (3.75), at each node at $t = 3520\,\mathrm{s}$ (left) and comparison of the evolution of the experimental and simulated relative displacements in x and y-direction over time (right) for nodes P1, P2 and P3.

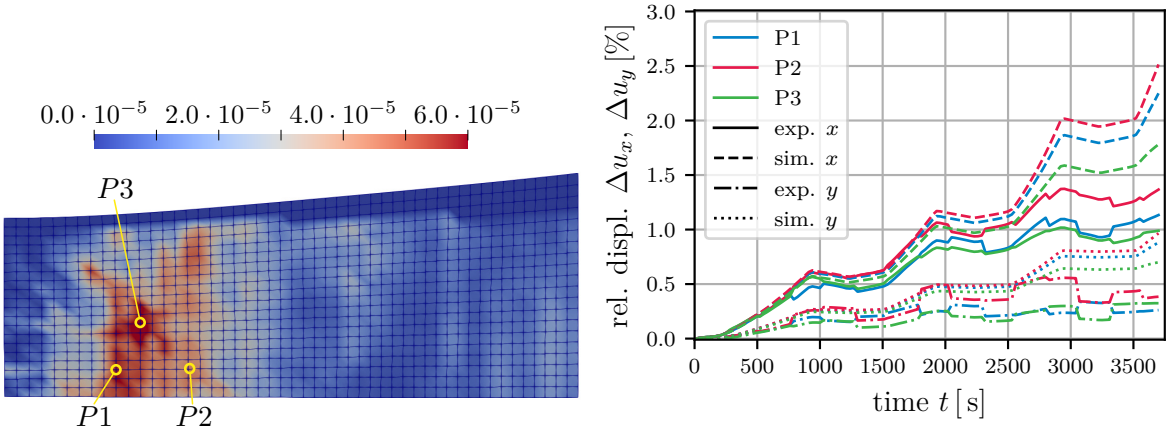

Figure 3.24: Depiction of the relative displacement $\Delta \boldsymbol{u}$ of the identified parameter set PI5u. Contour plot of the squared absolute error of the relative displacement, i.e. objective function $g_{\Delta \boldsymbol{u}}$, see (3.75), at each node at $t = 3520\,\mathrm{s}$ (left) and comparison of the evolution of the experimental and simulated relative displacements in x and y-direction over time (right) for nodes P1, P2 and P3.

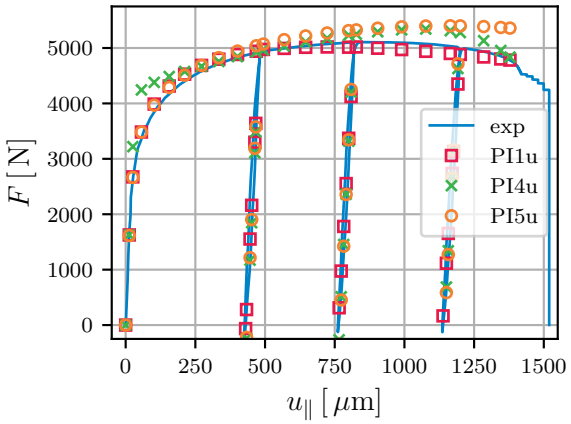

Figure 3.25: Load displacement diagram of the tensile test of specimen A07 and the simulation response with parameter sets PI1u, PI4u and PI5u. Force in N over optically measured displacement in tensile direction in mm. The experimental response is displayed as a blue continuous line and the identifications by means of square, x and circle.

4 A regularised framework for anisotropic damage coupled to finite plasticity

This chapter deals with a finite strain anisotropic ductile damage model based on the fictitious configuration concept. Large parts of this chapter are adopted from the publication [162].

Focus is placed on two key aspects: First, the introduction of effective driving forces is discussed in detail and different approaches are proposed. The definition of effective stresses is extended from isotropic damage to anisotropic damage in straightforward manner. More importantly, the introduction of an effective damage driving force aims to remove the sole dependence of damage evolution on elastic strains, thereby allowing the material model to predict the onset of failure. If the onset of failure can be predicted accurately, the safety margin of a produced part will be known, ultimately saving costs and resources. The second focus is the regularisation of the response of the proposed model. Whereas most contributions in the past considered only the regularisation of damage itself, the necessity of additionally regularising evolution of plasticity is analysed.

This chapter starts by introducing the fictitious configuration and the required strain and damage measures to formulate the model. Co- and contra-variant metric tensors are introduced but no distinction is made in the notation of co- and contra-variant tensorial quantities to improve readability. The modelling framework, detailing the two-surface setup and the associated evolution equations follows in Section 4.2. Section 4.3 deals with effective stresses and effective damage driving forces. Thereafter, the constitutive relations are specified in Section 4.4 and their algorithmic implementation is described in Section 4.5. Details of the implemented regularisation approaches of the proposed model are discussed in Section 4.6, followed by the stresses, driving forces and global tangent contributions for the FE-formulation. The response of the local model, cf. Section 4.9, and the discussion of the regularisation properties, cf. Section 4.10, highlight the features of the proposed model. The chapter closes with a formulation of the model in terms of Haigh-Westergaard coordinates, related to triaxiality and Lode parameter, whereby convexity of the damage initiation surface can be evaluated.

4.1 Fictitious configuration framework

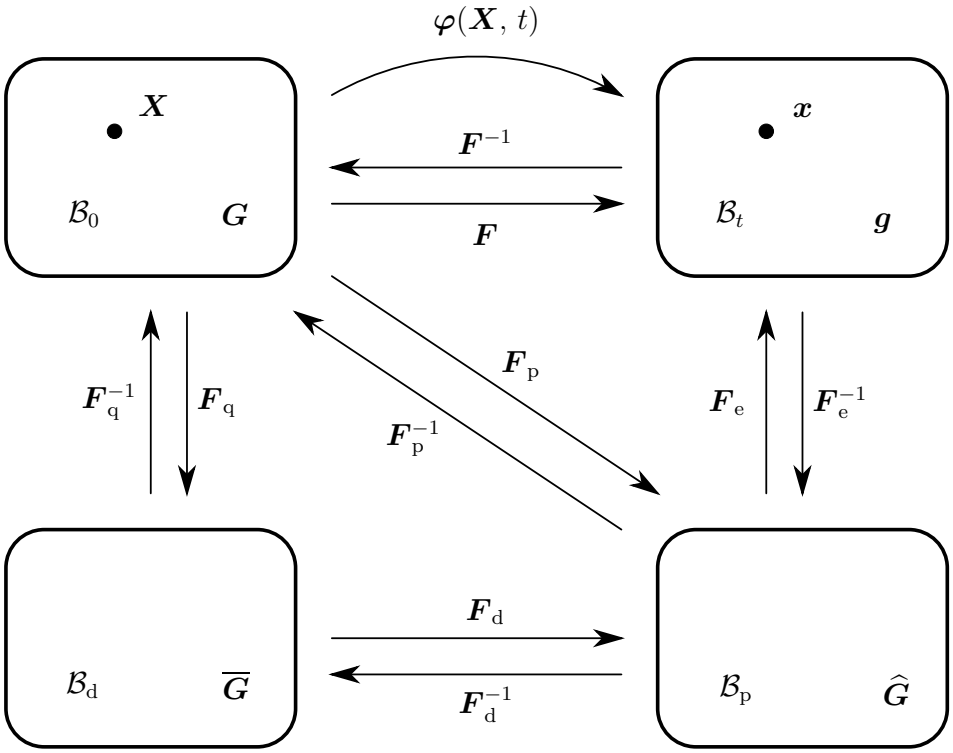

Figure 4.1: Kinematics of the proposed modelling framework including the plastic intermediate configuration $\mathcal{B}_{\mathrm{p}}$ with (covariant) metric tensor $\widehat{\boldsymbol{G}}$ as well as the fictitious configuration $\mathcal{B}_{\mathrm{d}}$ with (covariant) metric tensor $\overline{\boldsymbol{G}}$.

Repeating the kinematics introduced in Section 2.1, let the reference (or material) configuration be denoted by $\mathcal{B}_0$ and let $\boldsymbol{X}$ be the related placement vector, see Figure 4.1 as an extension of Figure 2.1. Furthermore, let $\mathcal{B}_t$ denote the current (or spatial) configuration with placement vector $\boldsymbol{x}$. A deformation map $\boldsymbol{\varphi}(\boldsymbol{X}, t)$ is introduced, mapping placements from the reference configuration to the spatial configuration, i.e. $\boldsymbol{x} = \boldsymbol{\varphi}(\boldsymbol{X}, t)$ with t denoting time. The mapping between the tangent spaces of both configurations is introduced as the deformation gradient $\boldsymbol{F}$. The co-variant metric tensors are denoted by $\boldsymbol{G}$ in the reference configuration and by $\boldsymbol{g}$ in the current configuration.

In addition, an intermediate stress-free configuration $\mathcal{B}_{\mathrm{p}}$ is considered, cf. e.g. [114]. The co-variant metric tensor in the intermediate configuration is denoted by $\widehat{\boldsymbol{G}}$. Tangent vectors in the reference configuration are mapped to the intermediate configuration via the plastic part of the deformation gradient $\boldsymbol{F}_{\mathrm{p}}$ and tangent vectors in the intermediate configuration are mapped to the current configuration by means of the elastic part of the deformation gradient $\boldsymbol{F}_{\mathrm{e}}$. The intermediate configuration is (in general) incompatible,

i.e. no deformation maps exist, the gradients of which correspond to $\boldsymbol{F}_\mathrm{p}$, respectively $\boldsymbol{F}_\mathrm{e}$. Consequently, the deformation gradient is split multiplicatively into

$$\boldsymbol{F} = \boldsymbol{F}_\mathrm{e} \cdot \boldsymbol{F}_\mathrm{p} \,. \tag{4.1}$$

Attached to the intermediate configuration is the (incompatible) fictitious configuration $\mathcal{B}_\mathrm{d}$, where the material is assumed to be undamaged, cf. [28, 34, 61, 123, 125, 130, 157]. The co-variant metric tensor of the fictitious configuration is denoted by $\overline{\boldsymbol{G}}$. Tangent vectors in the fictitious configuration are mapped to the intermediate configuration via the damage related tensor $\boldsymbol{F}_\mathrm{d}$. It is straightforward to find the mapping between the fictitious and the reference configuration, in the following denoted by $\boldsymbol{F}_\mathrm{q}$, as

$$\boldsymbol{F}_\mathrm{q} = \boldsymbol{F}_\mathrm{d}^{-1} \cdot \boldsymbol{F}_\mathrm{p} \,. \tag{4.2}$$

All four introduced mappings can be expressed in terms of the respective co- and contra-variant natural base vectors (whereby no explicit distinction between the dual and the transposed of a tensor is made), i.e.

$$\begin{aligned}
&\boldsymbol{F} = \boldsymbol{g}_i \otimes \boldsymbol{G}^i \,, && \boldsymbol{F}^\mathrm{t} = \boldsymbol{G}^i \otimes \boldsymbol{g}_i \,, && \boldsymbol{F}^{-1} = \boldsymbol{G}_i \otimes \boldsymbol{g}^i \,, && \boldsymbol{F}^{-\mathrm{t}} = \boldsymbol{g}^i \otimes \boldsymbol{G}_i \,, \\
&\boldsymbol{F}_\mathrm{p} = \widehat{\boldsymbol{G}}_i \otimes \boldsymbol{G}^i \,, && \boldsymbol{F}_\mathrm{p}^\mathrm{t} = \boldsymbol{G}^i \otimes \widehat{\boldsymbol{G}}_i \,, && \boldsymbol{F}_\mathrm{p}^{-1} = \boldsymbol{G}_i \otimes \widehat{\boldsymbol{G}}^i \,, && \boldsymbol{F}_\mathrm{p}^{-\mathrm{t}} = \widehat{\boldsymbol{G}}^i \otimes \boldsymbol{G}_i \,, \\
&\boldsymbol{F}_\mathrm{e} = \boldsymbol{g}_i \otimes \widehat{\boldsymbol{G}}^i \,, && \boldsymbol{F}_\mathrm{e}^\mathrm{t} = \widehat{\boldsymbol{G}}^i \otimes \boldsymbol{g}_i \,, && \boldsymbol{F}_\mathrm{e}^{-1} = \widehat{\boldsymbol{G}}_i \otimes \boldsymbol{g}^i \,, && \boldsymbol{F}_\mathrm{e}^{-\mathrm{t}} = \boldsymbol{g}^i \otimes \widehat{\boldsymbol{G}}_i \,, \\
&\boldsymbol{F}_\mathrm{d} = \widehat{\boldsymbol{G}}_i \otimes \overline{\boldsymbol{G}}^i \,, && \boldsymbol{F}_\mathrm{d}^\mathrm{t} = \overline{\boldsymbol{G}}^i \otimes \widehat{\boldsymbol{G}}_i \,, && \boldsymbol{F}_\mathrm{d}^{-1} = \overline{\boldsymbol{G}}_i \otimes \widehat{\boldsymbol{G}}^i \,, && \boldsymbol{F}_\mathrm{d}^{-\mathrm{t}} = \widehat{\boldsymbol{G}}^i \otimes \overline{\boldsymbol{G}}_i \,.
\end{aligned} \tag{4.3}$$

With these different configurations and tensorial quantities at hand, various deformation measures can be introduced. The right Cauchy-Green tensor $\boldsymbol{C}$ is defined as the pull-back of the co-variant spatial metric $\boldsymbol{g}$ to the reference configuration. Transformation of the right Cauchy-Green tensor to the intermediate or the fictitious configuration yield $\widehat{\boldsymbol{C}}_\mathrm{e}$ and $\overline{\boldsymbol{C}}_\mathrm{ed}$, respectively. The mappings are given by

$$\boldsymbol{C} = \boldsymbol{F}^\mathrm{t} \cdot \boldsymbol{g} \cdot \boldsymbol{F} \,, \qquad \widehat{\boldsymbol{C}}_\mathrm{e} = \boldsymbol{F}_\mathrm{e}^\mathrm{t} \cdot \boldsymbol{g} \cdot \boldsymbol{F}_\mathrm{e} \,, \qquad \overline{\boldsymbol{C}}_\mathrm{ed} = \boldsymbol{F}_\mathrm{d}^\mathrm{t} \cdot \boldsymbol{F}_\mathrm{e}^\mathrm{t} \cdot \boldsymbol{g} \cdot \boldsymbol{F}_\mathrm{e} \cdot \boldsymbol{F}_\mathrm{d} \,. \tag{4.4}$$

The Finger tensor $\boldsymbol{b}$ is defined as the push-forward of the contra-variant referential metric $\boldsymbol{G}^{-1}$ to the spatial configuration. Related representations in the intermediate and fictitious configuration, $\widehat{\boldsymbol{b}}_\mathrm{p}$ and $\overline{\boldsymbol{b}}_\mathrm{q}$, can be obtained as

$$\boldsymbol{b} = \boldsymbol{F} \cdot \boldsymbol{G}^{-1} \cdot \boldsymbol{F}^\mathrm{t} \,, \qquad \widehat{\boldsymbol{b}}_\mathrm{p} = \boldsymbol{F}_\mathrm{p} \cdot \boldsymbol{G}^{-1} \cdot \boldsymbol{F}_\mathrm{p}^\mathrm{t} \,, \qquad \overline{\boldsymbol{b}}_\mathrm{q} = \boldsymbol{F}_\mathrm{q} \cdot \boldsymbol{G}^{-1} \cdot \boldsymbol{F}_\mathrm{q}^\mathrm{t} \,. \tag{4.5}$$

Additional deformation measures arise from the introduction of the intermediate configuration. The elastic Finger tensor $\boldsymbol{b}_\mathrm{e}$, a measure of elastic deformation, is defined as the push-forward of the contra-variant intermediate metric $\widehat{\boldsymbol{G}}^{-1}$ and the plastic right Cauchy-Green tensor $\boldsymbol{C}_\mathrm{p}$, measuring plastic deformation, is defined as the pull-back of the co-variant intermediate metric $\widehat{\boldsymbol{G}}$, i.e.

$$\boldsymbol{b}_\mathrm{e} = \boldsymbol{F}_\mathrm{e} \cdot \widehat{\boldsymbol{G}}^{-1} \cdot \boldsymbol{F}_\mathrm{e}^\mathrm{t} \,, \qquad \boldsymbol{C}_\mathrm{p} = \boldsymbol{F}_\mathrm{p}^\mathrm{t} \cdot \widehat{\boldsymbol{G}} \cdot \boldsymbol{F}_\mathrm{p} \,. \tag{4.6}$$

In the same way that deformation measures are introduced, it is possible to introduce damage measures. Sticking to the naming convention of small 'b' for contra-variant measures and capital 'C' for co-variant measures, the contra-variant damage measure $\widehat{\boldsymbol{b}}_{\mathrm{d}}$ and the co-variant damage measure $\overline{\boldsymbol{C}}_{\mathrm{d}}$ are introduced as

$$\widehat{\boldsymbol{b}}_{\mathrm{d}} = \boldsymbol{F}_{\mathrm{d}} \cdot \overline{\boldsymbol{G}}^{-1} \cdot \boldsymbol{F}_{\mathrm{d}}^{\mathrm{t}} \,, \qquad \overline{\boldsymbol{C}}_{\mathrm{d}} = \boldsymbol{F}_{\mathrm{d}}^{\mathrm{t}} \cdot \widehat{\boldsymbol{G}} \cdot \boldsymbol{F}_{\mathrm{d}} \,. \tag{4.7}$$

In order to only measure how the material under consideration changed from one configuration to another, strain measures are introduced as comparison of two metrics. A multitude of different strain measures has been introduced and analysed in the literature — the interested reader is referred to the original contributions [154] and [81], monographs such as [158], or the works [47, 121, 128] and literature cited therein. The model described in the following is formulated based on Green-Lagrange strains, i.e.

$$\boldsymbol{E} = \frac{1}{2}\left[\boldsymbol{C} - \boldsymbol{G}\right], \quad \widehat{\boldsymbol{E}} = \frac{1}{2}\left[\widehat{\boldsymbol{C}}_{\mathrm{e}} - \widehat{\boldsymbol{b}}_{\mathrm{p}}^{-1}\right], \quad \overline{\boldsymbol{E}} = \frac{1}{2}\left[\overline{\boldsymbol{C}}_{\mathrm{ed}} - \overline{\boldsymbol{b}}_{\mathrm{q}}^{-1}\right], \tag{4.8}$$

where the referential co-variant metric is compared to the pull-back of the spatial co-variant metric. Typically, in elasto-plastic model formulations, only the reversible elastic part of the deformation enters the strain-energy. Consequently, the elastic Green-Lagrange strains are defined by comparing the co-variant intermediate metric to the pull-back of the spatial co-variant metric into the intermediate configuration, i.e.

$$\boldsymbol{E}_{\mathrm{e}} = \frac{1}{2}\left[\boldsymbol{C} - \boldsymbol{C}_{\mathrm{p}}\right], \quad \widehat{\boldsymbol{E}}_{\mathrm{e}} = \frac{1}{2}\left[\widehat{\boldsymbol{C}}_{\mathrm{e}} - \widehat{\boldsymbol{G}}\right], \quad \overline{\boldsymbol{E}}_{\mathrm{e}} = \frac{1}{2}\left[\overline{\boldsymbol{C}}_{\mathrm{ed}} - \overline{\boldsymbol{C}}_{\mathrm{d}}\right]. \tag{4.9}$$

Analogously, the plastic Green-Lagrange strains are defined by comparing the co-variant referential metric to the pull-back of the intermediate co-variant metric into the reference configuration and one obtains

$$\boldsymbol{E}_{\mathrm{p}} = \frac{1}{2}\left[\boldsymbol{C}_{\mathrm{p}} - \boldsymbol{G}\right], \quad \widehat{\boldsymbol{E}}_{\mathrm{p}} = \frac{1}{2}\left[\widehat{\boldsymbol{G}} - \widehat{\boldsymbol{b}}_{\mathrm{p}}^{-1}\right], \quad \overline{\boldsymbol{E}}_{\mathrm{p}} = \frac{1}{2}\left[\overline{\boldsymbol{C}}_{\mathrm{d}} - \overline{\boldsymbol{b}}_{\mathrm{q}}^{-1}\right]. \tag{4.10}$$

Remarkably, one observes an additive split of the strains, i.e. $\boldsymbol{E} = \boldsymbol{E}_{\mathrm{e}} + \boldsymbol{E}_{\mathrm{p}}$, even though the deformation gradient is split multiplicatively. The following section describes the setup of the modelling framework in terms of the strain and damage measures derived here.

4.2 Modelling framework

Let the local free Helmholtz energy Ψ be additively composed of an elastic strain energy contribution Ψ^{e}, a contribution from plastic hardening Ψ^{p} and a contribution from damage hardening Ψ^{d}. The functional dependence of the free Helmholtz energy is then given by

$$\Psi(\boldsymbol{F},\, \boldsymbol{F}_{\mathrm{p}},\, \boldsymbol{F}_{\mathrm{d}},\, \boldsymbol{\mathcal{I}}_{\mathrm{p}},\, \boldsymbol{\mathcal{I}}_{\mathrm{d}}) = \widetilde{\Psi}^{\mathrm{e}}(\boldsymbol{F},\, \boldsymbol{F}_{\mathrm{p}},\, \boldsymbol{F}_{\mathrm{d}}) + \Psi^{\mathrm{p}}(\boldsymbol{\mathcal{I}}_{\mathrm{p}}) + \Psi^{\mathrm{d}}(\boldsymbol{\mathcal{I}}_{\mathrm{d}}) \,, \tag{4.11}$$

where $\boldsymbol{\mathcal{I}}_\bullet$ is the set of internal variables related to plastic and, respectively, damage hardening.

With the aforementioned deformation, strain and damage measures at hand, quantities which are suitable to enter the strain energy can be set up. A well established approach is to formulate the elastic strain energy in terms of invariants [29]. Assuming the fictitious configuration to be initially isotropic allows the formulation of the elastic strain energy Ψ^{e} in terms of the first three invariants $\overline{I}_i^{\overline{\boldsymbol{E}}_{\mathrm{e}}}$ of the fictitious elastic Green-Lagrange strain tensor $\overline{\boldsymbol{E}}_{\mathrm{e}}$, namely

$$\Psi^{\mathrm{e}}(\overline{I}_{1,2,3}^{\overline{\boldsymbol{E}}_{\mathrm{e}}}) \qquad \text{with} \quad \overline{I}_i^{\overline{\boldsymbol{E}}_{\mathrm{e}}} = \overline{\boldsymbol{I}} : \left[\overline{\boldsymbol{G}}^{-1} \cdot \overline{\boldsymbol{E}}_{\mathrm{e}}\right]^i = \widehat{\boldsymbol{I}} : \left[\widehat{\boldsymbol{b}}_{\mathrm{d}} \cdot \widehat{\boldsymbol{E}}_{\mathrm{e}}\right]^i \quad \text{and} \quad i = 1,2,3\,, \tag{4.12}$$

wherein $\overline{\boldsymbol{I}} = \overline{\boldsymbol{G}} \cdot \overline{\boldsymbol{G}}^{-1}$ and $\widehat{\boldsymbol{I}} = \widehat{\boldsymbol{G}} \cdot \widehat{\boldsymbol{G}}^{-1}$ denote the related second order identity tensors. The proposed form of the invariants introduces (deformation induced) anisotropy to the elastic material response, see Remark 6. The thermodynamically conjugated driving forces of the (co-variant) elastic Green-Lagrange strain tensor $\overline{\boldsymbol{E}}_{\mathrm{e}}$ — the (contra-variant) elastic Piola-Kirchhoff stress tensor $\overline{\boldsymbol{S}}_{\mathrm{e}}$ — and of the (contra-variant) damage measure $\overline{\boldsymbol{G}}^{-1}$ — the (co-variant) damage driving force $\overline{\boldsymbol{Q}}$ — can then be expressed as

$$\overline{\boldsymbol{S}}_{\mathrm{e}} = \frac{\partial \Psi}{\partial \overline{\boldsymbol{E}}_{\mathrm{e}}} = \sum_{i=1}^{3} \frac{\partial \Psi}{\partial \overline{I}_i^{\overline{\boldsymbol{E}}_{\mathrm{e}}}}\, i\, \left[\overline{\boldsymbol{G}}^{-1} \cdot \overline{\boldsymbol{E}}_{\mathrm{e}}\right]^{i-1} \cdot \overline{\boldsymbol{G}}^{-1}\,, \tag{4.13}$$

$$\overline{\boldsymbol{Q}} = -\frac{\partial \Psi}{\partial \overline{\boldsymbol{G}}^{-1}} = -\sum_{i=1}^{3} \frac{\partial \Psi}{\partial \overline{I}_i^{\overline{\boldsymbol{E}}_{\mathrm{e}}}}\, i\, \overline{\boldsymbol{E}}_{\mathrm{e}} \cdot \left[\overline{\boldsymbol{G}}^{-1} \cdot \overline{\boldsymbol{E}}_{\mathrm{e}}\right]^{i-1}\,. \tag{4.14}$$

Remark 6 *The representation of the stresses in the fictitious configuration, see* (4.13)*, suggests an isotropic relation between stresses and strains. This holds true in the fictitious configuration only, since the invariants introduced in* (4.12) *do not include standard trace operations when referred to, e.g., the intermediate configuration, but trace operations (modified) with respect to (positive definite) damage related tensors. This approach can be shown to represent a special (reduced) case of elastically orthotropic response as modelled based on structural tensors, see [124]. In this context, the related representation of the (Piola-Kirchhoff type) stresses in the intermediate configuration, i.e.*

$$\widehat{\boldsymbol{S}}_{\mathrm{e}} = \frac{\partial \Psi}{\partial \widehat{\boldsymbol{E}}_{\mathrm{e}}} = \sum_{i=1}^{3} \frac{\partial \Psi}{\partial \overline{I}_i^{\overline{\boldsymbol{E}}_{\mathrm{e}}}}\, i\, \left[\widehat{\boldsymbol{b}}_{\mathrm{d}} \cdot \widehat{\boldsymbol{E}}_{\mathrm{e}}\right]^{i-1} \cdot \widehat{\boldsymbol{b}}_{\mathrm{d}}\,, \tag{4.15}$$

shows the anisotropic nature of the relation once damage has evolved so that $\widehat{\boldsymbol{b}}_{\mathrm{d}}$ *is no longer proportional to* $\widehat{\boldsymbol{G}}^{-1}$ *which, in general, yields* $\widehat{\boldsymbol{S}}_{\mathrm{e}}$ *and* $\widehat{\boldsymbol{E}}_{\mathrm{e}}$ *non-coaxial. In order to link the present approach to a St. Venant-Kirchhoff type model, let the elastic energy contribution depend on the first and second invariant only, which results in*

$$\widehat{\boldsymbol{S}}_{\mathrm{e}} = \frac{\partial \Psi}{\partial \overline{I}_1^{\overline{\boldsymbol{E}}_{\mathrm{e}}}}\, \widehat{\boldsymbol{b}}_{\mathrm{d}} + 2\, \frac{\partial \Psi}{\partial \overline{I}_2^{\overline{\boldsymbol{E}}_{\mathrm{e}}}}\, \widehat{\boldsymbol{b}}_{\mathrm{d}} \cdot \widehat{\boldsymbol{E}}_{\mathrm{e}} \cdot \widehat{\boldsymbol{b}}_{\mathrm{d}}\,. \tag{4.16}$$

Moreover, assuming $\partial\Psi/\partial\overline{I}_1^{\overline{\boldsymbol{E}}_\mathrm{e}} = c_1\,\overline{I}_1^{\overline{\boldsymbol{E}}_\mathrm{e}}$ *and* $\partial\Psi/\partial\overline{I}_2^{\overline{\boldsymbol{E}}_\mathrm{e}} = c_2$*, with* c_1 *and* c_2 *positive constants, further reduces this constitutive relation to*

$$\widehat{\boldsymbol{S}}_\mathrm{e} = \Big[c_1\,\widehat{\boldsymbol{b}}_\mathrm{d}\otimes\widehat{\boldsymbol{b}}_\mathrm{d} + 2\,c_2\,\widehat{\boldsymbol{b}}_\mathrm{d}\,\overline{\underline{\otimes}}\,\widehat{\boldsymbol{b}}_\mathrm{d}\Big] : \widehat{\boldsymbol{E}}_\mathrm{e}\,. \tag{4.17}$$

The fourth order tensor in (4.17) *takes the form of the elasticity tensor for an isotropic St. Venant-Kirchhoff model with the classic second order identity tensor replaced by* $\widehat{\boldsymbol{b}}_\mathrm{d}$*. This yields the elastic properties captured by the model to reflect (a reduced form of) orthotropic elastic response. Conceptually speaking, the damage measure* $\widehat{\boldsymbol{b}}_\mathrm{d}$ *can be compared to structural tensors which evolve (and degrade) induced by deformation; see also [125]. The isotropic representation in the fictitious configuration is one of the main advantages of the present formulation and is used to simplify e.g. the algorithmic formulation.*

Due to the structure of the invariants and $\Psi^\mathrm{e}(\overline{I}_{1,2,3}^{\overline{\boldsymbol{E}}_\mathrm{e}})$, one obtains the relation

$$\overline{\boldsymbol{Q}}\cdot\overline{\boldsymbol{G}}^{-1} = -\overline{\boldsymbol{E}}_\mathrm{e}\cdot\overline{\boldsymbol{S}}_\mathrm{e}\,. \tag{4.18}$$

Based on the proposed format of the free Helmholtz energy Ψ, dissipation $\mathcal{D}$ (in the case of isothermal conditions) using the stress power formulated in terms of the Piola stresses $\boldsymbol{P}$ can be expressed as

$$\begin{aligned}
&\mathcal{D} = \boldsymbol{P} : \dot{\boldsymbol{F}} - \dot{\Psi} \geq 0 \quad \text{with}\\
&\dot{\Psi} = \frac{\partial\Psi}{\partial\boldsymbol{F}} : \dot{\boldsymbol{F}} + \frac{\partial\Psi}{\partial\boldsymbol{F}_\mathrm{p}} : \dot{\boldsymbol{F}}_\mathrm{p} + \frac{\partial\Psi}{\partial\boldsymbol{F}_\mathrm{d}} : \dot{\boldsymbol{F}}_\mathrm{d} + \frac{\partial\Psi}{\partial\boldsymbol{\mathcal{I}}_\mathrm{p}} \bullet \dot{\boldsymbol{\mathcal{I}}}_\mathrm{p} + \frac{\partial\Psi}{\partial\boldsymbol{\mathcal{I}}_\mathrm{d}} \bullet \dot{\boldsymbol{\mathcal{I}}}_\mathrm{d}\,,
\end{aligned} \tag{4.19}$$

where $\dot{\bullet}$ represents the material time derivative and $\bullet$ represents the appropriate scalar product for the chosen set of internal variables $\boldsymbol{\mathcal{I}}_\mathrm{p}$ and $\boldsymbol{\mathcal{I}}_\mathrm{d}$, respectively. The derivatives of the Helmholtz energy with respect to the deformation gradients can be calculated as

$$\begin{aligned}
\frac{\partial\Psi}{\partial\boldsymbol{F}} &= \frac{\partial\Psi}{\partial\overline{\boldsymbol{E}}_\mathrm{e}} : \frac{\partial\overline{\boldsymbol{E}}_\mathrm{e}}{\partial\boldsymbol{F}} &&= \boldsymbol{g}\cdot\boldsymbol{F}\cdot\boldsymbol{F}_\mathrm{p}^{-1}\cdot\boldsymbol{F}_\mathrm{d}\cdot\overline{\boldsymbol{S}}_\mathrm{e}\cdot\boldsymbol{F}_\mathrm{d}^\mathrm{t}\cdot\boldsymbol{F}_\mathrm{p}^{-\mathrm{t}}\,,\\
\frac{\partial\Psi}{\partial\boldsymbol{F}_\mathrm{p}} &= \frac{\partial\Psi}{\partial\overline{\boldsymbol{E}}_\mathrm{e}} : \frac{\partial\overline{\boldsymbol{E}}_\mathrm{e}}{\partial\boldsymbol{F}_\mathrm{p}} &&= -\boldsymbol{F}_\mathrm{d}^{-\mathrm{t}}\cdot\overline{\boldsymbol{C}}_\mathrm{ed}\cdot\overline{\boldsymbol{S}}_\mathrm{e}\cdot\boldsymbol{F}_\mathrm{d}^\mathrm{t}\cdot\boldsymbol{F}_\mathrm{p}^{-\mathrm{t}}\,,\\
\frac{\partial\Psi}{\partial\boldsymbol{F}_\mathrm{d}} &= \frac{\partial\Psi}{\partial\overline{\boldsymbol{E}}_\mathrm{e}} : \frac{\partial\overline{\boldsymbol{E}}_\mathrm{e}}{\partial\boldsymbol{F}_\mathrm{d}} &&= 2\,\boldsymbol{F}_\mathrm{d}^{-\mathrm{t}}\cdot\overline{\boldsymbol{E}}_\mathrm{e}\cdot\overline{\boldsymbol{S}}_\mathrm{e}\,.
\end{aligned} \tag{4.20}$$

First, one obtains the established definition of the Piola stresses $\boldsymbol{P} = \partial_{\boldsymbol{F}}\Psi$. Secondly, combining the derivatives (4.20) with the corresponding rates and rewriting terms yields representations for Mandel stresses and velocity gradients in the fictitious configuration, i.e.

$$\begin{aligned}
-\frac{\partial\Psi}{\partial\boldsymbol{F}_\mathrm{p}} : \dot{\boldsymbol{F}}_\mathrm{p} &= \big[\overline{\boldsymbol{C}}_\mathrm{ed}\cdot\overline{\boldsymbol{S}}_\mathrm{e}\big] : \Big[\boldsymbol{F}_\mathrm{d}^{-1}\cdot\dot{\boldsymbol{F}}_\mathrm{p}\cdot\boldsymbol{F}_\mathrm{p}^{-1}\cdot\boldsymbol{F}_\mathrm{d}\Big] &&= \overline{\boldsymbol{M}}_\mathrm{e} : \overline{\boldsymbol{L}}_\mathrm{p}\,,\\
-\frac{\partial\Psi}{\partial\boldsymbol{F}_\mathrm{d}} : \dot{\boldsymbol{F}}_\mathrm{d} &= \big[-2\,\overline{\boldsymbol{E}}_\mathrm{e}\cdot\overline{\boldsymbol{S}}_\mathrm{e}\big] : \Big[\boldsymbol{F}_\mathrm{d}^{-1}\cdot\dot{\boldsymbol{F}}_\mathrm{d}\Big] &&= \overline{\boldsymbol{M}}_\mathrm{d} : \overline{\boldsymbol{L}}_\mathrm{d}\,.
\end{aligned} \tag{4.21}$$

Introducing the definitions $\boldsymbol{\mathcal{F}}_{\mathrm{p}} := -\partial_{\boldsymbol{\mathcal{I}}_{\mathrm{p}}}\Psi$ and $\boldsymbol{\mathcal{F}}_{\mathrm{d}} := -\partial_{\boldsymbol{\mathcal{I}}_{\mathrm{d}}}\Psi$ and inserting these, together with the definition of the Mandel stresses (4.21) and of the Piola stresses $\boldsymbol{P} = \partial_{\boldsymbol{F}}\Psi$, into the dissipation inequality results in the reduced dissipation inequality, namely

$$\mathcal{D}^{\mathrm{red}} = \overline{\boldsymbol{M}}_{\mathrm{e}} : \overline{\boldsymbol{L}}_{\mathrm{p}} + \overline{\boldsymbol{M}}_{\mathrm{d}} : \overline{\boldsymbol{L}}_{\mathrm{d}} + \boldsymbol{\mathcal{F}}_{\mathrm{p}} \bullet \dot{\boldsymbol{\mathcal{I}}}_{\mathrm{p}} + \boldsymbol{\mathcal{F}}_{\mathrm{d}} \bullet \dot{\boldsymbol{\mathcal{I}}}_{\mathrm{d}} \geq 0\,. \tag{4.22}$$

The evolution of damage and plasticity related variables is governed by the elastic domain

$$\mathbb{E} := \{\boldsymbol{\mathcal{F}} \in \mathbb{R}^{9+9+m+n} \,|\, \mathbb{E}_{\mathrm{p}} \cup \mathbb{E}_{\mathrm{d}}\}\,, \tag{4.23}$$

where $\boldsymbol{\mathcal{F}}$ are the driving forces $\overline{\boldsymbol{M}}_{\mathrm{e}}$, $\overline{\boldsymbol{M}}_{\mathrm{d}}$, $\boldsymbol{\mathcal{F}}_{\mathrm{p}}$ and $\boldsymbol{\mathcal{F}}_{\mathrm{d}}$. The plastic and damage domains $\mathbb{E}_{\mathrm{p}}$ and, respectively, $\mathbb{E}_{\mathrm{d}}$ are defined as

$$\mathbb{E}_{\mathrm{p}} := \{\{\overline{\boldsymbol{M}}_{\mathrm{e}}, \boldsymbol{\mathcal{I}}_{\mathrm{p}}\} \in \mathbb{R}^{9+m} \,|\, \Phi_{\mathrm{p}} \leq 0\}\,, \tag{4.24}$$

$$\mathbb{E}_{\mathrm{d}} := \{\{\overline{\boldsymbol{M}}_{\mathrm{d}}, \boldsymbol{\mathcal{I}}_{\mathrm{d}}\} \in \mathbb{R}^{9+n} \,|\, \Phi_{\mathrm{d}} \leq 0\}\,, \tag{4.25}$$

with Φ_{p} and Φ_{d} being the potentials governing the onset of damage and plasticity, respectively. Evolution equations are formulated in an associative manner, such that the terms in (4.22) take a quadratic form and non-negative dissipation can be guaranteed. Maximising the dissipation under the constraints of staying in the elastic domain $\mathbb{E}$ results in the evolution equations

$$\begin{aligned} \overline{\boldsymbol{L}}_{\mathrm{p}} &= \lambda_{\mathrm{p}} \frac{\partial \Phi_{\mathrm{p}}}{\partial \overline{\boldsymbol{M}}_{\mathrm{e}}}\,, \qquad & \dot{\boldsymbol{\mathcal{I}}}_{\mathrm{p}} &= \lambda_{\mathrm{p}} \frac{\partial \Phi_{\mathrm{p}}}{\partial \boldsymbol{\mathcal{F}}_{\mathrm{p}}}\,, \\ \overline{\boldsymbol{L}}_{\mathrm{d}} &= \lambda_{\mathrm{d}} \frac{\partial \Phi_{\mathrm{d}}}{\partial \overline{\boldsymbol{M}}_{\mathrm{d}}}\,, \qquad & \dot{\boldsymbol{\mathcal{I}}}_{\mathrm{d}} &= \lambda_{\mathrm{d}} \frac{\partial \Phi_{\mathrm{d}}}{\partial \boldsymbol{\mathcal{F}}_{\mathrm{d}}}\,, \end{aligned} \tag{4.26}$$

where λ_{p} and λ_{d} are the Lagrange multipliers subject to loading and unloading conditions, i.e.

$$\begin{aligned} &\Phi_{\mathrm{p}} \leq 0 \qquad \lambda_{\mathrm{p}} \geq 0 \qquad \lambda_{\mathrm{p}}\,\Phi_{\mathrm{p}} = 0\,, \\ &\Phi_{\mathrm{d}} \leq 0 \qquad \lambda_{\mathrm{d}} \geq 0 \qquad \lambda_{\mathrm{d}}\,\Phi_{\mathrm{d}} = 0\,. \end{aligned} \tag{4.27}$$

4.3 Coupling of damage and plasticity — effective driving forces

The modelling framework described in the previous section clearly exhibits a coupling of damage and plasticity, i.e. both driving forces, $\overline{\boldsymbol{S}}_{\mathrm{e}}$ and $\overline{\boldsymbol{Q}}$, directly depend on the plastic part of the deformation gradient $\boldsymbol{F}_{\mathrm{p}}$ as well as on the damage mapping $\boldsymbol{F}_{\mathrm{d}}$. However, the coupling is intrinsic to the modelling framework and cannot be influenced by e.g. the choice of the strain energy or of the inelastic potentials. More specifically speaking, one observes the following features (under monotonous tensile loading) which do not align with the experimentally expected material behaviour

a) no (further) plasticity evolves after damage initiation (assuming no damage hardening) since stresses only decrease,

b) no (further) damage evolves after initiation of plasticity (assuming perfect plasticity) since the damage driving force $\overline{\boldsymbol{Q}}$ only depends on the elastic part of the strains $\overline{\boldsymbol{E}}_{\mathrm{e}}$.

Even if taking hardening into consideration, evolution of, say, plasticity will be directly proportional to damage hardening and vice versa. Several approaches exist in order to improve control over the coupling behaviour (aside from choosing a different strain energy formulation as in e.g. [65, 83]. Certainly, one could introduce suitable non-associative evolution equations — however, this approach will not be pursued in this work. Instead, the focus lies on modifications of the governing inelastic potentials which are assumed of the form

$$\begin{aligned} \Phi_{\mathrm{p}}(\overline{\boldsymbol{M}}_{\mathrm{e}},\, \boldsymbol{\mathcal{F}}_{\mathrm{p}}) &= M_{\mathrm{e}}^{\mathrm{eq}}(\overline{\boldsymbol{M}}_{\mathrm{e}}) - M_{\mathrm{e}}^{\max}(\boldsymbol{\mathcal{F}}_{\mathrm{p}})\,, \\ \Phi_{\mathrm{d}}(\overline{\boldsymbol{M}}_{\mathrm{d}},\, \boldsymbol{\mathcal{F}}_{\mathrm{d}}) &= M_{\mathrm{d}}^{\mathrm{eq}}(\overline{\boldsymbol{M}}_{\mathrm{d}}) - M_{\mathrm{d}}^{\max}(\boldsymbol{\mathcal{F}}_{\mathrm{d}})\,. \end{aligned} \tag{4.28}$$

Focussing on the structure of the potentials in (4.28), one can either modify how the equivalent value of the driving force is computed, $M_{\bullet}^{\mathrm{eq}}(\overline{\boldsymbol{M}}_{\bullet})$, or modify the threshold value, $M_{\bullet}^{\max}(\boldsymbol{\mathcal{F}}_{\bullet})$. Focussing on modifications of the equivalent values first, the effective driving forces

$$\begin{aligned} \widehat{\boldsymbol{M}}_{\mathrm{e}}^{\mathrm{eff}} &= \widehat{\boldsymbol{C}}_{\mathrm{e}} \cdot \widehat{\boldsymbol{G}}^{-1} \cdot \widehat{\boldsymbol{b}}_{\mathrm{d}}^{-1} \cdot \widehat{\boldsymbol{S}}_{\mathrm{e}} \cdot \widehat{\boldsymbol{b}}_{\mathrm{d}}^{-1} \cdot \widehat{\boldsymbol{G}}^{-1}\,, \\ \overline{\boldsymbol{M}}_{\mathrm{e}}^{\mathrm{eff}} &= \overline{\boldsymbol{C}}_{\mathrm{ed}} \cdot \overline{\boldsymbol{C}}_{\mathrm{d}}^{-1} \cdot \overline{\boldsymbol{G}} \cdot \overline{\boldsymbol{S}}_{\mathrm{e}} \cdot \overline{\boldsymbol{G}} \cdot \overline{\boldsymbol{C}}_{\mathrm{d}}^{-1}\,, \\ \widehat{\boldsymbol{M}}_{\mathrm{d}}^{\mathrm{eff}} &= 2\, \widehat{\boldsymbol{b}}_{\mathrm{d}}^{-1} \cdot \widehat{\boldsymbol{b}}_{\mathrm{p}} \cdot \widehat{\boldsymbol{Q}} \cdot \widehat{\boldsymbol{b}}_{\mathrm{p}}\,, \\ \overline{\boldsymbol{M}}_{\mathrm{d}}^{\mathrm{eff}} &= 2\, \overline{\boldsymbol{G}} \cdot \overline{\boldsymbol{b}}_{\mathrm{q}} \cdot \overline{\boldsymbol{Q}} \cdot \overline{\boldsymbol{b}}_{\mathrm{q}}\,, \end{aligned} \tag{4.29}$$

are introduced. The idea behind the format of (4.29) derives from the uncoupled material model, i.e. where either damage or plasticity evolves: These cases are approximately equivalent to evaluating the Mandel stresses $\widehat{\boldsymbol{M}}_{\mathrm{e}} = \widehat{\boldsymbol{C}}_{\mathrm{e}} \cdot \widehat{\boldsymbol{S}}_{\mathrm{e}}$ for no evolution of damage, i.e. $\widehat{\boldsymbol{b}}_{\mathrm{d}} = \widehat{\boldsymbol{G}}^{-1}$, and evaluating $\overline{\boldsymbol{M}}_{\mathrm{d}} = 2\,\overline{\boldsymbol{G}} \cdot \overline{\boldsymbol{Q}}$ for no evolution of plasticity, i.e. $\widehat{\boldsymbol{b}}_{\mathrm{p}} = \widehat{\boldsymbol{G}}^{-1}$. The associative format requires a (mathematically) functional dependence of the inelastic potentials upon the Mandel stresses themselves. However, since an expression in the form of, e.g., the modified Mandel stresses $\widehat{\boldsymbol{M}}_{\mathrm{e}}|_{\widehat{\boldsymbol{b}}_{\mathrm{d}}=\widehat{\boldsymbol{G}}^{-1}}$ as a function of the unmodified Mandel stresses $\widehat{\boldsymbol{M}}_{\mathrm{e}}$ and of the deformation gradients and metric tensors ($\boldsymbol{F}$, $\boldsymbol{F}_{\mathrm{p}}$, $\boldsymbol{F}_{\mathrm{d}}$, $\boldsymbol{G}$, $\widehat{\boldsymbol{G}}$, $\overline{\boldsymbol{G}}$) seems impossible or at least very complex to find, an alternative, but simpler, approach is pursued.

The effective elastic Mandel stresses $\widehat{\boldsymbol{M}}_{\mathrm{e}}^{\mathrm{eff}}$ are modified such that evolving damage does not affect the effective elastic Mandel stresses (assuming a fixed elastic strain state). The metric tensors referred to the intermediate configuration — the configuration where

plastic flow naturally is described — are included in order to guarantee proper contractions. Modifying the effective damage Mandel stresses $\overline{\boldsymbol{M}}_{\mathrm{d}}^{\mathrm{eff}}$ is conceptually not that straightforward. In principle, the damage Mandel stresses should depend on the total strains $\overline{\boldsymbol{E}}$ instead of on the elastic strains $\overline{\boldsymbol{E}}_{\mathrm{e}}$. However, no multiplication of any metric or deformation measure with the elastic strains exists such that one obtains the total strains. Instead, the effective damage Mandel stresses are set up analogously to the elastic Mandel stresses — these stresses are multiplied with the transformed Finger tensor $\overline{\boldsymbol{b}}_{\mathrm{q}}$ and metric tensors referred to the fictitious configuration are included in order to guarantee proper contractions.

The alternative approach focusses on modifying the threshold contributions of the inelastic potentials. This approach is conceptually more straightforward and offers the opportunity to directly influence the evolution of damage and plasticity. To this end, the threshold values in the potentials (4.28) are each multiplied with an influence function taking values between zero and one, i.e.

$$f_{\mathrm{pd}} : \mathbb{R}_0^+ \to (0,1]\,, \tag{4.30}$$
$$f_{\mathrm{dp}} : \mathbb{R}_0^+ \to (0,1]\,, \tag{4.31}$$

where f_{pd} describes the influence of damage on the plastic yield limit and f_{dp} describes the influence of plasticity on the damage threshold. The arguments of the influence functions need to be scalar quantities (or tensors reduced to scalars by means of suitable operators) representing damage or, respectively, plasticity, i.e. $f_{\mathrm{pd}}(\bullet_{\mathrm{d}})$ and $f_{\mathrm{dp}}(\bullet_{\mathrm{p}})$. One may choose an isotropic hardening variable, or, alternatively, one may consider scalar reductions of tensorial quantities representing evolution of damage and plasticity, e.g. $\|\overline{\boldsymbol{C}}_{\mathrm{d}}\|$ and $\|\widehat{\boldsymbol{b}}_{\mathrm{p}}\|$. Non-accumulated quantities, such as $\|\widehat{\boldsymbol{b}}_{\mathrm{p}}\|$, however, do in general not increase monotonically. Consider, for example, a cyclic loading case under tension and subsequent compression. Plastic deformation contributions, measured by e.g. $\|\widehat{\boldsymbol{b}}_{\mathrm{p}}|$, may increase under tensile loading but may decrease under subsequent compressive loading. In such case, the influence function f_{dp} can be smaller during tension than during subsequent compression. The structure of the inelastic potentials considered reads

$$\Phi_{\mathrm{p}}(\overline{\boldsymbol{M}}_{\mathrm{e}},\, \boldsymbol{\mathcal{F}}_{\mathrm{p}};\, \bullet_{\mathrm{d}}) = M_{\mathrm{e}}^{\mathrm{eq}}(\overline{\boldsymbol{M}}_{\mathrm{e}}) - f_{\mathrm{pd}}(\bullet_{\mathrm{d}})\, M_{\mathrm{e}}^{\mathrm{max}}(\boldsymbol{\mathcal{F}}_{\mathrm{p}})\,, \tag{4.32}$$
$$\Phi_{\mathrm{d}}(\overline{\boldsymbol{M}}_{\mathrm{d}},\, \boldsymbol{\mathcal{F}}_{\mathrm{d}};\, \bullet_{\mathrm{p}}) = M_{\mathrm{d}}^{\mathrm{eq}}(\overline{\boldsymbol{M}}_{\mathrm{d}}) - f_{\mathrm{dp}}(\bullet_{\mathrm{p}})\, M_{\mathrm{d}}^{\mathrm{max}}(\boldsymbol{\mathcal{F}}_{\mathrm{d}})\,, \tag{4.33}$$

where the argument of functions f_{pd} and f_{dp} shall be a suitable quantity to describe evolution of plasticity or damage, respectively. These influence functions should be chosen with great care, since otherwise a scenario without any valid solution becomes possible — e.g. the influence functions decrease the threshold values faster than damage and plasticity can evolve. Further details regarding the chosen influence functions and arguments thereof are discussed in Section 4.4.

4.4 Choice of constitutive relations

The previously derived framework is now particularised by choosing specific formats for the energies and potentials. For the sake of simplicity the strain energy Ψ^{e} is chosen to be of St. Venant-Kirchhoff type, see Remark 7, resulting in

$$\Psi^{\mathrm{e}}(\overline{I}^{\overline{\boldsymbol{E}}_{\mathrm{e}}}_{1,2,3}) = \frac{1}{2}\,\lambda\left[\overline{I}^{\overline{\boldsymbol{E}}_{\mathrm{e}}}_{1}\right]^2 + \mu\,\overline{I}^{\overline{\boldsymbol{E}}_{\mathrm{e}}}_{2}\,, \tag{4.34}$$

with Lamé parameters λ and μ.

Remark 7 *The St. Venant-Kirchhoff type energy is chosen here for the sake of simplicity despite its problems to accurately represent compressive states. Compressive loading is neither accounted for correctly in the damage initiation potential nor in the damage evolution equation, such that an update of the formulation is necessary if compressive load states are to be analysed, see e.g. the formulation in Chapter 5. Moreover, the St. Venant-Kirchhoff type form of the Helmholtz energy can also be extended in line with established related energy functions.*

The set of additional internal variables related to plasticity $\boldsymbol{\mathcal{I}}_{\mathrm{p}}$ is given by the scalar proportional plastic hardening variable α_{p} and, similarly, $\boldsymbol{\mathcal{I}}_{\mathrm{d}}$ is given by the scalar proportional damage hardening variable α_{d}. A Swift-type ansatz, see e.g. [151, 164, 167], is chosen for the inelastic plastic energy contribution as well as the inelastic damage energy contributions, i.e.

$$\Psi^{\mathrm{p}}(\alpha_{\mathrm{p}}) = \frac{h_{\mathrm{p}}}{n_{\mathrm{p}}+1}\left[\alpha_{\mathrm{p0}}+\alpha_{\mathrm{p}}\right]^{n_{\mathrm{p}}+1}\,, \quad \text{with} \quad \alpha_{\mathrm{p0}} = \left[\frac{M_{\mathrm{e}}^{\mathrm{max0}}}{h_{\mathrm{p}}}\right]^{\frac{1}{n_{\mathrm{p}}}} \tag{4.35}$$

$$\Psi^{\mathrm{d}}(\alpha_{\mathrm{d}}) = \frac{h_{\mathrm{d}}}{n_{\mathrm{d}}+1}\left[\alpha_{\mathrm{d0}}+\alpha_{\mathrm{d}}\right]^{n_{\mathrm{d}}+1}\,, \quad \text{with} \quad \alpha_{\mathrm{d0}} = \left[\frac{M_{\mathrm{d}}^{\mathrm{max0}}}{h_{\mathrm{d}}}\right]^{\frac{1}{n_{\mathrm{d}}}} \tag{4.36}$$

including hardening moduli h_{p} and h_{d}, exponents n_{p} and n_{d} subject to $0 < n_{\mathrm{p}} \leq 1$ and $0 < n_{\mathrm{d}} \leq 1$ as well as the initial yield limit $M_{\mathrm{e}}^{\mathrm{max0}}$ and the damage initiation threshold $M_{\mathrm{d}}^{\mathrm{max0}}$. In the limit cases of $n_{\mathrm{p}} = 1$, respectively $n_{\mathrm{d}} = 1$, typical linear hardening formats are obtained.

With the given energies, related conjugated quantities can be calculated as

$$\overline{\boldsymbol{S}}_{\mathrm{e}} = \frac{\partial \Psi}{\partial \overline{\boldsymbol{E}}_{\mathrm{e}}} = \lambda\,\overline{I}^{\overline{\boldsymbol{E}}_{\mathrm{e}}}_{1}\,\overline{\boldsymbol{G}}^{-1} + 2\,\mu\,\overline{\boldsymbol{G}}^{-1}\cdot\overline{\boldsymbol{E}}_{\mathrm{e}}\cdot\overline{\boldsymbol{G}}^{-1}\,, \tag{4.37}$$

$$\beta_{\mathrm{p}} := -\frac{\partial \Psi}{\partial \alpha_{\mathrm{p}}} = -h_{\mathrm{p}}\,\left[\alpha_{\mathrm{p0}}+\alpha_{\mathrm{p}}\right]^{n_{\mathrm{p}}}\,, \tag{4.38}$$

$$\beta_{\mathrm{d}} := -\frac{\partial \Psi}{\partial \alpha_{\mathrm{d}}} = -h_{\mathrm{d}}\,\left[\alpha_{\mathrm{d0}}+\alpha_{\mathrm{d}}\right]^{n_{\mathrm{d}}}\,, \tag{4.39}$$

where the isotropic plastic and damage hardening stresses β_p and β_d have been introduced. Adhering to the format of the inelastic potentials postulated in (4.28), the plastic yield surface Φ_p and the damage initiation surface Φ_d are chosen as

$$\Phi_\mathrm{p} = M_\mathrm{e}^\mathrm{eq}(\overline{\boldsymbol{M}}_\mathrm{e}^\mathrm{eff}) - M_\mathrm{e}^\mathrm{max}(\beta_\mathrm{p})\,, \tag{4.40}$$

$$\Phi_\mathrm{d} = M_\mathrm{d}^\mathrm{eq}(\overline{\boldsymbol{M}}_\mathrm{d}) - f_\mathrm{dp}(\alpha_\mathrm{p})\, M_\mathrm{d}^\mathrm{max}(\beta_\mathrm{d})\,. \tag{4.41}$$

Following the discussion of effective driving forces, see Section 4.3, the plastic yield surface shall depend on the effective stresses $\overline{\boldsymbol{M}}_\mathrm{e}^\mathrm{eff}$, because these stresses can be motivated from micro-mechanics [130] and, in contrast to (isotropically) influencing the threshold value, the effective stresses properly account for the inherent anisotropy of the damage formulation. The damage initiation surface, on the other hand, shall be modified by means of the influence function $f_\mathrm{dp}(\alpha_\mathrm{p})$, since the effective damage driving force leads to a problematic evolution of the damage deformation gradient $\boldsymbol{F}_\mathrm{d}$ in this associative framework, see Remark 8.

Remark 8 *While the dissipation inequality can be shown to be fulfilled even with the effective damage stresses* $\overline{\boldsymbol{M}}_\mathrm{d}^\mathrm{eff}$ (4.29) *— the proof is analogous to Remark 10 — the requirement of a negative semi-definite evolution direction* $\overline{\boldsymbol{L}}_\mathrm{d}$*, in order to guarantee a monotonous growth of damage, is (in this associative setting) not always fulfilled. In analogy to the effective plastic return direction, cf.* (4.49)*, one obtains for the effective damage return direction*

$$\overline{\boldsymbol{\nu}}_\mathrm{d}^\mathrm{eff} = \frac{\partial M_\mathrm{d}^\mathrm{eq}}{\partial \overline{\boldsymbol{M}}_\mathrm{d}^\mathrm{eff}} = \frac{2}{3\, M_\mathrm{d}^\mathrm{eq}(\overline{\boldsymbol{M}}_\mathrm{d}^\mathrm{eff})} \left[\zeta_\mathrm{d}\, \overline{I}_1^{\overline{\boldsymbol{M}}_\mathrm{d}^\mathrm{eff}}\, \overline{\boldsymbol{I}} + [1-\zeta_\mathrm{d}]\, \overline{\boldsymbol{M}}_\mathrm{d}^\mathrm{t,eff}\right], \tag{4.42}$$

cf. (4.45)*, and the corresponding total damage return direction is given by*

$$\overline{\boldsymbol{\nu}}_\mathrm{d} = \frac{\partial M_\mathrm{d}^\mathrm{eq}}{\partial \overline{\boldsymbol{M}}_\mathrm{d}^\mathrm{eff}} : \frac{\partial \overline{\boldsymbol{M}}_\mathrm{d}^\mathrm{eff}}{\partial \overline{\boldsymbol{M}}_\mathrm{d}} = \overline{\boldsymbol{b}}_\mathrm{q} \cdot \overline{\boldsymbol{G}} \cdot \overline{\boldsymbol{\nu}}_\mathrm{d}^\mathrm{eff} \cdot \overline{\boldsymbol{b}}_\mathrm{q} \cdot \overline{\boldsymbol{G}}\,. \tag{4.43}$$

The damage Mandel stresses $\overline{\boldsymbol{M}}_\mathrm{d}$ *are negative semi-definite except for certain cases with combined tension-compression loading, specifically (in terms of eigenvalues of* $\overline{\boldsymbol{E}}_\mathrm{e}$ *and Poisson-ratio* $\nu = \lambda/[2\,\lambda + 2\,\mu]$ *if* $0 > \lambda_1^{\overline{\boldsymbol{E}}_\mathrm{e}}/[\lambda_2^{\overline{\boldsymbol{E}}_\mathrm{e}} + \lambda_3^{\overline{\boldsymbol{E}}_\mathrm{e}}] > -\nu/[1-\nu]$*, see also [186].*

While neither $\overline{\boldsymbol{M}}_\mathrm{d}$ *nor* $\overline{\boldsymbol{M}}_\mathrm{d}^\mathrm{eff}$ *are (always) negative semi-definite, the trace of the non-effective Mandel stresses* $\overline{\boldsymbol{I}} : \overline{\boldsymbol{M}}_\mathrm{d}$ *is always negative due to a quadratic form in the fictitious elastic strains* $\overline{\boldsymbol{E}}_\mathrm{e}$*. Consequently, the term including the trace operation in* (4.50) *is able to compensate a positive contribution from the other term. In the examples shown in this work, no cases of non-negative semi-definite damage return directions* $\overline{\boldsymbol{\nu}}_\mathrm{d}$ *have been observed. Since damage evolution under compression is not accounted for correctly in the model, the model behaviour under compression has not been studied. An extension of the model to more accurately describe behaviour under compression*

is addressed in Chapter 5. A straightforward correction, respectively extension, may be achieved by using only the negative contributions — i.e. those related to negative eigenvalues — of the return direction $\overline{\boldsymbol{\nu}}_{\mathrm{d}}$ for evolution of damage.

In the case of the effective Mandel stresses, the trace of the effective Mandel stresses is not always negative due to the additional multiplication with $\overline{\boldsymbol{b}}_{\mathrm{q}}$. This even results in non-negative semi-definite damage return directions in specific cases of, e.g., simple shear loading. Consequently, the approach using effective (damage) Mandel stresses is not pursued further.

The structure of the equivalent stress and threshold functions is identical for plastic yield and damage initiation, namely

$$M_{\mathrm{e}}^{\mathrm{eq}}(\overline{\boldsymbol{M}}_{\mathrm{e}}^{\mathrm{eff}}) = \sqrt{\zeta_{\mathrm{p}} \left[\overline{I}_1^{\overline{\boldsymbol{M}}_{\mathrm{e}}^{\mathrm{eff}}}\right]^2 + [1-\zeta_{\mathrm{p}}]\, \overline{I}_2^{\overline{\boldsymbol{M}}_{\mathrm{e}}^{\mathrm{eff}}}}\,, \qquad M_{\mathrm{e}}^{\max}(\beta_{\mathrm{p}}) = -\sqrt{\tfrac{2}{3}}\,\beta_{\mathrm{p}}\,, \tag{4.44}$$

$$M_{\mathrm{d}}^{\mathrm{eq}}(\overline{\boldsymbol{M}}_{\mathrm{d}}) = \sqrt{\zeta_{\mathrm{d}} \left[\overline{I}_1^{\overline{\boldsymbol{M}}_{\mathrm{d}}}\right]^2 + [1-\zeta_{\mathrm{d}}]\, \overline{I}_2^{\overline{\boldsymbol{M}}_{\mathrm{d}}}}\,, \qquad M_{\mathrm{d}}^{\max}(\beta_{\mathrm{d}}) = -\sqrt{\tfrac{2}{3}}\,\beta_{\mathrm{d}}\,, \tag{4.45}$$

where $\zeta_{\mathrm{p}} = -\frac{1}{2}$ corresponds to a von Mises type yield surface and ζ_{d} controls the degree of anisotropy induced by damage evolution, with $\zeta_{\mathrm{d}} = 1$ resulting in isotropic damage evolution. The coupling function

$$f_{\mathrm{dp}}(\alpha_{\mathrm{p}}) = \frac{\tanh(h_{\mathrm{dp}}\,[\alpha_{\mathrm{p,max}} - \alpha_{\mathrm{p}}]) + 1}{\tanh(h_{\mathrm{dp}}\,\alpha_{\mathrm{p,max}}) + 1} \tag{4.46}$$

is chosen as a hyperbolic tangens function, which strongly — depending on material parameter h_{dp} — reduces the damage threshold as soon as plastic hardening surpasses the value of $\alpha_{\mathrm{p,max}}$; see Figure 4.2 for a graphical illustration of the influence of the parameters. Alternative types of functions are briefly discussed in Remark 9.

Remark 9 *Other possibilities for the formulation of $f_{\mathrm{dp}}(\alpha_{\mathrm{p}})$ exist. Whereas a dependence on the scalar proportional hardening variable α_{p} is rather simple, other dependencies may offer more information. Formulating f_{dp} in terms of suitable functions, respectively quantities, of the plastic deformation gradient $\boldsymbol{F}_{\mathrm{p}}$, such as $\widehat{\boldsymbol{E}}_{\mathrm{p}}$, allows a reversal of the effect of degradation if the plastic deformation is reduced due to load reversal. However, this also requires the choice of an appropriate measure and an appropriate norm. In addition, a more intricate coupling between plasticity and damage evolution ensues.*

Moreover, let the plastic and damage velocity gradients be determined by means of the plastic and damage flow directions, respectively, as

$$\overline{\boldsymbol{L}}_{\mathrm{p}} = \lambda_{\mathrm{p}}\, \overline{\boldsymbol{\nu}}_{\mathrm{p}}\,, \tag{4.47}$$

$$\overline{\boldsymbol{L}}_{\mathrm{d}} = \lambda_{\mathrm{d}}\, \overline{\boldsymbol{\nu}}_{\mathrm{d}}\,. \tag{4.48}$$

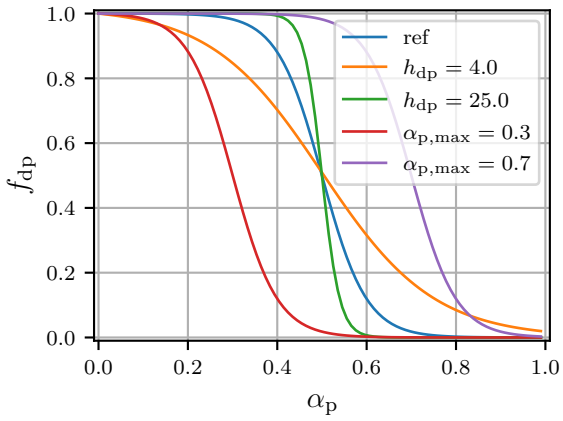

Figure 4.2: Plot of the coupling function f_{dp} over the isotropic hardening variable α_{p}. The blue (reference) curve shows the function values for $\alpha_{\mathrm{p,max}} = 0.5$ and $h_{\mathrm{dp}} = 10.0$. The other curves have one of the parameters varied as indicated by the legend.

Furthermore, the derivatives of the equivalent stress functions (4.44) and (4.45) are introduced as

$$\overline{\boldsymbol{\nu}}_{\mathrm{p}}^{\mathrm{eff}}(\overline{\boldsymbol{M}}_{\mathrm{e}}^{\mathrm{eff}}) := \frac{\partial M_{\mathrm{e}}^{\mathrm{eq}}}{\partial \overline{\boldsymbol{M}}_{\mathrm{e}}^{\mathrm{eff}}} = \frac{2}{3\, M_{\mathrm{e}}^{\mathrm{eq}}(\overline{\boldsymbol{M}}_{\mathrm{e}}^{\mathrm{eff}})} \left[\zeta_{\mathrm{p}}\, \overline{I}_1^{\overline{\boldsymbol{M}}_{\mathrm{e}}^{\mathrm{eff}}}\, \boldsymbol{I} + [1-\zeta_{\mathrm{p}}]\, \overline{\boldsymbol{M}}_{\mathrm{e}}^{\mathrm{t,eff}}\right], \tag{4.49}$$

$$\overline{\boldsymbol{\nu}}_{\mathrm{d}}(\overline{\boldsymbol{M}}_{\mathrm{d}}) := \frac{\partial M_{\mathrm{d}}^{\mathrm{eq}}}{\partial \overline{\boldsymbol{M}}_{\mathrm{d}}} = \frac{2}{3\, M_{\mathrm{d}}^{\mathrm{eq}}(\overline{\boldsymbol{M}}_{\mathrm{d}})} \left[\zeta_{\mathrm{d}} \overline{I}_1^{\overline{\boldsymbol{M}}_{\mathrm{d}}}\, \boldsymbol{I} + [1-\zeta_{\mathrm{d}}] \overline{\boldsymbol{M}}_{\mathrm{d}}^{\mathrm{t}}\right], \tag{4.50}$$

where the damage flow direction could already be identified. In order to formulate the plastic flow direction $\overline{\boldsymbol{\nu}}_{\mathrm{p}}$, the derivative of the Mandel stresses $\overline{\boldsymbol{M}}_{\mathrm{e}}$ with respect to their effective counterpart $\overline{\boldsymbol{M}}_{\mathrm{e}}^{\mathrm{eff}}$ is required. Inserting $\overline{\boldsymbol{S}}_{\mathrm{e}} = \overline{\boldsymbol{C}}_{\mathrm{ed}}^{-1} \cdot \overline{\boldsymbol{M}}_{\mathrm{e}}$ into the definition of the effective Mandel stresses (4.29) yields the desired derivative to be determined straight-forwardly. The resulting plastic flow direction then reads

$$\overline{\boldsymbol{\nu}}_{\mathrm{p}} = \frac{\partial \Phi_{\mathrm{p}}}{\partial \overline{\boldsymbol{M}}_{\mathrm{e}}} = \overline{\boldsymbol{\nu}}_{\mathrm{p}}^{\mathrm{eff}}(\overline{\boldsymbol{M}}_{\mathrm{e}}^{\mathrm{eff}}) : \frac{\partial \overline{\boldsymbol{M}}_{\mathrm{e}}^{\mathrm{eff}}}{\partial \overline{\boldsymbol{M}}_{\mathrm{e}}} = \overline{\boldsymbol{C}}_{\mathrm{ed}}^{-1} \cdot \overline{\boldsymbol{G}} \cdot \overline{\boldsymbol{C}}_{\mathrm{d}}^{-1} \cdot \overline{\boldsymbol{C}}_{\mathrm{ed}} \cdot \overline{\boldsymbol{\nu}}_{\mathrm{p}}^{\mathrm{eff}}(\overline{\boldsymbol{M}}_{\mathrm{e}}^{\mathrm{eff}}) \cdot \overline{\boldsymbol{C}}_{\mathrm{d}}^{-1} \cdot \overline{\boldsymbol{G}}\,. \tag{4.51}$$

Inserting the obtained return directions into the dissipation inequality results in expressions which are guaranteed to be positive even with the modification of using effective stresses, see Remark 10. Moreover, the evolution equations for plastic hardening and damage hardening are obtained as

$$\dot{\alpha_{\mathrm{p}}} = \lambda_{\mathrm{p}} \frac{\partial \Phi_{\mathrm{p}}}{\partial \beta_{\mathrm{p}}} = \sqrt{\tfrac{2}{3}}\, \lambda_{\mathrm{p}}\,, \tag{4.52}$$

$$\dot{\alpha_{\mathrm{d}}} = \lambda_{\mathrm{d}} \frac{\partial \Phi_{\mathrm{d}}}{\partial \beta_{\mathrm{d}}} = \sqrt{\tfrac{2}{3}}\, \lambda_{\mathrm{d}}\, f_{\mathrm{dp}}(\alpha_{\mathrm{p}})\,. \tag{4.53}$$

Remark 10 *Non-negative dissipation can be guaranteed by generating a (positive semi-definite) quadratic form. To this end, the Mandel stresses* $\overline{\boldsymbol{M}}_{\mathrm{e}}$ *are expressed in terms of the effective Mandel stresses* $\overline{\boldsymbol{M}}_{\mathrm{e}}^{\mathrm{eff}}$ *by inversion of* (4.29) *and based on the definition of the Mandel stresses in* (4.21)*, i.e.*

$$\overline{\boldsymbol{M}}_{\mathrm{e}} = \overline{\boldsymbol{C}}_{\mathrm{ed}} \cdot \overline{\boldsymbol{G}}^{-1} \cdot \overline{\boldsymbol{C}}_{\mathrm{d}} \cdot \overline{\boldsymbol{C}}_{\mathrm{ed}}^{-1} \cdot \overline{\boldsymbol{M}}_{\mathrm{e}}^{\mathrm{eff}} \cdot \overline{\boldsymbol{C}}_{\mathrm{d}} \cdot \overline{\boldsymbol{G}}^{-1} \,. \tag{4.54}$$

The relevant part of the dissipation inequality is represented by $\overline{\boldsymbol{M}}_{\mathrm{e}} : \overline{\boldsymbol{L}}_{\mathrm{p}}$ *and after inserting the respective quantities one obtains*

$$\begin{aligned} \overline{\boldsymbol{M}}_{\mathrm{e}} : \overline{\boldsymbol{L}}_{\mathrm{p}} = &\left[\overline{\boldsymbol{C}}_{\mathrm{ed}} \cdot \overline{\boldsymbol{G}}^{-1} \cdot \overline{\boldsymbol{C}}_{\mathrm{d}} \cdot \overline{\boldsymbol{C}}_{\mathrm{ed}}^{-1} \cdot \overline{\boldsymbol{M}}_{\mathrm{e}}^{\mathrm{eff}} \cdot \overline{\boldsymbol{C}}_{\mathrm{d}} \cdot \overline{\boldsymbol{G}}^{-1}\right] : \\ &\left[\overline{\boldsymbol{C}}_{\mathrm{ed}}^{-1} \cdot \overline{\boldsymbol{G}} \cdot \overline{\boldsymbol{C}}_{\mathrm{d}}^{-1} \cdot \overline{\boldsymbol{C}}_{\mathrm{ed}} \cdot \overline{\boldsymbol{\nu}}_{\mathrm{p}}^{\mathrm{eff}}(\overline{\boldsymbol{M}}_{\mathrm{e}}^{\mathrm{eff}}) \cdot \overline{\boldsymbol{C}}_{\mathrm{d}}^{-1} \cdot \overline{\boldsymbol{G}}\right] \lambda_{\mathrm{p}} = \overline{\boldsymbol{M}}_{\mathrm{e}}^{\mathrm{eff}} : \overline{\boldsymbol{\nu}}_{\mathrm{p}}^{\mathrm{eff}} \, \lambda_{\mathrm{p}} \,, \end{aligned} \tag{4.55}$$

which is guaranteed to be non-negative due to $\boldsymbol{T} : \boldsymbol{T}^{\mathrm{t}} = \boldsymbol{I} : [\boldsymbol{T} \cdot \boldsymbol{T}] \geq 0$*, for* $\boldsymbol{T}$ *being the product of two symmetric second order tensors with one of these being positive definite (so that* $\boldsymbol{T}$ *possesses real eigenvalues), cf.* (4.49)*.*

Next, explicit expressions for the rates of the deformation gradients $\dot{\boldsymbol{F}}_{\mathrm{d}}$ and $\dot{\boldsymbol{F}}_{\mathrm{p}}$ are required. Typically, the rate of the plastic deformation gradient is determined from the intermediate plastic velocity gradient, i.e.

$$\widehat{\boldsymbol{L}}_{\mathrm{p}} = \dot{\boldsymbol{F}}_{\mathrm{p}} \cdot \boldsymbol{F}_{\mathrm{p}}^{-1} = \lambda_{\mathrm{p}} \, \widehat{\boldsymbol{\nu}}_{\mathrm{p}} \,, \tag{4.56}$$

such that the time derivative of the plastic part of the deformation gradient can be expressed as

$$\dot{\boldsymbol{F}}_{\mathrm{p}} = \widehat{\boldsymbol{L}}_{\mathrm{p}} \cdot \boldsymbol{F}_{\mathrm{p}} \,. \tag{4.57}$$

In this formulation, however, an expression fully referred to the fictitious configuration is desired, because it reduces the numerical effort, see Section 4.5. The pull-back operation of the intermediate plastic velocity gradient $\widehat{\boldsymbol{L}}_{\mathrm{p}}$ to the fictitious configuration is analogous (dual) to the pull-back of the intermediate Mandel stresses $\widehat{\boldsymbol{M}}_{\mathrm{e}}$, i.e.

$$\overline{\boldsymbol{M}}_{\mathrm{e}} = \overline{\boldsymbol{C}}_{\mathrm{ed}} \cdot \overline{\boldsymbol{S}}_{\mathrm{e}} = \boldsymbol{F}_{\mathrm{d}}^{\mathrm{t}} \cdot \widehat{\boldsymbol{C}}_{\mathrm{e}} \cdot \boldsymbol{F}_{\mathrm{d}} \cdot \boldsymbol{F}_{\mathrm{d}}^{-1} \cdot \widehat{\boldsymbol{S}}_{\mathrm{e}} \cdot \boldsymbol{F}_{\mathrm{d}}^{-\mathrm{t}} = \boldsymbol{F}_{\mathrm{d}}^{\mathrm{t}} \cdot \widehat{\boldsymbol{M}}_{\mathrm{e}}^{\mathrm{t}} \cdot \boldsymbol{F}_{\mathrm{d}}^{-\mathrm{t}} \,, \tag{4.58}$$

so that the pull-back operation of the plastic velocity gradient $\widehat{\boldsymbol{L}}_{\mathrm{p}}$ is given by

$$\overline{\boldsymbol{L}}_{\mathrm{p}} = \boldsymbol{F}_{\mathrm{d}}^{-1} \cdot \widehat{\boldsymbol{L}}_{\mathrm{p}} \cdot \boldsymbol{F}_{\mathrm{d}} \,. \tag{4.59}$$

The time derivative of the plastic part of the deformation gradient can now also be expressed as

$$\dot{\boldsymbol{F}}_{\mathrm{p}} = \boldsymbol{F}_{\mathrm{d}} \cdot \overline{\boldsymbol{L}}_{\mathrm{p}} \cdot \boldsymbol{F}_{\mathrm{d}}^{-1} \cdot \boldsymbol{F}_{\mathrm{p}} \,. \tag{4.60}$$

Considering the time derivative of the mapping $\boldsymbol{F}_{\mathrm{q}} = \boldsymbol{F}_{\mathrm{d}}^{-1} \cdot \boldsymbol{F}_{\mathrm{p}}$ results in

$$\dot{\boldsymbol{F}}_{\mathrm{q}} = \boldsymbol{F}_{\mathrm{d}}^{-1} \cdot \dot{\boldsymbol{F}}_{\mathrm{p}} - \boldsymbol{F}_{\mathrm{d}}^{-1} \cdot \dot{\boldsymbol{F}}_{\mathrm{d}} \cdot \boldsymbol{F}_{\mathrm{d}}^{-1} \cdot \boldsymbol{F}_{\mathrm{p}} \quad \text{with} \quad \dot{\overline{\boldsymbol{F}_{\mathrm{d}}^{-1}}} = -\boldsymbol{F}_{\mathrm{d}}^{-1} \cdot \dot{\boldsymbol{F}}_{\mathrm{d}} \cdot \boldsymbol{F}_{\mathrm{d}}^{-1} \,. \tag{4.61}$$

One can correlate the first term of the righthand side in $(4.61)_1$ to the plastic velocity gradient referred to the fictitious configuration by making use of (4.60), i.e.

$$\boldsymbol{F}_{\mathrm{d}}^{-1} \cdot \dot{\boldsymbol{F}}_{\mathrm{p}} = \overline{\boldsymbol{L}}_{\mathrm{p}} \cdot \boldsymbol{F}_{\mathrm{q}} \,, \tag{4.62}$$

and the second term can be correlated to the damage velocity gradient referred to the fictitious configuration given by

$$\overline{\boldsymbol{L}}_{\mathrm{d}} = \boldsymbol{F}_{\mathrm{d}}^{-1} \cdot \dot{\boldsymbol{F}}_{\mathrm{d}} \,. \tag{4.63}$$

Summarising, one obtains

$$\dot{\boldsymbol{F}}_{\mathrm{q}} = \left[\overline{\boldsymbol{L}}_{\mathrm{p}} - \overline{\boldsymbol{L}}_{\mathrm{d}}\right] \cdot \boldsymbol{F}_{\mathrm{q}} \,, \tag{4.64}$$

i.e. an evolution equation referred to the fictitious configuration including plasticity contributions.

4.5 Algorithmic treatment

To simplify the notation as well as to improve readability, metric tensors are replaced with the identity tensor as this work proceeds.

4.5.1 Discretisation of the evolution equations

Implementing the proposed constitutive model requires a discretisation in time. Let t_n be the time at the previous time step n and let $t_{n+1} = t_n + \Delta t$ denote the current time step with step size Δt. For the sake of readability, the index $n+1$ is omitted except when emphasising an updated quantity. The rates of the deformation gradients $\boldsymbol{F}_{\mathrm{q}}$ and $\boldsymbol{F}_{\mathrm{d}}$ are discretised by means of the exponential map so that

$$\boldsymbol{F}_{\mathrm{q},n+1} = \exp(\Delta t\, \overline{\boldsymbol{L}}_{\mathrm{p}} - \Delta t\, \overline{\boldsymbol{L}}_{\mathrm{d}}) \cdot \boldsymbol{F}_{\mathrm{q},n} \,, \tag{4.65}$$

$$\boldsymbol{F}_{\mathrm{d},n+1} = \boldsymbol{F}_{\mathrm{d},n} \cdot \exp(\Delta t\, \overline{\boldsymbol{L}}_{\mathrm{d}}) \,. \tag{4.66}$$

Splitting $\boldsymbol{F}_{\mathrm{q},n+1}$ into $\boldsymbol{F}_{\mathrm{p},n+1}$ and $\boldsymbol{F}_{\mathrm{d},n+1}$ and inverting (4.65) results in

$$\boldsymbol{F}_{\mathrm{p},n+1}^{-1} \cdot \boldsymbol{F}_{\mathrm{d},n+1} = \boldsymbol{F}_{\mathrm{p},n}^{-1} \cdot \boldsymbol{F}_{\mathrm{d},n} \cdot \exp(\Delta t\, \overline{\boldsymbol{L}}_{\mathrm{d}} - \Delta t\, \overline{\boldsymbol{L}}_{\mathrm{p}}) \,, \tag{4.67}$$

and together with (4.66) allows the update for the plastic deformation gradient to be written as

$$\boldsymbol{F}_{\mathrm{p},n+1}^{-1} = \boldsymbol{F}_{\mathrm{p},n}^{-1} \cdot \boldsymbol{F}_{\mathrm{d},n} \cdot \exp(\Delta t\, \overline{\boldsymbol{L}}_{\mathrm{d}} - \Delta t\, \overline{\boldsymbol{L}}_{\mathrm{p}}) \cdot \exp(-\Delta t\, \overline{\boldsymbol{L}}_{\mathrm{d}}) \cdot \boldsymbol{F}_{\mathrm{d},n}^{-1} \,. \tag{4.68}$$

Applying the exponential map to $\boldsymbol{F}_\mathrm{q}$ and $\boldsymbol{F}_\mathrm{d}$ fulfils plastic incompressibility $\det(\boldsymbol{F}_\mathrm{p}) = 1$, see Remark 11. The scalar evolution equations for proportional plastic and damage hardening, α_p and α_d, are discretised by using a backward Euler scheme, i.e.

$$\alpha_{\mathrm{p},n+1} = \alpha_{\mathrm{p},n} + \Delta t \sqrt{\tfrac{2}{3}}\, \lambda_\mathrm{p}\,, \tag{4.69}$$

$$\alpha_{\mathrm{d},n+1} = \alpha_{\mathrm{d},n} + \Delta t \sqrt{\tfrac{2}{3}}\, \lambda_\mathrm{d}\, f_\mathrm{dp}(\alpha_{\mathrm{p},n+1})\,. \tag{4.70}$$

Remark 11 *Proper algorithmic treatment of deviatoric plastic flow needs to fulfil plastic incompressibility, i.e.* $\det(\boldsymbol{F}_\mathrm{p}) = 1$. *Starting by computing the determinant of the update of* $\boldsymbol{F}_\mathrm{q}$ *from* (4.65) *and making use of* $\det(\boldsymbol{A}\cdot\boldsymbol{B}) = \det(\boldsymbol{A})\,\det(\boldsymbol{B})$ *as well as* $\det(\exp(\boldsymbol{A})) = \exp(\mathrm{tr}(\boldsymbol{A}))$ *one obtains*

$$\det(\boldsymbol{F}_{\mathrm{q},n+1}) = \det(\exp(\Delta t\overline{\boldsymbol{L}}_\mathrm{d} - \Delta t\overline{\boldsymbol{L}}_\mathrm{p}))\,\frac{\det(\boldsymbol{F}_{\mathrm{p},n})}{\det(\boldsymbol{F}_{\mathrm{d},n})} \tag{4.71}$$

$$= \exp(\mathrm{tr}(\Delta t\overline{\boldsymbol{L}}_\mathrm{d} - \Delta t\overline{\boldsymbol{L}}_\mathrm{p}))\,\frac{\det(\boldsymbol{F}_{\mathrm{p},n})}{\det(\boldsymbol{F}_{\mathrm{d},n})} \tag{4.72}$$

$$= \frac{\exp(\Delta t\ \mathrm{tr}(\overline{\boldsymbol{L}}_\mathrm{p}))}{\exp(\Delta t\ \mathrm{tr}(\overline{\boldsymbol{L}}_\mathrm{d}))}\,\frac{\det(\boldsymbol{F}_{\mathrm{p},n})}{\det(\boldsymbol{F}_{\mathrm{d},n})} = \frac{\det(\boldsymbol{F}_{\mathrm{p},n+1})}{\det(\boldsymbol{F}_{\mathrm{d},n+1})}\,. \tag{4.73}$$

Computing the determinant of the update of $\boldsymbol{F}_\mathrm{d}$ *from* (4.66) *yields*

$$\det(\boldsymbol{F}_{\mathrm{d},n+1}) = \det(\boldsymbol{F}_{\mathrm{d},n})\,\exp(\Delta t\ \mathrm{tr}(\overline{\boldsymbol{L}}_\mathrm{d}))\,, \tag{4.74}$$

which, after insertion into (4.73)*, results in*

$$\det(\boldsymbol{F}_{\mathrm{p},n+1}) = \exp(\Delta t\ \mathrm{tr}(\overline{\boldsymbol{L}}_\mathrm{p}))\,\det(\boldsymbol{F}_{\mathrm{p},n})\,. \tag{4.75}$$

Thus, in order to fulfil plastic incompressibility, $\mathrm{tr}(\overline{\boldsymbol{L}}_\mathrm{p}) = 0$ *needs to hold. This can straight-forwardly be shown, i.e.*

$$\mathrm{tr}(\overline{\boldsymbol{L}}_\mathrm{p}) = \mathrm{tr}(\boldsymbol{F}_\mathrm{d}^{-1}\cdot\widehat{\boldsymbol{L}}_\mathrm{p}\cdot\boldsymbol{F}_\mathrm{d}) = \mathrm{tr}(\boldsymbol{F}_\mathrm{d}\cdot\boldsymbol{F}_\mathrm{d}^{-1}\cdot\widehat{\boldsymbol{L}}_\mathrm{p}) = \mathrm{tr}(\widehat{\boldsymbol{L}}_\mathrm{p}) = 0\,. \tag{4.76}$$

The update of the damage deformation gradient $\boldsymbol{F}_\mathrm{d}$ depends, besides quantities from the previous time step as well as Lagrange multipliers λ_p and λ_d, solely on the fictitious elastic Green-Lagrange strains $\overline{\boldsymbol{E}}_\mathrm{e}$ through $\overline{\boldsymbol{L}}_\mathrm{d}(\overline{\boldsymbol{M}}_\mathrm{d}(\overline{\boldsymbol{E}}_\mathrm{e}))$. The update of the plastic deformation gradient ultimately also only depends on the fictitious elastic Green-Lagrange strains $\overline{\boldsymbol{E}}_\mathrm{e}$ and quantities from previous time steps as well as Lagrange multipliers λ_p and λ_d, since the effective Mandel stresses $\overline{\boldsymbol{M}}_\mathrm{e}^\mathrm{eff}$ depend on $\overline{\boldsymbol{C}}_\mathrm{ed} = 2\,\overline{\boldsymbol{E}}_\mathrm{e} + \overline{\boldsymbol{C}}_\mathrm{d}$, $\overline{\boldsymbol{C}}_\mathrm{d}(\boldsymbol{F}_\mathrm{d})$ and

$\overline{\boldsymbol{S}}_{\mathrm{e}}(\overline{\boldsymbol{E}}_{\mathrm{e}})$ only through $\boldsymbol{F}_{\mathrm{d}}(\overline{\boldsymbol{E}}_{\mathrm{e}})$ and $\overline{\boldsymbol{E}}_{\mathrm{e}}$. Hence, in order to solve these non-linear equations, the Lagrange multipliers λ_{p} and λ_{d} as well as the fictitious elastic Green-Lagrange strains $\overline{\boldsymbol{E}}_{\mathrm{e}}$ are considered as unknowns. The corresponding residuals

$$r_{\mathrm{p}} = \sqrt{\Phi_{\mathrm{p}}^2 + {\lambda_{\mathrm{p}}}^2 + \epsilon} + \Phi_{\mathrm{p}} - \lambda_{\mathrm{p}} \,, \tag{4.77}$$

$$r_{\mathrm{d}} = \sqrt{\Phi_{\mathrm{d}}^2 + {\lambda_{\mathrm{d}}}^2 + \epsilon} + \Phi_{\mathrm{d}} - \lambda_{\mathrm{d}} \,, \tag{4.78}$$

$$\boldsymbol{R}_{\mathrm{e}} = \overline{\boldsymbol{E}}_{\mathrm{e}} - \frac{1}{2}\, \boldsymbol{F}_{\mathrm{d}}^{\mathrm{t}} \cdot \left[\boldsymbol{F}_{\mathrm{p}}^{-\mathrm{t}} \cdot \boldsymbol{C} \cdot \boldsymbol{F}_{\mathrm{p}}^{-1} - \widehat{\boldsymbol{I}} \right] \cdot \boldsymbol{F}_{\mathrm{d}} \,, \tag{4.79}$$

are solved by means of a Newton-Raphson method for which the Armijo-Goldstein condition [6, 50] determines the step-length — with reduction rate $\tau = 0.8$, maximum search attempts $j_{\max} = 10$ and sufficient residuum decrease $c = 0.1$. The algorithm is summarised in Table 4.1 together with Table 4.2. These tables already contain quantities necessary for regularisation, which are introduced in Section 2.2 and which are further specified in Section 4.6. In particular, the tables include the non-local fields ϕ_{p} and ϕ_{d} related to plasticity and damage, respectively, as well as their gradients $\nabla_{\boldsymbol{X}}\phi_{\mathrm{p}}$ and $\nabla_{\boldsymbol{X}}\phi_{\mathrm{d}}$ and the corresponding driving forces Y_{p}, Y_{d} and $\boldsymbol{Y}_{\mathrm{p}}$, $\boldsymbol{Y}_{\mathrm{d}}$, cf. (4.123).

Remark 12 *Setting the anisotropy parameter $\zeta_{\mathrm{d}} = 1$ results in an isotropic evolution of damage. In this case, one obtains a constant damage return direction, see* (4.50)*, i.e.*

$$\overline{\boldsymbol{\nu}}_{\mathrm{d}} = \frac{2}{3\, M_{\mathrm{d}}^{\mathrm{eq}}}\, \mathrm{tr}(\overline{\boldsymbol{M}}_{\mathrm{d}})\, \boldsymbol{I} = -\frac{2}{3}\, \boldsymbol{I} \,, \quad \textit{with} \quad M_{\mathrm{d}}^{\mathrm{eq}} = -\,\mathrm{tr}(\overline{\boldsymbol{M}}_{\mathrm{d}}) \,, \tag{4.80}$$

see also Remark 8. Insertion into the evolution equation of the damage deformation gradient $\boldsymbol{F}_{\mathrm{d}}$, see (4.66)*, yields*

$$\boldsymbol{F}_{\mathrm{d},n+1} = \boldsymbol{F}_{\mathrm{d},n}\, \exp\left(-\frac{2}{3}\, \Delta t\, \lambda_{\mathrm{d}} \right) \tag{4.81}$$

$$= \boldsymbol{F}_{\mathrm{d},n-1}\, \exp\left(-\frac{2}{3}\, \Delta t_n\, \lambda_{\mathrm{d}n} - \frac{2}{3}\, \Delta t\, \lambda_{\mathrm{d}} \right) . \tag{4.82}$$

Introducing a new damage variable $\widetilde{d}$ with evolution equation

$$\widetilde{d}_{n+1} = \widetilde{d}_n + \Delta t\, \lambda_{\mathrm{d}} \,, \quad \textit{with} \quad \widetilde{d}|_{t=0} = 0 \,, \tag{4.83}$$

and assuming the damage deformation gradient is initially given by the unit tensor, i.e. $\boldsymbol{F}_{\mathrm{d}}|_{t=0} = \boldsymbol{I}$, allows to write the update of the damage deformation gradient as

$$\boldsymbol{F}_{\mathrm{d},n+1} = \exp\left(-\frac{2}{3}\, \widetilde{d}_{n+1} \right) \boldsymbol{I} \,. \tag{4.84}$$

Thereby, the elastic Helmholtz energy can be formulated as

$$\Psi^{\mathrm{e}}_{\mathrm{aniso}} = \frac{1}{2}\,\lambda\,\exp\left(-\frac{8}{3}\,\widetilde{d}\right)\,\left[\boldsymbol{I} : \widehat{\boldsymbol{E}}_{\mathrm{e}}\right]^2 + \mu\,\exp\left(-\frac{8}{3}\,\widetilde{d}\right)\,\widehat{\boldsymbol{E}}_{\mathrm{e}} : \widehat{\boldsymbol{E}}_{\mathrm{e}}\,. \tag{4.85}$$

This representation of the elastic Helmholtz energy is nearly identical to the elastic energy of the isotropic model, compare (3.4)*, given as*

$$\Psi^{\mathrm{e}}_{\mathrm{iso}} = \frac{1}{2}\,K\,\exp(-\xi_{\mathrm{vol}}\,d)\,\left[\boldsymbol{I} : \boldsymbol{\varepsilon}_{\mathrm{e}}\right]^2 + G\,\exp(-d)\,\boldsymbol{\varepsilon}^{\mathrm{dev}}_{\mathrm{e}} : \boldsymbol{\varepsilon}^{\mathrm{dev}}_{\mathrm{e}}\,, \tag{4.86}$$

where the corresponding evolution equation of the local damage variable is obtained in (3.29) *as*

$$d_{n+1} = d_n + \lambda_{\mathrm{d}}\,, \tag{4.87}$$

assuming the function $f^{\alpha_{\mathrm{p}}}(\alpha_{\mathrm{p}})$ to be identically one (by choosing $\eta_{\mathrm{p}} = 0$).

The comparison revealed that the proposed anisotropic damage model is a generalisation of the previously proposed isotropic damage model — ignoring the fact that different strain measures are chosen and that it holds only for specific parameter combinations.

4.5.2 Local tangent contributions

The local analytical tangent $\boldsymbol{J}$ of the residuum for the system of equations to be solved in every integration point, cf. (4.79), is given as

$$\boldsymbol{J} = \begin{bmatrix} J_{\mathrm{pp}} & J_{\mathrm{pd}} & \boldsymbol{J}_{\mathrm{pe}} \\ J_{\mathrm{dp}} & J_{\mathrm{dd}} & \boldsymbol{J}_{\mathrm{de}} \\ \boldsymbol{J}_{\mathrm{ep}} & \boldsymbol{J}_{\mathrm{ed}} & \mathbf{J}_{\mathrm{ee}} \end{bmatrix}\,. \tag{4.88}$$

The individual tangent contributions are, with $\mathbf{I} = \boldsymbol{I} \,\overline{\otimes}\, \boldsymbol{I}$, obtained as

$$J_{\mathrm{pp}} = \frac{\partial r_{\mathrm{p}}}{\partial \lambda_{\mathrm{p}}} = \left[\frac{\Phi_{\mathrm{p}}}{\sqrt{\Phi^2_{\mathrm{p}} + \lambda^2_{\mathrm{p}} + \epsilon}} + 1\right]\,\frac{\partial \Phi_{\mathrm{p}}}{\partial \lambda_{\mathrm{p}}} + \frac{\lambda_{\mathrm{p}}}{\sqrt{\Phi^2_{\mathrm{p}} + \lambda^2_{\mathrm{p}} + \epsilon}} - 1\,, \tag{4.89}$$

$$J_{\mathrm{pd}} = \frac{\partial r_{\mathrm{p}}}{\partial \lambda_{\mathrm{d}}} = \left[\frac{\Phi_{\mathrm{p}}}{\sqrt{\Phi^2_{\mathrm{p}} + \lambda^2_{\mathrm{p}} + \epsilon}} + 1\right]\,\frac{\partial \Phi_{\mathrm{p}}}{\partial \lambda_{\mathrm{d}}}\,, \tag{4.90}$$

$$\boldsymbol{J}_{\mathrm{pe}} = \frac{\partial r_{\mathrm{p}}}{\partial \overline{\boldsymbol{E}}_{\mathrm{e}}} = \left[\frac{\Phi_{\mathrm{p}}}{\sqrt{\Phi^2_{\mathrm{p}} + \lambda^2_{\mathrm{p}} + \epsilon}} + 1\right]\,\overline{\boldsymbol{\nu}}^{\mathrm{eff}}_{\mathrm{p}} : \frac{\partial \overline{\boldsymbol{M}}^{\mathrm{eff}}_{\mathrm{e}}}{\partial \overline{\boldsymbol{E}}_{\mathrm{e}}}\,, \tag{4.91}$$

$$J_{\mathrm{dp}} = \frac{\partial r_{\mathrm{d}}}{\partial \lambda_{\mathrm{p}}} = \left[\frac{\Phi_{\mathrm{d}}}{\sqrt{\Phi^2_{\mathrm{d}} + \lambda^2_{\mathrm{d}} + \epsilon}} + 1\right]\,\frac{\partial \Phi_{\mathrm{d}}}{\partial \lambda_{\mathrm{p}}}\,, \tag{4.92}$$

$$J_{\mathrm{dd}} = \frac{\partial r_{\mathrm{d}}}{\partial \lambda_{\mathrm{d}}} = \left[\frac{\Phi_{\mathrm{d}}}{\sqrt{\Phi^2_{\mathrm{d}} + \lambda^2_{\mathrm{d}} + \epsilon}} + 1\right]\,\frac{\partial \Phi_{\mathrm{d}}}{\partial \lambda_{\mathrm{d}}} + \frac{\lambda_{\mathrm{d}}}{\sqrt{\Phi^2_{\mathrm{d}} + \lambda^2_{\mathrm{d}} + \epsilon}} - 1\,, \tag{4.93}$$

Table 4.1: Algorithmic outline for the anisotropic ductile damage model.

0. given: $\boldsymbol{F}$, ϕ_p, $\nabla_{\boldsymbol{X}}\phi_\mathrm{p}$, ϕ_d, $\nabla_{\boldsymbol{X}}\phi_\mathrm{d}$ and $\boldsymbol{F}_{\mathrm{p},n}^{-1}$, $\boldsymbol{F}_{\mathrm{d},n}$, α_{p_n}, $\alpha_{\mathrm{d}n}$
1. initialise: $i = 0$, $\lambda_\mathrm{p} = 0$, $\lambda_\mathrm{d} = 0$, $\overline{\boldsymbol{E}}_\mathrm{e} = \frac{1}{2}\,\boldsymbol{F}_{\mathrm{d},n}^{\mathrm{t}} \cdot [\boldsymbol{F}_{\mathrm{p},n}^{-\mathrm{t}} \cdot \boldsymbol{C} \cdot \boldsymbol{F}_{\mathrm{p},n}^{-1} - \widehat{\boldsymbol{I}}] \cdot \boldsymbol{F}_{\mathrm{d},n}$, $\boldsymbol{x}^\mathrm{t} = [\lambda_\mathrm{p},\, \lambda_\mathrm{d},\, \overline{\boldsymbol{E}}_\mathrm{e}]$
2. evaluate residuum $\boldsymbol{r}$ and update state variables for given $\boldsymbol{x}$ $\longrightarrow$ see Table 4.2
3. if Newton-Raphson algorithm has converged, i.e. $\|\boldsymbol{r}\| < \mathrm{tol}$, goto 8
4. compute tangent $\boldsymbol{J}$, see Section 4.5.2
5. compute Newton-Raphson increment $\Delta\boldsymbol{x} = -\boldsymbol{J}^{-1} \cdot \boldsymbol{r}$
6. determine step-length a via Armijo-Goldstein
   a) initialise $j = 0$, $a_j = \|\Delta\boldsymbol{x}\|$, search direction $\boldsymbol{s} = \Delta\boldsymbol{x}/a_0$ and $m = c\,\|\boldsymbol{J}^\mathrm{t} \cdot \Delta\boldsymbol{x}\|$
   b) evaluate residuum $\tilde{\boldsymbol{r}}$ for $\tilde{\boldsymbol{x}} = \boldsymbol{x}_i + a_j\,\boldsymbol{s}$
   c) if $\|\boldsymbol{r}\| - \|\tilde{\boldsymbol{r}}\| \geq a_j\,m$ set $a = a_j$ and goto 7
   d) update $a_{j+1} = \tau\,a_j$, $j = j + 1$
   e) if $j > j_\mathrm{max}$ set $a = a_0$ and goto 7 else goto 6b
7. update unknowns $\boldsymbol{x}_{i+1} = \boldsymbol{x}_i + a\,\boldsymbol{s}$, update $i = i + 1$, goto 2
8. compute stresses and driving forces, cf. Section 4.7

$$\boldsymbol{P} = \boldsymbol{F}_\mathrm{e} \cdot \boldsymbol{F}_\mathrm{d} \cdot \overline{\boldsymbol{S}}_\mathrm{e} \cdot \boldsymbol{F}_\mathrm{d}^{\mathrm{t}} \cdot \boldsymbol{F}_\mathrm{p}^{-\mathrm{t}}$$

$$Y_\mathrm{p} = h_\mathrm{p}\,b_\mathrm{p}\,[\phi_\mathrm{p} - \alpha_\mathrm{p}]\,, \qquad \boldsymbol{Y}_\mathrm{p} = h_\mathrm{p}\,b_\mathrm{p}\,c_\mathrm{p}\,\nabla_{\boldsymbol{X}}\phi_\mathrm{p}$$

$$Y_\mathrm{d} = h_\mathrm{d}\,b_\mathrm{d}\,[\phi_\mathrm{d} - \alpha_\mathrm{d}]\,, \qquad \boldsymbol{Y}_\mathrm{d} = h_\mathrm{d}\,b_\mathrm{d}\,c_\mathrm{d}\,\nabla_{\boldsymbol{X}}\phi_\mathrm{d}$$

9. compute tangent moduli $\longrightarrow$ Section 4.8

Table 4.2: Algorithmic outline for the computation of the local residual.

1. compute driving forces

$$\begin{aligned}
\overline{\boldsymbol{S}}_{\mathrm{e}} &= \lambda\,[\overline{\boldsymbol{I}} : \overline{\boldsymbol{E}}_{\mathrm{e}}]\,\overline{\boldsymbol{I}} + 2\,\mu\,\overline{\boldsymbol{E}}_{\mathrm{e}} \\
\overline{\boldsymbol{M}}_{\mathrm{d}} &= -2\,\overline{\boldsymbol{E}}_{\mathrm{e}} \cdot \overline{\boldsymbol{S}}_{\mathrm{e}} \\
\beta_{\mathrm{p}} &= h_{\mathrm{p}}\,\left[\alpha_{\mathrm{p0}} + \alpha_{\mathrm{p}}\right]^{n_{\mathrm{p}}}\,, \quad \alpha_{\mathrm{p}} = \alpha_{\mathrm{p},n} + \Delta t\,\lambda_{\mathrm{p}}\,\sqrt{\tfrac{2}{3}} \\
\beta_{\mathrm{d}} &= h_{\mathrm{d}}\,\left[\alpha_{\mathrm{d0}} + \alpha_{\mathrm{d}}\right]^{n_{\mathrm{d}}}\,, \quad \alpha_{\mathrm{d}} = \alpha_{\mathrm{d},n} + \Delta t\,\lambda_{\mathrm{d}}\,\sqrt{\tfrac{2}{3}}\,f_{\mathrm{dp}}(\alpha_{\mathrm{p}})
\end{aligned}$$

2. compute damage potential Φ_{d}, flow direction $\overline{\boldsymbol{\nu}}_{\mathrm{d}}$ and update of damage deformation gradient $\boldsymbol{F}_{\mathrm{d}}$

$$\begin{aligned}
\Phi_{\mathrm{d}} &= M_{\mathrm{d}}^{\mathrm{eq}} - \sqrt{\tfrac{2}{3}}\,\beta_{\mathrm{d}}\,f_{\mathrm{dp}}(\alpha_{\mathrm{p}})\,, \quad M_{\mathrm{d}}^{\mathrm{eq}} = \sqrt{\tfrac{2}{3}}\,\sqrt{\zeta_{\mathrm{d}}\,\left[\overline{\boldsymbol{I}} : \overline{\boldsymbol{M}}_{\mathrm{d}}\right]^2 + [1-\zeta_{\mathrm{d}}]\,\overline{\boldsymbol{M}}_{\mathrm{d}} : \overline{\boldsymbol{M}}_{\mathrm{d}}} \\
\overline{\boldsymbol{\nu}}_{\mathrm{d}} &= \frac{2}{3\,M_{\mathrm{d}}^{\mathrm{eq}}}\,\left[\zeta_{\mathrm{d}}\,\left[\overline{\boldsymbol{I}} : \overline{\boldsymbol{M}}_{\mathrm{d}}\right]\,\overline{\boldsymbol{I}} + [1-\zeta_{\mathrm{d}}]\,\overline{\boldsymbol{M}}_{\mathrm{d}}^{\mathrm{t}}\right] \\
\boldsymbol{F}_{\mathrm{d},n+1} &= \boldsymbol{F}_{\mathrm{d},n} \cdot \exp\left(\Delta t\,\lambda_{\mathrm{d}}\,\overline{\boldsymbol{\nu}}_{\mathrm{d}}\right)
\end{aligned}$$

3. compute plastic potential Φ_{p}, flow direction $\overline{\boldsymbol{\nu}}_{\mathrm{p}}$ and update of plastic deformation gradient $\boldsymbol{F}_{\mathrm{p}}$

$$\begin{aligned}
\overline{\boldsymbol{M}}_{\mathrm{e}}^{\mathrm{eff}} &= \overline{\boldsymbol{C}}_{\mathrm{ed}} \cdot \overline{\boldsymbol{C}}_{\mathrm{d}}^{-1} \cdot \overline{\boldsymbol{S}}_{\mathrm{e}} \cdot \overline{\boldsymbol{C}}_{\mathrm{d}}^{-1} \\
\Phi_{\mathrm{p}} &= M_{\mathrm{e}}^{\mathrm{eq}} - \sqrt{\tfrac{2}{3}}\,\beta_{\mathrm{p}}\,, \quad M_{\mathrm{e}}^{\mathrm{eq}} = \sqrt{\tfrac{2}{3}}\,\sqrt{\zeta_{\mathrm{p}}\,\left[\overline{\boldsymbol{I}} : \overline{\boldsymbol{M}}_{\mathrm{e}}^{\mathrm{eff}}\right]^2 + [1-\zeta_{\mathrm{p}}]\,\overline{\boldsymbol{M}}_{\mathrm{e}}^{\mathrm{eff}} : \overline{\boldsymbol{M}}_{\mathrm{e}}^{\mathrm{eff}}} \\
\overline{\boldsymbol{\nu}}_{\mathrm{p}}^{\mathrm{eff}} &= \frac{2}{3\,M_{\mathrm{e}}^{\mathrm{eq}}}\,\left[\zeta_{\mathrm{p}}\,\left[\overline{\boldsymbol{I}} : \overline{\boldsymbol{M}}_{\mathrm{e}}^{\mathrm{eff}}\right]\,\overline{\boldsymbol{I}} + [1-\zeta_{\mathrm{p}}]\,\overline{\boldsymbol{M}}_{\mathrm{e}}^{\mathrm{t,eff}}\right] \\
\overline{\boldsymbol{\nu}}_{\mathrm{p}} &= \overline{\boldsymbol{C}}_{\mathrm{ed}}^{-1} \cdot \overline{\boldsymbol{C}}_{\mathrm{d}}^{-1} \cdot \overline{\boldsymbol{C}}_{\mathrm{ed}} \cdot \overline{\boldsymbol{\nu}}_{\mathrm{p}}^{\mathrm{eff}} \cdot \overline{\boldsymbol{C}}_{\mathrm{d}}^{-1} \\
\boldsymbol{F}_{\mathrm{p},n+1}^{-1} &= \boldsymbol{F}_{\mathrm{p},n}^{-1} \cdot \boldsymbol{F}_{\mathrm{d},n} \cdot \exp\left(\Delta t\,\lambda_{\mathrm{d}}\,\overline{\boldsymbol{\nu}}_{\mathrm{d}} - \Delta t\,\lambda_{\mathrm{p}}\,\overline{\boldsymbol{\nu}}_{\mathrm{p}}\right) \cdot \exp\left(-\Delta t\,\lambda_{\mathrm{d}}\,\overline{\boldsymbol{\nu}}_{\mathrm{d}}\right) \cdot \boldsymbol{F}_{\mathrm{d},n}^{-1}
\end{aligned}$$

4. compute residual $\boldsymbol{r} = [r_{\mathrm{p}},\, r_{\mathrm{d}},\, \boldsymbol{R}_{\mathrm{e}}]$ with

$$\begin{aligned}
r_{\mathrm{p}} &= \sqrt{\Phi_{\mathrm{p}}^2 + {\lambda_{\mathrm{p}}}^2 + \epsilon} + \Phi_{\mathrm{p}} - \lambda_{\mathrm{p}} \\
r_{\mathrm{d}} &= \sqrt{\Phi_{\mathrm{d}}^2 + {\lambda_{\mathrm{d}}}^2 + \epsilon} + \Phi_{\mathrm{d}} - \lambda_{\mathrm{d}} \\
\boldsymbol{R}_{\mathrm{e}} &= \overline{\boldsymbol{E}}_{\mathrm{e}} - \frac{1}{2}\,\boldsymbol{F}_{\mathrm{d}}^{\mathrm{t}} \cdot \left[\boldsymbol{F}_{\mathrm{p}}^{-\mathrm{t}} \cdot \boldsymbol{C} \cdot \boldsymbol{F}_{\mathrm{p}}^{-1} - \widehat{\boldsymbol{I}}\right] \cdot \boldsymbol{F}_{\mathrm{d}}
\end{aligned}$$

$$\boldsymbol{J}_{\mathrm{de}} = \frac{\partial r_{\mathrm{d}}}{\partial \overline{\boldsymbol{E}}_{\mathrm{e}}} = \left[\frac{\Phi_{\mathrm{d}}}{\sqrt{\Phi_{\mathrm{d}}^2 + \lambda_{\mathrm{d}}^2 + \epsilon}} + 1 \right] \overline{\boldsymbol{\nu}}_{\mathrm{d}} : \frac{\partial \overline{\boldsymbol{M}}_{\mathrm{d}}}{\partial \overline{\boldsymbol{E}}_{\mathrm{e}}} \,, \tag{4.94}$$

$$\boldsymbol{J}_{\mathrm{ep}} = \frac{\partial \boldsymbol{R}_{\mathrm{e}}}{\partial \lambda_{\mathrm{p}}} = \frac{\partial \boldsymbol{R}_{\mathrm{e}}}{\partial \boldsymbol{F}_{\mathrm{p}}^{-1}} : \frac{\partial \boldsymbol{F}_{\mathrm{p}}^{-1}}{\partial \lambda_{\mathrm{p}}} \,, \tag{4.95}$$

$$\boldsymbol{J}_{\mathrm{ed}} = \frac{\partial \boldsymbol{R}_{\mathrm{e}}}{\partial \lambda_{\mathrm{d}}} = \frac{\partial \boldsymbol{R}_{\mathrm{e}}}{\partial \boldsymbol{F}_{\mathrm{p}}^{-1}} : \frac{\partial \boldsymbol{F}_{\mathrm{p}}^{-1}}{\partial \lambda_{\mathrm{d}}} + \frac{\partial \boldsymbol{R}_{\mathrm{e}}}{\partial \boldsymbol{F}_{\mathrm{d}}} : \frac{\partial \boldsymbol{F}_{\mathrm{d}}}{\partial \lambda_{\mathrm{d}}} \,, \tag{4.96}$$

$$\mathbf{J}_{\mathrm{ee}} = \frac{\partial \boldsymbol{R}_{\mathrm{e}}}{\partial \overline{\boldsymbol{E}}_{\mathrm{e}}} = \mathbf{I} + \frac{\partial \boldsymbol{R}_{\mathrm{e}}}{\partial \boldsymbol{F}_{\mathrm{p}}^{-1}} : \frac{\partial \boldsymbol{F}_{\mathrm{p}}^{-1}}{\partial \overline{\boldsymbol{E}}_{\mathrm{e}}} + \frac{\partial \boldsymbol{R}_{\mathrm{e}}}{\partial \boldsymbol{F}_{\mathrm{d}}} : \frac{\partial \boldsymbol{F}_{\mathrm{d}}}{\partial \overline{\boldsymbol{E}}_{\mathrm{e}}} \,. \tag{4.97}$$

The occurring partial derivatives are given by

$$\frac{\partial \Phi_{\mathrm{p}}}{\partial \lambda_{\mathrm{p}}} = -\ \frac{2}{3} \Delta t \, h_{\mathrm{p}} \left[n_{\mathrm{p}} \left[\alpha_{\mathrm{p}0} + \alpha_{\mathrm{p}} \right]^{n_{\mathrm{p}}-1} + b_{\mathrm{p}} \right] \,, \tag{4.98}$$

$$\frac{\partial \Phi_{\mathrm{p}}}{\partial \lambda_{\mathrm{d}}} = \overline{\boldsymbol{\nu}}_{\mathrm{p}}^{\mathrm{eff}} : \frac{\partial \overline{\boldsymbol{M}}_{\mathrm{e}}^{\mathrm{eff}}}{\partial \boldsymbol{F}_{\mathrm{d}}} : \frac{\partial \boldsymbol{F}_{\mathrm{d}}}{\partial \lambda_{\mathrm{d}}} \,, \tag{4.99}$$

$$\frac{\partial \Phi_{\mathrm{d}}}{\partial \lambda_{\mathrm{p}}} = -\ \frac{2}{3} \Delta t \, \lambda_{\mathrm{d}} \, f_{\mathrm{dp}}(\alpha_{\mathrm{p}}) \, h_{\mathrm{d}} \left[n_{\mathrm{d}} \left[\alpha_{\mathrm{d}0} + \alpha_{\mathrm{d}} \right]^{n_{\mathrm{d}}-1} + b_{\mathrm{d}} \right] - \frac{2}{3} \Delta t \, \beta_{\mathrm{d}} \, f'_{\mathrm{dp}}(\alpha_{\mathrm{p}}) \,, \tag{4.100}$$

$$\frac{\partial \Phi_{\mathrm{d}}}{\partial \lambda_{\mathrm{d}}} = -\ \frac{2}{3} \Delta t \, f_{\mathrm{dp}}^2(\alpha_{\mathrm{p}}) \, h_{\mathrm{d}} \left[n_{\mathrm{d}} \left[\alpha_{\mathrm{d}0} + \alpha_{\mathrm{d}} \right]^{n_{\mathrm{d}}-1} + b_{\mathrm{d}} \right] \,, \tag{4.101}$$

$$\frac{\partial \boldsymbol{R}_{\mathrm{e}}}{\partial \boldsymbol{F}_{\mathrm{p}}^{-1}} = -\ \frac{1}{2} \left[\boldsymbol{F}_{\mathrm{d}}^{\mathrm{t}} \underline{\otimes} \boldsymbol{F}_{\mathrm{d}}^{\mathrm{t}} \cdot \boldsymbol{F}_{\mathrm{p}}^{-\mathrm{t}} \cdot \boldsymbol{C} + \boldsymbol{F}_{\mathrm{d}}^{\mathrm{t}} \cdot \boldsymbol{F}_{\mathrm{p}}^{-\mathrm{t}} \cdot \boldsymbol{C} \overline{\otimes} \boldsymbol{F}_{\mathrm{d}}^{\mathrm{t}} \right] \,, \tag{4.102}$$

$$\frac{\partial \boldsymbol{R}_{\mathrm{e}}}{\partial \boldsymbol{F}_{\mathrm{d}}} = -\ \frac{1}{2} \left[\boldsymbol{F}_{\mathrm{d}}^{\mathrm{t}} \cdot \widehat{\boldsymbol{E}}_{\mathrm{e}} \overline{\otimes} \boldsymbol{I} + \boldsymbol{I} \underline{\otimes} \boldsymbol{F}_{\mathrm{d}}^{\mathrm{t}} \cdot \widehat{\boldsymbol{E}}_{\mathrm{e}} \right] \,, \quad \text{with} \quad \widehat{\boldsymbol{E}}_{\mathrm{e}} = \boldsymbol{F}_{\mathrm{p}}^{-\mathrm{t}} \cdot \boldsymbol{C} \cdot \boldsymbol{F}_{\mathrm{p}}^{-1} - \boldsymbol{I} \,, \tag{4.103}$$

$$\frac{\partial \boldsymbol{F}_{\mathrm{p}}^{-1}}{\partial \lambda_{\mathrm{p}}} = -\ \Delta t \, \boldsymbol{F}_{\mathrm{p}n}^{-1} \cdot \left[\boldsymbol{F}_{\mathrm{d}n} \overline{\otimes} \boldsymbol{F}_{\mathrm{d}}^{-\mathrm{t}} \right] : \frac{\partial \exp(\overline{\boldsymbol{L}}_{\mathrm{d}} - \overline{\boldsymbol{L}}_{\mathrm{p}})}{\partial \overline{\boldsymbol{L}}_{\mathrm{d}} - \overline{\boldsymbol{L}}_{\mathrm{p}}} : \overline{\boldsymbol{\nu}}_{\mathrm{p}} \,, \tag{4.104}$$

$$\begin{aligned} \frac{\partial \boldsymbol{F}_{\mathrm{p}}^{-1}}{\partial \lambda_{\mathrm{d}}} = &-\ \Delta t \, \boldsymbol{F}_{\mathrm{p}n}^{-1} \cdot \left[\boldsymbol{F}_{\mathrm{d}n} \overline{\otimes} \boldsymbol{F}_{\mathrm{d}}^{-\mathrm{t}} \right] : \frac{\partial \exp(\overline{\boldsymbol{L}}_{\mathrm{d}} - \overline{\boldsymbol{L}}_{\mathrm{p}})}{\partial \overline{\boldsymbol{L}}_{\mathrm{d}} - \overline{\boldsymbol{L}}_{\mathrm{p}}} : \left[\lambda_{\mathrm{p}} \frac{\partial \overline{\boldsymbol{\nu}}_{\mathrm{p}}}{\partial \lambda_{\mathrm{d}}} - \overline{\boldsymbol{\nu}}_{\mathrm{d}} \right] \\ &+\ \boldsymbol{F}_{\mathrm{p}n}^{-1} \cdot \boldsymbol{F}_{\mathrm{d}n} \cdot \exp(\overline{\boldsymbol{L}}_{\mathrm{d}} - \overline{\boldsymbol{L}}_{\mathrm{p}}) \cdot \boldsymbol{F}_{\mathrm{d}}^{-1} \overline{\otimes} \boldsymbol{F}_{\mathrm{d}}^{-\mathrm{t}} : \frac{\partial \boldsymbol{F}_{\mathrm{d}}}{\partial \lambda_{\mathrm{d}}} \,, \end{aligned} \tag{4.105}$$

$$\begin{aligned} \frac{\partial \boldsymbol{F}_{\mathrm{p}}^{-1}}{\partial \overline{\boldsymbol{E}}_{\mathrm{e}}} = &-\ \Delta t \, \boldsymbol{F}_{\mathrm{p}n}^{-1} \cdot \left[\boldsymbol{F}_{\mathrm{d}n} \overline{\otimes} \boldsymbol{F}_{\mathrm{d}}^{-\mathrm{t}} \right] : \frac{\partial \exp(\overline{\boldsymbol{L}}_{\mathrm{d}} - \overline{\boldsymbol{L}}_{\mathrm{p}})}{\partial \overline{\boldsymbol{L}}_{\mathrm{d}} - \overline{\boldsymbol{L}}_{\mathrm{p}}} : \left[\lambda_{\mathrm{p}} \frac{\partial \overline{\boldsymbol{\nu}}_{\mathrm{p}}}{\partial \overline{\boldsymbol{E}}_{\mathrm{e}}} - \lambda_{\mathrm{d}} \frac{\partial \overline{\boldsymbol{\nu}}_{\mathrm{d}}}{\partial \overline{\boldsymbol{M}}_{\mathrm{d}}} : \frac{\partial \overline{\boldsymbol{M}}_{\mathrm{d}}}{\partial \overline{\boldsymbol{E}}_{\mathrm{e}}} \right] \\ &+\ \boldsymbol{F}_{\mathrm{p}n}^{-1} \cdot \boldsymbol{F}_{\mathrm{d}n} \cdot \exp(\overline{\boldsymbol{L}}_{\mathrm{d}} - \overline{\boldsymbol{L}}_{\mathrm{p}}) \cdot \boldsymbol{F}_{\mathrm{d}}^{-1} \overline{\otimes} \boldsymbol{F}_{\mathrm{d}}^{-\mathrm{t}} : \frac{\partial \boldsymbol{F}_{\mathrm{d}}}{\partial \overline{\boldsymbol{E}}_{\mathrm{e}}} \,, \end{aligned} \tag{4.106}$$

$$\frac{\partial \boldsymbol{F}_{\mathrm{d}}}{\partial \lambda_{\mathrm{d}}} = \Delta t \, \boldsymbol{F}_{\mathrm{d}n} \cdot \frac{\partial \exp(\overline{\boldsymbol{L}}_{\mathrm{d}})}{\partial \overline{\boldsymbol{L}}_{\mathrm{d}}} : \overline{\boldsymbol{\nu}}_{\mathrm{d}} \,, \tag{4.107}$$

$$\frac{\partial \boldsymbol{F}_{\mathrm{d}}}{\partial \overline{\boldsymbol{E}}_{\mathrm{e}}} = \Delta t \, \lambda_{\mathrm{d}} \, \boldsymbol{F}_{\mathrm{d}n} \cdot \frac{\partial \exp(\overline{\boldsymbol{L}}_{\mathrm{d}})}{\partial \overline{\boldsymbol{L}}_{\mathrm{d}}} : \frac{\partial \overline{\boldsymbol{\nu}}_{\mathrm{d}}}{\partial \overline{\boldsymbol{M}}_{\mathrm{d}}} : \frac{\partial \overline{\boldsymbol{M}}_{\mathrm{d}}}{\partial \overline{\boldsymbol{E}}_{\mathrm{e}}} \,. \tag{4.108}$$

The derivative of the exponent of a tensor is described in Appendix A and the derivatives of the stresses and return directions are obtained as

$$\frac{\partial \overline{\boldsymbol{M}}_{\mathrm{e}}^{\mathrm{eff}}}{\partial \boldsymbol{F}_{\mathrm{d}}} = \left[\boldsymbol{I} \,\overline{\otimes}\, \overline{\boldsymbol{C}}_{\mathrm{d}}^{-1} \cdot \overline{\boldsymbol{S}}_{\mathrm{e}}^{\mathrm{t}} \cdot \overline{\boldsymbol{C}}_{\mathrm{d}}^{-1}\right] : \left[\boldsymbol{F}_{\mathrm{d}}^{\mathrm{t}} \,\overline{\otimes}\, \boldsymbol{I} + \boldsymbol{I} \,\underline{\otimes}\, \boldsymbol{F}_{\mathrm{d}}^{\mathrm{t}}\right] \tag{4.109}$$

$$- \overline{\boldsymbol{C}}_{\mathrm{ed}} \cdot \left[\overline{\boldsymbol{C}}_{\mathrm{d}}^{-1} \cdot \overline{\boldsymbol{S}}_{\mathrm{e}} \,\underline{\otimes}\, \boldsymbol{I} + \boldsymbol{I} \,\underline{\otimes}\, \overline{\boldsymbol{C}}_{\mathrm{d}}^{-1} \cdot \overline{\boldsymbol{S}}_{\mathrm{e}}^{\mathrm{t}}\right] : \overline{\boldsymbol{C}}_{\mathrm{d}}^{-1} \,\underline{\overline{\otimes}}\, \overline{\boldsymbol{C}}_{\mathrm{d}}^{-1} : \left[\boldsymbol{F}_{\mathrm{d}}^{\mathrm{t}} \,\overline{\otimes}\, \boldsymbol{I} + \boldsymbol{I} \,\underline{\otimes}\, \boldsymbol{F}_{\mathrm{d}}^{\mathrm{t}}\right], \tag{4.110}$$

$$\frac{\partial \overline{\boldsymbol{M}}_{\mathrm{e}}^{\mathrm{eff}}}{\partial \overline{\boldsymbol{E}}_{\mathrm{e}}} = 2\,\boldsymbol{I} \,\overline{\otimes}\, \overline{\boldsymbol{C}}_{\mathrm{d}}^{-1} \cdot \overline{\boldsymbol{S}}_{\mathrm{e}}^{\mathrm{t}} \cdot \overline{\boldsymbol{C}}_{\mathrm{d}}^{-1} + \left[\overline{\boldsymbol{C}}_{\mathrm{ed}} \cdot \overline{\boldsymbol{C}}_{\mathrm{d}}^{-1} \,\overline{\otimes}\, \overline{\boldsymbol{C}}_{\mathrm{d}}^{-1}\right] : \frac{\partial \overline{\boldsymbol{S}}_{\mathrm{e}}}{\partial \overline{\boldsymbol{E}}_{\mathrm{e}}} + \frac{\partial \overline{\boldsymbol{M}}_{\mathrm{e}}^{\mathrm{eff}}}{\partial \boldsymbol{F}_{\mathrm{d}}} : \frac{\partial \boldsymbol{F}_{\mathrm{d}}}{\partial \overline{\boldsymbol{E}}_{\mathrm{e}}}, \tag{4.111}$$

$$\frac{\partial \overline{\boldsymbol{S}}_{\mathrm{e}}}{\partial \overline{\boldsymbol{E}}_{\mathrm{e}}} = [K - \frac{2}{3}G]\,\boldsymbol{I} \otimes \boldsymbol{I} + 2\,G\,\mathbf{I}, \tag{4.112}$$

$$\frac{\partial \overline{\boldsymbol{M}}_{\mathrm{d}}}{\partial \overline{\boldsymbol{E}}_{\mathrm{e}}} = -[\boldsymbol{I} \,\overline{\otimes}\, \overline{\boldsymbol{E}}_{\mathrm{e}}] : \frac{\partial \overline{\boldsymbol{S}}_{\mathrm{e}}}{\partial \overline{\boldsymbol{E}}_{\mathrm{e}}} + \overline{\boldsymbol{S}}_{\mathrm{e}} \,\overline{\otimes}\, \boldsymbol{I}, \tag{4.113}$$

$$\frac{\partial \overline{\boldsymbol{\nu}}_{\mathrm{p}}^{\mathrm{eff}}}{\partial \overline{\boldsymbol{M}}_{\mathrm{e}}^{\mathrm{eff}}} = \frac{1}{M_{\mathrm{e}}^{\mathrm{eq}}} \left[\frac{2}{3}\,\zeta_{\mathrm{p}}\,\boldsymbol{I} \otimes \boldsymbol{I} + \frac{2}{3}\,[1-\zeta_{\mathrm{p}}]\,\boldsymbol{I} \,\underline{\otimes}\, \boldsymbol{I} - \overline{\boldsymbol{\nu}}_{\mathrm{p}}^{\mathrm{eff}} \otimes \overline{\boldsymbol{\nu}}_{\mathrm{p}}^{\mathrm{eff}}\right], \tag{4.114}$$

$$\frac{\partial \overline{\boldsymbol{\nu}}_{\mathrm{d}}}{\partial \overline{\boldsymbol{M}}_{\mathrm{d}}} = \frac{1}{M_{\mathrm{d}}^{\mathrm{eq}}} \left[\frac{2}{3}\,\zeta_{\mathrm{d}}\,\boldsymbol{I} \otimes \boldsymbol{I} + \frac{2}{3}\,[1-\zeta_{\mathrm{d}}]\,\boldsymbol{I} \,\underline{\otimes}\, \boldsymbol{I} - \overline{\boldsymbol{\nu}}_{\mathrm{d}} \otimes \overline{\boldsymbol{\nu}}_{\mathrm{d}}\right], \tag{4.115}$$

$$\frac{\partial \overline{\boldsymbol{\nu}}_{\mathrm{p}}}{\partial \overline{\boldsymbol{C}}_{\mathrm{ed}}} = -\left[\boldsymbol{I} \,\overline{\otimes}\, \overline{\boldsymbol{C}}_{\mathrm{d}}^{-1} \cdot \overline{\boldsymbol{\nu}}_{\mathrm{p}}^{\mathrm{eff,t}} \cdot \overline{\boldsymbol{C}}_{\mathrm{ed}}^{\mathrm{t}} \cdot \overline{\boldsymbol{C}}_{\mathrm{d}}^{-1}\right] : \overline{\boldsymbol{C}}_{\mathrm{ed}}^{-1} \,\overline{\otimes}\, \overline{\boldsymbol{C}}_{\mathrm{ed}}^{-\mathrm{t}} + \overline{\boldsymbol{C}}_{\mathrm{ed}}^{-1} \cdot \overline{\boldsymbol{C}}_{\mathrm{d}}^{-1} \,\overline{\otimes}\, \overline{\boldsymbol{C}}_{\mathrm{d}}^{-1} \cdot \overline{\boldsymbol{\nu}}_{\mathrm{p}}^{\mathrm{eff,t}}, \tag{4.116}$$

$$\begin{aligned}\frac{\partial \overline{\boldsymbol{\nu}}_{\mathrm{p}}}{\partial \lambda_{\mathrm{d}}} = {} & \left[\left[-\overline{\boldsymbol{C}}_{\mathrm{ed}}^{-1} \cdot \left[\boldsymbol{I} \,\underline{\overline{\otimes}}\, \overline{\boldsymbol{C}}_{\mathrm{d}}^{-1} \cdot \overline{\boldsymbol{\nu}}_{\mathrm{p}}^{\mathrm{eff,t}} \cdot \overline{\boldsymbol{C}}_{\mathrm{ed}}^{\mathrm{t}} + \overline{\boldsymbol{C}}_{\mathrm{d}}^{-1} \cdot \overline{\boldsymbol{C}}_{\mathrm{ed}} \cdot \overline{\boldsymbol{\nu}}_{\mathrm{p}}^{\mathrm{eff}} \,\underline{\overline{\otimes}}\, \boldsymbol{I}\right] : \left[\overline{\boldsymbol{C}}_{\mathrm{d}}^{-1} \,\underline{\overline{\otimes}}\, \overline{\boldsymbol{C}}_{\mathrm{d}}^{-1}\right]\right. \\ & \left. + \frac{\partial \overline{\boldsymbol{\nu}}_{\mathrm{p}}}{\partial \overline{\boldsymbol{C}}_{\mathrm{ed}}}\right] : \left[\boldsymbol{F}_{\mathrm{d}}^{\mathrm{t}} \,\overline{\otimes}\, \boldsymbol{I} + \boldsymbol{I} \,\underline{\otimes}\, \boldsymbol{F}_{\mathrm{d}}^{\mathrm{t}}\right] \\ & + \left[\overline{\boldsymbol{C}}_{\mathrm{ed}}^{-1} \cdot \overline{\boldsymbol{C}}_{\mathrm{d}}^{-1} \cdot \overline{\boldsymbol{C}}_{\mathrm{ed}} \,\overline{\otimes}\, \overline{\boldsymbol{C}}_{\mathrm{d}}^{-1}\right] : \frac{\partial \overline{\boldsymbol{\nu}}_{\mathrm{p}}^{\mathrm{eff}}}{\partial \overline{\boldsymbol{M}}_{\mathrm{e}}^{\mathrm{eff}}} : \frac{\partial \overline{\boldsymbol{M}}_{\mathrm{e}}^{\mathrm{eff}}}{\partial \boldsymbol{F}_{\mathrm{d}}} : \frac{\partial \boldsymbol{F}_{\mathrm{d}}}{\partial \lambda_{\mathrm{d}}},\end{aligned} \tag{4.117}$$

$$\begin{aligned}\frac{\partial \overline{\boldsymbol{\nu}}_{\mathrm{p}}}{\partial \overline{\boldsymbol{E}}_{\mathrm{e}}} = {} & \frac{\partial \overline{\boldsymbol{\nu}}_{\mathrm{p}}}{\partial \overline{\boldsymbol{C}}_{\mathrm{ed}}} : \left[2\,\mathbf{I} + \left[\boldsymbol{F}_{\mathrm{d}}^{\mathrm{t}} \,\overline{\otimes}\, \boldsymbol{I} + \boldsymbol{I} \,\underline{\otimes}\, \boldsymbol{F}_{\mathrm{d}}^{\mathrm{t}}\right] : \frac{\partial \boldsymbol{F}_{\mathrm{d}}}{\partial \overline{\boldsymbol{E}}_{\mathrm{e}}}\right] \\ & - \overline{\boldsymbol{C}}_{\mathrm{ed}}^{-1} \cdot \left[\boldsymbol{I} \,\underline{\overline{\otimes}}\, \overline{\boldsymbol{C}}_{\mathrm{d}}^{-1} \cdot \overline{\boldsymbol{\nu}}_{\mathrm{p}}^{\mathrm{eff,t}} \cdot \overline{\boldsymbol{C}}_{\mathrm{ed}}^{\mathrm{t}} + \overline{\boldsymbol{C}}_{\mathrm{d}}^{-1} \cdot \overline{\boldsymbol{C}}_{\mathrm{ed}} \cdot \overline{\boldsymbol{\nu}}_{\mathrm{p}}^{\mathrm{eff}} \,\underline{\overline{\otimes}}\, \boldsymbol{I}\right] : \frac{\partial \boldsymbol{F}_{\mathrm{d}}}{\partial \overline{\boldsymbol{E}}_{\mathrm{e}}} \\ & + \left[\overline{\boldsymbol{C}}_{\mathrm{ed}}^{-1} \cdot \overline{\boldsymbol{C}}_{\mathrm{d}}^{-1} \cdot \overline{\boldsymbol{C}}_{\mathrm{ed}} \,\overline{\otimes}\, \overline{\boldsymbol{C}}_{\mathrm{d}}^{-1}\right] : \frac{\partial \overline{\boldsymbol{\nu}}_{\mathrm{p}}^{\mathrm{eff}}}{\partial \overline{\boldsymbol{M}}_{\mathrm{e}}^{\mathrm{eff}}} : \frac{\partial \overline{\boldsymbol{M}}_{\mathrm{e}}^{\mathrm{eff}}}{\partial \overline{\boldsymbol{E}}_{\mathrm{e}}}.\end{aligned} \tag{4.118}$$

4.6 Specific choice of non-local energy

From the multitude of proposed formulations to regularise anisotropic damage, this contribution follows the approach in [63], i.e. anisotropic damage is regularised in a numerically efficient way by coupling the non-local damage variable to the (scalar) damage hardening variable α_d. Analogously, the non-local plasticity variable ϕ_p is coupled to plastic proportional hardening α_p, as the non-linear hardening approach itself may lead to localisation, see Section 4.10.3. Alternative choices for the non-local variables are briefly discussed in Remark 13.

Remark 13 *The regularisation approach pursued in this work uses two non-local fields to regularise damage and plasticity. Solely regularising damage does not seem to be sufficient for this model, see Section 4.10.4. Alternatively, regularisation approaches with only one non-local field variable could be analysed, where the non-local field is coupled to some aggregated inelastic quantity, e.g. to a combination of damage and plastic hardening, $\alpha_\mathrm{p} + \alpha_\mathrm{d}$, or where the non-local field is coupled to some equivalent strain ε^eq, e.g. $\varepsilon^\mathrm{eq} = \|\overline{\boldsymbol{E}}_\mathrm{p}\|$. It is important that this single non-local field variable is coupled to a quantity which is affected by damage as well as by plasticity.*

The coupling energy contribution Ψ^cpl is set up analogously for both damage and plasticity, as

$$\Psi^\mathrm{cpl}(\alpha_\mathrm{p},\, \phi_\mathrm{p},\, \alpha_\mathrm{d},\, \phi_\mathrm{d}) = \frac{1}{2}\, h_\mathrm{p}\, b_\mathrm{p}\, \left[\phi_\mathrm{p} - \alpha_\mathrm{p}\right]^2 + \frac{1}{2}\, h_\mathrm{d}\, b_\mathrm{d}\, \left[\phi_\mathrm{d} - \alpha_\mathrm{d}\right]^2 \,, \tag{4.119}$$

where b_p and b_d are penalty-type parameters controlling the 'stiffness' of the coupling. The hardening moduli h_p and h_d have been added to scale the contributions to their local counter parts in the hardening stresses, cf. (4.121) and (4.122). The gradients of the non-local variables enter the formulation by means of the gradient energy contribution

$$\Psi^\mathrm{grd}(\nabla_{\boldsymbol{X}}\phi_\mathrm{p},\, \nabla_{\boldsymbol{X}}\phi_\mathrm{d}) = \frac{1}{2}\, h_\mathrm{p}\, b_\mathrm{p}\, c_\mathrm{p}\, \nabla_{\boldsymbol{X}}\phi_\mathrm{p} \cdot \nabla_{\boldsymbol{X}}\phi_\mathrm{p} + \frac{1}{2}\, h_\mathrm{d}\, b_\mathrm{d}\, c_\mathrm{d}\, \nabla_{\boldsymbol{X}}\phi_\mathrm{d} \cdot \nabla_{\boldsymbol{X}}\phi_\mathrm{d} \,, \tag{4.120}$$

where each contribution is scaled according to its coupling counterpart, and where c_p and c_d are then added to weight the influence of the gradients compared to the coupling term in order to control the width of the localisation zone. As a result of these energies, non-local contributions to the hardening stresses (4.38) and (4.39) occur, namely

$$\beta_\mathrm{p} = \beta_\mathrm{p}^\mathrm{loc} + h_\mathrm{p}\, b_\mathrm{p}\, \left[\alpha_\mathrm{p} - \phi_\mathrm{p}\right] \,, \tag{4.121}$$

$$\beta_\mathrm{d} = \beta_\mathrm{d}^\mathrm{loc} + h_\mathrm{d}\, b_\mathrm{d}\, \left[\alpha_\mathrm{d} - \phi_\mathrm{d}\right] \,. \tag{4.122}$$

Furthermore, the additional volume and flux contributions can be straightforwardly computed to

$$\begin{aligned} Y_{\mathrm{p}} &= h_{\mathrm{p}}\, b_{\mathrm{p}}\, [\phi_{\mathrm{p}} - \alpha_{\mathrm{p}}] \,, \\ Y_{\mathrm{d}} &= h_{\mathrm{d}}\, b_{\mathrm{d}}\, [\phi_{\mathrm{d}} - \alpha_{\mathrm{d}}] \,, \\ \boldsymbol{Y}_{\mathrm{p}} &= h_{\mathrm{p}}\, b_{\mathrm{p}}\, c_{\mathrm{p}}\, \nabla_{\boldsymbol{X}} \phi_{\mathrm{p}} \,, \\ \boldsymbol{Y}_{\mathrm{d}} &= h_{\mathrm{d}}\, b_{\mathrm{d}}\, c_{\mathrm{d}}\, \nabla_{\boldsymbol{X}} \phi_{\mathrm{d}} \,. \end{aligned} \tag{4.123}$$

4.7 Stresses and driving forces for the Finite Element formulation

The local problem is formulated in terms of the Piola-Kirchhoff-stresses $\boldsymbol{S}$ and the right Cauchy-Green tensor $\boldsymbol{C}$, while the derived FE-formulation uses Piola-stresses $\boldsymbol{P}$ and the deformation gradient $\boldsymbol{F}$. Conversion between both formulations is straightforwardly obtained as

$$\boldsymbol{P} = \boldsymbol{F} \cdot \boldsymbol{S} \,, \tag{4.124}$$

$$\boldsymbol{S} = \boldsymbol{F}_{\mathrm{p}}^{-1} \cdot \widehat{\boldsymbol{S}}_{\mathrm{e}} \cdot \boldsymbol{F}_{\mathrm{p}}^{-\mathrm{t}} \,, \tag{4.125}$$

$$\widehat{\boldsymbol{S}}_{\mathrm{e}} = \boldsymbol{F}_{\mathrm{d}} \cdot \overline{\boldsymbol{S}}_{\mathrm{e}} \cdot \boldsymbol{F}_{\mathrm{d}}^{\mathrm{t}} \,. \tag{4.126}$$

The aggregated non-local field variable $\boldsymbol{\phi}$, cf. Section 2.2, aggregates the non-local plastic variable ϕ_{p} and the non-local damage variable ϕ_{d} and, analogously, the aggregated driving forces, $\boldsymbol{Y}$ and $\boldsymbol{Y}_{\mathrm{grd}}$, aggregate the corresponding plastic and damage contributions, i.e.

$$\boldsymbol{\phi} = \begin{bmatrix} \phi_{\mathrm{p}} \\ \phi_{\mathrm{d}} \end{bmatrix} \,, \qquad \boldsymbol{Y} = \begin{bmatrix} Y_{\mathrm{p}} \\ Y_{\mathrm{d}} \end{bmatrix} \,, \qquad \boldsymbol{Y}_{\mathrm{grd}} = \begin{bmatrix} \boldsymbol{Y}_{\mathrm{p}} \\ \boldsymbol{Y}_{\mathrm{d}} \end{bmatrix} \,. \tag{4.127}$$

The residuals (2.16) of the Finite Element method can now be computed and the contributions to the global tangent will be given next.

4.8 Global tangent contributions for the Finite Element formulation

The aggregated stiffness contributions related to the aggregated non-local field variable $\boldsymbol{\phi}$, see (2.19)-(2.22), are given by

$$\frac{\mathrm{d}\boldsymbol{P}}{\mathrm{d}\boldsymbol{\phi}} = \begin{bmatrix} \frac{\mathrm{d}\boldsymbol{P}}{\mathrm{d}\phi_{\mathrm{p}}} \\ \frac{\mathrm{d}\boldsymbol{P}}{\mathrm{d}\phi_{\mathrm{d}}} \end{bmatrix} \,, \qquad \frac{\mathrm{d}\boldsymbol{Y}}{\mathrm{d}\boldsymbol{F}} = \begin{bmatrix} \frac{\mathrm{d}Y_{\mathrm{p}}}{\mathrm{d}\boldsymbol{F}} \\ \frac{\mathrm{d}Y_{\mathrm{d}}}{\mathrm{d}\boldsymbol{F}} \end{bmatrix} \,, \tag{4.128}$$

and

$$\frac{\mathrm{d}\boldsymbol{Y}}{\mathrm{d}\boldsymbol{\phi}} = \begin{bmatrix} \frac{\mathrm{d}Y_\mathrm{p}}{\mathrm{d}\phi_\mathrm{p}} & \frac{\mathrm{d}Y_\mathrm{p}}{\mathrm{d}\phi_\mathrm{d}} \\ \frac{\mathrm{d}Y_\mathrm{d}}{\mathrm{d}\phi_\mathrm{p}} & \frac{\mathrm{d}Y_\mathrm{d}}{\mathrm{d}\phi_\mathrm{d}} \end{bmatrix}, \qquad \frac{\mathrm{d}\boldsymbol{Y}_{\,\mathrm{grd}}}{\mathrm{d}\nabla_{\boldsymbol{X}}\boldsymbol{\phi}} = \begin{bmatrix} \frac{\mathrm{d}\boldsymbol{Y}_\mathrm{p}}{\mathrm{d}\nabla_{\boldsymbol{X}}\phi_\mathrm{p}} & \frac{\mathrm{d}\boldsymbol{Y}_\mathrm{p}}{\mathrm{d}\nabla_{\boldsymbol{X}}\phi_\mathrm{d}} \\ \frac{\mathrm{d}\boldsymbol{Y}_\mathrm{d}}{\mathrm{d}\nabla_{\boldsymbol{X}}\phi_\mathrm{p}} & \frac{\mathrm{d}\boldsymbol{Y}_\mathrm{d}}{\mathrm{d}\nabla_{\boldsymbol{X}}\phi_\mathrm{d}} \end{bmatrix}. \tag{4.129}$$

Since at material point level the model is formulated in terms of the right Cauchy-Green tensor $\boldsymbol{C}$, derivatives need to be transformed, i.e.

$$\frac{\mathrm{d}\boldsymbol{P}}{\mathrm{d}\boldsymbol{F}} = \boldsymbol{F}\cdot\frac{\mathrm{d}\boldsymbol{S}}{\mathrm{d}\boldsymbol{C}} : \left[\boldsymbol{I}\underline{\otimes}\boldsymbol{F}^\mathrm{t} + \boldsymbol{F}^\mathrm{t}\overline{\otimes}\boldsymbol{I}\right] + \boldsymbol{I}\overline{\otimes}\boldsymbol{S}\,, \tag{4.130}$$

$$\frac{\mathrm{d}\boldsymbol{P}}{\mathrm{d}\phi_\mathrm{p}} = \boldsymbol{F}\cdot\frac{\mathrm{d}\boldsymbol{S}}{\mathrm{d}\phi_\mathrm{p}}\,, \tag{4.131}$$

$$\frac{\mathrm{d}\boldsymbol{P}}{\mathrm{d}\phi_\mathrm{d}} = \boldsymbol{F}\cdot\frac{\mathrm{d}\boldsymbol{S}}{\mathrm{d}\phi_\mathrm{d}}\,, \tag{4.132}$$

$$\frac{\mathrm{d}Y_\mathrm{p}}{\mathrm{d}\boldsymbol{F}} = \frac{\mathrm{d}Y_\mathrm{p}}{\mathrm{d}\boldsymbol{C}} : \left[\boldsymbol{I}\underline{\otimes}\boldsymbol{F}^\mathrm{t} + \boldsymbol{F}^\mathrm{t}\overline{\otimes}\boldsymbol{I}\right]\,, \tag{4.133}$$

$$\frac{\mathrm{d}Y_\mathrm{d}}{\mathrm{d}\boldsymbol{F}} = \frac{\mathrm{d}Y_\mathrm{d}}{\mathrm{d}\boldsymbol{C}} : \left[\boldsymbol{I}\underline{\otimes}\boldsymbol{F}^\mathrm{t} + \boldsymbol{F}^\mathrm{t}\overline{\otimes}\boldsymbol{I}\right]\,. \tag{4.134}$$

The global tangent contributions can be obtained by making use of the implicit function theorem. The derivative of the iteratively determined quantities $\boldsymbol{x} = \left[\lambda_\mathrm{p},\, \lambda_\mathrm{d},\, \overline{\boldsymbol{E}}_\mathrm{e}\right]$ with respect to the right Cauchy-Green tensor $\boldsymbol{C}$ as well as to the non-local field variables ϕ_p and ϕ_d is obtained from the last converged local Newton-Raphson iteration i^conv (in incremental form) as

$$\mathrm{d}\boldsymbol{x} = -\boldsymbol{J}^{-1}_{i^\mathrm{conv}} \bullet \mathrm{d}\boldsymbol{r}|_{\boldsymbol{x}=const}\,, \tag{4.135}$$

where the incremental residuum is given as

$$\mathrm{d}\boldsymbol{r} = \left[\frac{\mathrm{d}r_\mathrm{p}}{\mathrm{d}\phi_\mathrm{p}}\,\mathrm{d}\phi_\mathrm{p},\, \frac{\mathrm{d}r_\mathrm{d}}{\mathrm{d}\phi_\mathrm{d}}\,\mathrm{d}\phi_\mathrm{d},\, \frac{\mathrm{d}\boldsymbol{R}_\mathrm{e}}{\mathrm{d}\boldsymbol{C}} : \mathrm{d}\boldsymbol{C}\right]\,, \tag{4.136}$$

where the derivatives are obtained as

$$\frac{\mathrm{d}r_\mathrm{p}}{\mathrm{d}\phi_\mathrm{p}} = -\sqrt{\frac{2}{3}}\left[\frac{\Phi_\mathrm{p}}{\sqrt{\Phi_\mathrm{p}^2 + \lambda_\mathrm{p}^2 + \epsilon}} + 1\right] h_\mathrm{p}\, b_\mathrm{p}\,, \tag{4.137}$$

$$\frac{\mathrm{d}r_\mathrm{d}}{\mathrm{d}\phi_\mathrm{d}} = -\sqrt{\frac{2}{3}}\left[\frac{\Phi_\mathrm{d}}{\sqrt{\Phi_\mathrm{d}^2 + \lambda_\mathrm{d}^2 + \epsilon}} + 1\right] f_\mathrm{dp}(\alpha_\mathrm{p})\, h_\mathrm{d}\, b_\mathrm{d}\,, \tag{4.138}$$

$$\frac{\mathrm{d}\boldsymbol{R}_\mathrm{e}}{\mathrm{d}\boldsymbol{C}} = -\frac{1}{2}\,\boldsymbol{F}_\mathrm{d}^\mathrm{t}\cdot\boldsymbol{F}_\mathrm{p}^{-\mathrm{t}}\,\overline{\otimes}\,\boldsymbol{F}_\mathrm{d}^\mathrm{t}\cdot\boldsymbol{F}_\mathrm{p}^{-\mathrm{t}}\,. \tag{4.139}$$

This enables to determine the global tangent contributions to

$$\frac{\mathrm{d}\boldsymbol{S}}{\mathrm{d}\boldsymbol{C}} = \frac{\mathrm{d}\boldsymbol{S}}{\mathrm{d}\boldsymbol{F}_\mathrm{p}^{-1}} : \frac{\mathrm{d}\boldsymbol{F}_\mathrm{p}^{-1}}{\mathrm{d}\boldsymbol{C}} + \frac{\mathrm{d}\boldsymbol{S}}{\mathrm{d}\boldsymbol{F}_\mathrm{d}} : \frac{\mathrm{d}\boldsymbol{F}_\mathrm{d}}{\mathrm{d}\boldsymbol{C}} + \frac{\mathrm{d}\boldsymbol{S}}{\mathrm{d}\overline{\boldsymbol{S}}_\mathrm{e}} : \frac{\partial\overline{\boldsymbol{S}}_\mathrm{e}}{\partial\overline{\boldsymbol{E}}_\mathrm{e}} : \frac{\mathrm{d}\overline{\boldsymbol{E}}_\mathrm{e}}{\mathrm{d}\boldsymbol{C}}\,, \tag{4.140}$$

$$\frac{\mathrm{d}\boldsymbol{S}}{\mathrm{d}\phi_\mathrm{p}} = \frac{\mathrm{d}\boldsymbol{S}}{\mathrm{d}\boldsymbol{F}_\mathrm{p}^{-1}} : \frac{\mathrm{d}\boldsymbol{F}_\mathrm{p}^{-1}}{\mathrm{d}\phi_\mathrm{p}} + \frac{\mathrm{d}\boldsymbol{S}}{\mathrm{d}\boldsymbol{F}_\mathrm{d}} : \frac{\mathrm{d}\boldsymbol{F}_\mathrm{d}}{\mathrm{d}\phi_\mathrm{p}} + \frac{\mathrm{d}\boldsymbol{S}}{\mathrm{d}\overline{\boldsymbol{S}}_\mathrm{e}} : \frac{\partial\overline{\boldsymbol{S}}_\mathrm{e}}{\partial\overline{\boldsymbol{E}}_\mathrm{e}} : \frac{\mathrm{d}\overline{\boldsymbol{E}}_\mathrm{e}}{\mathrm{d}\phi_\mathrm{p}}\,, \tag{4.141}$$

$$\frac{\mathrm{d}\boldsymbol{S}}{\mathrm{d}\phi_\mathrm{d}} = \frac{\mathrm{d}\boldsymbol{S}}{\mathrm{d}\boldsymbol{F}_\mathrm{p}^{-1}} : \frac{\mathrm{d}\boldsymbol{F}_\mathrm{p}^{-1}}{\mathrm{d}\phi_\mathrm{d}} + \frac{\mathrm{d}\boldsymbol{S}}{\mathrm{d}\boldsymbol{F}_\mathrm{d}} : \frac{\mathrm{d}\boldsymbol{F}_\mathrm{d}}{\mathrm{d}\phi_\mathrm{d}} + \frac{\mathrm{d}\boldsymbol{S}}{\mathrm{d}\overline{\boldsymbol{S}}_\mathrm{e}} : \frac{\partial\overline{\boldsymbol{S}}_\mathrm{e}}{\partial\overline{\boldsymbol{E}}_\mathrm{e}} : \frac{\mathrm{d}\overline{\boldsymbol{E}}_\mathrm{e}}{\mathrm{d}\phi_\mathrm{d}}\,, \tag{4.142}$$

$$\frac{\mathrm{d}Y_\mathrm{p}}{\mathrm{d}\boldsymbol{C}} = -\sqrt{\frac{2}{3}}\,\Delta t\, h_\mathrm{p}\, b_\mathrm{p}\, \frac{\mathrm{d}\lambda_\mathrm{p}}{\mathrm{d}\boldsymbol{C}}\,, \tag{4.143}$$

$$\frac{\mathrm{d}Y_\mathrm{d}}{\mathrm{d}\boldsymbol{C}} = -\Delta t\, h_\mathrm{d}\, b_\mathrm{d}\, \left[\frac{2}{3}\,\Delta t^2\,\lambda_\mathrm{d}\, f'_\mathrm{dp}(\alpha_\mathrm{p})\, \frac{\mathrm{d}\lambda_\mathrm{p}}{\mathrm{d}\boldsymbol{C}} + \sqrt{\frac{2}{3}}\, f_\mathrm{dp}(\alpha_\mathrm{p}) \frac{\mathrm{d}\lambda_\mathrm{d}}{\mathrm{d}\boldsymbol{C}}\right]\,, \tag{4.144}$$

$$\frac{\mathrm{d}Y_\mathrm{p}}{\mathrm{d}\phi_\mathrm{p}} = h_\mathrm{p}\, b_\mathrm{p}\, \left[1 - \sqrt{\frac{2}{3}}\,\Delta t\, \frac{\mathrm{d}\lambda_\mathrm{p}}{\mathrm{d}\phi_\mathrm{p}}\right]\,, \tag{4.145}$$

$$\frac{\mathrm{d}Y_\mathrm{p}}{\mathrm{d}\phi_\mathrm{d}} = -\sqrt{\frac{2}{3}}\, h_\mathrm{p}\, b_\mathrm{p}\, \Delta t\, \frac{\mathrm{d}\lambda_\mathrm{p}}{\mathrm{d}\phi_\mathrm{d}}\,, \tag{4.146}$$

$$\frac{\mathrm{d}Y_\mathrm{d}}{\mathrm{d}\phi_\mathrm{p}} = -\sqrt{\frac{2}{3}}\,\Delta t\, h_\mathrm{d}\, b_\mathrm{d}\, \left[\lambda_\mathrm{d}\, \sqrt{\frac{2}{3}}\,\Delta t\, f'_\mathrm{dp}(\alpha_\mathrm{p})\, \frac{\mathrm{d}\lambda_\mathrm{p}}{\mathrm{d}\phi_\mathrm{d}} + f_\mathrm{dp}(\alpha_\mathrm{p})\, \frac{\mathrm{d}\lambda_\mathrm{d}}{\mathrm{d}\phi_\mathrm{d}}\right]\,, \tag{4.147}$$

$$\frac{\mathrm{d}Y_\mathrm{d}}{\mathrm{d}\phi_\mathrm{d}} = h_\mathrm{d}\, b_\mathrm{d}\, \left[1 - \lambda_\mathrm{d}\, \frac{2}{3}\,\Delta t^2\, f'_\mathrm{dp}(\alpha_\mathrm{p})\, \frac{\mathrm{d}\lambda_\mathrm{p}}{\mathrm{d}\phi_\mathrm{d}} + \sqrt{\frac{2}{3}}\,\Delta t\, f_\mathrm{dp}(\alpha_\mathrm{p})\, \frac{\mathrm{d}\lambda_\mathrm{d}}{\mathrm{d}\phi_\mathrm{d}}\right]\,, \tag{4.148}$$

$$\frac{\mathrm{d}\boldsymbol{Y}_\mathrm{p}}{\mathrm{d}\nabla_{\boldsymbol{X}}\phi_\mathrm{p}} = h_\mathrm{p}\, b_\mathrm{p}\, c_\mathrm{p}\, \boldsymbol{I}\,, \tag{4.149}$$

$$\frac{\mathrm{d}\boldsymbol{Y}_\mathrm{d}}{\mathrm{d}\nabla_{\boldsymbol{X}}\phi_\mathrm{d}} = h_\mathrm{d}\, b_\mathrm{d}\, c_\mathrm{d}\, \boldsymbol{I}\,, \tag{4.150}$$

with the remaining derivatives being given as

$$\frac{\mathrm{d}\boldsymbol{S}}{\mathrm{d}\boldsymbol{F}_\mathrm{p}^{-1}} = \boldsymbol{I} \mathbin{\overline{\otimes}} \left[\boldsymbol{F}_\mathrm{p}^{-1} \cdot \widehat{\boldsymbol{S}}_\mathrm{e}\right] + \boldsymbol{F}_\mathrm{p}^{-1} \cdot \widehat{\boldsymbol{S}}_\mathrm{e} \mathbin{\underline{\otimes}} \boldsymbol{I}\,, \tag{4.151}$$

$$\frac{\mathrm{d}\boldsymbol{S}}{\mathrm{d}\boldsymbol{F}_\mathrm{d}} = \boldsymbol{F}_\mathrm{p}^{-1} \mathbin{\overline{\otimes}} \left[\boldsymbol{F}_\mathrm{p}^{-1} \cdot \boldsymbol{F}_\mathrm{d} \cdot \overline{\boldsymbol{S}}_\mathrm{e}\right] + \boldsymbol{F}_\mathrm{p}^{-1} \cdot \boldsymbol{F}_\mathrm{d} \cdot \overline{\boldsymbol{S}}_\mathrm{e} \mathbin{\underline{\otimes}} \boldsymbol{F}_\mathrm{p}^{-1}\,, \tag{4.152}$$

$$\frac{\mathrm{d}\boldsymbol{S}}{\mathrm{d}\overline{\boldsymbol{S}}_\mathrm{e}} = \boldsymbol{F}_\mathrm{p}^{-1} \cdot \boldsymbol{F}_\mathrm{d} \mathbin{\overline{\otimes}} \left[\boldsymbol{F}_\mathrm{p}^{-1} \cdot \boldsymbol{F}_\mathrm{d}\right]\,, \tag{4.153}$$

$$\frac{\mathrm{d}\boldsymbol{F}_\mathrm{p}^{-1}}{\mathrm{d}\boldsymbol{C}} = \frac{\partial\boldsymbol{F}_\mathrm{p}^{-1}}{\partial\lambda_\mathrm{p}} \otimes \frac{\mathrm{d}\lambda_\mathrm{p}}{\mathrm{d}\boldsymbol{C}} + \frac{\partial\boldsymbol{F}_\mathrm{p}^{-1}}{\partial\lambda_\mathrm{d}} \otimes \frac{\mathrm{d}\lambda_\mathrm{d}}{\mathrm{d}\boldsymbol{C}} + \frac{\partial\boldsymbol{F}_\mathrm{p}^{-1}}{\partial\overline{\boldsymbol{E}}_\mathrm{e}} : \frac{\mathrm{d}\overline{\boldsymbol{E}}_\mathrm{e}}{\mathrm{d}\boldsymbol{C}}\,, \tag{4.154}$$

$$\frac{\mathrm{d}\boldsymbol{F}_\mathrm{p}^{-1}}{\mathrm{d}\phi_\mathrm{p}} = \frac{\partial\boldsymbol{F}_\mathrm{p}^{-1}}{\partial\lambda_\mathrm{p}}\, \frac{\mathrm{d}\lambda_\mathrm{p}}{\mathrm{d}\phi_\mathrm{p}} + \frac{\partial\boldsymbol{F}_\mathrm{p}^{-1}}{\partial\lambda_\mathrm{d}}\, \frac{\mathrm{d}\lambda_\mathrm{d}}{\mathrm{d}\phi_\mathrm{p}} + \frac{\partial\boldsymbol{F}_\mathrm{p}^{-1}}{\partial\overline{\boldsymbol{E}}_\mathrm{e}} : \frac{\mathrm{d}\overline{\boldsymbol{E}}_\mathrm{e}}{\mathrm{d}\phi_\mathrm{p}}\,, \tag{4.155}$$

$$\frac{\mathrm{d}\boldsymbol{F}_\mathrm{p}^{-1}}{\mathrm{d}\phi_\mathrm{d}} = \frac{\partial\boldsymbol{F}_\mathrm{p}^{-1}}{\partial\lambda_\mathrm{p}}\, \frac{\mathrm{d}\lambda_\mathrm{p}}{\mathrm{d}\phi_\mathrm{d}} + \frac{\partial\boldsymbol{F}_\mathrm{p}^{-1}}{\partial\lambda_\mathrm{d}}\, \frac{\mathrm{d}\lambda_\mathrm{d}}{\mathrm{d}\phi_\mathrm{d}} + \frac{\partial\boldsymbol{F}_\mathrm{p}^{-1}}{\partial\overline{\boldsymbol{E}}_\mathrm{e}} : \frac{\mathrm{d}\overline{\boldsymbol{E}}_\mathrm{e}}{\mathrm{d}\phi_\mathrm{d}}\,, \tag{4.156}$$

$$\frac{\mathrm{d}\boldsymbol{F}_\mathrm{d}}{\mathrm{d}\boldsymbol{C}} = \frac{\partial\boldsymbol{F}_\mathrm{d}}{\partial\lambda_\mathrm{d}} \otimes \frac{\mathrm{d}\lambda_\mathrm{d}}{\mathrm{d}\boldsymbol{C}} + \frac{\partial\boldsymbol{F}_\mathrm{d}}{\partial\overline{\boldsymbol{E}}_\mathrm{e}} : \frac{\mathrm{d}\overline{\boldsymbol{E}}_\mathrm{e}}{\mathrm{d}\boldsymbol{C}}\,, \tag{4.157}$$

$$\frac{\mathrm{d}\boldsymbol{F}_\mathrm{d}}{\mathrm{d}\phi_\mathrm{p}} = \frac{\partial \boldsymbol{F}_\mathrm{d}}{\partial \lambda_\mathrm{d}} \frac{\mathrm{d}\lambda_\mathrm{d}}{\mathrm{d}\phi_\mathrm{p}} + \frac{\partial \boldsymbol{F}_\mathrm{d}}{\partial \overline{\boldsymbol{E}}_\mathrm{e}} : \frac{\mathrm{d}\overline{\boldsymbol{E}}_\mathrm{e}}{\mathrm{d}\phi_\mathrm{p}} \,, \tag{4.158}$$

$$\frac{\mathrm{d}\boldsymbol{F}_\mathrm{d}}{\mathrm{d}\phi_\mathrm{d}} = \frac{\partial \boldsymbol{F}_\mathrm{d}}{\partial \lambda_\mathrm{d}} \frac{\mathrm{d}\lambda_\mathrm{d}}{\mathrm{d}\phi_\mathrm{d}} + \frac{\partial \boldsymbol{F}_\mathrm{d}}{\partial \overline{\boldsymbol{E}}_\mathrm{e}} : \frac{\mathrm{d}\overline{\boldsymbol{E}}_\mathrm{e}}{\mathrm{d}\phi_\mathrm{d}} \,. \tag{4.159}$$

4.9 Response under homogeneous deformation

This section deals with an analysis of the basic model properties. In order to study the model behaviour in a state where it resembles a real material, a local parameter identification is performed first and the influence of each of the parameters in this identified parameter set is analysed thereafter, see Section 4.9.2. The behaviour of the model under simple shear is analysed in Section 4.9.3 and the combination of simple shear and uniaxial tension, by applying simple shear first followed by uniaxial tension and vice versa, is studied in Section 4.9.4.

4.9.1 Homogeneous uniaxial tension — local parameter identification

The experimental data used for this parameter identification is taken from Figure 3.8. The stress vs. stretch response is referred to the short middle section (of length 800 μm) of the specimen, see Figure 4.3a), and assumed to undergo uniaxial tension, i.e. the deformation gradient $\boldsymbol{F}$ is expressed as

$$\boldsymbol{F} = \lambda_\parallel \, \boldsymbol{e} \otimes \boldsymbol{e} + \lambda_\perp \left[\boldsymbol{I} - \boldsymbol{e} \otimes \boldsymbol{e}\right] \quad \text{with} \quad \|\boldsymbol{e}\| = 1 \,, \tag{4.160}$$

where $\boldsymbol{e}$ is the direction of tension and, consequently, stresses are given by $\boldsymbol{P} = P_\parallel \, \boldsymbol{e} \otimes \boldsymbol{e}$. The simulations utilising the model proposed in the present work are performed by using a single finite element and boundary conditions resembling uniaxial tension. The additional non-local fields, ϕ_d and ϕ_p, are fixed to zero by means of Dirichlet boundary conditions and the coupling parameters, b_d and b_p, are set to zero to disable any influence on the local model. The uniaxial tension load is prescribed by means of Dirichlet boundary conditions and the load path includes three load reversing steps — approximately representing unloading of the specimen, see Figure 4.3b). The parameter identification is based on a minimisation of an objective function based on the difference of the reaction forces of the simulation, F^sim, and the experiment, F^exp, i.e.

$$g = \sum_k \left[F^\mathrm{exp}(t_k) - F^\mathrm{sim}(t_k)\right]^2 \,, \tag{4.161}$$

where t_k represent discrete points in time. The numerical minimisation uses a Nelder-Mead simplex algorithm [134]. The parameters to be identified as well as their starting and finally obtained values are listed in Table 4.3, where the starting parameters are

Table 4.3: List of material parameters for the basic parameter identification. The third column contains the start values of the parameters and the fourth column lists the identified parameters.

Symbol	Description	Value start	Value identified	Unit
E	Young's modulus	208.0	—	GPa
ν	Poisson's ratio	0.3	—	–
$M_{\mathrm{e}}^{\mathrm{max0}}$	yield stress	250.0	—	MPa
h_{p}	plastic hardening modulus	1700.0	2344.3	MPa
n_{p}	plastic hardening exponent	0.25	0.23146	–
ζ_{d}	damage anisotropy	0.5	—	–
$M_{\mathrm{d}}^{\mathrm{max0}}$	damage initiation	50.0	0.0	MPa
h_{d}	damage hardening modulus	5.0	163.29	MPa
n_{d}	damage hardening exponent	1.0	—	–
h_{dp}	damage deterioration	10.0	40.828	–
$\alpha_{\mathrm{p,max}}$	deterioration offset	0.15	0.50118	–

chosen similar to the identified parameters in [161]. Not all parameters are included in the identification process. The elastic parameters are set to common values for steel, since only very few experimental data points are in the initial elastic domain. Using the same reasoning, the initial yield stress is set to the yield stress identified in [161]. The damage anisotropy parameter ζ_{d} cannot be identified from one-dimensional data and as such is also not part of the parameters to be identified here. Damage hardening will be kept linear ($n_{\mathrm{d}} = 1$) in the examples presented here.

The stress vs. stretch diagram of the experimental response together with the response of the simulation using the identified parameters is shown in Figure 4.3b). The model is able to match the experimental response quite well. However, the point of failure which occurs in the experimental response at a stretch of approximately $\lambda_{\parallel} = 1.4$ could not be identified by means of this local parameter identification, i.e. the damage deterioration offset was identified as $\alpha_{\mathrm{p,max}} \approx 0.5$, which is much higher than the maximum of the plastic hardening variable at the end of the simulation ($\alpha_{\mathrm{p}_{\mathrm{max}}} \approx 0.18$). Improvements in this regard might be possible by including experimental data points in the parameter identification process which lie beyond the point of failure. Since necking is very dominant at this stage of the experiment, the assumption of a homogeneous deformation is inaccurate. However, setting up a parameter identification utilising full-field data and a corresponding inhomogeneous boundary value problem is beyond the scope of this work.

4.9.2 Homogeneous uniaxial tension — parameter variation

Based on the identified parameters from the previous section, a parameter variation study is set up to highlight the influence of each parameter in the model. The loading history is kept identical to the parameter identification process, i.e. Figure 4.3b). The values of the reference parameters as well as the modified parameters — each parameter

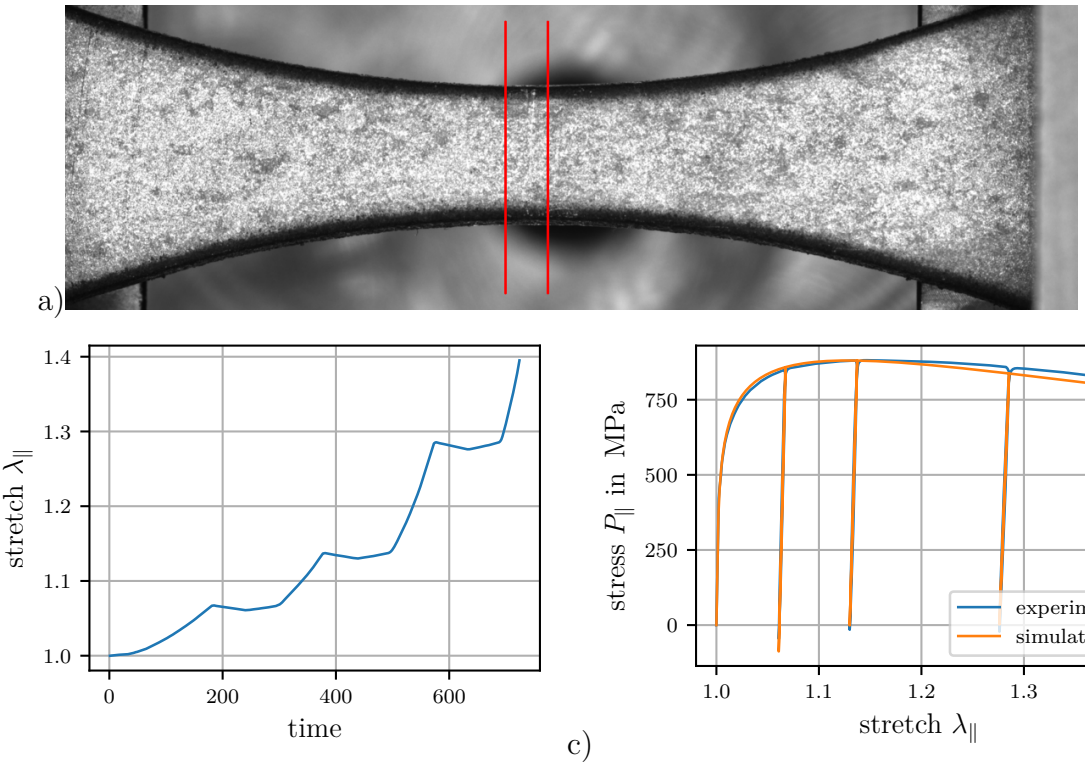

Figure 4.3: Results of the basic parameter identification. a) Image of the specimen used for the generation of the experimental data; taken from [161, Figure 7b]. The red lines mark the centre section of the specimen and possess a width of 800 μm. b) Loading history in form of tensile stretch $\lambda_{\|}$ measured and averaged over the centre section, c) stress vs. stretch diagram with the (homogenised) response of the experiment (blue coloured) taken from [161, Figure 8a] and the response of the simulation (orange coloured) based on the model proposed in the present work. Source (a+c): Reproduced from [161] under the terms of the Creative Commons Attribution License (CC BY).

is varied to a higher and to a lower value — are listed in Table 4.4. The responses of the simulations with varied parameters are shown in Figure 4.4 and Figure 4.5. Each column of diagrams, e.g. a), c), e), contains the response of two modified parameters. Displayed are the stress vs. stretch diagrams, the evolution of the hardening variables and the evolution of the eigenvalues of the damage tensor $\widehat{\boldsymbol{b}}_{\mathrm{d}}$ — or rather $1 - \lambda_i^{\widehat{\boldsymbol{b}}_{\mathrm{d}}}$ in order to visualise a monotonically increasing damage measure starting at zero by analogy with a classic $[\,1 - d\,]$ approach. The stress measure in the figures is the Kirchhoff stress $\boldsymbol{\tau} = \det(\boldsymbol{F})\,\boldsymbol{\sigma}$, with the Cauchy stresses $\boldsymbol{\sigma}$ relating (spatial) force to current cross-section, to be specific

$$\boldsymbol{\tau} = \boldsymbol{P} \cdot \boldsymbol{F}^{\mathrm{t}} = \lambda_{\parallel}\, P_{\parallel}\, \boldsymbol{e} \otimes \boldsymbol{e}\,. \tag{4.162}$$

The influence of most parameters is as expected. A non-obvious interaction between plastic hardening and damage evolution is observed, see Figure 4.4a), c) and e). A decrease in plastic hardening also decreases evolution of damage since elastic strains evolve less with less hardening. Thus, the damage driving force rises more slowly due to depending mainly on elastic strains, cf. (4.14).

Varying the damage initiation $M_{\mathrm{d}}^{\max 0}$ or the damage hardening modulus h_{d} leads to expected changes of the response before deterioration sets in, see Figure 4.4b), d) and f). Thereafter a counter-intuitive behaviour is observed, i.e. a stiffer response before deterioration leads to a quicker deterioration afterwards. A higher hardening modulus leads to a higher value of the corresponding driving force — in this case to higher values of the elastic strains. Consequently, after the threshold value is decreased by the influence function f_{dp}, the higher driving force leads to more damage evolution.

If more of the energy in the damage potential is "stored" in the threshold value, e.g. by increased hardening, more energy is available to evolve damage after the threshold value has been deteriorated.

The parameters controlling the deterioration function also show expected behaviour, see the left column in Figure 4.5. The damage deterioration h_{dp} controls the speed of the deterioration, respectively the steepness of the drop in force, and the deterioration offset $\alpha_{\mathrm{p,max}}$ determines the amount of plastic deformation after which the deterioration starts.

Variation of the initial yield stress $M_{\mathrm{e}}^{\max 0}$, depicted in Figure 4.5b), d) and f), shows that, for the current parameter combination and especially for hardening exponent $n_{\mathrm{p}} = 0.23$, the initial yield stress has a very low impact on the overall response. Only a significant increase of the initial yield stress leads to a visible influence in the response. Variation of the damage anisotropy ζ_{d} also does not influence the stress response or the evolution of hardening, but it plays a major role with respect to the non-dominating eigenvalue of the damage tensor, see Figure 4.5.

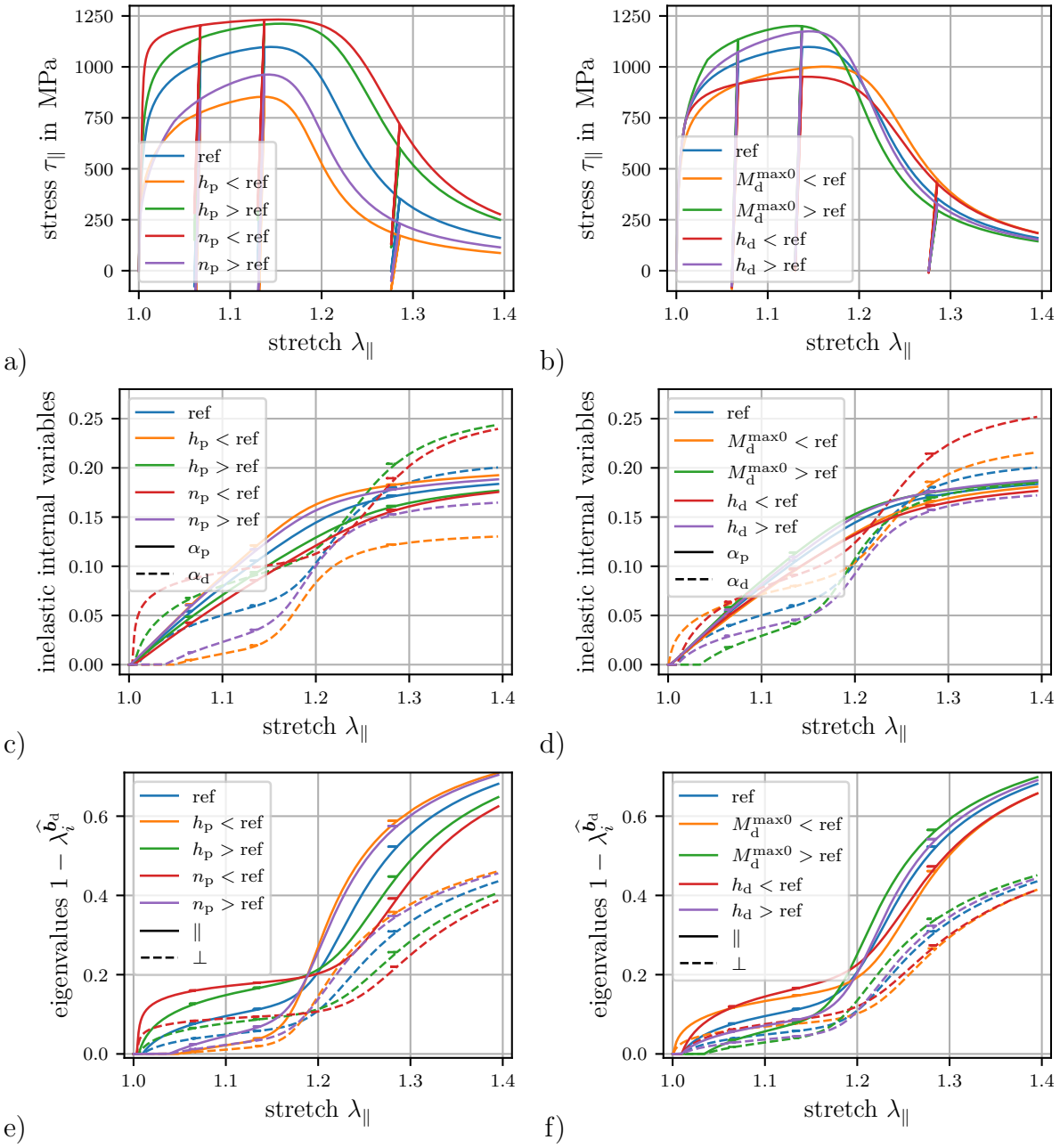

Figure 4.4: Stress vs. stretch diagrams a) and b), proportional hardening vs. stretch diagrams c) and d) and damage vs. stretch diagrams e) and f). Displayed are the influence of the hardening modulus h_p and of the hardening exponent n_p in a), c) and e) as well as the influence of the initial damage threshold $M_\mathrm{d}^{\max 0}$ and of the damage hardening modulus h_d in b), d) and f) on the material response under homogeneous tension.

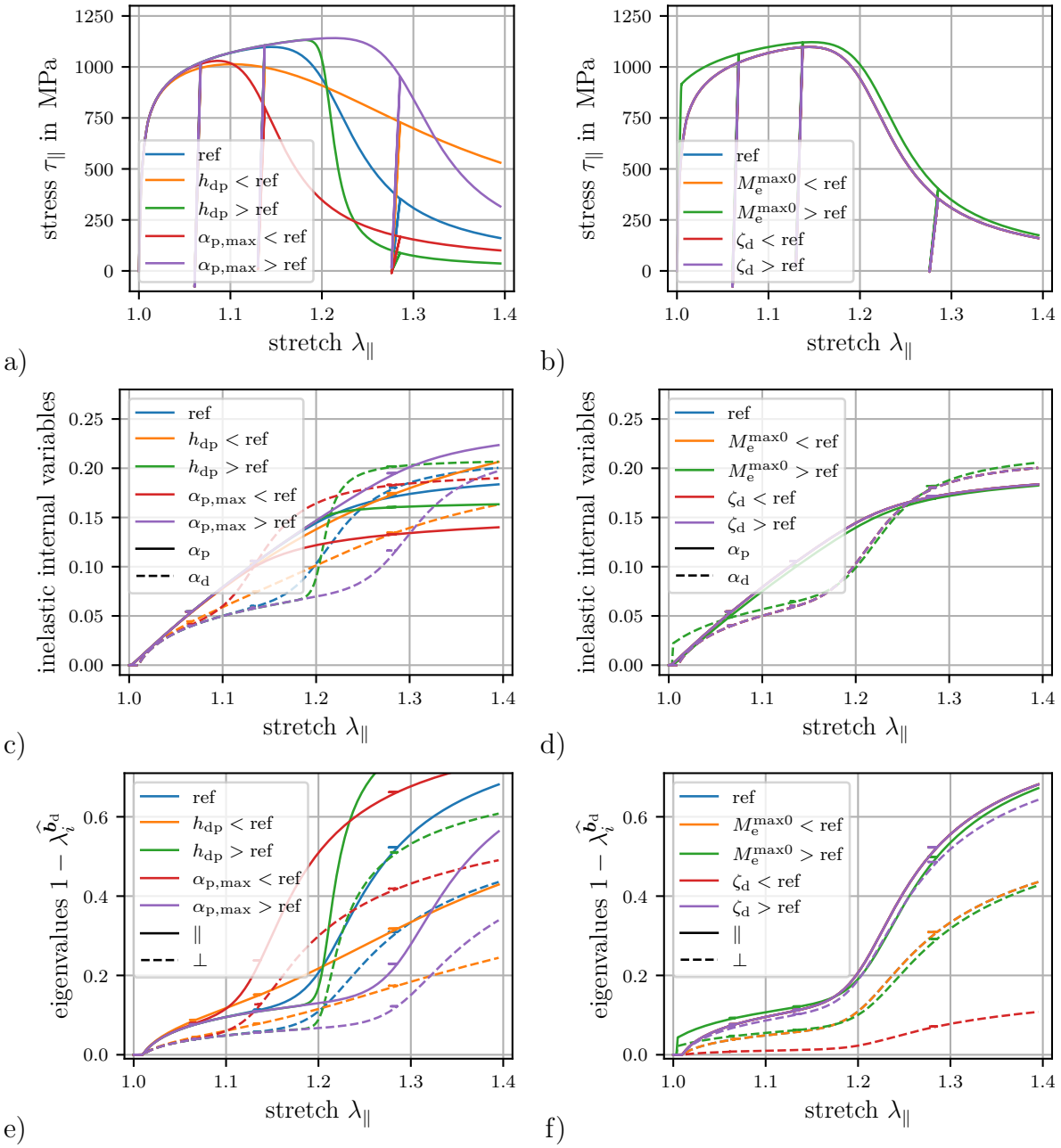

Figure 4.5: Stress vs. stretch diagrams a) and b), proportional hardening vs. stretch diagrams c) and d) and damage vs. stretch diagrams e) and f). Displayed are the influence of the damage deterioration h_dp and of the deterioration offset $\alpha_\mathrm{p,max}$ in a), c) and e) as well as the influence of the initial yield stress $M_\mathrm{e}^{\mathrm{max}0}$ and of the damage anisotropy factor ζ_d in b), d) and f) on the material response under homogeneous tension.

Table 4.4: List of material parameters for the homogeneous tension test. The third column contains the reference set, subsequent columns list the decreased and increased values of each parameter.

		Value			
Symbol	Description	reference	lower	higher	Unit
E	Young's modulus	208.0	—	—	GPa
ν	Poisson's ratio	0.3	—	—	–
$M_{\mathrm{e}}^{\mathrm{max0}}$	yield stress	250.0	50.0	1000.0	MPa
h_{p}	plastic hardening modulus	2340.0	1500.0	3000.0	MPa
n_{p}	plastic hardening exponent	0.23	0.1	0.35	–
ζ_{d}	damage anisotropy	0.5	0.05	0.95	–
$M_{\mathrm{d}}^{\mathrm{max0}}$	damage initiation	5.0	0.0	10.0	MPa
h_{d}	damage hardening modulus	160.0	80.0	240.0	MPa
n_{d}	damage hardening exponent	1.0	—	—	–
h_{dp}	damage deterioration	40.0	10.0	160.0	–
$\alpha_{\mathrm{p,max}}$	deterioration offset	0.15	0.1	0.2	–

4.9.3 Homogeneous simple shear

The behaviour of the model is studied for simple shear loading where the deformation gradient is given by

$$\boldsymbol{F} = \boldsymbol{I} + \gamma\, \boldsymbol{e}_1 \otimes \boldsymbol{e}_2\,, \tag{4.163}$$

with $\{\boldsymbol{e}_{1,2,3}\}$ as orthonormal basis. The simulation is performed by using the reference parameter set, see Table 4.4. The stress response, depicted in Figure 4.6a), as well as the evolution of the hardening variables α_{p} and α_{d}, depicted in Figure 4.6b), yield expected results. Unexpectedly, the damage driving force $\overline{\boldsymbol{M}}_{\mathrm{d}}$, depicted in Figure 4.6c), has no (or very small) off-diagonal coefficients, i.e. its eigen-directions remain constant, respectively aligned with $\{\boldsymbol{e}_{1,2,3}\}$. This results from the fact that the off-diagonal coefficients of the driving force scale (in this quasi two-dimensional setting) with the trace of the fictitious elastic strains and since the volumetric elastic strains are small, the off-diagonal coefficients are also small. The overall evolution of damage is comparable to the example under uniaxial tension discussed previously, but with the two damage eigenvalue contributions related to the plane of shearing taking higher degradation levels than the damage contribution in transverse direction; see Figure 4.6d).

4.9.4 Homogeneous simple shear combined with uniaxial tension

After analysing the behaviour under simple shear loading, a combination of simple shear and uniaxial tension loading is analysed next. Figure 4.7 shows the response of the model for uniaxial tension loading followed by simple shear loading by means of solid lines and for simple shear loading followed by uniaxial tension loading by means of dashed lines.

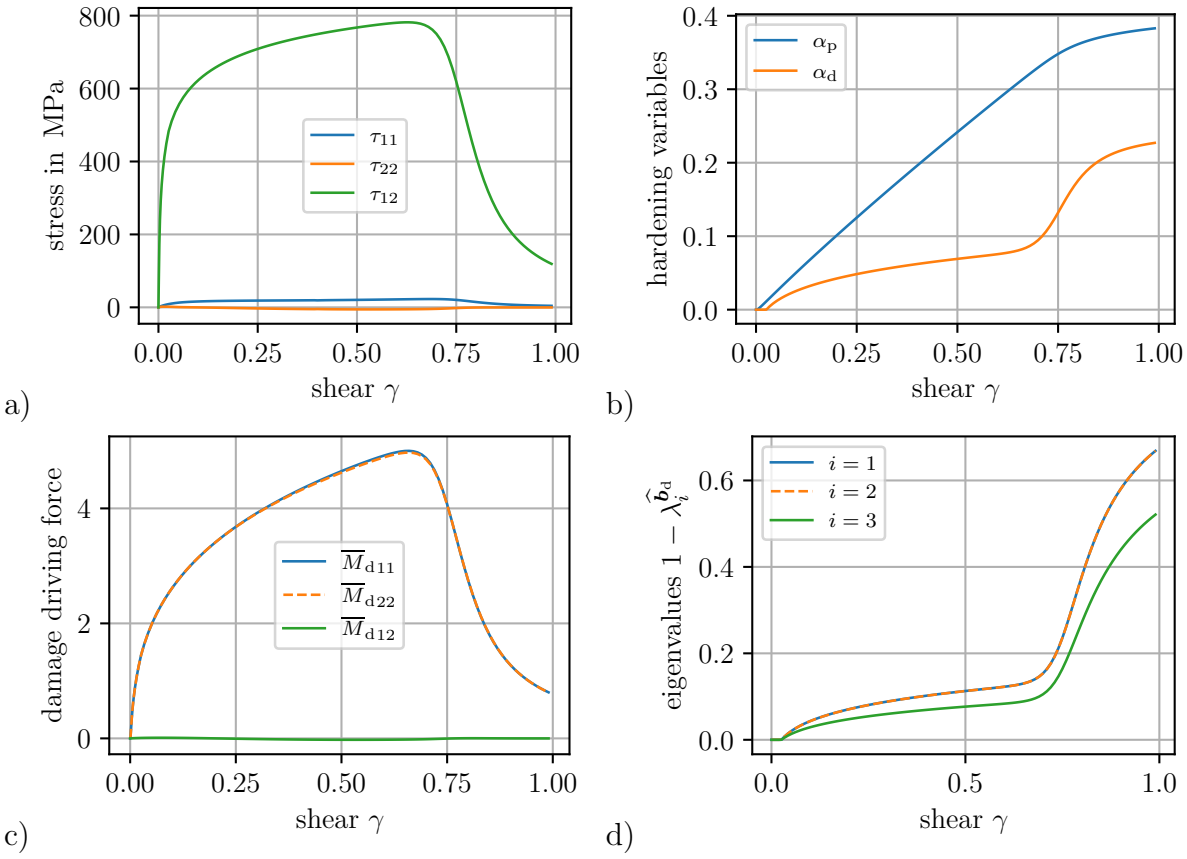

Figure 4.6: Response of the material model under homogeneous simple shear. Displayed are the stress vs. shear diagram in a), the evolution of proportional hardening in b), the damage driving force $\overline{\boldsymbol{M}}_\mathrm{d}$ vs. shear diagram in c) and the evolution of the damage eigenvalues in d).

Every loading is followed by an unloading stage. The loading can be expressed by $\overline{\boldsymbol{F}}$ for the case where uniaxial tension is followed by shearing and by $\widehat{\boldsymbol{F}}$ in the other case, with

$$\overline{\boldsymbol{F}} = \overline{\lambda}_\parallel \, \boldsymbol{e}_2 \otimes \boldsymbol{e}_2 + \overline{\lambda}_\perp \, [\boldsymbol{I} - \boldsymbol{e}_2 \otimes \boldsymbol{e}_2] + \overline{\gamma} \, \boldsymbol{e}_1 \otimes \boldsymbol{e}_2 \,, \tag{4.164}$$

$$\widehat{\boldsymbol{F}} = \widehat{\lambda}_\parallel \, \boldsymbol{e}_2 \otimes \boldsymbol{e}_2 + \widehat{\lambda}_\perp \, [\boldsymbol{I} - \boldsymbol{e}_2 \otimes \boldsymbol{e}_2] + \widehat{\gamma} \, \boldsymbol{e}_1 \otimes \boldsymbol{e}_2 \,, \tag{4.165}$$

where $\overline{\lambda}_\parallel = 1.0$ and $\widehat{\gamma} = 1.0$ are prescribed to be reached at $t = 90$ and $\overline{\gamma} = 0.75$ and $\widehat{\lambda}_\parallel = 1.0$ are prescribed to be reached at $t = 190$.

While the final unloaded deformation is nearly identical for both load cases, see Figure 4.7a), the evolution of the inelastic variables differs significantly, see Figure 4.7b) as well as e) and f). The resulting plastic deformation gradients are, apart from the flipped sign of the shear component, nearly identical. Applying shear loading first leads to a higher damaged state. The explanation can be found in the load case where uniaxial tension is applied first (solid line). The coefficients $\overline{\boldsymbol{M}}_{\mathrm{d}11}$ and $\overline{\boldsymbol{M}}_{\mathrm{d}22}$ of the damage driving force take similar values during shear loading subsequent to tensile loading, see

Figure 4.7d) (solid lines). For the other loading case considered (dashed lines) however, the magnitude of $\overline{\boldsymbol{M}}_{\mathrm{d}\,22}$ is significantly larger than the magnitude of $\overline{\boldsymbol{M}}_{\mathrm{d}\,11}$ during tensile loading subsequent to shear loading. Hence, the load case with subsequent shear loading does not lead to further evolution of damage and thereby to less evolution of plasticity compared to the load case with subsequent uniaxial tension loading. The differences in material response depending on the particular loading path chosen become most obvious in the graphs of the respective stress responses highlighted in Figure 4.7c).

4.10 Analysis of regularisation behaviour

At first, the setup of the inhomogeneous examples is described. The analysis starts with a discussion of the regularisation of a response with damage evolution only, i.e. with $M_{\mathrm{e}}^{\mathrm{max0}} = 9.0 \times 10^9\,\mathrm{MPa}$ in Section 4.10.2. Thereafter, the opposite case of a response with only plasticity, i.e. with $M_{\mathrm{d}}^{\mathrm{max0}} = 9.0 \times 10^9\,\mathrm{MPa}$, is analysed, see Section 4.10.3 followed by a study of the regularisation behaviour of the fully coupled model in Section 4.10.4. Finally, Section 4.10.5 demonstrates the influence of the deterioration function f_{dp} on the response of the inhomogeneous problem.

4.10.1 Setup of the numerical examples

In order to study the regularisation behaviour of the proposed model, the response of a plate ($200\,\mathrm{mm} \times 200\,\mathrm{mm} \times 20\,\mathrm{mm}$) with a central hole (diameter 100 mm) subjected to tensile loading — applied by means of a linear increasing prescribed displacement u — is analysed for different discretisations. A suitable approximation for the gradient-enhanced model is the choice of a quadratic approximation for the displacement field in combination with a linear approximation of the additional gradient-related field; see, e.g., [112, 178] and references cited therein. Consequently, the plate with a hole is discretised by using mixed Serendipiti elements — displacements $\boldsymbol{u}$ are approximated quadratically with 20 nodes and the non-local field variables, ϕ_{d} and ϕ_{p}, are approximated linearly with 8 nodes per element. Integration is carried out by using 8 integration points. An eighth of the plate with a hole is discretised with $n_{\mathrm{el}} = \{384,\ 1350,\ 5400\}$ elements. The results obtained from the different discretisations are depicted in the force-displacement diagrams by means of different line styles, i.e. the solid line represents the coarse discretisation, the dashed line represents the medium discretisation and the dash-dotted line represents the fine discretisation.

The material parameters are chosen close to the identified set of the uniaxial parameter identification in Figure 4.3 and are listed in Table 4.5. The damage anisotropy parameter is (arbitrarily) chosen as $\zeta_{\mathrm{d}} = 0.5$. The parameters related to regularisation are chosen such that sufficient regularisation is achieved for the examples elaborated in this work. All following examples use the values listed in the 'reference' column, unless they are explicitly given. The columns 'var. 1' and 'var. 2' list some of the variations

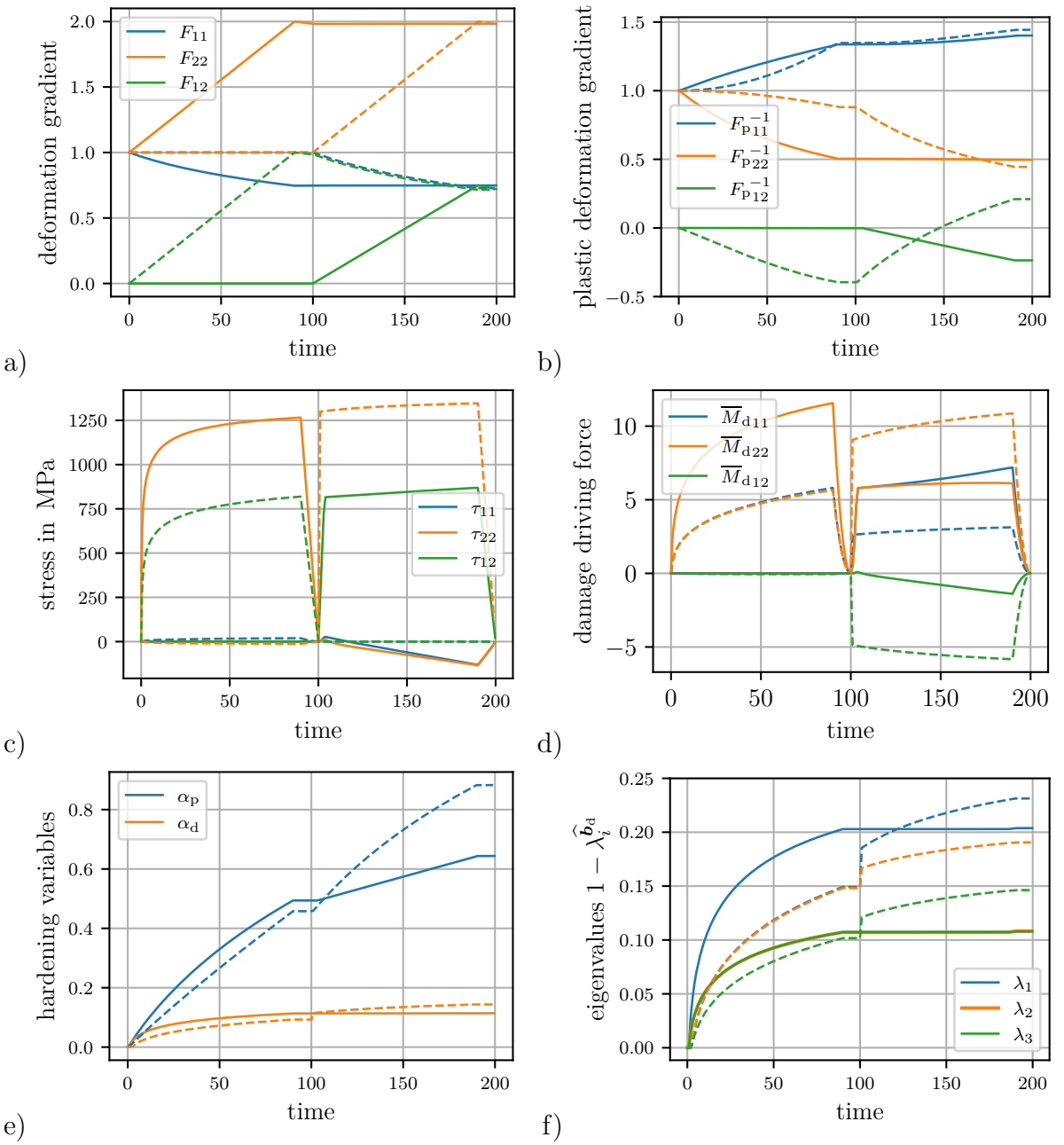

Figure 4.7: Response of the material model under sequential loading of homogeneous uniaxial tension followed by simple shear (solid line) as well as homogeneous simple shear followed by uniaxial tension (dashed line). Displayed are the relevant components of the deformation gradient $\boldsymbol{F}$ a) and the plastic deformation gradient $\boldsymbol{F}_{\mathrm{p}}$ b), the stress vs. time diagram c), the damage driving force $\overline{\boldsymbol{M}}_{\mathrm{d}}$ vs. time diagram d), the evolution of proportional hardening e) and the evolution of the damage eigenvalues f).

Table 4.5: List of material parameters for the regularisation examples. The third column contains the reference set, subsequent columns list variations for specific examples.

Symbol	Description	Value reference	var. 1	var. 2	Unit
E	Young's modulus	210.0	—	—	GPa
ν	Poisson's ratio	0.3	—	—	–
$M_{\mathrm{e}}^{\mathrm{max0}}$	yield stress	250.0	9.0×10^9	—	MPa
h_{p}	plastic hardening modulus	2000.0	—	—	MPa
n_{p}	plastic hardening exponent	0.25	1.0	—	–
ζ_{d}	damage anisotropy	0.5	—	—	–
$M_{\mathrm{d}}^{\mathrm{max0}}$	damage initiation	5.0	9.0×10^9	2.0	MPa
h_{d}	damage hardening modulus	100.0	—	20.0	MPa
n_{d}	damage hardening exponent	1.0	—	—	–
h_{dp}	damage deterioration	0.0	10.0	—	–
$\alpha_{\mathrm{p,max}}$	deterioration offset	0.0	0.6	—	–
b_{d}	damage coupling parameter	100.0	10.0	1000.0	–
c_{d}	damage regularisation parameter	10.0	1.0	100.0	mm^2
b_{p}	plastic coupling parameter	10.0	1.0	100.0	–
c_{p}	plastic regularisation parameter	10.0	1.0	100.0	mm^2

used in specific examples in the following sections. Whenever a coupling parameter (b_{p} or b_{d}) is set to zero, the corresponding field (ϕ_{p} or ϕ_{d}) is prescribed to zero throughout the body, i.e. the influence of the respective field variable in the model is disabled.

4.10.2 Elasticity with damage

First, the regularisation of the model exhibiting only damage evolution is studied, i.e. the yield limit is raised to $M_{\mathrm{e}}^{\mathrm{max0}} = 9.0 \times 10^9\,\mathrm{MPa}$. Damage initiation threshold and damage hardening modulus are lowered, i.e. $M_{\mathrm{d}}^{\mathrm{max0}} = 2.0\,\mathrm{MPa}$ and $h_{\mathrm{d}} = 20.0\,\mathrm{MPa}$ and maximum loading is reduced to $u = 10\,\mathrm{mm}$. The gradient contribution of the plastic non-local variable ϕ_{p} is not necessary and consequently $\phi_{\mathrm{p}} = 0$ is enforced by boundary conditions together with setting $b_{\mathrm{p}} = 0$.

The force-displacement responses of the simulations with three discretisations ($n_{\mathrm{el}} = \{384, 1350, 5400\}$) are depicted in Figure 4.8, where the influence of the damage regularisation parameter c_{d} is studied for damage coupling parameters $b_{\mathrm{d}} = 10.0$ and $b_{\mathrm{d}} = 100.0$. One clearly observes different force-displacement responses of the different discretisations for the lower damage coupling parameter b_{d}, see Figure 4.8a). The point at which localisation starts is especially visible for the response with $c_{\mathrm{d}} = 100.0\,\mathrm{mm}^2$ (green line) where, shortly after the force reaches its peak, the force responses diverge. Increasing the damage coupling parameter to $b_{\mathrm{d}} = 100.0$ regularises the response for all discretisations and for all tested regularisation parameters c_{d}, as exhibited by Figure 4.8b). The contour plots of the minimum eigenvalue in the form of $1 - \lambda_{\min}^{\widehat{\boldsymbol{b}}_{\mathrm{d}}}$ of the damage measure

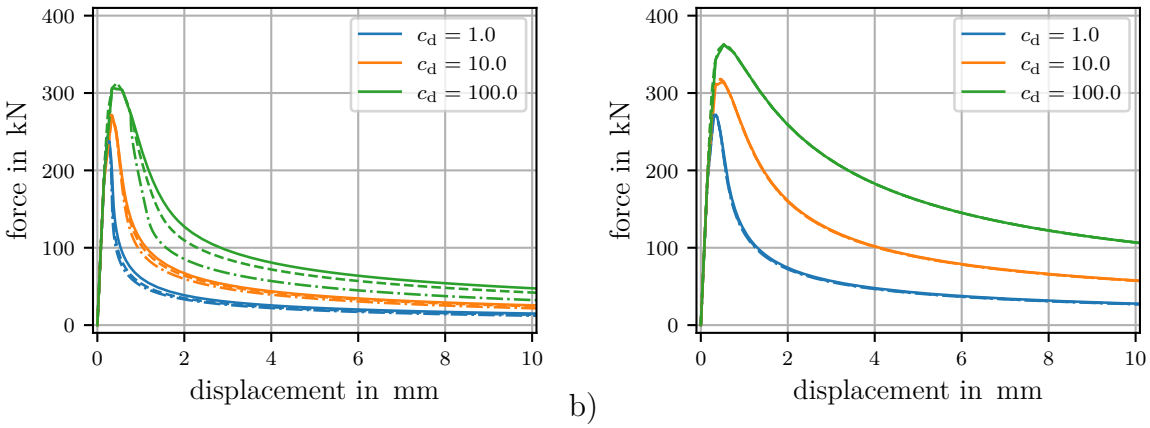

Figure 4.8: Load displacement diagrams of the plate with a hole without plasticity evolution discretised with $n_{el} = 384$ (solid line), $n_{el} = 1350$ (dashed line) or $n_{el} = 5400$ (dash-dotted line) elements for three different values of the regularisation parameter c_d in mm^2. a) Partial regularisation with a low coupling parameter ($b_d = 10.0$). b) Regularisation with a higher coupling parameter ($b_d = 100.0$).

$\widehat{\boldsymbol{b}}_d$ on the deformed contours of the simulations discretised with $n_{el} = 1350$ on the left and $n_{el} = 5400$ on the right are depicted in Figure 4.9. In the contour plots with the simulations using the low coupling parameter $b_d = 10.0$, Figure 4.9a), the deformation evidently localises in the first element row. Although damage mostly evolves in the first element row, the second row is also damaged. Localisation starts only after some damage already evolved. The response is partially regularised, i.e. localisation only starts after a certain amount of loading is surpassed. The contour plot of the simulations with $b_d = 100.0$, Figure 4.9b), show no localisation, i.e. damage evolved gradually decreasing from bottom to top with matching responses for both depicted discretisations.

As shown by these examples, regularisation of the anisotropic (brittle) damage model can be achieved by a micromorphic extension based on the scalar damage hardening variable α_d.

4.10.3 Elastoplasticity

After demonstrating a successful regularisation of the model without plasticity evolution, the response of the model without damage evolution is studied next, i.e. the damage initiation threshold is raised to $M_d^{max0} = 9.0 \times 10^9$ MPa. In contrast to the previous examples, it is first analysed whether the response of the elastoplastic model without evolution of damage actually localises and whether a regularisation is required. To this end, the non-local field variables ϕ_d and ϕ_p are constrained to zero and the coupling parameters b_p and b_d are set to zero as well.

The response of the boundary value problem using linear hardening ($n_p = 1.0$), see Figure 4.10a), only exhibits localisation for comparatively low values of the hardening modulus h_p and especially for $h_p = 2000$ MPa no localisation is observed. In contrast,

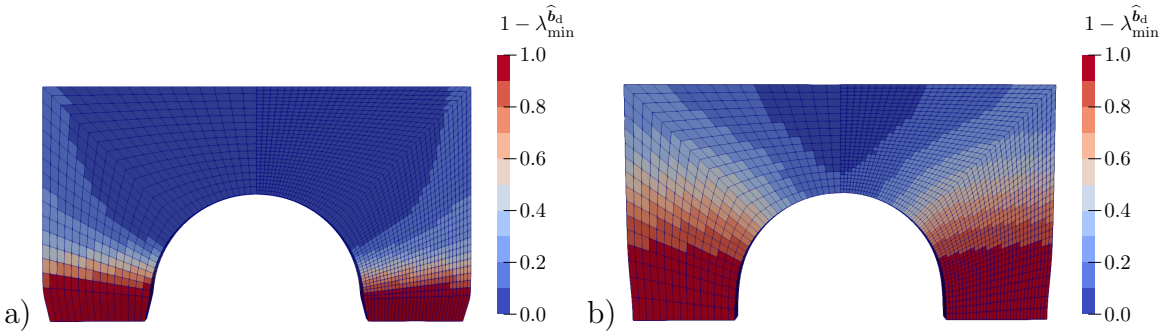

Figure 4.9: Contour plots of the minimum eigenvalue in the form of $1-\lambda^{\widehat{\boldsymbol{b}}_{\mathrm{d}}}_{\mathrm{min}}$ of the damage measure $\widehat{\boldsymbol{b}}_{\mathrm{d}}$ with $c_{\mathrm{d}}=10.0$ for the medium ($n_{\mathrm{el}}=1350$) and fine ($n_{\mathrm{el}}=5400$) discretisations of the plate with a hole simulation without plasticity evolution at a prescribed displacement of $u=10\,\mathrm{mm}$. a) Plot of the simulation with damage coupling parameter $b_{\mathrm{d}}=10.0$ resulting in localisation. b) Plot of the simulation with coupling parameter $b_{\mathrm{d}}=100.0$ resulting in a regularised response.

the response of the boundary value problem using non-linear hardening ($n_{\mathrm{p}}=0.25$), see Figure 4.10b), typically localises as the rate of hardening decreases. The localisation can be prevented by choosing a sufficiently large coupling parameter, as evident from Figure 4.10c), where a partially regularised response is obtained with a coupling parameter $b_{\mathrm{p}}=1.0$, and Figure 4.10d), where regularisation is achieved by increasing the coupling parameter to $b_{\mathrm{p}}=10.0$. The contour plots of the plastic hardening variable α_{p} for the simulations without gradient contributions, depicted in Figure 4.11a), lead to localisation as most of the deformation as well as most of the evolution of plasticity are localised in the first element row. Activating the plastic gradient contribution, see Figure 4.11b), results in a regularised response where deformation and evolution of plasticity is spread over multiple element rows.

4.10.4 Elastoplasticity with damage

The analysis of the regularisation behaviour of the coupled model is, with the findings from the previous section in mind, performed separately for linear and non-linear hardening. Considering non-linear hardening first, one observes an unsuccessful regularisation if only one of the non-local fields is active, i.e. neither by solely incorporating non-local damage ϕ_{d}, Figure 4.13a), nor by solely incorporating non-local plasticity ϕ_{p}, Figure 4.13b), regularisation can be achieved. Figure 4.14 depicts a) evolution of damage in form of the minimum eigenvalue of the damage metric $\widehat{\boldsymbol{b}}_{\mathrm{d}}$ and b) evolution of plasticity by means of the plastic hardening variable for the simulation where only non-local damage is incorporated. One observes a distributed evolution of damage, but on the contrary a strongly localised evolution of plasticity. Increasing the coupling parameters b_{p} or, respectively, b_{d} further — $b_{\mathrm{p}}=100$ and $b_{\mathrm{d}}=1000$ were tested — leads to less stable numerical solutions and still does not regularise the response.

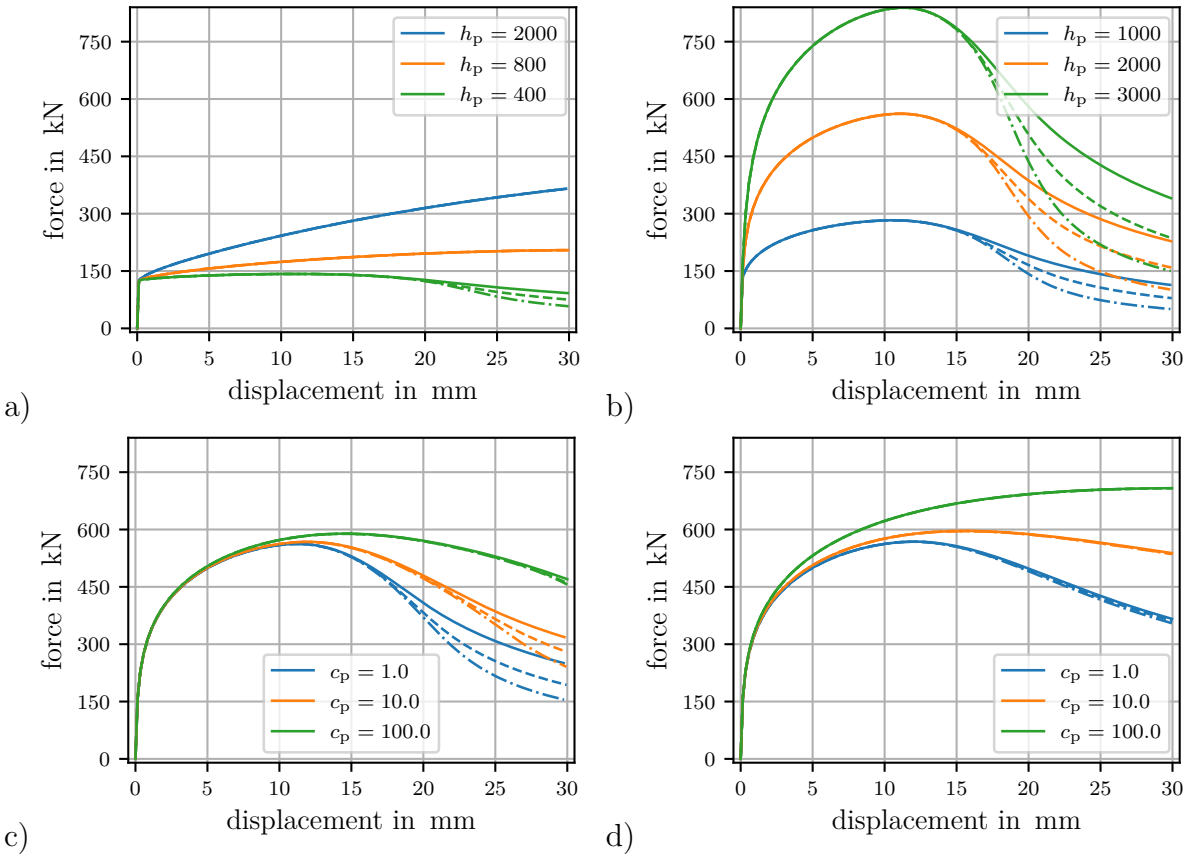

Figure 4.10: Load displacement diagrams of the plate with a hole without damage evolution discretised with $n_{el} = \{384, 1350, 5400\}$ elements. a) Partial localisation for linear hardening ($n_p = 1.0$) with three different hardening moduli h_p in MPa. b) Localisation for non-linear hardening ($n_p = 0.25$). c) Incomplete regularisation with $b_p = 1.0$ for three different values of the plastic regularisation parameter c_p in mm^2. d) Successful regularisation with $b_p = 10.0$.

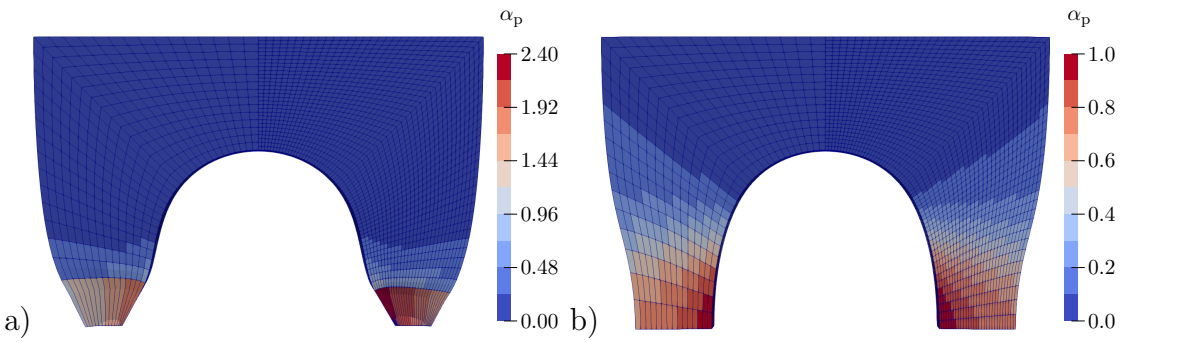

Figure 4.11: Contour plots of plastic hardening variable α_p for the medium ($n_{el} = 1350$) and fine ($n_{el} = 5400$) discretisations of the plate with a hole simulation without damage evolution and with non-linear hardening ($h_p = 2000$ MPa, $n_p = 0.25$) at a prescribed displacement of $u = 30$ mm. a) Plot of the simulation without any gradient contributions ($b_p = 0.0$) resulting in localisation. b) Plot of the simulation with coupling parameter $b_p = 10.0$ and $c_p = 10.0$ mm^2 resulting in a regularised response.

Knowing that plasticity and damage evolution each lead to localisation on their own, it is not surprising that the coupled response cannot be regularised by considering only one of the non-local field variables. Consequently, the response is regularised once both non-local variables are active and once the coupling parameter b_d (and b_p) is chosen to be sufficiently large, see Figure 4.13c) and d). In this case, evolution of damage as well as plasticity is independent of discretisation, see Figure 4.15.

Figure 4.16 shows contour plots of the scalar anisotropy measure

$$\chi_\mathrm{d} := \frac{[1-\lambda^{\widehat{\boldsymbol{b}}_\mathrm{d}}_{\mathrm{min}}]-[1-\lambda^{\widehat{\boldsymbol{b}}_\mathrm{d}}_{\mathrm{max}}]}{\max(1-\lambda^{\widehat{\boldsymbol{b}}_\mathrm{d}}_{\mathrm{min}},\epsilon)}\,, \tag{4.166}$$

with $\epsilon = 10^{-12}$, for simulations with damage anisotropies of $\zeta_\mathrm{d} = 0.25$ and $\zeta_\mathrm{d} = 0.75$. One observes, the anisotropy measure χ_d to be constant where damage evolved (and zero where no damage evolved). Apparently, the parameter ζ_d directly influences the difference between the eigenvalues of the damage metric $\widehat{\boldsymbol{b}}_\mathrm{d}$ and the relation $\chi_\mathrm{d} = 1-\zeta_\mathrm{d}$ (at least in case of monotonous loading) seems to hold.

Remark 14 *The damage anisotropy parameter ζ_d may be correlated to experimental data of crack angle distributions. Consider a patch of material with several micro-cracks as depicted in Figure 4.12, which schematically represents an image obtained from electron microscopy. While it is not possible to determine absolute values of damage variables solely from these images, relative measures may be deducted. Let $\overline{d}_{0^\circ}$ and $\overline{d}_{90^\circ}$ be the two-dimensional damage variable horizontally (along the tensile axis) and vertically (perpendicular to the tensile axis), respectively. Furthermore, let $\overline{l}_{0^\circ}$ and $\overline{l}_{90^\circ}$ be the projected crack lengths onto the horizontal or vertical axis, respectively, i.e.*

$$\overline{l}_{0^\circ} = \sum_i l_i|\cos(\alpha_i)|\,, \quad \textit{and} \quad \overline{l}_{90^\circ} = \sum_i l_i|\sin(\alpha_i)|\,, \tag{4.167}$$

then, two-dimensional damage variables may be given by

$$\overline{d}_{0^\circ} = \frac{\overline{l}_{0^\circ}}{l_0}\,, \quad \textit{and} \quad \overline{d}_{90^\circ} = \frac{\overline{l}_{90^\circ}}{l_0}\,, \tag{4.168}$$

with l_0 being the length of the considered patch of microstructure.

The definition of the damage variables based on the projected crack-lengths equally assigns a damage value to a microstructure with a single long crack and two cracks with half the length stacked on top of each other. In reality, two shorter cracks result in a less degraded stiffness (and lower damage values). A more accurate approach might be a FE-simulation of a specific (observed) patch of microstructure where cracks are resolved explicitly in order to determine differences of the effective stiffness compared to a reference stiffness of an undamaged patch of material. For the purpose of evaluating the anisotropy parameter and the given data from [120] the herein described (simpler) methodology seems to be sufficient.

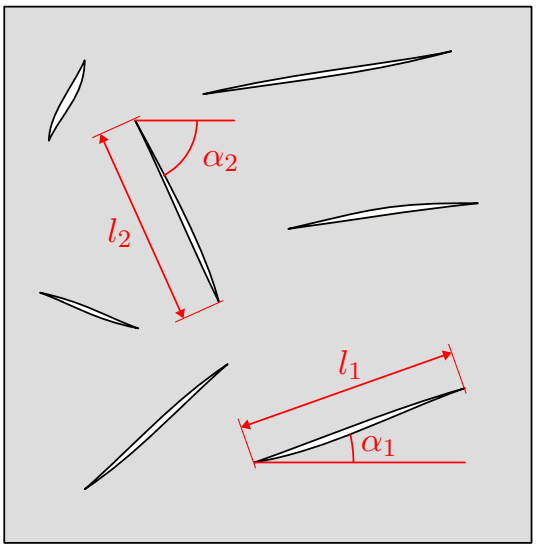

Figure 4.12: Schematic illustration of micro-cracks of various lengths and orientations. Two cracks with lengths l_1 and l_2 are highlighted which are oriented with respect to the horizontal axis by angles α_1 and α_2.

Formulating the scalar anisotropy measure χ_d*, cf.* (4.166)*, with these two-dimensional damage variables yields*

$$\chi_\mathrm{d} = \frac{\overline{d}_{90^\circ} - \overline{d}_{0^\circ}}{\overline{d}_{90^\circ}} = \frac{\overline{l}_{90^\circ} - \overline{l}_{0^\circ}}{\overline{l}_{90^\circ}} \,. \tag{4.169}$$

In [120] Figure 7a provides the crack angle distribution of martensite cracks in DP800 under uniaxial tension by means of a neural network working on images obtained from electron microscopy. The data is summarised in Table 4.6[1] *and extended by the projected lengths. The given data results in* $\chi_\mathrm{d} = 0.6814$*, which indicates* $\zeta_\mathrm{d} = 1 - \chi_\mathrm{d} = 0.3186$*.*

In order to study the regularisation behaviour in the case of linear hardening, the localisation due to damage initiation and evolution needs to occur earlier. To this end, the damage initiation threshold is reduced to $M_\mathrm{d}^{\max 0} = 2.0\,\mathrm{MPa}$ and the damage hardening modulus is reduced to $h_\mathrm{d} = 20.0\,\mathrm{MPa}$. In addition, the maximum loading is increased to $u = 60\,\mathrm{mm}$.

As evident in Figure 4.17a), solely using the non-local damage variable ϕ_d for regularisation does not lead to a (completely) regularised response. The contour plots of the evolution of damage, left column of Figure 4.18, and of plasticity, left column of Figure 4.19, depict a localising evolution of plasticity, but no localisation of the evolution of damage — surprisingly, since the model without damage evolution in case of linear hardening ($h_\mathrm{p} = 2000\,\mathrm{MPa}$) does not localise.

[1] All fractions in Figure 7a of [120] only accumulate to approximately 85% (bar heights were measured in pixels and converted with given axis). Normalisation by dividing all fractions with 85% yields the values listed in the column "corrected fraction".

Table 4.6: Accumulated probabilities of martensite crack angle distribution for uniaxial tension, taken from [120], and the projected crack lengths assuming uniform crack lengths.

α_i	fraction	corrected fraction	$l_{i,0^\circ}$	$l_{i,90^\circ}$
5°	2.98%	3.5%	0.0349	0.0031
15°	0.85%	1.0%	0.0097	0.0026
25°	0.00%	0.0%	0.0000	0.0000
35°	0.85%	1.0%	0.0082	0.0057
45°	2.98%	3.5%	0.0247	0.0247
55°	3.83%	4.5%	0.0258	0.0369
65°	17.87%	21.0%	0.0887	0.1903
75°	20.00%	23.5%	0.0608	0.2270
85°	35.74%	42.0%	0.0366	0.4184
summation	85.11%	100.0%	0.2895	0.9087

Activating the non-local plastic variable ϕ_p yields a (mostly) regularised response, see Figure 4.17b). In the right columns in Figure 4.18 and Figure 4.19 one observes a successful regularisation of the evolution of damage and plasticity at a prescribed displacement of $u = 45\,\mathrm{mm}$. However, at $u = 60\,\mathrm{mm}$, localisation (especially of plasticity) seems to have occurred.

4.10.5 Elastoplasticity with damage and activated deterioration function

Finally, the influence of an activated damage deterioration function f_dp (with $\alpha_\mathrm{p,max} = 0.6$ and $h_\mathrm{dp} = 10.0$) is analysed for an inhomogeneous problem, i.e. the same plate with a hole which was considered previously. Figure 4.20 depicts the response of the plate with a hole simulation for different values of the damage deterioration h_dp and damage deterioration offset $\alpha_\mathrm{p,max}$ for three different discretisations. The principal behaviour is as expected (identical to the findings for the homogeneous case). A higher offset leads to a later drop in force and a higher damage deterioration leads to a sharper, more abrupt drop.

Comparing the response of the different discretisations, one notices successful regularisation only up until the point of the sudden drop in force. The parameters concerned with regularisation are varied and the results are depicted in Figure 4.21. One observes that neither a variation of the damage gradient parameter c_d nor a variation of the plastic gradient parameter c_p leads to a completely regularised response. The contour plots in Figure 4.22 of the evolution of damage and plasticity at a prescribed displacement of $u = 18\,\mathrm{mm}$ (before the drop in force) depict a regularised response. Increasing the loading further to $u = 21\,\mathrm{mm}$ (beyond the drop in force) leads to clearly visible localisation in the first (bottom) row of elements, see Figure 4.23.

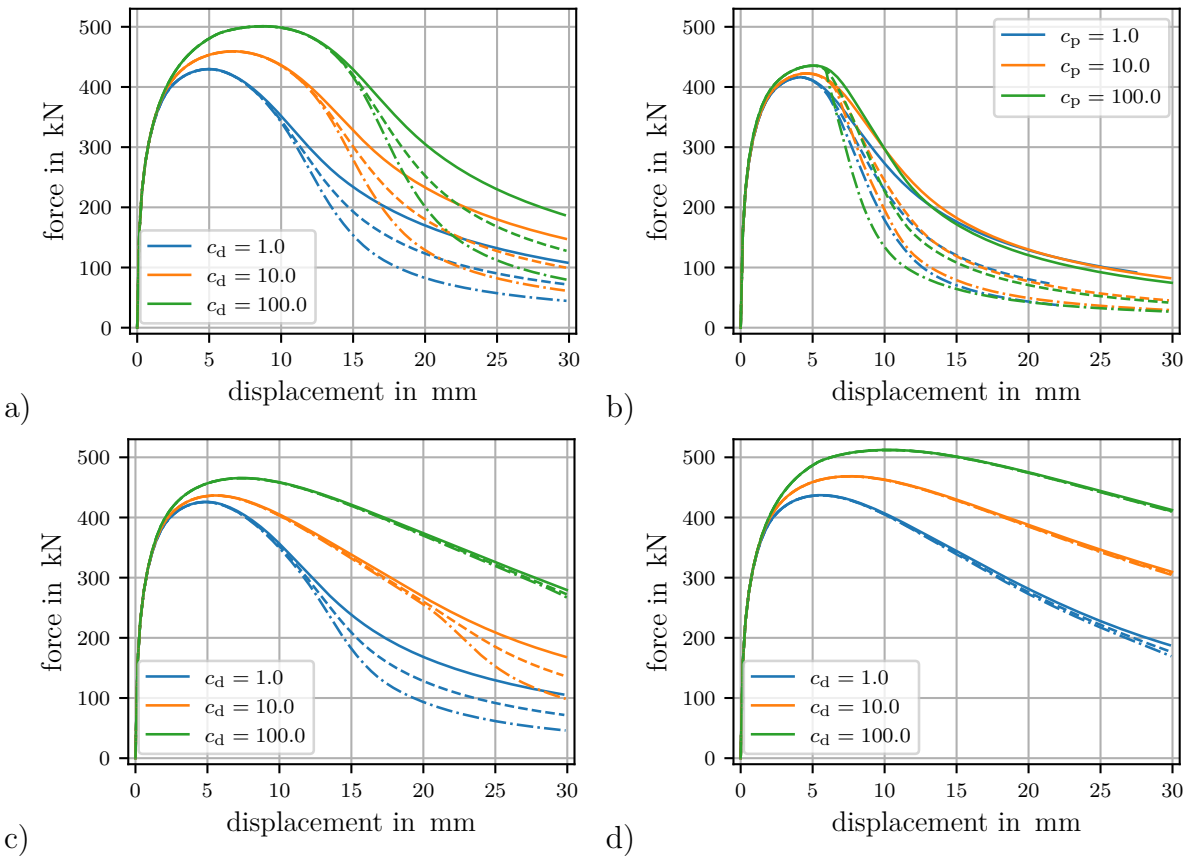

Figure 4.13: Load displacement diagrams of the plate with a hole using the coupled model with nonlinear hardening ($n_p = 0.25$) discretised with $n_{el} = \{384, 1350, 5400\}$ elements. Variation of the damage regularisation parameter c_d or, respectively, plastic regularisation parameter c_p in mm^2 is represented by different line colours. a) Incomplete regularisation with $b_d = 100.0$ and $b_p = 0.0$, b) incomplete regularisation with $b_d = 0.0$ and $b_p = 10.0$, c) incomplete regularisation with $b_d = 10.0$ and $b_p = 10.0$, d) regularisation with $b_d = 100.0$ and $b_p = 10.0$.

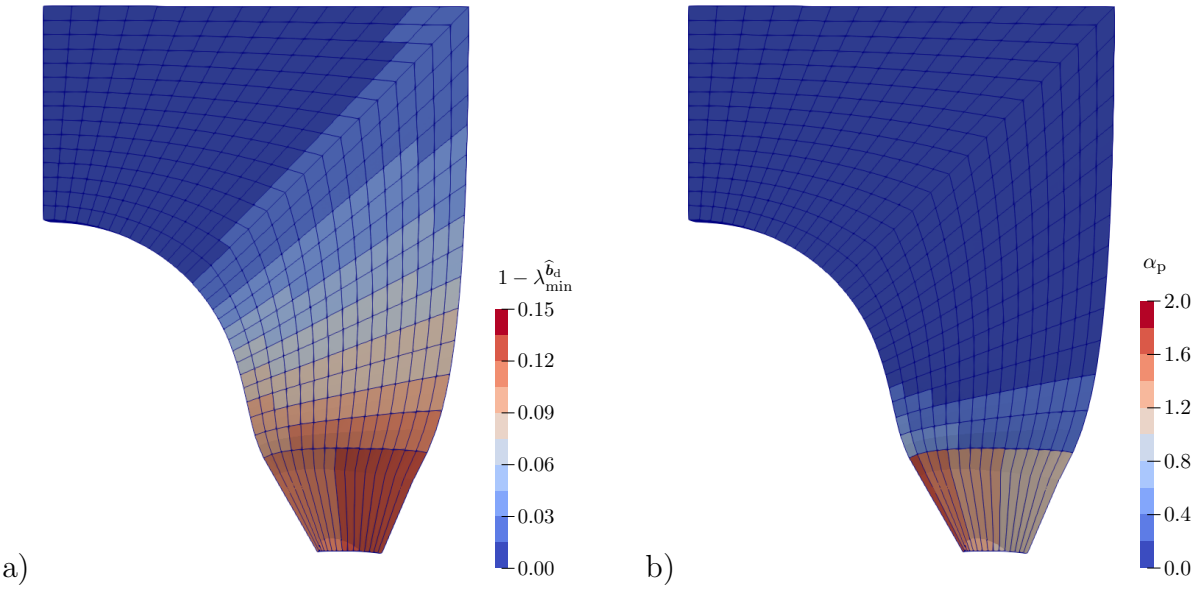

Figure 4.14: Contour plots of the plate with a hole (discretised with 1350 elements) simulation results at a prescribed displacement of $u = 30\,\mathrm{mm}$. Localising response where only damage is regularised with $b_\mathrm{d} = 100.0$ and $c_\mathrm{d} = 10.0\,\mathrm{mm}^2$ and plasticity is allowed to localise, i.e. $b_\mathrm{p} = 0.0$ together with $\phi_\mathrm{p} = 0$ as boundary condition. a) Plot of the minimum eigenvalue in the form of $1 - \lambda^{\widehat{\boldsymbol{b}}_\mathrm{d}}_\mathrm{min}$ of the damage measure $\widehat{\boldsymbol{b}}_\mathrm{d}$. b) Plot of the plastic hardening variable α_p.

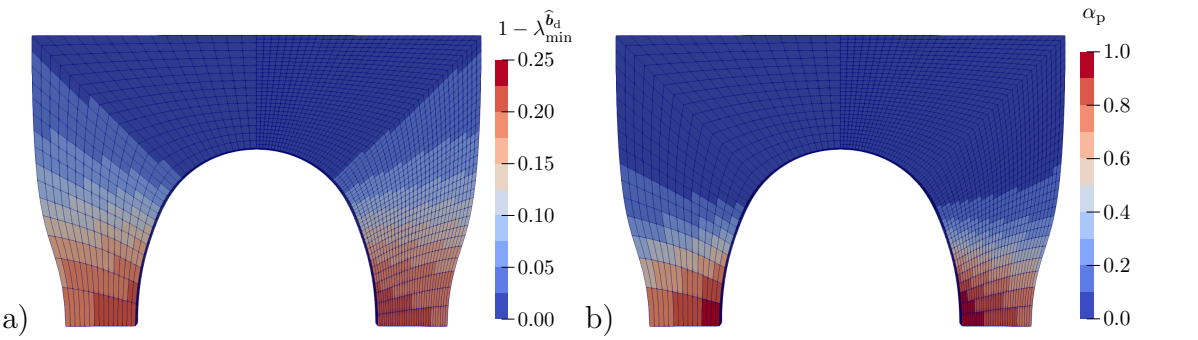

Figure 4.15: Contour plots of the simulations of the plate with a hole with medium ($n_\mathrm{el} = 1350$) and fine ($n_\mathrm{el} = 5400$) discretisations at a prescribed displacement of $u = 30\,\mathrm{mm}$. Regularised response with $b_\mathrm{d} = 100.0$, $b_\mathrm{p} = 10.0$, $c_\mathrm{d} = 10.0\,\mathrm{mm}^2$ and $c_\mathrm{p} = 10.0\,\mathrm{mm}^2$. a) Plot of the minimum eigenvalue in the form of $1 - \lambda^{\widehat{\boldsymbol{b}}_\mathrm{d}}_\mathrm{min}$ of the damage measure $\widehat{\boldsymbol{b}}_\mathrm{d}$. b) Plot of the plastic hardening variable α_p.

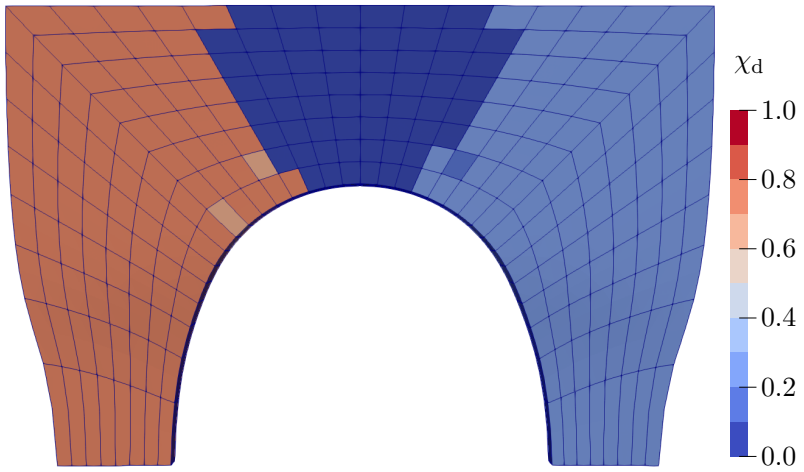

Figure 4.16: Contour plot of the anisotropy measure χ_d for the regularised ($b_\mathrm{d} = 100.0$, $c_\mathrm{d} = 10.0\,\mathrm{mm}^2$, $b_\mathrm{p} = 10.0$, $c_\mathrm{p} = 10.0\,\mathrm{mm}^2$) simulation of the plate with a hole with coarse ($n_\mathrm{el} = 384$) discretisation at a prescribed displacement of $u = 30\,\mathrm{mm}$. The left side shows the simulation with $\zeta_\mathrm{d} = 0.25$ and the right side the simulation with $\zeta_\mathrm{d} = 0.75$.

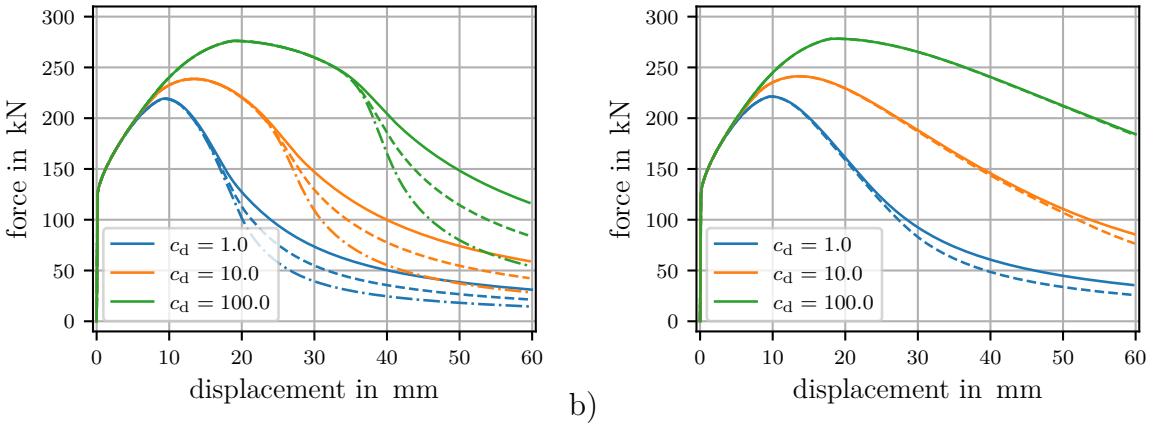

Figure 4.17: Load displacement diagrams of the plate with a hole using the coupled model with linear hardening ($n_\mathrm{p} = 1.0$) discretised with $n_\mathrm{el} = 384$, 1350, 5400 elements. The loading amplitude is doubled to $u = 60\,\mathrm{mm}$ because localisation did not occur until $u = 30\,\mathrm{mm}$. Variation of the damage regularisation parameter c_d in mm^2. a) incomplete regularisation with $b_\mathrm{d} = 100.0$ and $b_\mathrm{p} = 0.0$, b) partial regularisation with $b_\mathrm{d} = 100.0$ and $b_\mathrm{p} = 10.0$.

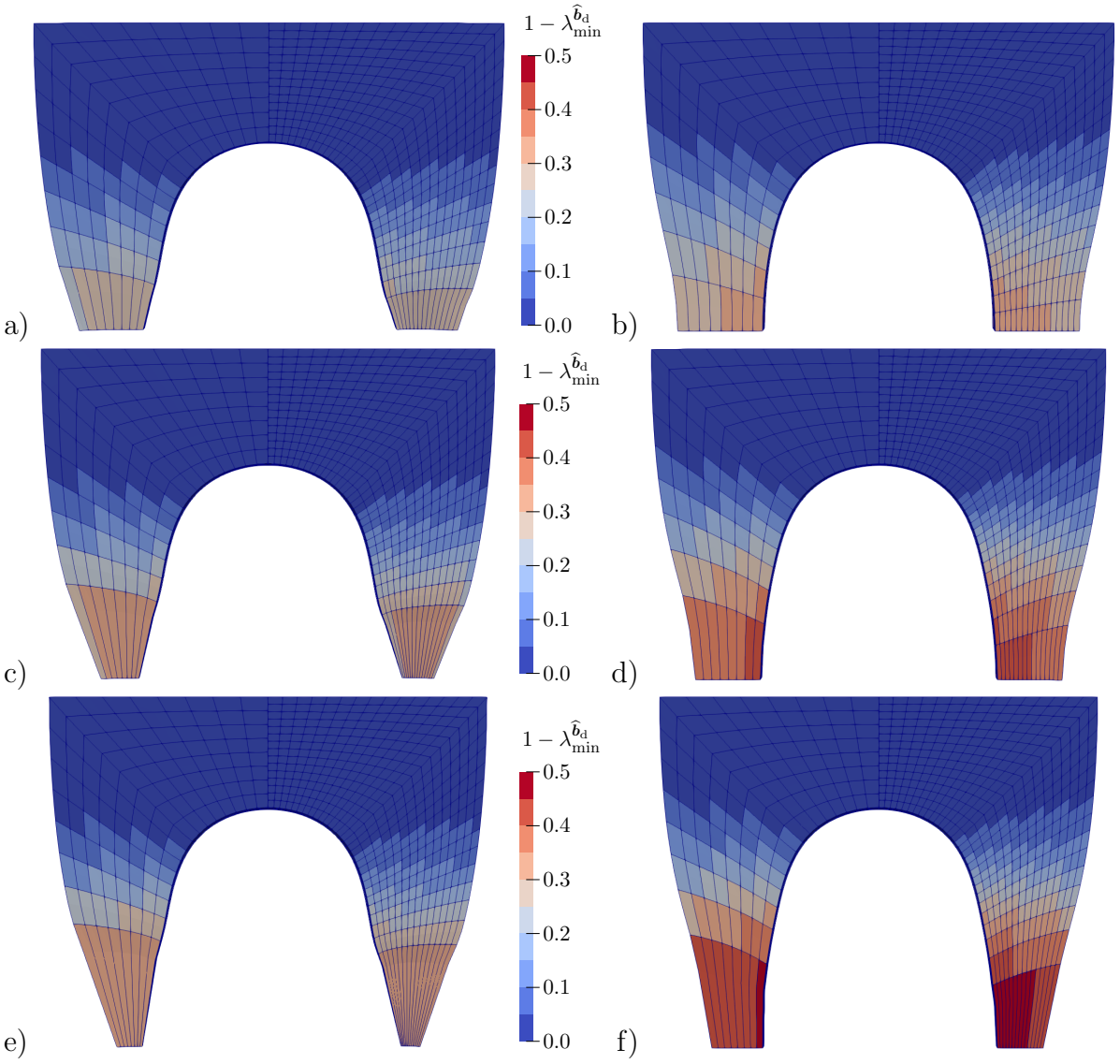

Figure 4.18: Contour plots of the minimum eigenvalue in the form of $1 - \lambda^{\widehat{\boldsymbol{b}}_\mathrm{d}}_\mathrm{min}$ of the damage measure $\widehat{\boldsymbol{b}}_\mathrm{d}$ of the simulations of the plate with a hole with coarse ($n_\mathrm{el} = 384$) and medium ($n_\mathrm{el} = 1350$) discretisations using linear hardening ($h_\mathrm{p} = 2000\,\mathrm{MPa}$). Localising response with $b_\mathrm{d} = 100.0$ and $c_\mathrm{d} = 10.0\,\mathrm{mm}^2$ while $b_\mathrm{p} = 0.0$ together with $\phi_\mathrm{p} = 0$ as boundary condition on the left side a), c), e) and partially regularising response with $b_\mathrm{d} = 100.0$ and $c_\mathrm{d} = 10.0\,\mathrm{mm}^2$ as well as $b_\mathrm{p} = 10.0$ and $c_\mathrm{p} = 10.0\,\mathrm{mm}^2$ on the right side b), d), f). Plot at a prescribed displacement of $u = 30\,\mathrm{mm}$ in a) and b), of $u = 45\,\mathrm{mm}$ in c) and d), and of $u = 60\,\mathrm{mm}$ in e) and f).

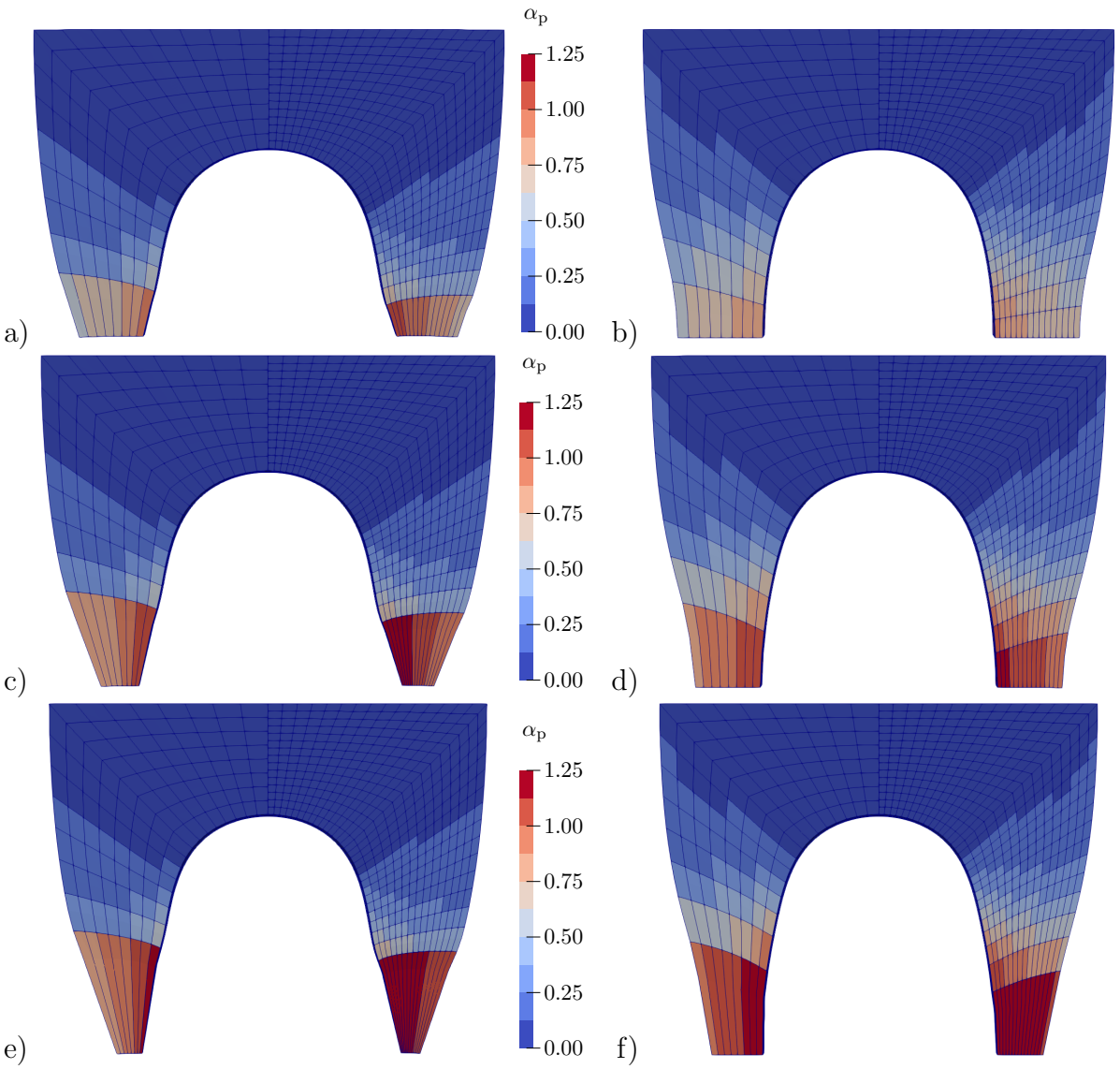

Figure 4.19: Contour plots of the plastic hardening variable α_p of the simulations of the plate with a hole with coarse ($n_{el} = 384$) and medium ($n_{el} = 1350$) discretisations using linear hardening ($h_p = 2000\,\text{MPa}$). Localising response with $b_d = 100.0$ and $c_d = 10.0\,\text{mm}^2$ while $b_p = 0.0$ together with $\phi_p = 0$ as boundary condition on the left side a), c), e) and partially regularising response with $b_d = 100.0$ and $c_d = 10.0\,\text{mm}^2$ as well as $b_p = 10.0$ and $c_p = 10.0\,\text{mm}^2$ on the right side b), d), f). Plot at a prescribed displacement of $u = 30\,\text{mm}$ in a) and b), of $u = 45\,\text{mm}$ in c) and d), and of $u = 60\,\text{mm}$ in e) and f).

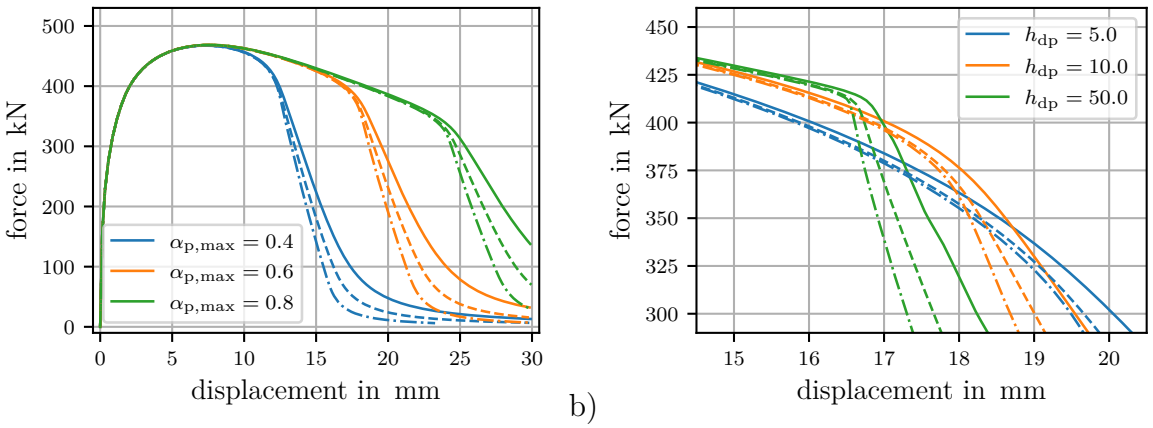

Figure 4.20: Load displacement diagrams of the plate with a hole using the coupled model with activated deterioration function f_{dp} discretised with $n_{el} = 384, 1350, 5400$ elements. a) Influence of the deterioration offset $\alpha_{p,max}$ using $h_{dp} = 10.0$. b) Influence of the damage deterioration h_{dp} using $\alpha_{p,max} = 0.6$ (zoomed in).

The lack of regularisation beyond the point of drop in force is not surprising, since the deterioration function f_{dp} also affects the non-local part of the damage hardening stress β_d^{nl}. However, the localised response after the point of drop in force is not in the focus of the present work, which mainly focusses on the prediction of states before, respectively up to failure. This point of failure is predicted nearly identical regardless of which discretisation is chosen, but the parameters influencing the regularisation do have a significant impact on the point of failure, which poses challenges for an eventual parameter identification.

4.11 Formulation in terms of Haigh-Westergaard coordinates

Often, initiation of damage or plasticity during experiments is described in terms of stress triaxiality and Lode angle, see also Section 1.3.2. From the modelling perspective, however, formulating the damage initiation criterion in terms of the damage driving force has the advantage of guaranteed positive dissipation if the governing potential is convex in the driving force (and if evolution equations are of associative nature). The goal of this section is to derive the conditions for convexity of the damage initiation potential with respect to the driving force if formulated in terms of stress triaxiality η_e and Lode angle θ_e. To this end, the damage initiation surface $\mathcal{S}$ is interpreted as a geometric surface in the space of the eigenvalues of the damage driving force, i.e. $M_{d,i}$ with $i = 1, 2, 3$. Thereafter, the convexity conditions can be obtained by making use of a differential geometry based approach, cf. [75, 169], requiring the surface to be

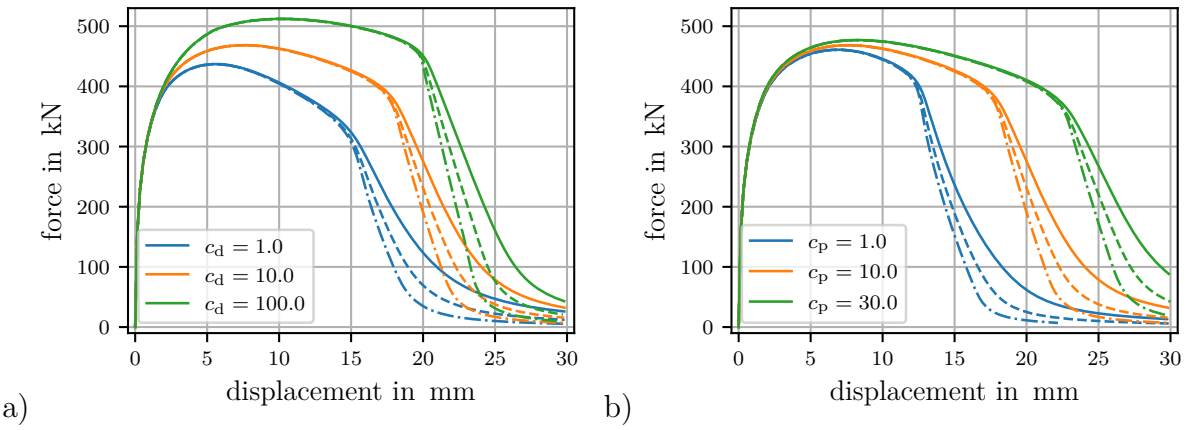

Figure 4.21: Load displacement diagrams of the plate with a hole using the coupled model with activated deterioration function f_{dp} ($h_{\mathrm{dp}} = 10.0$, $\alpha_{\mathrm{p,max}} = 0.6$) discretised with $n_{\mathrm{el}} = 384$, 1350, 5400 elements. a) influence of the regularisation parameter c_{d} (in mm^2) with $b_{\mathrm{d}} = 100.0$, $c_{\mathrm{p}} = 10.0\,\mathrm{mm}^2$ and $b_{\mathrm{p}} = 10.0$. b) influence of the regularisation parameter c_{p} (in mm^2) with $b_{\mathrm{p}} = 10.0$, $c_{\mathrm{d}} = 10.0\,\mathrm{mm}^2$ and $b_{\mathrm{d}} = 100.0$.

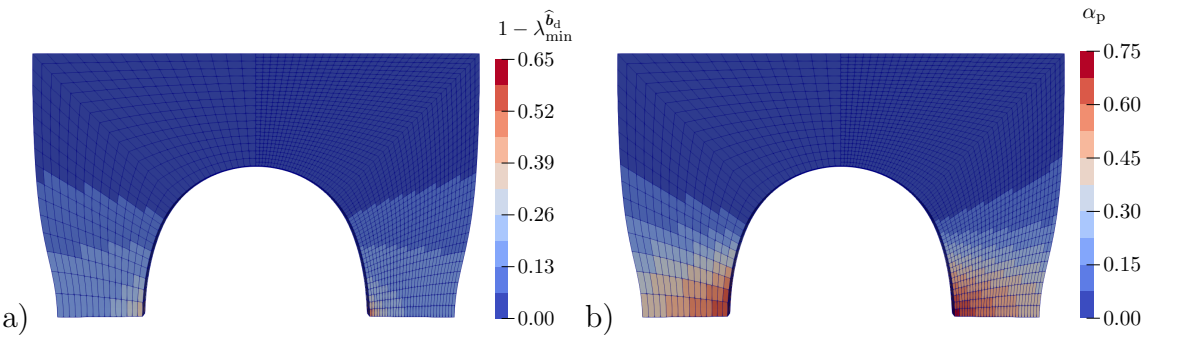

Figure 4.22: Contour plots of the simulations of the plate with a hole with medium ($n_{\mathrm{el}} = 1350$) and fine ($n_{\mathrm{el}} = 5400$) discretisations with activated deterioration function ($h_{\mathrm{dp}} = 10.0$, $\alpha_{\mathrm{p,max}} = 0.6$) at a prescribed displacement of $u = 18\,\mathrm{mm}$. Response with $b_{\mathrm{d}} = 100.0$ and $c_{\mathrm{d}} = 10.0\,\mathrm{mm}^2$ as well as $b_{\mathrm{p}} = 10.0$ and $c_{\mathrm{p}} = 10.0\,\mathrm{mm}^2$. a) Plot of the minimum eigenvalue in the form of $1 - \lambda^{\widehat{\boldsymbol{b}}_{\mathrm{d}}}_{\mathrm{min}}$ of the damage measure $\widehat{\boldsymbol{b}}_{\mathrm{d}}$ and b) plot of the plastic hardening variable α_{p}.

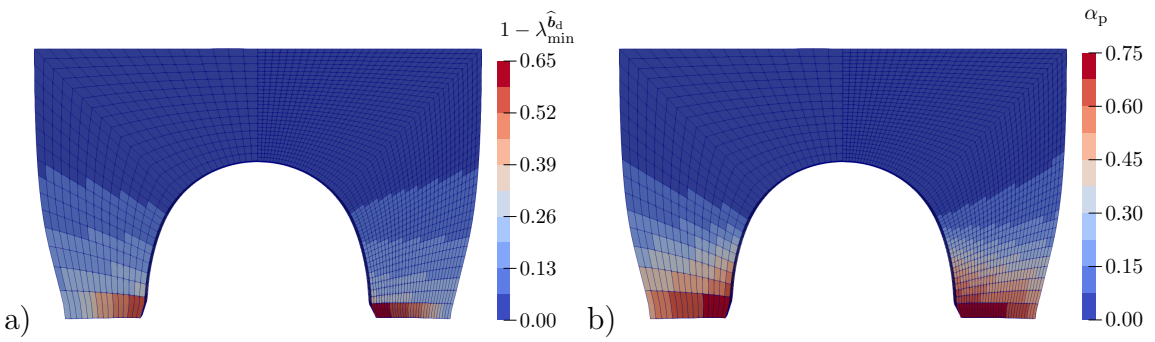

Figure 4.23: Contour plots of the simulations of the plate with a hole with medium ($n_{el} = 1350$) and fine ($n_{el} = 5400$) discretisations with activated deterioration function ($h_{dp} = 10.0$, $\alpha_{p,max} = 0.6$) at a prescribed displacement of $u = 21\,\text{mm}$. Response with $b_d = 100.0$ and $c_d = 10.0\,\text{mm}^2$ as well as $b_p = 10.0$ and $c_p = 10.0\,\text{mm}^2$. a) Plot of the minimum eigenvalue in the form of $1 - \lambda^{\widehat{b}_d}_{min}$ of the damage measure $\widehat{\boldsymbol{b}}_d$ and b) plot of the plastic hardening variable α_p.

parametrised in the form of

$$\left[M^{\boldsymbol{S}}_{d,1},\, M^{\boldsymbol{S}}_{d,2},\, M^{\boldsymbol{S}}_{d,3}\right] \in \mathcal{S} \subset \mathbb{R}^3\,, \quad \text{with} \quad \left[M^{\boldsymbol{S}}_{d,1},\, M^{\boldsymbol{S}}_{d,2},\, M^{\boldsymbol{S}}_{d,3}\right] = \boldsymbol{S}(\eta_e,\, \theta_e)\,. \tag{4.170}$$

4.11.1 Parametrisation of the damage initiation surface

Let $\boldsymbol{s}$ be some symmetric stress measure with the eigenvalues s_1, s_2, s_3. Haigh-Westergaard coordinates, cf. [78, 140, 182], are given in terms of pressure p, deviatoric stress q and Lode angle θ and may be formulated in terms of the eigenvalues s_i as

$$\begin{aligned}
p &:= \frac{1}{3}\left[s_1 + s_2 + s_3\right], && p \in (-\infty;\, \infty)\,,\\
q &:= \sqrt{\frac{1}{3}\left[[s_3 - s_2]^2 + [s_1 - s_3]^2 + [s_2 - s_1]^2\right]} = \sqrt{2\,J_2^{\boldsymbol{s}}}\,, && q \in [0;\, \infty)\,,\\
\theta &:= \frac{1}{3}\arccos\left(\frac{\sqrt{54}}{q^3}\left[[s_1 - p]\,[s_2 - p]\,[s_3 - p]\right]\right), && \theta \in (-\frac{\pi}{3};\, \frac{\pi}{3})
\end{aligned} \tag{4.171}$$

and, inversely, the eigenvalues in terms of Haigh-Westergaard coordinates are given by

$$s_i = p + \sqrt{\frac{2}{3}}\,q\,\cos(\theta + \alpha_i)\,, \qquad \text{with} \qquad \alpha_i = [i-1]\,\frac{2\,\pi}{3}\,, \quad i = 1,\, 2,\, 3\,. \tag{4.172}$$

Triaxiality can be expressed in terms of pressure and deviatoric stress as

$$\eta = \sqrt{\frac{2}{3}}\,\frac{p}{q}\,, \quad \text{and equivalently} \quad p = \sqrt{\frac{3}{2}}\,\eta\,q\,, \tag{4.173}$$

which, if inserted into (4.172), yields the eigenvalues in the form of

$$s_i = \sqrt{\frac{3}{2}}q\,\left[\eta + \frac{2}{3}\,\cos(\theta + \alpha_i)\right]\,. \tag{4.174}$$

The triaxiality measure η is not defined for zero deviatoric stress ($q = 0$). However, the damage surface for purely volumetric states of damage driving force is trivially solved such that $q > 0$ is assumed in the following.

The damage initiation potential Φ_d, cf. (4.41), is determined by the equivalent stress function $M_\mathrm{d}^\mathrm{eq}(\overline{\boldsymbol{M}}_\mathrm{d})$, cf. (4.45), in terms of the first and second invariant

$$\begin{aligned} I_1^{\overline{\boldsymbol{M}}_\mathrm{d}} &= \boldsymbol{I} : \overline{\boldsymbol{M}}_\mathrm{d} = \sqrt{\frac{27}{2}}\,\eta_\mathrm{d}\,q_\mathrm{d}\,, \\ I_2^{\overline{\boldsymbol{M}}_\mathrm{d}} &= J_2^{\overline{\boldsymbol{M}}_\mathrm{d}} + \frac{1}{3}\left[I_1^{\overline{\boldsymbol{M}}_\mathrm{d}}\right]^2 = \frac{1}{2}\,q_\mathrm{d}^2\,\left[1 + 9\,\eta_\mathrm{d}^2\right]\,. \end{aligned} \tag{4.175}$$

The equivalent stress function can now be reformulated in terms of Haigh-Westergaard coordinates as

$$M_\mathrm{d}^\mathrm{eq}(\eta_\mathrm{d},\, q_\mathrm{d}) = \frac{1}{\sqrt{2}}\,q_\mathrm{d}\,\sqrt{9\,[1 + 2\,\zeta_\mathrm{d}]\,\eta_\mathrm{d}^2 + 1 - \zeta_\mathrm{d}}\,. \tag{4.176}$$

In order to obtain the damage initiation surface in terms of stress triaxiality η_e and Lode-angle θ_e, the equivalent damage Mandel stresses (4.176) need to be restated in terms of η_e, q_e and θ_e. To this end, a relation between the damage Mandel stresses in terms of (η_d, q_d, θ_d) and the fictitious elastic Piola-Kirchhoff stresses in terms of (η_e, q_e, θ_e) is required. The damage Mandel stresses are related to the elastic stresses via the relation $\overline{\boldsymbol{M}}_\mathrm{d} = -2\,\overline{\boldsymbol{S}}_\mathrm{e} \cdot \overline{\boldsymbol{E}}_\mathrm{e}$, cf. (4.21). Since the fictitious elastic Piola-Kirchhoff stresses $\overline{\boldsymbol{S}}_\mathrm{e}$ are linear in the fictitious elastic strains $\overline{\boldsymbol{E}}_\mathrm{e}$, the coordinates η_E, q_E and θ_E related to the fictitious elastic strains $\overline{\boldsymbol{E}}_\mathrm{e}$ can be expressed in terms of the stresses by inversion of relation (4.37) as

$$\eta_E = \frac{1 - 2\,\nu}{1 + \nu}\,\eta_\mathrm{e}\,, \qquad q_E = \frac{[1 + \nu]\,q_\mathrm{e}}{E}\,, \qquad \theta_E = \theta_\mathrm{e}\,. \tag{4.177}$$

Combining relations (4.174) with (4.21) and (4.177) allows to write

$$q_\mathrm{d} = \frac{q_\mathrm{e}^2}{E}\,\chi(\eta_\mathrm{e},\,\theta_\mathrm{e})\,, \qquad \eta_\mathrm{d} = -\frac{9\,[1 - 2\,\nu]\,\eta_\mathrm{e}^2 + 2\,[1 + \nu]}{3\,\chi(\eta_\mathrm{e},\,\theta_\mathrm{e})}\,, \tag{4.178}$$

$$\text{with} \quad \chi(\eta_\mathrm{e},\,\theta_\mathrm{e}) := [2 - \nu]\,\sqrt{\frac{1}{6}\,\left[\frac{1 + \nu}{2 - \nu}\right]^2 + \frac{1 + \nu}{2 - \nu}\,\eta_\mathrm{e}\,\cos(3\,\theta_\mathrm{e}) + \frac{3}{2}\,\eta_\mathrm{e}^2}\,. \tag{4.179}$$

Insertion into (4.176) yields

$$M_\mathrm{d}^\mathrm{eq}(\eta_\mathrm{e},\, q_\mathrm{e},\, \theta_\mathrm{e}) = \frac{1}{\sqrt{2}\,E}\,q_\mathrm{e}^2\,\sqrt{\frac{1}{6}\,[1 + 2\,\zeta_\mathrm{d}]\,\left[9\,[1 - 2\,\nu]\,\eta_\mathrm{e}^2 + 2\,[1 + \nu]\right]^2 + [1 - \zeta_\mathrm{d}]\,\chi^2}\,. \tag{4.180}$$

The damage initiation surface $\mathcal{S}$ is set by

$$\Phi_\mathrm{d} = M_\mathrm{d}^\mathrm{eq} - M_\mathrm{d}^\mathrm{max} = 0\,, \tag{4.181}$$

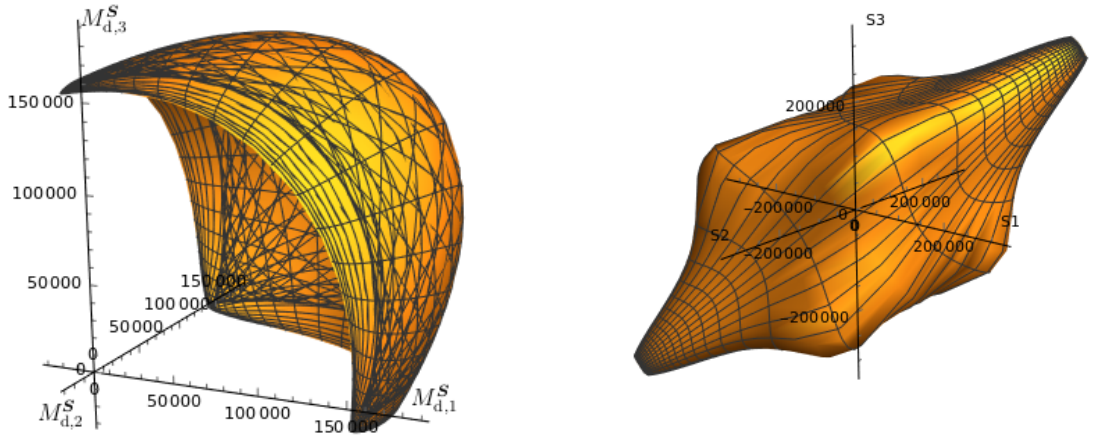

a) b)

Figure 4.24: Graphical representation of the damage initiation surface. a) In the space of (the eigenvalues of) the damage driving force $\widehat{\boldsymbol{M}}_{\mathrm{d}}$ and b) in the space of (the eigenvalues of) the elastic Mandel stresses $\widehat{\boldsymbol{M}}_{\mathrm{e}}$.

which, in combination with (4.180), results in a relation for all $\widetilde{q}_{\mathrm{e}}$ on the surface $\mathcal{S}$ in terms of η_{e} and θ_{e}, i.e.

$$\widetilde{q}^2_{\mathrm{e}}(\eta_{\mathrm{e}},\,\theta_{\mathrm{e}}) = \frac{\sqrt{12}\,E\,M^{\max}_{\mathrm{d}}}{\sqrt{\left[1+2\,\zeta_{\mathrm{d}}\right]\,\left[9\,\left[1-2\,\nu\right]\,\eta^2_{\mathrm{e}}+2\,\left[1+\nu\right]\right]^2+6\,\left[1-\zeta_{\mathrm{d}}\right]\,\chi^2}}\,. \tag{4.182}$$

Consequently, all states of damage Mandel stresses $\overline{\boldsymbol{M}}_{\mathrm{d}}$ on the limit surface $\mathcal{S}$ representing initiation of damage, expressed in terms of eigenvalues by making use of (4.174) for $\overline{\boldsymbol{E}}_{\mathrm{e}}$ and $\overline{\boldsymbol{S}}_{\mathrm{e}}$, are given by

$$M^{\boldsymbol{S}}_{\mathrm{d},i}(\eta_{\mathrm{e}},\,\theta_{\mathrm{e}}) = -\frac{\widetilde{q}^2_{\mathrm{e}}}{E}\,\left[3\,\eta_{\mathrm{e}}+2\,\cos(\theta_{\mathrm{e}}+\alpha_i)\right]\,\left[\left[3-6\,\nu\right]\,\eta_{\mathrm{e}}+\left[2+2\,\nu\right]\,\cos(\theta_{\mathrm{e}}+\alpha_i)\right]\,. \tag{4.183}$$

For the damage initiation surface, cf. (4.45), one obtains — with $\zeta_{\mathrm{d}} = \frac{1}{2}$ — the graphical representation shown in Figure 4.24. The elastic material parameters are assumed to $E = 210\,\mathrm{GPa}$ and $\nu = 0.33$. Seemingly, the surface is convex in the space of the damage driving force but definitely not convex in the space of the elastic Mandel stresses.

4.11.2 Convexity condition of the parametrised damage initiation surface

The derivation of the convexity conditions closely follows the procedure outlined in [169]: A surface $\mathcal{S}$ is convex, if the Gaussian curvature κ_{G} is positive and the mean curvature κ_{M} is negative, i.e.

$$\kappa_{\mathrm{G}} > 0\,, \quad \text{and} \quad \kappa_{\mathrm{M}} < 0\,. \tag{4.184}$$

Let all position vectors $\widehat{\boldsymbol{x}}$ of a surface $\mathcal{S} \subset \mathbb{R}^3$ be given by $\widehat{\boldsymbol{x}} = \boldsymbol{x}(a, b)$ with $a, b \in \mathbb{R}$. The Gaussian and the mean curvature can be expressed in terms of the coefficients of the first and second fundamental form as

$$\kappa_{\mathrm{G}} = \frac{f\,h - g^2}{F\,H - G^2}\,, \quad \text{and} \quad \kappa_{\mathrm{M}} = \frac{f\,H - 2\,g\,G + h\,F}{2\,F\,H - 2\,G^2}\,, \tag{4.185}$$

where the coefficients of the first fundamental form are given by

$$\begin{aligned} F &= \partial_a \boldsymbol{x} \cdot \partial_a \boldsymbol{x}\,, \\ G &= \partial_a \boldsymbol{x} \cdot \partial_b \boldsymbol{x}\,, \\ H &= \partial_b \boldsymbol{x} \cdot \partial_b \boldsymbol{x}\,, \end{aligned} \tag{4.186}$$

and the coefficients of the second fundamental form by

$$\begin{aligned} f &= \boldsymbol{\nu} \cdot \partial_{aa} \boldsymbol{x}\,, \\ g &= \boldsymbol{\nu} \cdot \partial_{ab} \boldsymbol{x}\,, \\ h &= \boldsymbol{\nu} \cdot \partial_{bb} \boldsymbol{x}\,. \end{aligned} \tag{4.187}$$

The coefficients of the second fundamental form (4.187) are defined with the outward unit normal vector

$$\boldsymbol{\nu} = \operatorname{sign}(s)\,\frac{\partial_a \boldsymbol{x} \times \partial_b \boldsymbol{x}}{\|\partial_a \boldsymbol{x} \times \partial_b \boldsymbol{x}\|}\,, \quad \text{with} \quad s = \boldsymbol{x} \cdot [\partial_a \boldsymbol{x} \times \partial_b \boldsymbol{x}]\,, \tag{4.188}$$

where the definition of s uses that the point $(0,\,0,\,0)$ always needs to be inside the surface. Using the Cauchy-Schwarz inequality yields $F\,H > G^2$ and the convexity conditions (4.184) can be simplified to

$$f\,h > g^2\,, \quad \text{and} \quad f\,H + h\,F < 2\,g\,G\,. \tag{4.189}$$

Applying this procedure to the parametrised damage surface (4.183) requires the first and second derivatives of $\boldsymbol{S}(\eta_{\mathrm{e}},\,\theta_{\mathrm{e}})$. In order to keep the terms short, the deviatoric stress $\widetilde{q}_{\mathrm{e}}(\eta_{\mathrm{e}},\,\theta_{\mathrm{e}})$ and its derivatives are left as is, such that one obtains

$$\begin{aligned} E\,\frac{\partial M^{\boldsymbol{S}}_{\mathrm{d},i}}{\partial \eta_{\mathrm{e}}} =& -\left[18\,[1-2\,\nu]\,\eta_{\mathrm{e}} + 6\,[2-\nu]\,\cos(\theta_i)\right]\widetilde{q}_{\mathrm{e}}^{\,2} \\ & - \left[6\,\eta_{\mathrm{e}} + 4\,\cos(\theta_i)\right]\left[3\,[1-2\,\nu]\,\eta + 2\,[1+\nu]\,\cos(\theta_i)\right]\widetilde{q}_{\mathrm{e}}\,\frac{\partial \widetilde{q}_{\mathrm{e}}}{\partial \eta_{\mathrm{e}}}\,, \end{aligned} \tag{4.190}$$

$$\begin{aligned} E\,\frac{\partial M^{\boldsymbol{S}}_{\mathrm{d},i}}{\partial \theta_{\mathrm{e}}} =& -\widetilde{q}_{\mathrm{e}}\left[6\,\eta_{\mathrm{e}} + 4\,\cos(\theta_i)\right]\left[3\,[1-2\,\nu]\,\eta + 2\,[1+\nu]\,\cos(\theta_i)\right]\frac{\partial \widetilde{q}_{\mathrm{e}}}{\partial \theta_{\mathrm{e}}} \\ & + \left[6\,[2-\nu]\,\eta_{\mathrm{e}} + 8\,[1+\nu]\,\cos(\theta_i)\right]\widetilde{q}_{\mathrm{e}}^{\,2}\,\sin(\theta_i)\,, \end{aligned} \tag{4.191}$$

$$E\,\frac{\partial^2 M^{\boldsymbol{S}}_{\mathrm{d},i}}{\partial \eta_\mathrm{e}^2} = -\,18\,\widetilde{q}_\mathrm{e}\left[\widetilde{q}_\mathrm{e}\,[1-2\,\nu] + \frac{\partial \widetilde{q}_\mathrm{e}}{\partial \eta_\mathrm{e}}\left[3\,[1-2\,\nu]\,\eta_\mathrm{e} + [2-\nu]\,\cos(\theta_i)\right]\right] - \left[\widetilde{q}_\mathrm{e}\,\frac{\partial^2 \widetilde{q}_\mathrm{e}}{\partial \eta_\mathrm{e}^2} + \left[\frac{\partial \widetilde{q}_\mathrm{e}}{\partial \eta_\mathrm{e}}\right]^2\right]\left[6\,\eta_\mathrm{e} + 4\,\cos(\theta_i)\right]\left[3\,[1-2\,\nu]\,\eta + 2\,[1+\nu]\,\cos(\theta_i)\right], \tag{4.192}$$

$$E\,\frac{\partial^2 M^{\boldsymbol{S}}_{\mathrm{d},i}}{\partial \eta_\mathrm{e}\,\partial \theta_\mathrm{e}} = -\,\widetilde{q}_\mathrm{e}^2\left[6\,[2-\nu]\,\sin(\theta_i)\right] - \widetilde{q}_\mathrm{e}\,\frac{\partial \widetilde{q}_\mathrm{e}}{\partial \theta_\mathrm{e}}\left[36\,[1-2\,\nu]\,\eta_\mathrm{e} + 12\,[2-\nu]\,\cos(\theta_i)\right] - \left[\frac{\partial \widetilde{q}_\mathrm{e}}{\partial \eta_\mathrm{e}}\,\frac{\partial \widetilde{q}_\mathrm{e}}{\partial \theta_\mathrm{e}} + \widetilde{q}_\mathrm{e}\,\frac{\partial^2 \widetilde{q}_\mathrm{e}}{\partial \eta_\mathrm{e}\,\partial \theta_\mathrm{e}}\right]\left[6\,\eta_\mathrm{e} + 4\,\cos(\theta_i)\right]\left[3\,[1-2\,\nu]\,\eta_\mathrm{e} + 2\,[1+\nu]\,\cos(\theta_i)\right] + \widetilde{q}_\mathrm{e}\,\frac{\partial \widetilde{q}_\mathrm{e}}{\partial \eta_\mathrm{e}}\left[6\,[2-\nu]\,\eta_\mathrm{e} + 8\,[1+\nu]\,\cos(\theta_i)\right]\,\sin(\theta_i), \tag{4.193}$$

$$E\,\frac{\partial^2 M^{\boldsymbol{S}}_{\mathrm{d},i}}{\partial \theta_\mathrm{e}^2} = -\left[3\,\widetilde{q}_\mathrm{e}\,\frac{\partial \widetilde{q}_\mathrm{e}}{\partial \theta_\mathrm{e}}\,\sin(\theta_i) - \widetilde{q}_\mathrm{e}^2\,\cos(\theta_i)\right]\left[6\,[2-\nu]\,\eta_\mathrm{e} + 8\,[1+\nu]\,\cos(\theta_i)\right] - \left[\left[\frac{\partial \widetilde{q}_\mathrm{e}}{\partial \theta_\mathrm{e}}\right]^2 + \widetilde{q}_\mathrm{e}\,\frac{\partial^2 \widetilde{q}_\mathrm{e}}{\partial \theta_\mathrm{e}^2}\right]\left[6\,\eta_\mathrm{e} + 4\,\cos(\theta_i)\right]\left[3\,[1-2\,\nu]\,\eta + 2\,[1+\nu]\,\cos(\theta_i)\right] - 8\,\widetilde{q}_\mathrm{e}^2\,\sin^2(\theta_i)\,[1+\nu], \tag{4.194}$$

where $\theta_i = \theta_\mathrm{e} + [i-1]\,\frac{2}{3}\,\pi$.

The director for the inward, respectively outward, unit normal vector can be simplified to

$$s = 18\,(\nu^2\,(3+\nu) - 2)\,\eta_\mathrm{e} + 27\,(2-\nu)^2\,(1-2\,\nu)\,\eta_\mathrm{e}^3 + 4\,(2-\nu)\,(1+\nu)^2\,\cos(3\,\theta_\mathrm{e})\,. \tag{4.195}$$

Insertion of the deviatoric elastic stress expression into coefficients f, g, h, cf. (4.182), and a lot of algebra (with the help of Mathematica) yields, that the first of the convexity conditions (4.189) is always fulfilled (assuming $0 < \zeta_\mathrm{d} < 1$ and $0 < \nu < \frac{1}{2}$), as one obtains

$$f\,h - g^2 = 9\,\zeta_\mathrm{d}\,[1-\zeta_\mathrm{d}]^2\,A(\eta_\mathrm{e},\,\theta_\mathrm{e})^4\left[1-\nu-2\,\nu^2\right]^{-6}\,B(\eta_\mathrm{e},\,\theta_\mathrm{e})^{-4} > 0\,, \tag{4.196}$$

$$A(\eta_\mathrm{e},\,\theta_\mathrm{e}) = 9\,\eta_\mathrm{e}\left[4 - 12\,\eta_\mathrm{e}^2 + 36\,\nu\,\eta_\mathrm{e}^2 - \nu^3\left[2 - 6\,\eta_\mathrm{e}^2\right] - 3\,\nu^2\left[2 + 9\,\eta_\mathrm{e}^2\right]\right] - 4\left[2-\nu\right]\left[1+\nu\right]^2\,\cos\left(3\,\theta_\mathrm{e}\right), \tag{4.197}$$

$$\begin{aligned} B(\eta_\mathrm{e},\,\theta_\mathrm{e}) = {} & 6 - 2\,\zeta_\mathrm{d} + 216\,\eta_\mathrm{e}^2 - 180\,\zeta_\mathrm{d}\,\eta_\mathrm{e}^2 + 81\,\zeta_\mathrm{d}\,\eta_\mathrm{e}^4 \\ & + 4\,\nu\,[3 - \zeta_\mathrm{d} - 54\,\eta_\mathrm{e}^2 + 45\,\zeta_\mathrm{d}\,\eta_\mathrm{e}^2 - 81\,\zeta_\mathrm{d}\,\eta_\mathrm{e}^4] \\ & + 2\,\nu^2\,[3 + 27\,\eta_\mathrm{e}^2 - \zeta_\mathrm{d}\,[1 + 63\,\eta_\mathrm{e}^2 - 162\,\eta_\mathrm{e}^4]] \\ & + 36\,[2 + \nu - \nu^2]\,[1-\zeta_\mathrm{d}]\,\eta_\mathrm{e}\,\cos\left(3\,\theta_\mathrm{e}\right). \end{aligned} \tag{4.198}$$

However, evaluation of the other condition from (4.189) reveals it to be not guaranteed to be fulfilled (the very long expression is not depicted here). Since no general statement

can be made, this condition needs to be evaluated on a case by case basis in order to determine convexity of the damage initiation surface for the parameters at hand.

The idea to develop a more general formulation of the initiation surface in terms of triaxiality and Lode angle of the elastic stresses poses to be very challenging. One approach could be to generalise $\widetilde{q}_{\mathrm{e}}$, cf. (4.182), e.g.

$$\widehat{q}_{\mathrm{e}}^{2}(\eta_{\mathrm{e}},\,\theta_{\mathrm{e}}) = \frac{\sqrt{12}\,E\,M_{\mathrm{d}}^{\max}}{\sqrt{f_{\eta}(\eta_{\mathrm{e}}) + f_{\theta}(\theta_{\mathrm{e}})\,\chi^{2}}}\,. \tag{4.199}$$

The standard formulation is obtained by setting

$$f_{\eta}(\eta_{\mathrm{e}}) = [1 + 2\,\zeta_{\mathrm{d}}]\,\left[9\,[1 - 2\,\nu]\,\eta_{\mathrm{e}}^{2} + 2\,[1 + \nu]\right]^{2}\,, \tag{4.200}$$

$$f_{\theta}(\theta_{\mathrm{e}}) = 6\,[1 - \zeta_{\mathrm{d}}]\,. \tag{4.201}$$

The difficulty arises from fulfilling the condition

$$f_{\eta}(\eta_{\mathrm{e}}) + f_{\theta}(\theta_{\mathrm{e}})\,\chi^{2} > 0 \tag{4.202}$$

which is necessary to guarantee only real values result from the root. Finding suitable functions f_{η} and f_{θ} which on the one hand fulfil above condition and on the other hand yield an initiation surface with the desired properties is left for future work.

5 Microcrack closure and reopening for ductile damage

The following chapter discusses the integration of the microcrack closure and reopening effect into the previously established anisotropic ductile damage model. The chapter further develops the ideas proposed in [64] and [61] and applies the concepts to ductile damage where plastic strains need to be considered and significantly alter the characteristic behaviour of the model. The characteristic behaviour is derived from micro-mechanical considerations — reversing the loading from compression to tension may result in a jump in stiffness as cracks may carry a load under compression but fail to do so under tension loading. Consequently, two separate damage variables are introduced describing the degradation of stiffness under tension and compression separately. This idea is similar to the approach pursued in [39].

The modelling framework from the previous chapter is adapted to include two damage variables for tension and for compression — facilitating a split of the strains. A novel split into tensile/compressive and volumetric/deviatoric contributions is proposed.

A prototype model, which is very similar to the model from Chapter 4 is discussed in Section 5.3. While evolution of tensile damage is still governed by an initiation potential, evolution of compressive damage is governed by a non-associated evolution equation.

The last section describes the implementation of the prototype model — reduced to scalar damage — into the framework established in Chapter 3. Two variants of the evolution equation for compressive damage are compared regarding their influence on the dissipation inequality and on the response of the model.

5.1 Micromechanical motivation

Consider a segment of microstructure with cross section A_0, as depicted in Figure 5.1a), which is already damaged such that the initial load-bearing cross section is reduced, i.e. the projection of the load-bearing cross section perpendicular to the loading direction is $A_\mathrm{d} < A_0$. Applying sufficiently large tension loading on the microstructure leads to plastic deformation as well as growth (and initiation) of microcracks and microvoids, see

Figure 5.1b). Consequently, the projected load-bearing cross section is reduced further to $A_\mathrm{d}^+ < A_\mathrm{d}$. Subsequent application of a compressive load may lead (after sufficient plastic deformation) to a state as depicted in Figure 5.1c), where some microcracks are completely closed and others are closed only partially. The projected load-bearing cross section may increase during compressive loading as more and more microcracks close, i.e. $A_\mathrm{d}^- > A_\mathrm{d}^+$. Reversing the load to tension loading again, see d), immediately switches the projected load-bearing cross section back to A_d^+, i.e. a jump in stiffness may be observed if the loading direction is switched — assuming that micro-cracks do not heal. It is important to observe that the load-bearing cross section for compression A_d^- is reduced during tension loading as plastic deformation reopens the microcracks which were previously closed under compressive loading.

The idea for the modelling approach is to correlate the load-bearing cross section with a damage variable. Since the load-bearing cross sections for tension and for compression develop differently, two separate damage variables need to be introduced in order to capture the differently evolving stiffness under tension and compression. In analogy to the fictitious configuration framework, cf. Section 4.1, the damage deformation gradients $\boldsymbol{F}_{\mathrm{d}+}$ and $\boldsymbol{F}_{\mathrm{d}-}$ are introduced. However, interpretation of $\boldsymbol{F}_{\mathrm{d}+}$ and $\boldsymbol{F}_{\mathrm{d}-}$ as tangent mappings between specific (yet to be introduced) configurations is not straightforward and beyond the scope of the current work. Based on these damage deformation gradients, damage measures analogous to (4.7) are defined, i.e.

$$\begin{aligned} \widehat{\boldsymbol{b}}_{\mathrm{d}+} &:= \boldsymbol{F}_{\mathrm{d}+} \cdot \overline{\boldsymbol{G}}^{-1} \cdot \boldsymbol{F}_{\mathrm{d}+}^{\mathrm{t}} \,, & \overline{\boldsymbol{C}}_{\mathrm{d}+} &:= \boldsymbol{F}_{\mathrm{d}+}^{\mathrm{t}} \cdot \widehat{\boldsymbol{G}} \cdot \boldsymbol{F}_{\mathrm{d}+} \,, \\ \widehat{\boldsymbol{b}}_{\mathrm{d}-} &:= \boldsymbol{F}_{\mathrm{d}-} \cdot \overline{\boldsymbol{G}}^{-1} \cdot \boldsymbol{F}_{\mathrm{d}-}^{\mathrm{t}} \,, & \overline{\boldsymbol{C}}_{\mathrm{d}-} &:= \boldsymbol{F}_{\mathrm{d}-}^{\mathrm{t}} \cdot \widehat{\boldsymbol{G}} \cdot \boldsymbol{F}_{\mathrm{d}-}^{\mathrm{t}} \,. \end{aligned} \tag{5.1}$$

The eigenvalues of the damage measures $\widehat{\boldsymbol{b}}_{\mathrm{d}+/-}$ are correlated to the (relative) load-bearing cross section (perpendicular to the related eigendirection) for tension A_d^+/A_0 and for compression A_d^-/A_0, respectively.

5.2 Modelling framework

Similarly to Section 4.2, the free Helmholtz energy Ψ is additively composed of an elastic strain energy contribution Ψ^e and contributions from plastic and damage hardening. The hardening contributions are (in most parts) unaffected by the introduction of separate damage variables for tension and compression. The elastic strain energy is again formulated in terms of invariants. However, since the tensile damage variable $\boldsymbol{F}_{\mathrm{d}+}$ shall only affect the response under tension and, vice versa, the compressive damage variable $\boldsymbol{F}_{\mathrm{d}-}$ shall only affect the response under compression, the elastic strains are split into tensile and compressive parts.

This framework shall be formulated in terms of logarithmic elastic strains $\widehat{\boldsymbol{\varepsilon}}_\mathrm{e}$ as they are capable of capturing the elastic response under compression well — similar to the

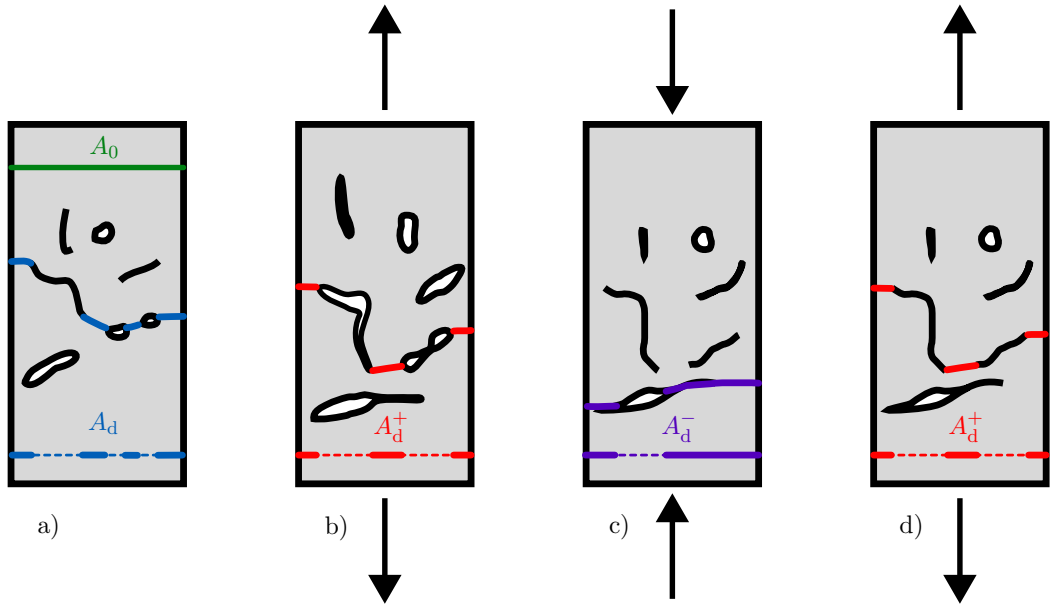

Figure 5.1: Idealised sketch of the microcrack closure-reopening effect by means of a segment (green cross section A_0) of microstructure. a) initial (pre-damaged) state with (blue) load-bearing cross section and its projection perpendicular to the applied loading A_d, b) tension loading with grown cracks and pores, c) subsequent compressive loading where cracks are (partially) closed after plastic deformation, d) load-reversal with tension loading.

isotropic ductile damage model proposed earlier but in the intermediate configuration instead, compare Section 3.1, i.e.

$$\widehat{\boldsymbol{\varepsilon}}_\mathrm{e} = \sum_{i=1}^{3} \varepsilon_{\mathrm{e},i}\, \widehat{\boldsymbol{P}}_i \quad \text{with} \quad \varepsilon_{\mathrm{e},i} := \ln(\lambda_{\mathrm{e},i})\,, \tag{5.2}$$

where the stretch eigenvalues $\lambda_{\mathrm{e},i}$ and the basis $\widehat{\boldsymbol{P}}_i$ are obtained from the elastic right Cauchy-Green tensor as

$$\widehat{\boldsymbol{C}}_\mathrm{e} = \sum_{i=1}^{3} \lambda_{\mathrm{e},i}^2\, \widehat{\boldsymbol{P}}_i \quad \text{with} \quad \widehat{\boldsymbol{P}}_i := \widehat{\boldsymbol{N}}_i \otimes \widehat{\boldsymbol{N}}_i\,. \tag{5.3}$$

The logarithmic elastic strains are split into volumetric and deviatoric contributions, $\widehat{\boldsymbol{\varepsilon}}_\mathrm{e}^\mathrm{vol}$ and $\widehat{\boldsymbol{\varepsilon}}_\mathrm{e}^\mathrm{dev}$, which are each split into tensile and compressive contributions, $\widehat{\boldsymbol{\varepsilon}}_{\mathrm{e}+}^\mathrm{vol}$, $\widehat{\boldsymbol{\varepsilon}}_{\mathrm{e}-}^\mathrm{vol}$, $\widehat{\boldsymbol{\varepsilon}}_{\mathrm{e}+}^\mathrm{dev}$ and $\widehat{\boldsymbol{\varepsilon}}_{\mathrm{e}-}^\mathrm{dev}$, i.e.

$$\widehat{\boldsymbol{\varepsilon}}_\mathrm{e} = \widehat{\boldsymbol{\varepsilon}}_\mathrm{e}^\mathrm{vol} + \widehat{\boldsymbol{\varepsilon}}_\mathrm{e}^\mathrm{dev} = \widehat{\boldsymbol{\varepsilon}}_{\mathrm{e}+}^\mathrm{vol} - \widehat{\boldsymbol{\varepsilon}}_{\mathrm{e}-}^\mathrm{vol} + \widehat{\boldsymbol{\varepsilon}}_{\mathrm{e}+}^\mathrm{dev} - \widehat{\boldsymbol{\varepsilon}}_{\mathrm{e}-}^\mathrm{dev} = \widehat{\boldsymbol{\varepsilon}}_{\mathrm{e}+} - \widehat{\boldsymbol{\varepsilon}}_{\mathrm{e}-}\,. \tag{5.4}$$

The main advantages of a split into these contributions are positive-semidefinite damage driving forces and a tensile damage driving force devoid of compressive contributions. A

more detailed discussion of the advantages can be found in Remark 15. The contributions are defined by means of the eigenvalues $\varepsilon_{\mathrm{e},i}$ and by means of the function

$$h : \mathbb{R} \to \mathbb{R}_0^+ \quad \text{with} \quad h(x) + h(-x) = |x| \quad \text{and} \quad h(x) - h(-x) = x\,, \tag{5.5}$$

which, for now, is assumed to be the Macauly bracket ($h(x > 0) = x$ and $h(x \leq 0) = 0$), but from a computational point of view it is beneficial to choose a regularised function, similar to the one in e.g. [61]. Additional properties of the splitting function are discussed in Remark 16. The individual strain contributions of the split (5.4) can be represented as

$$\widehat{\boldsymbol{\varepsilon}}_{\mathrm{e}+}^{\mathrm{vol}} = \frac{1}{3}\, h(\varepsilon_{\mathrm{e}}^{\mathrm{vol}})\, \widehat{\boldsymbol{G}} \qquad \text{with} \quad \varepsilon_{\mathrm{e}}^{\mathrm{vol}} := \sum_{i=1}^{3} \varepsilon_{\mathrm{e},i}\,, \tag{5.6}$$

$$\widehat{\boldsymbol{\varepsilon}}_{\mathrm{e}-}^{\mathrm{vol}} = \frac{1}{3}\, h(-\varepsilon_{\mathrm{e}}^{\mathrm{vol}})\, \widehat{\boldsymbol{G}}\,, \tag{5.7}$$

$$\widehat{\boldsymbol{\varepsilon}}_{\mathrm{e}+}^{\mathrm{dev}} = \sum_{i=1}^{3} h(\varepsilon_{\mathrm{e},i}^{\mathrm{dev}})\, \widehat{\boldsymbol{P}}_i \qquad \text{with} \quad \varepsilon_{\mathrm{e},i}^{\mathrm{dev}} := \varepsilon_{\mathrm{e},i} - \frac{1}{3}\,\varepsilon_{\mathrm{e}}^{\mathrm{vol}}\,, \tag{5.8}$$

$$\widehat{\boldsymbol{\varepsilon}}_{\mathrm{e}-}^{\mathrm{dev}} = \sum_{i=1}^{3} h(-\varepsilon_{\mathrm{e},i}^{\mathrm{dev}})\, \widehat{\boldsymbol{P}}_i\,, \tag{5.9}$$

such that the tensile contribution is given by $\widehat{\boldsymbol{\varepsilon}}_{\mathrm{e}+} = \widehat{\boldsymbol{\varepsilon}}_{\mathrm{e}+}^{\mathrm{vol}} + \widehat{\boldsymbol{\varepsilon}}_{\mathrm{e}+}^{\mathrm{dev}}$ and the compressive contribution by $\widehat{\boldsymbol{\varepsilon}}_{\mathrm{e}-} = \widehat{\boldsymbol{\varepsilon}}_{\mathrm{e}-}^{\mathrm{vol}} + \widehat{\boldsymbol{\varepsilon}}_{\mathrm{e}-}^{\mathrm{dev}}$.

In analogy to the definition of the strain invariants $\overline{I}_i^{\overline{\boldsymbol{E}}_{\mathrm{e}}}$ in (4.12), the strain invariants $\overline{I}_i^{\overline{\boldsymbol{\varepsilon}}_{\mathrm{e}+/-}}$ based on the individual contributions of the logarithmic strain measure (5.4) are defined as

$$\begin{aligned}
\overline{I}_1^{\overline{\boldsymbol{\varepsilon}}_{\mathrm{e}+}} &= \widehat{\boldsymbol{b}}_{\mathrm{d}+} : \widehat{\boldsymbol{\varepsilon}}_{\mathrm{e}+} &&= \overline{\boldsymbol{G}}^{-1} : \overline{\boldsymbol{\varepsilon}}_{\mathrm{e}+}\,, \\
\overline{I}_1^{\overline{\boldsymbol{\varepsilon}}_{\mathrm{e}-}} &= \widehat{\boldsymbol{b}}_{\mathrm{d}-} : \widehat{\boldsymbol{\varepsilon}}_{\mathrm{e}-} &&= \overline{\boldsymbol{G}}^{-1} : \overline{\boldsymbol{\varepsilon}}_{\mathrm{e}-}\,, \\
\overline{I}_i^{\overline{\boldsymbol{\varepsilon}}_{\mathrm{e}+}^{\mathrm{dev}}} &= \widehat{\boldsymbol{I}} : \left[\widehat{\boldsymbol{b}}_{\mathrm{d}+} \cdot \widehat{\boldsymbol{\varepsilon}}_{\mathrm{e}+}^{\mathrm{dev}}\right]^i &&= \overline{\boldsymbol{I}} : \left[\overline{\boldsymbol{G}}^{-1} \cdot \overline{\boldsymbol{\varepsilon}}_{\mathrm{e}+}^{\mathrm{dev}}\right]^i, \quad i = 2, 3\,, \\
\overline{I}_i^{\overline{\boldsymbol{\varepsilon}}_{\mathrm{e}-}^{\mathrm{dev}}} &= \widehat{\boldsymbol{I}} : \left[\widehat{\boldsymbol{b}}_{\mathrm{d}-} \cdot \widehat{\boldsymbol{\varepsilon}}_{\mathrm{e}-}^{\mathrm{dev}}\right]^i &&= \overline{\boldsymbol{I}} : \left[\overline{\boldsymbol{G}}^{-1} \cdot \overline{\boldsymbol{\varepsilon}}_{\mathrm{e}-}^{\mathrm{dev}}\right]^i, \quad i = 2, 3\,,
\end{aligned} \tag{5.10}$$

where the strain contributions of $\overline{\boldsymbol{\varepsilon}}_{\mathrm{e}} = \overline{\boldsymbol{\varepsilon}}_{\mathrm{e}+} - \overline{\boldsymbol{\varepsilon}}_{\mathrm{e}-}$ transform according to

$$\begin{aligned}
\overline{\boldsymbol{\varepsilon}}_{\mathrm{e}+} &= \boldsymbol{F}_{\mathrm{d}+}^{\mathrm{t}} \cdot \widehat{\boldsymbol{\varepsilon}}_{\mathrm{e}+} \cdot \boldsymbol{F}_{\mathrm{d}+}\,, \qquad & \overline{\boldsymbol{\varepsilon}}_{\mathrm{e}+}^{\mathrm{dev}} &= \boldsymbol{F}_{\mathrm{d}+}^{\mathrm{t}} \cdot \widehat{\boldsymbol{\varepsilon}}_{\mathrm{e}+}^{\mathrm{dev}} \cdot \boldsymbol{F}_{\mathrm{d}+}\,, \\
\overline{\boldsymbol{\varepsilon}}_{\mathrm{e}-} &= \boldsymbol{F}_{\mathrm{d}-}^{\mathrm{t}} \cdot \widehat{\boldsymbol{\varepsilon}}_{\mathrm{e}-} \cdot \boldsymbol{F}_{\mathrm{d}-}\,, \qquad & \overline{\boldsymbol{\varepsilon}}_{\mathrm{e}-}^{\mathrm{dev}} &= \boldsymbol{F}_{\mathrm{d}-}^{\mathrm{t}} \cdot \widehat{\boldsymbol{\varepsilon}}_{\mathrm{e}-}^{\mathrm{dev}} \cdot \boldsymbol{F}_{\mathrm{d}-}\,.
\end{aligned} \tag{5.11}$$

Since the tensile and compressive contributions transform differently ($\boldsymbol{F}_{\mathrm{d}+}$ vs. $\boldsymbol{F}_{\mathrm{d}-}$), it is not possible to transform the intermediate logarithmic strains directly, i.e. there exists (in general) no quantity $\boldsymbol{F}_x$ for which

$$\overline{\boldsymbol{\varepsilon}}_{\mathrm{e}} = \boldsymbol{F}_x^{\mathrm{t}} \cdot \widehat{\boldsymbol{\varepsilon}}_{\mathrm{e}} \cdot \boldsymbol{F}_x\,, \tag{5.12}$$

holds. Consequently, a formulation of the whole model in the fictitious configuration is impractical.

The elastic part of the free Helmholtz energy is formulated in terms of the invariants $\overline{I}_i^{\overline{\boldsymbol{\varepsilon}}_{\mathrm{e}+/-}}$ from (5.10), i.e.

$$\Psi^{\mathrm{e}}(\overline{I}_1^{\overline{\boldsymbol{\varepsilon}}_{\mathrm{e}+}}, \overline{I}_1^{\overline{\boldsymbol{\varepsilon}}_{\mathrm{e}-}}, \overline{I}_{2,3}^{\overline{\boldsymbol{\varepsilon}}^{\mathrm{dev}}_{\mathrm{e}+}}, \overline{I}_{2,3}^{\overline{\boldsymbol{\varepsilon}}^{\mathrm{dev}}_{\mathrm{e}-}}) \,. \tag{5.13}$$

The thermodynamically conjugated driving forces of the elastic strains are split into four terms, analogous to the split of strains in (5.4), i.e. one obtains

$$\widehat{\boldsymbol{T}}^{\mathrm{vol}}_{\mathrm{e}+} := \frac{\partial \Psi}{\partial \overline{I}_1^{\overline{\boldsymbol{\varepsilon}}_{\mathrm{e}+}}} \frac{\partial \overline{I}_1^{\overline{\boldsymbol{\varepsilon}}_{\mathrm{e}+}}}{\partial \widehat{\boldsymbol{\varepsilon}}_{\mathrm{e}+}} = \frac{\partial \Psi}{\partial \overline{I}_1^{\overline{\boldsymbol{\varepsilon}}_{\mathrm{e}+}}} \widehat{\boldsymbol{b}}_{\mathrm{d}+} \,, \tag{5.14}$$

$$\widehat{\boldsymbol{T}}^{\mathrm{dev}}_{\mathrm{e}+} := \sum_{i=2}^{3} \frac{\partial \Psi}{\partial \overline{I}_i^{\overline{\boldsymbol{\varepsilon}}^{\mathrm{dev}}_{\mathrm{e}+}}} \frac{\partial \overline{I}_i^{\overline{\boldsymbol{\varepsilon}}^{\mathrm{dev}}_{\mathrm{e}+}}}{\partial \widehat{\boldsymbol{\varepsilon}}_{\mathrm{e}+}} = \sum_{i=2}^{3} \frac{\partial \Psi}{\partial \overline{I}_i^{\overline{\boldsymbol{\varepsilon}}^{\mathrm{dev}}_{\mathrm{e}+}}} i \big[\widehat{\boldsymbol{b}}_{\mathrm{d}+} \cdot \widehat{\boldsymbol{\varepsilon}}^{\mathrm{dev}}_{\mathrm{e}+}\big]^{i-1} \cdot \widehat{\boldsymbol{b}}_{\mathrm{d}+} \,, \tag{5.15}$$

$$\widehat{\boldsymbol{T}}^{\mathrm{vol}}_{\mathrm{e}-} := \frac{\partial \Psi}{\partial \overline{I}_1^{\overline{\boldsymbol{\varepsilon}}_{\mathrm{e}-}}} \frac{\partial \overline{I}_1^{\overline{\boldsymbol{\varepsilon}}_{\mathrm{e}-}}}{\partial \widehat{\boldsymbol{\varepsilon}}_{\mathrm{e}-}} = \frac{\partial \Psi}{\partial \overline{I}_1^{\overline{\boldsymbol{\varepsilon}}_{\mathrm{e}-}}} \widehat{\boldsymbol{b}}_{\mathrm{d}-} \,, \tag{5.16}$$

$$\widehat{\boldsymbol{T}}^{\mathrm{dev}}_{\mathrm{e}-} := \sum_{i=2}^{3} \frac{\partial \Psi}{\partial \overline{I}_i^{\overline{\boldsymbol{\varepsilon}}^{\mathrm{dev}}_{\mathrm{e}-}}} \frac{\partial \overline{I}_i^{\overline{\boldsymbol{\varepsilon}}^{\mathrm{dev}}_{\mathrm{e}-}}}{\partial \widehat{\boldsymbol{\varepsilon}}_{\mathrm{e}-}} = \sum_{i=2}^{3} \frac{\partial \Psi}{\partial \overline{I}_i^{\overline{\boldsymbol{\varepsilon}}^{\mathrm{dev}}_{\mathrm{e}-}}} i \big[\widehat{\boldsymbol{b}}_{\mathrm{d}-} \cdot \widehat{\boldsymbol{\varepsilon}}^{\mathrm{dev}}_{\mathrm{e}-}\big]^{i-1} \cdot \widehat{\boldsymbol{b}}_{\mathrm{d}-} \,. \tag{5.17}$$

Based on these quantities, the total elastic Piola-Kirchhoff stresses in the intermediate configuration can be expressed by

$$\widehat{\boldsymbol{S}}_{\mathrm{e}} = 2 \frac{\partial \Psi}{\partial \widehat{\boldsymbol{C}}_{\mathrm{e}}} = \widehat{\boldsymbol{S}}_{\mathrm{e}+} - \widehat{\boldsymbol{S}}_{\mathrm{e}-} \,, \quad \text{with} \quad \widehat{\boldsymbol{S}}_{\mathrm{e}+/-} = \widehat{\boldsymbol{T}}^{\mathrm{vol}}_{\mathrm{e}+/-} : \mathbf{P}^{\mathrm{vol}}_{\varepsilon+/-} + \widehat{\boldsymbol{T}}^{\mathrm{dev}}_{\mathrm{e}+/-} : \mathbf{P}^{\mathrm{dev}}_{\varepsilon+/-} \,. \tag{5.18}$$

Therein, the quantities $\mathbf{P}^{\mathrm{vol/dev}}_{\varepsilon+/-}$ contain the derivatives of the respective portion of the logarithmic strains with respect to $\widehat{\boldsymbol{C}}_{\mathrm{e}}$ and are defined as

$$\mathbf{P}^{\mathrm{vol}}_{\varepsilon+} = \quad 2 \frac{\partial \widehat{\boldsymbol{\varepsilon}}^{\mathrm{vol}}_{\mathrm{e}+}}{\partial \widehat{\boldsymbol{C}}_{\mathrm{e}}} = h'(\varepsilon^{\mathrm{vol}}_{\mathrm{e}}) \, \widehat{\boldsymbol{G}} \otimes \widehat{\boldsymbol{C}}_{\mathrm{e}}^{-1} \,, \tag{5.19}$$

$$\mathbf{P}^{\mathrm{dev}}_{\varepsilon+} = \quad 2 \frac{\partial \widehat{\boldsymbol{\varepsilon}}^{\mathrm{dev}}_{\mathrm{e}+}}{\partial \widehat{\boldsymbol{C}}_{\mathrm{e}}} = \sum_{i=1}^{3} \Big[h'(\varepsilon^{\mathrm{dev}}_{\mathrm{e},i}) \, \widehat{\boldsymbol{P}}_i \otimes \big[\lambda^{-2}_{\mathrm{e},i} \, \widehat{\boldsymbol{P}}_i - \frac{1}{3} \, \widehat{\boldsymbol{C}}_{\mathrm{e}}^{-1}\big] \tag{5.20}$$

$$+ 2 \, h(\varepsilon^{\mathrm{dev}}_{\mathrm{e},i}) \frac{\partial \widehat{\boldsymbol{P}}_i}{\partial \widehat{\boldsymbol{C}}_{\mathrm{e}}} \Big] \,,$$

$$\mathsf{P}^{\mathrm{vol}}_{\varepsilon-} = -2\,\frac{\partial \widehat{\boldsymbol{\varepsilon}}^{\mathrm{vol}}_{\mathrm{e}-}}{\partial \widehat{\boldsymbol{C}}_{\mathrm{e}}} = h'(-\varepsilon^{\mathrm{vol}}_{\mathrm{e}})\,\widehat{\boldsymbol{G}} \otimes \widehat{\boldsymbol{C}}_{\mathrm{e}}^{-1}\,, \tag{5.21}$$

$$\mathsf{P}^{\mathrm{dev}}_{\varepsilon-} = -2\,\frac{\partial \widehat{\boldsymbol{\varepsilon}}^{\mathrm{dev}}_{\mathrm{e}-}}{\partial \widehat{\boldsymbol{C}}_{\mathrm{e}}} = \sum_{i=1}^{3}\Big[h'(-\varepsilon^{\mathrm{dev}}_{\mathrm{e},i})\,\widehat{\boldsymbol{P}}_i \otimes \big[\lambda^{-2}_{\mathrm{e},i}\,\widehat{\boldsymbol{P}}_i - \frac{1}{3}\,\widehat{\boldsymbol{C}}_{\mathrm{e}}^{-1}\big] - 2\,h(-\varepsilon^{\mathrm{dev}}_{\mathrm{e},i})\,\frac{\partial \widehat{\boldsymbol{P}}_i}{\partial \widehat{\boldsymbol{C}}_{\mathrm{e}}}\Big]\,, \tag{5.22}$$

with $h'(x) := \partial_x h(x)$ and where the derivative of the eigenbasis $\widehat{\boldsymbol{P}}_i$ with respect to $\widehat{\boldsymbol{C}}_{\mathrm{e}}$ can be computed by means of, e.g., Sylvester's formula [168] or of the Dunford-Taylor integral, see e.g. [86].

The damage related driving forces $\widehat{\boldsymbol{Q}}_+$ and $\widehat{\boldsymbol{Q}}_-$, split into volumetric and deviatoric contributions, are given by the derivative of the (respective contribution to the) Helmholtz energy with respect to the damage metrics $\widehat{\boldsymbol{b}}_{\mathrm{d}+/-}$, i.e.

$$\widehat{\boldsymbol{Q}}_+ = \widehat{\boldsymbol{Q}}^{\mathrm{vol}}_+ + \widehat{\boldsymbol{Q}}^{\mathrm{dev}}_+ = \frac{\partial \Psi}{\partial \overline{I}^{\overline{\boldsymbol{\varepsilon}}_{\mathrm{e}+}}_1}\,\widehat{\boldsymbol{\varepsilon}}_{\mathrm{e}+} + \sum_{i=2}^{3}\frac{\partial \Psi}{\partial \overline{I}^{\overline{\boldsymbol{\varepsilon}}^{\mathrm{dev}}_{\mathrm{e}+}}_i}\,i\,\widehat{\boldsymbol{\varepsilon}}^{\mathrm{dev}}_{\mathrm{e}+}\cdot\big[\widehat{\boldsymbol{b}}_{\mathrm{d}+}\cdot\widehat{\boldsymbol{\varepsilon}}^{\mathrm{dev}}_{\mathrm{e}+}\big]^{i-1}\,, \tag{5.23}$$

$$\widehat{\boldsymbol{Q}}_- = \widehat{\boldsymbol{Q}}^{\mathrm{vol}}_- + \widehat{\boldsymbol{Q}}^{\mathrm{dev}}_- = \frac{\partial \Psi}{\partial \overline{I}^{\overline{\boldsymbol{\varepsilon}}_{\mathrm{e}-}}_1}\,\widehat{\boldsymbol{\varepsilon}}_{\mathrm{e}-} + \sum_{i=2}^{3}\frac{\partial \Psi}{\partial \overline{I}^{\overline{\boldsymbol{\varepsilon}}^{\mathrm{dev}}_{\mathrm{e}-}}_i}\,i\,\widehat{\boldsymbol{\varepsilon}}^{\mathrm{dev}}_{\mathrm{e}-}\cdot\big[\widehat{\boldsymbol{b}}_{\mathrm{d}-}\cdot\widehat{\boldsymbol{\varepsilon}}^{\mathrm{dev}}_{\mathrm{e}-}\big]^{i-1}\,. \tag{5.24}$$

Notably, the (total) damage driving forces can no longer be expressed in terms of the stresses as was possible before, cf. (4.18), due to the split into volumetric and deviatoric contributions in the Helmholtz energy. However, a relation between the individual contributions still holds, i.e.

$$\widehat{\boldsymbol{\varepsilon}}^{\mathrm{vol/dev}}_{+/-}\cdot\widehat{\boldsymbol{T}}^{\mathrm{vol/dev}}_{+/-} = \widehat{\boldsymbol{Q}}^{\mathrm{vol/dev}}_{+/-}\cdot\widehat{\boldsymbol{b}}_{\mathrm{d}+/-}\,. \tag{5.25}$$

Based on the format of the free Helmholtz energy (5.13), the dissipation (in the case of isothermal conditions) can, analogous to (4.19), be expressed as

$$\begin{aligned}
&\mathcal{D} = \boldsymbol{P} : \dot{\boldsymbol{F}} - \dot{\Psi} \geq 0 \quad \text{with}\\
&\dot{\Psi} = \frac{\partial \Psi}{\partial \boldsymbol{F}} : \dot{\boldsymbol{F}} + \frac{\partial \Psi}{\partial \boldsymbol{F}_{\mathrm{p}}} : \dot{\boldsymbol{F}}_{\mathrm{p}} + \frac{\partial \Psi}{\partial \boldsymbol{F}_{\mathrm{d}+}} : \dot{\boldsymbol{F}}_{\mathrm{d}+}\\
&\quad + \frac{\partial \Psi}{\partial \boldsymbol{F}_{\mathrm{d}-}} : \dot{\boldsymbol{F}}_{\mathrm{d}-} + \frac{\partial \Psi}{\partial \boldsymbol{\mathcal{I}}_{\mathrm{p}}} \bullet \dot{\boldsymbol{\mathcal{I}}}_{\mathrm{p}} + \frac{\partial \Psi}{\partial \boldsymbol{\mathcal{I}}_{\mathrm{d}}} \bullet \dot{\boldsymbol{\mathcal{I}}}_{\mathrm{d}}\,,
\end{aligned} \tag{5.26}$$

where the derivatives of the Helmholtz energy with respect to the deformation gradients can be calculated as

$$\frac{\partial \Psi}{\partial \boldsymbol{F}} = \frac{\partial \Psi}{\partial \widehat{\boldsymbol{C}}_{\mathrm{e}}} : \frac{\partial \widehat{\boldsymbol{C}}_{\mathrm{e}}}{\partial \boldsymbol{F}} = \boldsymbol{g}\cdot\boldsymbol{F}\cdot\boldsymbol{F}_{\mathrm{p}}^{-1}\cdot\widehat{\boldsymbol{S}}_{\mathrm{e}}\cdot\boldsymbol{F}_{\mathrm{p}}^{-\mathrm{t}}\,, \tag{5.27}$$

$$\frac{\partial \Psi}{\partial \boldsymbol{F}_{\mathrm{p}}} = \frac{\partial \Psi}{\partial \widehat{\boldsymbol{C}}_{\mathrm{e}}} : \frac{\partial \widehat{\boldsymbol{C}}_{\mathrm{e}}}{\partial \boldsymbol{F}_{\mathrm{p}}} = -\widehat{\boldsymbol{C}}_{\mathrm{e}}\cdot\widehat{\boldsymbol{S}}_{\mathrm{e}}\cdot\boldsymbol{F}_{\mathrm{p}}^{-\mathrm{t}}\,, \tag{5.28}$$

$$\frac{\partial \Psi}{\partial \boldsymbol{F}_{\mathrm{d}+}} = \frac{\partial \Psi}{\partial \widehat{\boldsymbol{b}}_{\mathrm{d}+}} : \frac{\partial \widehat{\boldsymbol{b}}_{\mathrm{d}+}}{\partial \boldsymbol{F}_{\mathrm{d}+}} = 2\,\widehat{\boldsymbol{Q}}_{+} \cdot \widehat{\boldsymbol{b}}_{\mathrm{d}+} \cdot \boldsymbol{F}_{\mathrm{d}+}^{-\mathrm{t}}\,, \tag{5.29}$$

$$\frac{\partial \Psi}{\partial \boldsymbol{F}_{\mathrm{d}-}} = \frac{\partial \Psi}{\partial \widehat{\boldsymbol{b}}_{\mathrm{d}-}} : \frac{\partial \widehat{\boldsymbol{b}}_{\mathrm{d}-}}{\partial \boldsymbol{F}_{\mathrm{d}-}} = 2\,\widehat{\boldsymbol{Q}}_{-} \cdot \widehat{\boldsymbol{b}}_{\mathrm{d}-} \cdot \boldsymbol{F}_{\mathrm{d}-}^{-\mathrm{t}}\,. \tag{5.30}$$

Evolution equations will be formulated in the intermediate configuration. To this end, Mandel stresses and the corresponding velocity gradients are derived in the intermediate configuration analogous to the previously discussed derivation in the fictitious configuration, cf. (4.21), i.e.

$$-\frac{\partial \Psi}{\partial \boldsymbol{F}_{\mathrm{p}}} : \dot{\boldsymbol{F}}_{\mathrm{p}} = \big[\widehat{\boldsymbol{C}}_{\mathrm{e}} \cdot \widehat{\boldsymbol{S}}_{\mathrm{e}}\big] : \big[\dot{\boldsymbol{F}}_{\mathrm{p}} \cdot \boldsymbol{F}_{\mathrm{p}}^{-1}\big] \qquad = \widehat{\boldsymbol{M}}_{\mathrm{e}} : \widehat{\boldsymbol{L}}_{\mathrm{p}}\,, \tag{5.31}$$

$$-\frac{\partial \Psi}{\partial \boldsymbol{F}_{\mathrm{d}+}} : \dot{\boldsymbol{F}}_{\mathrm{d}+} = \big[-2\,\widehat{\boldsymbol{Q}}_{+} \cdot \widehat{\boldsymbol{b}}_{\mathrm{d}+}\big] : \big[\dot{\boldsymbol{F}}_{\mathrm{d}+} \cdot \boldsymbol{F}_{\mathrm{d}+}^{-1}\big] = \widehat{\boldsymbol{M}}_{\mathrm{d}+} : \widehat{\boldsymbol{L}}_{\mathrm{d}+}\,, \tag{5.32}$$

$$-\frac{\partial \Psi}{\partial \boldsymbol{F}_{\mathrm{d}-}} : \dot{\boldsymbol{F}}_{\mathrm{d}-} = \big[-2\,\widehat{\boldsymbol{Q}}_{-} \cdot \widehat{\boldsymbol{b}}_{\mathrm{d}-}\big] : \big[\dot{\boldsymbol{F}}_{\mathrm{d}-} \cdot \boldsymbol{F}_{\mathrm{d}-}^{-1}\big] = \widehat{\boldsymbol{M}}_{\mathrm{d}-} : \widehat{\boldsymbol{L}}_{\mathrm{d}-}\,, \tag{5.33}$$

which defines the damage Mandel stresses $\widehat{\boldsymbol{M}}_{\mathrm{d}+/-}$. Using the Mandel stresses and the velocity gradients together with the definition of the Piola stresses $\boldsymbol{P} = \partial_{\boldsymbol{F}} \Psi$ yields the reduced dissipation inequality

$$\mathcal{D}^{\mathrm{red}} = \widehat{\boldsymbol{M}}_{\mathrm{e}} : \widehat{\boldsymbol{L}}_{\mathrm{p}} + \widehat{\boldsymbol{M}}_{\mathrm{d}+} : \widehat{\boldsymbol{L}}_{\mathrm{d}+} + \widehat{\boldsymbol{M}}_{\mathrm{d}-} : \widehat{\boldsymbol{L}}_{\mathrm{d}-} + \boldsymbol{\mathcal{F}}_{\mathrm{p}} \bullet \dot{\boldsymbol{\mathcal{I}}}_{\mathrm{p}} + \boldsymbol{\mathcal{F}}_{\mathrm{d}} \bullet \dot{\boldsymbol{\mathcal{I}}}_{\mathrm{d}} \geq 0\,, \tag{5.34}$$

where the driving forces related to the plastic internal variables $\boldsymbol{\mathcal{I}}_{\mathrm{p}} \in \mathbb{R}^m$ and to the damage internal variables $\boldsymbol{\mathcal{I}}_{\mathrm{d}} \in \mathbb{R}^n$ are introduced as

$$\boldsymbol{\mathcal{F}}_{\mathrm{p}} := -\frac{\partial \Psi}{\partial \boldsymbol{\mathcal{I}}_{\mathrm{p}}}\,, \qquad \boldsymbol{\mathcal{F}}_{\mathrm{d}} := -\frac{\partial \Psi}{\partial \boldsymbol{\mathcal{I}}_{\mathrm{d}}}\,. \tag{5.35}$$

Similar to the anisotropic model proposed earlier, the evolution of (tensile) damage and plasticity related variables is governed by an admissible domain

$$\mathbb{E} := \{\boldsymbol{\mathcal{F}} \in \mathbb{R}^{9+9+m+n} \,|\, \mathbb{E}_{\mathrm{p}} \cup \mathbb{E}_{\mathrm{d}+}\}\,, \tag{5.36}$$

with $\boldsymbol{\mathcal{F}}$ representing the set of driving forces $\widehat{\boldsymbol{M}}_{\mathrm{e}}$, $\widehat{\boldsymbol{M}}_{\mathrm{d}+}$, $\boldsymbol{\mathcal{F}}_{\mathrm{p}}$ and $\boldsymbol{\mathcal{F}}_{\mathrm{d}}$, i.e. without the compressive damage Mandel stresses $\widehat{\boldsymbol{M}}_{\mathrm{d}-}$. The plastic and tensile damage domains $\mathbb{E}_{\mathrm{p}}$ and, respectively, $\mathbb{E}_{\mathrm{d}+}$ are defined by means of the potentials Φ_{p} and Φ_{d}, i.e.

$$\mathbb{E}_{\mathrm{p}} := \{\{\widehat{\boldsymbol{M}}_{\mathrm{e}}, \boldsymbol{\mathcal{F}}_{\mathrm{p}}\} \in \mathbb{R}^{9+m} \,|\, \Phi_{\mathrm{p}} \leq 0\}\,, \tag{5.37}$$

$$\mathbb{E}_{\mathrm{d}+} := \{\{\widehat{\boldsymbol{M}}_{\mathrm{d}+}, \boldsymbol{\mathcal{F}}_{\mathrm{d}}\} \in \mathbb{R}^{9+n} \,|\, \Phi_{\mathrm{d}} \leq 0\}\,. \tag{5.38}$$

The evolution equations for the variables related to plasticity and tensile damage are derived in an associative manner. Maximising dissipation, while staying within the admissible domain $\mathbb{E}$, results in

$$\widehat{\boldsymbol{L}}_{\mathrm{p}} = \lambda_{\mathrm{p}} \frac{\partial \Phi_{\mathrm{p}}}{\partial \widehat{\boldsymbol{M}}_{\mathrm{e}}}\,, \qquad \dot{\boldsymbol{\mathcal{I}}}_{\mathrm{p}} = \lambda_{\mathrm{p}} \frac{\partial \Phi_{\mathrm{p}}}{\partial \boldsymbol{\mathcal{F}}_{\mathrm{p}}}\,, \tag{5.39}$$

$$\widehat{\boldsymbol{L}}_{\mathrm{d}+} = \lambda_{\mathrm{d}} \frac{\partial \Phi_{\mathrm{d}}}{\partial \widehat{\boldsymbol{M}}_{\mathrm{d}+}}\,, \qquad \dot{\boldsymbol{\mathcal{I}}}_{\mathrm{d}} = \lambda_{\mathrm{d}} \frac{\partial \Phi_{\mathrm{d}}}{\partial \boldsymbol{\mathcal{F}}_{\mathrm{d}}}\,, \tag{5.40}$$

with λ_{p} and λ_{d} being the Lagrange multipliers subject to loading and unloading conditions

$$\begin{aligned} &\Phi_{\mathrm{p}} \leq 0 \qquad \lambda_{\mathrm{p}} \geq 0 \qquad \lambda_{\mathrm{p}}\, \Phi_{\mathrm{p}} = 0\,, \\ &\Phi_{\mathrm{d}} \leq 0 \qquad \lambda_{\mathrm{d}} \geq 0 \qquad \lambda_{\mathrm{d}}\, \Phi_{\mathrm{d}} = 0\,. \end{aligned} \tag{5.41}$$

The evolution of compressive damage is separated into growth — proportional to the evolution of tensile damage — and into reduction — proportional to the evolution of (compressive) plasticity. Hence, the evolution equation is formulated in a non-associated manner and may formally be written as

$$\widehat{\boldsymbol{L}}_{\mathrm{d}-} = \begin{cases} \boldsymbol{\kappa}_{+}(\widehat{\boldsymbol{L}}_{\mathrm{d}+},\, ...) & \text{if } \lambda_{\mathrm{d}} > 0 \\ \boldsymbol{\kappa}_{-}(\widehat{\boldsymbol{L}}_{\mathrm{p}-},\, ...) & \text{if } \lambda_{\mathrm{d}} = 0 \,\wedge\, \lambda_{\mathrm{p}} > 0 \,\wedge\, \exists\, \varepsilon_{\mathrm{e},i} < 0 \end{cases}\,, \tag{5.42}$$

where the function $\boldsymbol{\kappa}_{+/-}$ and the compressive contribution to the plastic velocity gradient $\widehat{\boldsymbol{L}}_{\mathrm{p}-}$ need to be further specified. Furthermore, the specified function needs to be chosen such that dissipation is guaranteed to be positive. Instead of defining the evolution of the compressive damage variable as exclusively deteriorating or exclusively healing, another possibility could be to additively combine both, i.e.

$$\widehat{\boldsymbol{L}}_{\mathrm{d}-} = \boldsymbol{\kappa}_{+}(\widehat{\boldsymbol{L}}_{\mathrm{d}+},\, ...) + \boldsymbol{\kappa}_{-}(\widehat{\boldsymbol{L}}_{\mathrm{p}-},\, ...)\,. \tag{5.43}$$

Thereby, tension in one direction could lead to growth of damage while compression in a different direction may shrink the corresponding compressive damage contribution.

Remark 15 *The proposed decomposition of the logarithmic strains, see* (5.4)*, has several advantages compared to a decomposition into tensile and compressive contributions. Typically, splitting the strains into tensile and compressive parts requires the careful choice of the volumetric contribution in the strain energy, since*

$$\big[\sum_{i=1}^{3} h(\varepsilon_{\mathrm{e},i})\big]^2 + \big[\sum_{i=1}^{3} h(-\varepsilon_{\mathrm{e},i})\big]^2 \neq \big[\sum_{i=1}^{3} \varepsilon_{\mathrm{e},i}\big]^2\,. \tag{5.44}$$

Following the proposed split, however, volumetric strains are calculated prior to the split into tensile and compressive contributions, such that (in the case of $\widehat{\boldsymbol{b}}_{\mathrm{d}+/-} = \widehat{\boldsymbol{G}}^{-1}$*)*

$$\overline{I}_1^{\bar{\boldsymbol{\varepsilon}}_{\mathrm{e}+}\,2} + \overline{I}_1^{\bar{\boldsymbol{\varepsilon}}_{\mathrm{e}-}\,2} = \big[\sum_{i=1}^{3} \varepsilon_{\mathrm{e},i}\big]^2 \tag{5.45}$$

holds (assuming $h(x)$ is the Macauly bracket). Even with an appropriate regularised form of $h(x)$ the deviations are expected to be small and can be neglected. Furthermore, the strain energy can be formulated such that the tensile and the compressive damage driving forces are positive semi-definite, see e.g. (5.54)*. Consequently, it is straightforward to formulate (associated) evolution equations for the damage variables which guarantee monotonous evolution of damage. In addition, the damage growth criterion is fulfilled, cf. [186]. Lastly, since tensile damage only affects tensile strain contributions, the damage initiation potential can be formulated in terms of the tensile damage driving force and, thereby, remains independent of compressive strain contributions.*

Remark 16 *Let the splitting function h be given by the Macauly brackets, i.e.*

$$h(x) = \frac{1}{2}\left[x + |x|\right], \quad \textit{and} \quad h'(x) = \frac{1}{2\,|x|}\left[x + |x|\right]. \tag{5.46}$$

Additional properties — besides the defining properties $h(x) + h(-x) = |x|$ and $h(x) - h(-x) = x$ — are then obtained. For reasons of consistency the derivative at $x = 0$ is defined as $h'(0) = 0$. The following properties, with constant $a \in \mathbb{R}^+$, are observed

$$h(a\,x) = \frac{1}{2}\left[a\,x + |a\,x|\right] = a\,\frac{1}{2}\left[x + |x|\right] \qquad = a\,h(x)\,, \tag{5.47}$$

$$h'(a\,x) = \frac{1}{2\,|a\,x|}\left[a\,x + |a\,x|\right] = \frac{a}{2\,a\,|x|}\left[x + |x|\right] \qquad = h'(x)\,, \tag{5.48}$$

$$h(x)\,h'(x) = \frac{1}{4\,|x|}\left[|x|^2 + 2\,x\,|x| + |x|^2\right] \qquad = h(x)\,, \tag{5.49}$$

$$h(h(x)) = \frac{1}{2}\left[\frac{1}{2}[x + |x|] + \frac{1}{2}\,\Big|\,\underbrace{x + |x|}_{\geq 0}\,\Big|\right] \qquad = h(x)\,, \tag{5.50}$$

$$h(x)\,h(-x) = \frac{1}{4}\left[-x^2 - x\,|x| + x\,|-x| + |x|^2\right] \qquad = 0\,, \tag{5.51}$$

$$h(x)\,h'(-x) = \frac{1}{4\,|-x|}\left[-x^2 - x\,|x| + x\,|-x| + |x|^2\right] \qquad = 0\,, \tag{5.52}$$

$$h'(h(x)) = h'(x)\,, \tag{5.53}$$

where the last property utilises $h(x) = x$ if $x > 0$ and $h(x) = 0$ if $x \leq 0$ as well as the introduced definition $h'(0) = 0$.

5.3 A prototype model

The local strain energy is formulated in terms of the introduced invariants such, that the respective strain measures occur quadratically, as typical deficiencies under compression are reduced by the logarithmic strains, i.e.

$$\Psi^{\mathrm{e}}(\overline{I}_1^{\overline{\boldsymbol{\varepsilon}}_{\mathrm{e}+}},\, \overline{I}_1^{\overline{\boldsymbol{\varepsilon}}_{\mathrm{e}-}},\, \overline{I}_{2,3}^{\overline{\boldsymbol{\varepsilon}}^{\mathrm{dev}}_{\mathrm{e}+}},\, \overline{I}_{2,3}^{\overline{\boldsymbol{\varepsilon}}^{\mathrm{dev}}_{\mathrm{e}-}}) = \frac{1}{2}\,K\left[\overline{I}_1^{\overline{\boldsymbol{\varepsilon}}_{\mathrm{e}+}}\right]^2 + \frac{1}{2}\,K\left[\overline{I}_1^{\overline{\boldsymbol{\varepsilon}}_{\mathrm{e}-}}\right]^2 + G\,\overline{I}_2^{\overline{\boldsymbol{\varepsilon}}^{\mathrm{dev}}_{\mathrm{e}+}} + G\,\overline{I}_2^{\overline{\boldsymbol{\varepsilon}}^{\mathrm{dev}}_{\mathrm{e}-}}\,, \tag{5.54}$$

where quadratic forms of all strain contributions can be taken into account, since the strains are split into volumetric and deviatoric contributions prior to the split into tensile and compressive parts, see Remark 15. Following the formulation of the anisotropic model, see Section 4.4, the inelastic contributions to the Helmholtz energy, Ψ^{p} and Ψ^{d} are chosen identical to (4.35) and (4.36).

The plastic initiation potential Φ_{p} is formulated in terms of effective Mandel stresses $\widehat{\boldsymbol{M}}_{\mathrm{e}}^{\mathrm{eff}}$, which are defined in analogy to (4.29) as

$$\widehat{\boldsymbol{M}}_{\mathrm{e}}^{\mathrm{eff}} = \widehat{\boldsymbol{C}}_{\mathrm{e}} \cdot \widehat{\boldsymbol{G}}^{-1} \cdot \left[\widehat{\boldsymbol{b}}_{\mathrm{d}+}^{-1} \cdot \widehat{\boldsymbol{S}}_{\mathrm{e}+} \cdot \widehat{\boldsymbol{b}}_{\mathrm{d}+}^{-1} - \widehat{\boldsymbol{b}}_{\mathrm{d}-}^{-1} \cdot \widehat{\boldsymbol{S}}_{\mathrm{e}-} \cdot \widehat{\boldsymbol{b}}_{\mathrm{d}-}^{-1} \right] \cdot \widehat{\boldsymbol{G}}^{-1} \,. \tag{5.55}$$

With the updated effective stresses, the initiation potential is chosen identical to the previously proposed model, cf. (4.40) and (4.44), i.e.

$$\Phi_{\mathrm{p}} = M_{\mathrm{e}}^{\mathrm{eq}}(\widehat{\boldsymbol{M}}_{\mathrm{e}}^{\mathrm{eff}}) - M_{\mathrm{e}}^{\max}(\beta_{\mathrm{p}}) = \sqrt{\zeta_{\mathrm{p}} \left[I_1^{\widehat{\boldsymbol{M}}_{\mathrm{e}}^{\mathrm{eff}}} \right]^2 + [1-\zeta_{\mathrm{p}}]\, I_2^{\widehat{\boldsymbol{M}}_{\mathrm{e}}^{\mathrm{eff}}}} + \sqrt{\tfrac{2}{3}}\, \beta_{\mathrm{p}} \,. \tag{5.56}$$

Due to the modification of the effective stresses, the plastic return direction (in the intermediate configuration) needs to be recalculated. To this end, the derivative of the effective elastic Mandel stresses $\widehat{\boldsymbol{M}}_{\mathrm{e}}^{\mathrm{eff}}$ with respect to the (normal) elastic Mandel stresses $\widehat{\boldsymbol{M}}_{\mathrm{e}}$ is required and can be calculated via chain derivatives with respect to the tensile and compressive Piola-Kirchhoff stresses $\widehat{\boldsymbol{S}}_{\mathrm{e}+}$ and $\widehat{\boldsymbol{S}}_{\mathrm{e}-}$, respectively. Combining (5.18) with (5.31) yields expressions for these stress contributions in terms of the Mandel stresses, i.e.

$$\widehat{\boldsymbol{S}}_{\mathrm{e}+} = \widehat{\boldsymbol{C}}_{\mathrm{e}}^{-1} \cdot \widehat{\boldsymbol{M}}_{\mathrm{e}} + \widehat{\boldsymbol{S}}_{\mathrm{e}-} \,, \qquad \widehat{\boldsymbol{S}}_{\mathrm{e}-} = -\widehat{\boldsymbol{C}}_{\mathrm{e}}^{-1} \cdot \widehat{\boldsymbol{M}}_{\mathrm{e}} + \widehat{\boldsymbol{S}}_{\mathrm{e}+} \,, \tag{5.57}$$

and the plastic return direction can be determined straightforwardly — neglecting the contributions of $\widehat{\boldsymbol{S}}_{\mathrm{e}-}$ to the derivative of $\widehat{\boldsymbol{S}}_{\mathrm{e}+}$ with respect to $\widehat{\boldsymbol{M}}_{\mathrm{e}}$ and, vice versa, neglecting the contributions of $\widehat{\boldsymbol{S}}_{\mathrm{e}+}$ to the derivative of $\widehat{\boldsymbol{S}}_{\mathrm{e}-}$ with respect to $\widehat{\boldsymbol{M}}_{\mathrm{e}}$ — as

$$\widehat{\boldsymbol{\nu}}_{\mathrm{p}} = \left[\widehat{\boldsymbol{C}}_{\mathrm{e}}^{-1} \cdot \widehat{\boldsymbol{b}}_{\mathrm{d}+}^{-1} \overline{\otimes} \widehat{\boldsymbol{b}}_{\mathrm{d}+}^{-1} + \widehat{\boldsymbol{C}}_{\mathrm{e}}^{-1} \cdot \widehat{\boldsymbol{b}}_{\mathrm{d}-}^{-1} \overline{\otimes} \widehat{\boldsymbol{b}}_{\mathrm{d}-}^{-1} \right] : \left[\widehat{\boldsymbol{G}}^{-1} \cdot \widehat{\boldsymbol{C}}_{\mathrm{e}} \cdot \widehat{\boldsymbol{\nu}}_{\mathrm{p}}^{\mathrm{eff}} \cdot \widehat{\boldsymbol{G}}^{-1} \right] , \tag{5.58}$$

where $\widehat{\boldsymbol{\nu}}_{\mathrm{p}}^{\mathrm{eff}}$ is identical to (4.49) but substituting the fictitious effective Mandel stresses $\overline{\boldsymbol{M}}_{\mathrm{e}}^{\mathrm{eff}}$ with the effective Mandel stresses in the intermediate configuration $\widehat{\boldsymbol{M}}_{\mathrm{e}}^{\mathrm{eff}}$, i.e.

$$\widehat{\boldsymbol{\nu}}_{\mathrm{p}}^{\mathrm{eff}} = \frac{2}{3\, M_{\mathrm{e}}^{\mathrm{eq}}(\widehat{\boldsymbol{M}}_{\mathrm{e}}^{\mathrm{eff}})} \left[\zeta_{\mathrm{p}}\, \overline{I}_1^{\widehat{\boldsymbol{M}}_{\mathrm{e}}^{\mathrm{eff}}}\, \boldsymbol{I} + [1-\zeta_{\mathrm{p}}]\, \widehat{\boldsymbol{M}}_{\mathrm{e}}^{\mathrm{t,eff}} \right] . \tag{5.59}$$

Assuming $\zeta_{\mathrm{p}} = -\frac{1}{2}$, this relation for the effective return direction $\widehat{\boldsymbol{\nu}}_{\mathrm{p}}^{\mathrm{eff}}$ yields

$$\widehat{\boldsymbol{\nu}}_{\mathrm{p}}^{\mathrm{eff}} = \frac{\widehat{\boldsymbol{M}}_{\mathrm{e}}^{\mathrm{dev,eff}}}{M_{\mathrm{e}}^{\mathrm{eq}}(\widehat{\boldsymbol{M}}_{\mathrm{e}}^{\mathrm{eff}})} \,. \tag{5.60}$$

The resulting expression for $\widehat{\boldsymbol{\nu}}_{\mathrm{p}}$, cf. (5.58), contains multiplications of tensile and compressive contributions. Conceptually speaking, however, an expression where the return direction is separated into tensile and compressive parts may provide a 'cleaner' formulation, see Remark 17.

The evolution equations for the plastic variables are given by

$$\widehat{\boldsymbol{L}}_{\mathrm{p}} = \lambda_{\mathrm{p}}\, \widehat{\boldsymbol{\nu}}_{\mathrm{p}}\,, \quad \text{and} \quad \dot{\alpha}_{\mathrm{p}} = \sqrt{\tfrac{2}{3}}\, \lambda_{\mathrm{p}}\,. \tag{5.61}$$

Also the (tensile) damage initiation potential $\Phi_{\mathrm{d}+}$ is chosen identical to the previously proposed model, cf. (4.41) and (4.45), but it is now dependent on the tensile damage Mandel stresses $\widehat{\boldsymbol{M}}_{\mathrm{d}+}$, defined in (5.32), i.e.

$$\begin{aligned} \Phi_{\mathrm{d}} &= M_{\mathrm{d}}^{\mathrm{eq}}(\widehat{\boldsymbol{M}}_{\mathrm{d}+}) - f_{\mathrm{dp}}(\alpha_{\mathrm{p}})\, M_{\mathrm{d}}^{\max}(\beta_{\mathrm{d}}) \\ &= \sqrt{\zeta_{\mathrm{d}} \left[I_1^{\widehat{\boldsymbol{M}}_{\mathrm{d}+}}\right]^2 + [1-\zeta_{\mathrm{d}}]\, I_2^{\widehat{\boldsymbol{M}}_{\mathrm{d}+}}} + \sqrt{\tfrac{2}{3}}\, f_{\mathrm{dp}}(\alpha_{\mathrm{p}})\, \beta_{\mathrm{d}}\,. \end{aligned} \tag{5.62}$$

The damage return direction $\widehat{\boldsymbol{\nu}}_{\mathrm{d}+}$ is given analogously to the previous model, cf. (4.50), with the fictitious damage Mandel stresses $\overline{\boldsymbol{M}}_{\mathrm{d}}$ substituted by the intermediate tensile damage Mandel stresses $\widehat{\boldsymbol{M}}_{\mathrm{d}+}$. The evolution equations related to the (tensile) damage variables are thus formulated as

$$\widehat{\boldsymbol{L}}_{\mathrm{d}+} = \lambda_{\mathrm{d}}\, \widehat{\boldsymbol{\nu}}_{\mathrm{d}+}\,, \quad \text{and} \quad \dot{\alpha}_{\mathrm{d}} = \sqrt{\tfrac{2}{3}}\, f_{\mathrm{dp}}(\alpha_{\mathrm{p}})\, \lambda_{\mathrm{d}}\,. \tag{5.63}$$

The idea for the evolution of the compressive damage variable $\boldsymbol{F}_{\mathrm{d}-}$ is, on the one hand, to evolve alongside the tensile damage variable, i.e. with $\widehat{\boldsymbol{L}}_{\mathrm{d}+}$. This evolution shall be faster if the tensile damage variable has evolved further than the compressive damage variable — long closed micro-cracks can be opened faster than short closed micro-cracks. On the other hand, compressive damage is reduced if plasticity evolves under compression — i.e. alongside the compressive contribution of the plastic velocity gradient $\widehat{\boldsymbol{L}}_{\mathrm{p}-}$. This effect will be stronger the more compressive damage evolves — long micro-cracks can be closed faster than short micro-cracks. Following these ideas, the tensorial functions $\boldsymbol{\kappa}_+$ and $\boldsymbol{\kappa}_-$ defining the evolution of the compressive damage variable are proposed as

$$\boldsymbol{\kappa}_+ = \left[\widehat{\boldsymbol{G}}^{-1} + \widehat{\boldsymbol{b}}_{\mathrm{d}-} - \widehat{\boldsymbol{b}}_{\mathrm{d}+}\right] \cdot \widehat{\boldsymbol{L}}_{\mathrm{d}+} \cdot \left[\widehat{\boldsymbol{G}} + \widehat{\boldsymbol{b}}_{\mathrm{d}+}^{-1} - \widehat{\boldsymbol{b}}_{\mathrm{d}-}^{-1}\right], \tag{5.64}$$

$$\boldsymbol{\kappa}_- = -\left[\widehat{\boldsymbol{G}}^{-1} - \widehat{\boldsymbol{b}}_{\mathrm{d}-}\right] \cdot \widehat{\boldsymbol{L}}_{\mathrm{p}-} \cdot \left[\widehat{\boldsymbol{G}} + \widehat{\boldsymbol{b}}_{\mathrm{d}-}^{-1}\right], \tag{5.65}$$

where the compressive contribution of the plastic velocity gradient is defined as

$$\widehat{\boldsymbol{L}}_{\mathrm{p}-} = \lambda_{\mathrm{p}}\, \frac{\widehat{\boldsymbol{M}}_{\mathrm{e}-}^{\mathrm{eff,dev}}}{M_{\mathrm{e}}^{\mathrm{eq}}(\widehat{\boldsymbol{M}}_{\mathrm{e}}^{\mathrm{eff}})}\,, \tag{5.66}$$

see also Remark 17 in this context. The compressive contribution of the effective elastic Mandel stresses required in (5.66) is given by

$$\widehat{\boldsymbol{M}}_{\mathrm{e}-}^{\mathrm{eff,dev}} = \widehat{\boldsymbol{C}}_{\mathrm{e}} \cdot \widehat{\boldsymbol{G}}^{-1} \cdot \widehat{\boldsymbol{b}}_{\mathrm{d}-}^{-1} \cdot \left[\widehat{\boldsymbol{T}}_{\mathrm{e}-}^{\mathrm{dev}} : \mathsf{P}_{\varepsilon-}^{\mathrm{dev}}\right] \cdot \widehat{\boldsymbol{b}}_{\mathrm{d}-}^{-1} \cdot \widehat{\boldsymbol{G}}^{-1} \,. \tag{5.67}$$

Remark 17 *The expression for the plastic return direction $\widehat{\boldsymbol{\nu}}_{\mathrm{p}}$, cf.* (5.58)*, (surprisingly) contains multiplications of tensile and compressive contributions. An alternative expression for $\widehat{\boldsymbol{\nu}}_{\mathrm{p}}$ is given by*

$$\begin{aligned} \widehat{\boldsymbol{\nu}}_{\mathrm{p}} = \widehat{\boldsymbol{\nu}}_{\mathrm{p}+} - \widehat{\boldsymbol{\nu}}_{\mathrm{p}-} = \quad & \widehat{\boldsymbol{C}}_{\mathrm{e}}^{-1} \cdot \widehat{\boldsymbol{b}}_{\mathrm{d}+}^{-1} \cdot \widehat{\boldsymbol{G}}^{-1} \cdot \widehat{\boldsymbol{C}}_{\mathrm{e}} \cdot \widehat{\boldsymbol{\nu}}_{\mathrm{p}+}^{\mathrm{eff}} \cdot \widehat{\boldsymbol{G}}^{-1} \cdot \widehat{\boldsymbol{b}}_{\mathrm{d}+}^{-1} \\ & - \widehat{\boldsymbol{C}}_{\mathrm{e}}^{-1} \cdot \widehat{\boldsymbol{b}}_{\mathrm{d}-}^{-1} \cdot \widehat{\boldsymbol{G}}^{-1} \cdot \widehat{\boldsymbol{C}}_{\mathrm{e}} \cdot \widehat{\boldsymbol{\nu}}_{\mathrm{p}-}^{\mathrm{eff}} \cdot \widehat{\boldsymbol{G}}^{-1} \cdot \widehat{\boldsymbol{b}}_{\mathrm{d}-}^{-1} \,, \end{aligned} \tag{5.68}$$

where only the tensile contributions are multiplied with the inverse of the tensile damage variable and, analogously, only the compressive contributions are multiplied with the inverse of the compressive damage variable. In (5.68)*, the tensile and compressive contributions to the effective plastic return direction $\widehat{\boldsymbol{\nu}}_{\mathrm{p}}^{\mathrm{eff}}$ are defined as (assuming $\zeta_{\mathrm{p}} = -\frac{1}{2}$)*

$$\widehat{\boldsymbol{\nu}}_{\mathrm{p}+}^{\mathrm{eff}} = \frac{\widehat{\boldsymbol{M}}_{\mathrm{e}+}^{\mathrm{eff,dev}}}{M_{\mathrm{e}}^{\mathrm{eq}}(\widehat{\boldsymbol{M}}_{\mathrm{e}}^{\mathrm{eff}})} \,, \qquad \widehat{\boldsymbol{\nu}}_{\mathrm{p}-}^{\mathrm{eff}} = \frac{\widehat{\boldsymbol{M}}_{\mathrm{e}-}^{\mathrm{eff,dev}}}{M_{\mathrm{e}}^{\mathrm{eq}}(\widehat{\boldsymbol{M}}_{\mathrm{e}}^{\mathrm{eff}})} \,, \tag{5.69}$$

where the tensile and compressive contributions of the effective Mandel stresses are — identical to (5.67) *— given by*

$$\widehat{\boldsymbol{M}}_{\mathrm{e}+}^{\mathrm{eff,dev}} = \widehat{\boldsymbol{C}}_{\mathrm{e}} \cdot \widehat{\boldsymbol{G}}^{-1} \cdot \widehat{\boldsymbol{b}}_{\mathrm{d}+}^{-1} \cdot \left[\widehat{\boldsymbol{T}}_{\mathrm{e}+}^{\mathrm{dev}} : \mathsf{P}_{\varepsilon+}^{\mathrm{dev}}\right] \cdot \widehat{\boldsymbol{b}}_{\mathrm{d}+}^{-1} \cdot \widehat{\boldsymbol{G}}^{-1} \,, \tag{5.70}$$

$$\widehat{\boldsymbol{M}}_{\mathrm{e}-}^{\mathrm{eff,dev}} = \widehat{\boldsymbol{C}}_{\mathrm{e}} \cdot \widehat{\boldsymbol{G}}^{-1} \cdot \widehat{\boldsymbol{b}}_{\mathrm{d}-}^{-1} \cdot \left[\widehat{\boldsymbol{T}}_{\mathrm{e}-}^{\mathrm{dev}} : \mathsf{P}_{\varepsilon-}^{\mathrm{dev}}\right] \cdot \widehat{\boldsymbol{b}}_{\mathrm{d}-}^{-1} \cdot \widehat{\boldsymbol{G}}^{-1} \,. \tag{5.71}$$

Consequently, the plastic velocity gradient can be split into tensile and compressive contributions, i.e.

$$\widehat{\boldsymbol{L}}_{\mathrm{p}} = \widehat{\boldsymbol{L}}_{\mathrm{p}+} - \widehat{\boldsymbol{L}}_{\mathrm{p}-} = \lambda_{\mathrm{p}} \, \widehat{\boldsymbol{\nu}}_{\mathrm{p}+} - \lambda_{\mathrm{p}} \, \widehat{\boldsymbol{\nu}}_{\mathrm{p}-} \,, \tag{5.72}$$

from which $\widehat{\boldsymbol{L}}_{\mathrm{p}-}$ can be directly used for the formulation of $\boldsymbol{\kappa}_-$. A comparison with the prior definition of the compressive contribution of the plastic velocity gradient in (5.66) *reveals that it has to be formulated directly by means of the effective return direction $\widehat{\boldsymbol{\nu}}_{\mathrm{p}-}^{\mathrm{eff}}$ rather than $\widehat{\boldsymbol{\nu}}_{\mathrm{p}-}$.*

5.4 Reduction to scalar-valued damage variables

As a primary (simplified) step, the prototype model is reduced to isotropic damage evolution. Following Remark 12, the damage deformation gradients, in the case of isotropic damage, can be equally represented by exponential functions in the form of

$$\boldsymbol{F}_{\mathrm{d}+} = \exp(-\tfrac{1}{2}\, d_+)\, \boldsymbol{I}\,, \quad \text{and} \quad \boldsymbol{F}_{\mathrm{d}-} = \exp(-\tfrac{1}{2}\, d_-)\, \boldsymbol{I}\,. \tag{5.73}$$

In this isotropic setting, the model can be formulated in the framework proposed in Chapter 3. Therein, the logarithmic strains $\boldsymbol{\varepsilon}_{\mathrm{e}}$ are formulated based on the elastic Finger tensor $\boldsymbol{b}_{\mathrm{e}}$ and the formulation uses the Mandel stresses $\boldsymbol{m}$. The evolution of the inelastic quantities of that model is formulated in principal (strain) space, cf. Table 3.2. Analogously, the model proposed in the previous section is now reduced to a formulation in eigenvalues only.

The strain energy, expressed in terms of strain-eigenvalues, is given by

$$\begin{aligned} \Psi^{\mathrm{e}} = \Psi^{\mathrm{e}}_{+} + \Psi^{\mathrm{e}}_{-} = \frac{1}{2}\, K\, f^2(d_+)\, h^2(\varepsilon^{\mathrm{vol}}_{\mathrm{e}}) + G\, f^2(d_+) \sum_{i=1}^{3} h^2(\varepsilon^{\mathrm{dev}}_{\mathrm{e},i}) \\ + \frac{1}{2}\, K\, f^2(d_-)\, h^2(-\varepsilon^{\mathrm{vol}}_{\mathrm{e}}) + G\, f^2(d_-) \sum_{i=1}^{3} h^2(-\varepsilon^{\mathrm{dev}}_{\mathrm{e},i})\,, \end{aligned} \tag{5.74}$$

where the damage function f is introduced as

$$f : \mathbb{R}^{+}_{0} \to [1,\, 0)\,, \quad \text{with} \quad f(x) = \exp(-x)\,. \tag{5.75}$$

Unlike to the model proposed in Chapter 3, no additional material parameters are introduced in the damage function f in order to keep the model simple as well as to keep the analogy to (5.73). Especially in view of proving dissipation to be non-negative, see Section 5.4.2, the addition of these material parameters would result in additional constraints. The eigenvalues of the Mandel stresses are split into tensile and compressive contributions by means of the function h as

$$m_i = h(m_i) - h(-m_i) = m_{i+} - m_{i-}\,, \tag{5.76}$$

where the individual contributions — after making use of (5.49) — are obtained as

$$\begin{aligned} m_{i+} &= K\, f^2(d_+)\, h(\varepsilon^{\mathrm{vol}}_{\mathrm{e}}) \quad + \frac{2}{3}\, G\, f^2(d_-) \sum_{j=1}^{3} h(-\varepsilon^{\mathrm{dev}}_{\mathrm{e},j}) + 2\, G\, f^2(d_+)\, h(\varepsilon^{\mathrm{dev}}_{\mathrm{e},i})\,, \\ m_{i-} &= K\, f^2(d_-)\, h(-\varepsilon^{\mathrm{vol}}_{\mathrm{e}}) + \frac{2}{3}\, G\, f^2(d_+) \sum_{j=1}^{3} h(\varepsilon^{\mathrm{dev}}_{\mathrm{e},j}) + 2\, G\, f^2(d_-)\, h(-\varepsilon^{\mathrm{dev}}_{\mathrm{e},i})\,. \end{aligned} \tag{5.77}$$

The effective deviatoric Mandel stresses $m_i^{\mathrm{eff,dev}}$ are defined as

$$m_i^{\mathrm{eff,dev}} = f^{-2}(d_+)\, m^{\mathrm{dev}}_{i+} - f^{-2}(d_-)\, m^{\mathrm{dev}}_{i-} = 2\, G\, \varepsilon^{\mathrm{dev}}_{\mathrm{e},i}\,, \tag{5.78}$$

where the deviatoric parts of the stresses are assumed to be

$$m_{i+}^{\mathrm{dev}} = 2\,G\,f^2(d_+)\,h(\varepsilon_{\mathrm{e},i}^{\mathrm{dev}})\,h'(\varepsilon_{\mathrm{e},i}^{\mathrm{dev}})\,, \tag{5.79}$$

$$m_{i-}^{\mathrm{dev}} = 2\,G\,f^2(d_-)\,h(-\varepsilon_{\mathrm{e},i}^{\mathrm{dev}})\,h'(-\varepsilon_{\mathrm{e},i}^{\mathrm{dev}})\,. \tag{5.80}$$

Importantly, these are not the true deviatoric stresses, as

$$\sum_{i=1}^{3} m_i^{\mathrm{dev}} \neq 0 \quad \text{if} \quad d_+ < d_-\,, \quad \text{with} \quad m_i^{\mathrm{dev}} = m_{i+}^{\mathrm{dev}} - m_{i-}^{\mathrm{dev}}\,. \tag{5.81}$$

However, this definition yields a (true) deviatoric stress measure not influenced by damage, cf. (5.78). Unlike in the previous section, compare (5.18), the stresses are not split according to the split of the strains, but rather independently by means of the (same) splitting function h. Thereby, the derivative of the (deviatoric) effective Mandel stresses $\boldsymbol{m}^{\mathrm{eff,dev}}$ with respect to the (normal, deviatoric) Mandel stresses $\boldsymbol{m}^{\mathrm{dev}}$ — required for the plastic return direction $\boldsymbol{\nu}_{\mathrm{p}}$ — is determined straight-forwardly, i.e.

$$\mu_{ij} = \frac{\partial m_i^{\mathrm{eff,dev}}}{\partial m_j^{\mathrm{dev}}} = f^{-2}(d_+)\,h'(m_i^{\mathrm{dev}})\,\delta_{ij} + f^{-2}(d_-)\,h'(-m_i^{\mathrm{dev}})\,\delta_{ij}\,. \tag{5.82}$$

Thus, the plastic potential Φ_{p} is obtained as

$$\Phi_{\mathrm{p}} = 2\,G\,\widetilde{\varepsilon}_{\mathrm{e}} + \sqrt{\tfrac{2}{3}}\,\beta_{\mathrm{p}}\,, \quad \text{with} \quad \widetilde{\varepsilon}_{\mathrm{e}} = \left[\sum\nolimits_{k=1}^{3}\left[\varepsilon_{\mathrm{e},k}^{\mathrm{dev}}\right]^2\right]^{\frac{1}{2}} \tag{5.83}$$

which, in the associated format, yields the plastic return contributions

$$\nu_{\mathrm{p},i} = \frac{\partial \Phi_{\mathrm{p}}}{\partial m_i} = \sum_{j=1}^{3} \nu_{\mathrm{p},j}^{\mathrm{eff}}\,\mu_{jk}\,\delta_{ki}^{\mathrm{dev}}\,, \quad \text{with} \quad \nu_{\mathrm{p},j}^{\mathrm{eff}} = \widetilde{\varepsilon}_{\mathrm{e}}^{-1}\,\varepsilon_{\mathrm{e},j}^{\mathrm{dev}}\,. \tag{5.84}$$

5.4.1 Algorithmic implementation

The update of the (deviatoric part of the) logarithmic strains can now be stated as

$$\varepsilon_{\mathrm{e},i} = \frac{1}{3}\,\varepsilon_{\mathrm{e}}^{\mathrm{vol}} + \varepsilon_{\mathrm{e},i}^{\mathrm{tr,dev}} - \Delta\lambda_{\mathrm{p}} \sum_{j=1}^{3} \nu_{\mathrm{p},j}^{\mathrm{eff}}\,\mu_{ji}\,. \tag{5.85}$$

The update of the proportional plastic hardening variable α_{p} remains unchanged, cf. (3.28), i.e.

$$\alpha_{\mathrm{p}_{n+1}} = \alpha_{\mathrm{p}_n} + \tfrac{2}{3}\,\Delta\lambda_{\mathrm{p}}\,. \tag{5.86}$$

With the format of the strain energy given in (5.74) the damage driving forces are obtained as

$$q_+ = -f(d_+)\, f'(d_+) \left[K\, h^2(\varepsilon_{\mathrm{e}}^{\mathrm{vol}}) + 2\, G\, \widetilde{\varepsilon}_{\mathrm{e}+}^2 \right], \qquad \text{with} \quad \widetilde{\varepsilon}_{\mathrm{e}+}^2 = \sum_{i=1}^{3} h^2(\varepsilon_{\mathrm{e},i}^{\mathrm{dev}}), \tag{5.87}$$

$$q_- = -f(d_-)\, f'(d_-) \left[K\, h^2(-\varepsilon_{\mathrm{e}}^{\mathrm{vol}}) + 2\, G\, \widetilde{\varepsilon}_{\mathrm{e}-}^2 \right], \qquad \text{with} \quad \widetilde{\varepsilon}_{\mathrm{e}-}^2 = \sum_{i=1}^{3} h^2(-\varepsilon_{\mathrm{e},i}^{\mathrm{dev}}). \tag{5.88}$$

The (tensile) damage initiation potential — in the isotropic case the anisotropy parameter is $\zeta_{\mathrm{d}} = 1$, cf. (4.45) — can be calculated by

$$\Phi_{\mathrm{d}} = q_+ + \sqrt{\frac{2}{3}}\, f_{\mathrm{dp}}(\alpha_{\mathrm{p}})\, \beta_{\mathrm{d}}, \qquad \text{since } q_+ \geq 0 \text{ holds.} \tag{5.89}$$

Consequently, the updates of the tensile damage variable d_+ and the proportional damage hardening variable α_{d} are obtained as

$$d_+ = d_{+,n} + \Delta\lambda_{\mathrm{d}}, \quad \text{and} \quad \alpha_{\mathrm{d}n+1} = \alpha_{\mathrm{d}n} + \sqrt{\frac{2}{3}}\, \Delta\lambda_{\mathrm{d}}\, f_{\mathrm{dp}}(\alpha_{\mathrm{p}}). \tag{5.90}$$

The evolution of the compressive damage variable d_-, i.e.

$$d_- = d_{-,n} + \Delta t\, \kappa_+ + \Delta t\, \kappa_-, \tag{5.91}$$

is controlled by κ_+ (5.64) and κ_- (5.65). For the sake of algorithmic simplicity, damage no longer exclusively evolves along κ_+ or κ_-. In the isotropic setting $\kappa_{+/-}$ are given by

$$\kappa_+ = [1 + f(d_-) - f(d_+)]\, [1 + f^{-1}(d_+) - f^{-1}(d_-)]\, \lambda_{\mathrm{d}}, \tag{5.92}$$

$$\kappa_-^{(1)} = -\vartheta_-\, [f^{-1}(d_-) - f(d_-)]\, \lambda_{\mathrm{p}}\, \widetilde{\varepsilon}_{\mathrm{e}-}\, \widehat{\varepsilon}_{\mathrm{e}}^{-2}, \quad \text{with} \quad \widehat{\varepsilon}_{\mathrm{e}}^2 = \widetilde{\varepsilon}_{\mathrm{e}}^2 + \frac{K}{2\,G} \left| \varepsilon_{\mathrm{e}}^{\mathrm{vol}} \right|^2, \tag{5.93}$$

$$\kappa_-^{(2)} = -\vartheta_-\, [f^{-1}(d_-) - f(d_-)]\, \lambda_{\mathrm{p}}\, \widetilde{\varepsilon}_{\mathrm{e}-}\, \widehat{\varepsilon}_{\mathrm{e}}^{-1}, \tag{5.94}$$

with $\vartheta_- \in [0,\, 1]$ being a parameter controlling the rate of stiffness recovery under compression. Quantity $\widetilde{\varepsilon}_{\mathrm{e}}$ is defined as

$$\widetilde{\varepsilon}_{\mathrm{e}}^2 = \sum_{i=1}^{3} \left[\varepsilon_{\mathrm{e},i}^{\mathrm{dev}} \right]^2 = \widetilde{\varepsilon}_{\mathrm{e}+}^2 + \widetilde{\varepsilon}_{\mathrm{e}-}^2. \tag{5.95}$$

Variant 1 of the evolution equation for compressive damage $\kappa_-^{(1)}$ is a modified version of the evolution equation of the prototype model. It incorporates the volumetric strain and, additionally, it is divided with a measure of total strain. Thereby, $\kappa_-^{(1)}$ unconditionally yields non-negative dissipation, see Section 5.4.2. However, compressive damage under uniaxial tension loading barely evolves, which is not what one would expect to happen

in reality, see Section 5.5. To this end, $\kappa_-^{(2)}$ is introduced and both variants are discussed in the following sections.

Resulting from the highly non-linear evolution of the compressive damage variable d_- in terms of $\kappa_{+/-}$, the updates of the Lagrange multipliers and of the internal variables need to be determined implicitly, e.g. by means of a Newton-Raphson scheme. To this end, the vector of unknowns $\boldsymbol{x}$ and the corresponding residua $\boldsymbol{r}$ are set up as

$$\boldsymbol{x} = \begin{bmatrix} \Delta\lambda_\mathrm{p} \\ \Delta\lambda_\mathrm{d} \\ \varepsilon_{\mathrm{e},1} \\ \varepsilon_{\mathrm{e},2} \\ \varepsilon_{\mathrm{e},3} \\ d_- \end{bmatrix}, \qquad \boldsymbol{r} = \begin{bmatrix} r_\mathrm{p} \\ r_\mathrm{d} \\ r_{\varepsilon,1} \\ r_{\varepsilon,2} \\ r_{\varepsilon,3} \\ r_{d_-} \end{bmatrix}, \tag{5.96}$$

where the individual residuum contributions are given by

$$r_\mathrm{p} = \sqrt{\Phi_\mathrm{p}^2 + {\Delta\lambda_\mathrm{p}}^2 + \epsilon^\mathrm{FB}} + \Phi_\mathrm{p} - \Delta\lambda_\mathrm{p}\,, \tag{5.97}$$

$$r_\mathrm{d} = \sqrt{\Phi_\mathrm{d}^2 + {\Delta\lambda_\mathrm{d}}^2 + \epsilon^\mathrm{FB}} + \Phi_\mathrm{d} - \Delta\lambda_\mathrm{d}\,, \quad \text{with} \quad \epsilon^\mathrm{FB} \overset{\text{e.g.}}{=} 10^{-20}\,, \tag{5.98}$$

$$r_{\varepsilon,i} = \varepsilon_{\mathrm{e},i} - \varepsilon_{\mathrm{e},i,n} + \Delta\lambda_\mathrm{p}\,\nu_{\mathrm{p},i}\,, \quad \text{with} \quad i = 1,2,3\,, \tag{5.99}$$

$$r_{d_-} = d_- - d_{-_n} - \kappa_+ - \kappa_-\,. \tag{5.100}$$

The entries of the related Jacobian are determined by means of numerical perturbation by using the forward-difference method (perturbation factor $\epsilon^\mathrm{pert} \overset{\text{e.g.}}{=} 10^{-6}$). The Newton-Raphson method follows the scheme provided previously for the anisotropic model, cf. Table 4.1 steps 2 to 7, whereby in this case the evaluation of the residuum and the update of the internal variables are given in Table 5.2. The general algorithmic structure is summarised in Table 5.1. Therein, stresses and driving forces, see Table 5.1 step 9, analogous to the model proposed in Chapter 3 are specified, although inhomogeneous boundary value problems and regularisation are not discussed further within this work. It is assumed that only the tensile damage variable needs to be regularised, as the degradation from the evolution of compressive damage is proportional to the evolution of tensile damage.

5.4.2 Proof of non-negative dissipation

Since the evolution of the compressive damage variable is formulated in a non-associated sense, special attention is paid towards guaranteeing non-negative dissipation. The reduced dissipation $\mathcal{D}^\mathrm{red}$ of this model (neglecting hardening contributions) for the case of tensile damage evolution ($\lambda_\mathrm{d} > 0$) can be expressed as

$$\mathcal{D}^\mathrm{red} = \lambda_\mathrm{p} \sum_{i=1}^{3} m_i\,\nu_{\mathrm{p},i} + q_+\,\lambda_\mathrm{d} + q_-\,\kappa_+ \geq 0\,. \tag{5.101}$$

In this case, it is straight forward to show that dissipation is non-negative, as the damage driving forces q_+ (5.87) and q_- (5.88) as well as the function κ_+ are always positive ($f(d) > 0$, $f'(d) < 0$, $h(x) > 0$). In the other case ($\lambda_\mathrm{d} = 0$ and $\lambda_\mathrm{p} > 0$) positive dissipation needs to be shown; starting from the expression of the reduced dissipation

$$\mathcal{D}^\mathrm{red} = \lambda_\mathrm{p} \sum_{i=1}^{3} m_i \, \nu_{\mathrm{p},i} + q_- \, \kappa_- \geq 0 \,, \tag{5.102}$$

focus is first placed on the plasticity related term. Combining (5.77) and (5.84) together with Remark 16 allows the plasticity related term to be rewritten as

$$\begin{aligned} \sum_{i=1}^{3} m_i \, \nu_{\mathrm{p},i} = \frac{K}{\widetilde{\varepsilon}_\mathrm{e}} \sum_{i=1}^{3} h(-\varepsilon_{\mathrm{e},i}^\mathrm{dev}) \left[\left| \varepsilon_\mathrm{e}^\mathrm{vol} \right| - h(\varepsilon_\mathrm{e}^\mathrm{vol}) \, \frac{f^2(d_+)}{f^2(d_-)} - h(-\varepsilon_\mathrm{e}^\mathrm{vol}) \, \frac{f^2(d_-)}{f^2(d_+)} \right] \\ + 2\,G\,\widetilde{\varepsilon}_\mathrm{e} + \frac{2\,G}{3\,\widetilde{\varepsilon}_\mathrm{e}} \, \frac{\left[f^2(d_-) - f^2(d_+) \right]^2}{f^2(d_-)\, f^2(d_+)} \sum_{i=1}^{3} \sum_{j=1}^{3} h(\varepsilon_{\mathrm{e},i}^\mathrm{dev}) h(-\varepsilon_{\mathrm{e},j}^\mathrm{dev}) \,, \end{aligned} \tag{5.103}$$

where, for the derivation of the first (volumetric) term, the alternate representation of the plastic return contribution

$$\nu_{\mathrm{p},i} = \widetilde{\varepsilon}_\mathrm{e}^{-1} \left[f^{-2}(d_+) \varepsilon_{\mathrm{e},i}^\mathrm{dev} + \left[f^{-2}(d_+) - f^{-2}(d_-) \right] h(-\varepsilon_{\mathrm{e},i}^\mathrm{dev}) \right] , \tag{5.104}$$

is used together with $\sum_{i=1}^{3} \varepsilon_{\mathrm{e},i}^\mathrm{dev} = 0$. The last term in (5.103) is obtained from the terms in the stress contributions (5.77) which are multiplied with $\frac{2}{3}\,G$, i.e. the mentioned terms multiplied with $\nu_{\mathrm{p},i}$ — introducing the abbreviating notation $h_{\pm i} = h(\pm\varepsilon_{\mathrm{e},i}^\mathrm{dev})$ — yield

$$\frac{2\,G}{3\,\widetilde{\varepsilon}_\mathrm{e}} \sum_{i=1}^{3} \sum_{j=1}^{3} \left[\frac{f^2(d_+)}{f^2(d_-)} \, h_{-j} \, h_{+i} + \frac{f^2(d_-)}{f^2(d_+)} \, h_{+j} \, h_{-i} - h_{-j} \, h_{-i} - h_{+j} \, h_{+i} \right] . \tag{5.105}$$

After making use of the relation

$$\sum_{i=1}^{3} \sum_{j=1}^{3} h_{+j} \, h_{-i} = \sum_{i=1}^{3} \sum_{j=1}^{3} h_{+i} \, h_{-j} \,, \tag{5.106}$$

and considering that the basic algebraic relation $a\,b^{-1} + b\,a^{-1}$ can be equivalently represented as $2 + [a-b]^2\, a^{-1}\, b^{-1}$ one has

$$\frac{2\,G}{3\,\widetilde{\varepsilon}_\mathrm{e}} \sum_{i=1}^{3} \sum_{j=1}^{3} \left[\frac{\left[f^2(d_+) - f^2(d_-) \right]^2}{f^2(d_+)\, f^2(d_-)} \, h_{+j} \, h_{-i} + 2\, h_{+j} \, h_{-i} - h_{-j} \, h_{-i} - h_{+j} \, h_{+i} \right] . \tag{5.107}$$

Therein, the last three terms turn out to be equally zero, i.e.

$$-h_{+j} \, h_{+i} - h_{-i} \, h_{-j} + h_{+i} \, h_{-j} + h_{-i} \, h_{+j} = -[h_{+j} - h_{-j}] \, [h_{+i} - h_{-i}] = -\varepsilon_{\mathrm{e},i}^\mathrm{dev} \, \varepsilon_{\mathrm{e},j}^\mathrm{dev} \,. \tag{5.108}$$

The dissipation related to the compressive damage driving force — assuming $\kappa_-^{(1)}$ is used in the evolution equation — can be represented as

$$q_- \, \kappa_-^{(1)} = \lambda_\mathrm{p} \, \vartheta_- \, \frac{\widetilde{\varepsilon}_{\mathrm{e}-}}{\widehat{\varepsilon}_\mathrm{e}^2} \left[1 - f^2(d_-)\right] f'(d_-) \left[K \, h^2(-\varepsilon_\mathrm{e}^\mathrm{vol}) + 2\,G\,\widetilde{\varepsilon}_{\mathrm{e}-}^2\right], \tag{5.109}$$

which is negative due to $f'(d_-) < 0$. Since the recovery of compressive damage is related to the plastic Lagrange multiplier, the negative dissipation is compensated by the positive dissipation generated from plasticity, i.e. $2\,G\,\widetilde{\varepsilon}_\mathrm{e} + q_- \, \kappa_- \geq 0$ shall hold. Division of (5.109) by $2\,G\,\widetilde{\varepsilon}_\mathrm{e}$ and rewriting terms yields the representation

$$\left[1 - f^2(d_-)\right] |f'(d_-)| \frac{\widetilde{\varepsilon}_{\mathrm{e}-}}{\widetilde{\varepsilon}_\mathrm{e}} \left[\frac{K}{2\,G} \, \frac{h^2(-\varepsilon_\mathrm{e}^\mathrm{vol})}{\widehat{\varepsilon}_\mathrm{e}^2} + \frac{\widetilde{\varepsilon}_{\mathrm{e}-}^2}{\widehat{\varepsilon}_\mathrm{e}^2}\right] \vartheta_- \overset{!}{\leq} 1 \, . \tag{5.110}$$

This relation holds, as terms can be separately shown to be smaller than (or equal to) one, i.e. the damage function $f(d_-)$ related terms are smaller per definitionem while the strain related fractions all have only the compressive contribution in the numerator and both, the tensile and compressive, contributions in the denominator. The compressive evolution parameter ϑ_- has to be chosen in the bounds $[0,\, 1]$. The dissipation for variant 2 of the evolution equation is non-negative under the assumption of $\widehat{\varepsilon}_\mathrm{e} \leq 1$, as the analogous form of (5.110) for variant 2 reads

$$\left[1 - f^2(d_-)\right] |f'(d_-)| \frac{\widetilde{\varepsilon}_{\mathrm{e}-}}{\widetilde{\varepsilon}_\mathrm{e}} \left[\frac{K}{2\,G} \, \frac{h^2(-\varepsilon_\mathrm{e}^\mathrm{vol})}{\widehat{\varepsilon}_\mathrm{e}^2} + \frac{\widetilde{\varepsilon}_{\mathrm{e}-}^2}{\widehat{\varepsilon}_\mathrm{e}^2}\right] \vartheta_- \overset{!}{\leq} \widehat{\varepsilon}_\mathrm{e}^{-1} \, . \tag{5.111}$$

5.5 Response under homogeneous deformation

First, the response of the model — specifically the evolution of the damage variables — is analysed for uniaxial tension loading with subsequent unloading. The deformation is prescribed in the form of

$$\boldsymbol{F} = \lambda_\parallel \, \boldsymbol{e} \otimes \boldsymbol{e} + \lambda_\perp \left[\boldsymbol{I} - \boldsymbol{e} \otimes \boldsymbol{e}\right], \tag{5.112}$$

with $\|\boldsymbol{e}\| = 1$ and where the lateral stretch $\lambda_\perp$ can develop such that the stress is uniaxial in primary loading direction $\boldsymbol{e}$, i.e. $\boldsymbol{P} = P_\parallel \, \boldsymbol{e} \otimes \boldsymbol{e}$. The chosen material parameters are listed in Table 5.3.

In Figure 5.2a) a stress-stretch response typical for dual-phase steels with high ductility is observed. The damage evolution for model variant 1 using $\kappa_-^{(1)}$ (blue), Figure 5.2b), exhibits a significantly reduced evolution of the compressive damage variable d_- compared to the tensile damage variable d_+. Compressive damage evolves less, as the split into tensile and compressive contributions is related to the strain state rather than to

Table 5.1: Algorithmic outline for the ductile damage model including the microcrack-closure-reopening effect.

0. given: $\boldsymbol{F}$, ϕ_d, $\nabla_{\boldsymbol{X}}\phi_\mathrm{d}$ and $\boldsymbol{C}_n^{\mathrm{p}-1}$, $\alpha_{\mathrm{p}n}$, $\alpha_{\mathrm{d}n}$, d_{+n}, d_{-n}

1. compute trial elastic finger tensor and spectral decomposition

$$\boldsymbol{b}^{\mathrm{e,tr}} = \boldsymbol{F}\cdot\boldsymbol{C}_n^{\mathrm{p}-1}\cdot\boldsymbol{F}^{\mathrm{t}} = \sum_{i=1}^{3}[\lambda_i^{\mathrm{e,tr}}]^2\,\boldsymbol{n}_i\otimes\boldsymbol{n}_i\,, \qquad \varepsilon_i^{\mathrm{e,tr}} = \log(\lambda_i^{\mathrm{e,tr}})$$

2. initialise $\Delta\lambda_\mathrm{p} = \Delta\lambda_\mathrm{d} = 0$ and plastic return contribution $\nu_{\mathrm{p},i}^{\mathrm{eff}} = \|\boldsymbol{\varepsilon}_\mathrm{e}^{\mathrm{tr,dev}}\|^{-1}\,\varepsilon_{\mathrm{e},i}^{\mathrm{tr,dev}}$

3. evaluate residuum $\boldsymbol{r}$ and update state variables for given $\boldsymbol{x}$ → see Table 5.2

4. if Newton-Raphson algorithm has converged, i.e. $\|\boldsymbol{r}\| < \mathrm{tol}$, goto 9

5. compute tangent $\boldsymbol{J}$ by means of numerical perturbation

6. compute Newton-Raphson increment $\Delta\boldsymbol{x} = -\boldsymbol{J}^{-1}\cdot\boldsymbol{r}$

7. determine step-length a via Armijo-Goldstein algorithm
   a) initialise $j = 0$, $a_j = \|\Delta\boldsymbol{x}\|$, search direction $\boldsymbol{s} = \Delta\boldsymbol{x}/a_0$ and $m = c\,\|\boldsymbol{J}^{\mathrm{t}}\cdot\Delta\boldsymbol{x}\|$
   b) evaluate residuum $\tilde{\boldsymbol{r}}$ for $\tilde{\boldsymbol{x}} = \boldsymbol{x}_i + a_j\,\boldsymbol{s}$
   c) if $\|\boldsymbol{r}\| - \|\tilde{\boldsymbol{r}}\| \geq a_j\,m$ set $a = a_j$ and goto 8
   d) update $a_{j+1} = \tau\,a_j$, $j = j+1$
   e) if $j > j_{\max}$ set $a = a_0$ and goto 8 else goto 7b

8. update unknowns $\boldsymbol{x}_{i+1} = \boldsymbol{x}_i + a\,\boldsymbol{s}$, update $i = i+1$, goto 3

9. compute stresses and driving forces

$$\boldsymbol{m}^{\mathrm{t}} = \sum_{i=1}^{3} m_i\,\boldsymbol{n}_i\otimes\boldsymbol{n}_i\,, \qquad \text{with} \quad m_i \quad \text{from (5.76) and (5.77)}$$
$$Y_\mathrm{d} = b_\mathrm{d}\,[\phi_\mathrm{d} - d_+]$$
$$\boldsymbol{Y}_\mathrm{d} = c_\mathrm{d}\,\nabla_{\boldsymbol{X}}\phi_\mathrm{d}$$

10. compute tangent moduli ⟶ Table 3.3, required derivatives are determined by means of numerical perturbation

Table 5.2: Algorithmic outline to evaluate the residuum and update the state variables for the ductile damage model including the microcrack closure-reopening effect.

0. given: $\varepsilon^{\mathrm{tr}}_{\mathrm{e},i}$, ϕ_{d}, α_{p_n}, $\alpha_{\mathrm{d}n}$, d_{+n}, d_{-n} and $\boldsymbol{x}^{\mathrm{t}} = [\Delta\lambda_{\mathrm{p}},\, \Delta\lambda_{\mathrm{d}},\, \varepsilon_{\mathrm{e},i},\, d_{-}]$

1. update internal variables

$$\alpha_{\mathrm{p}} = \alpha_{\mathrm{p}_n} + \sqrt{\tfrac{2}{3}}\,\Delta\lambda_{\mathrm{p}}$$
$$\alpha_{\mathrm{d}} = \alpha_{\mathrm{d}n} + \sqrt{\tfrac{2}{3}}\, f_{\mathrm{dp}}(\alpha_{\mathrm{p}})\,\Delta\lambda_{\mathrm{d}}$$
$$d_{+} = d_{+n} + \Delta\lambda_{\mathrm{d}}$$

2. compute plastic initiation potential and return contribution

$$\Phi_{\mathrm{p}} = 2\,G\,\widetilde{\varepsilon}_{\mathrm{e}} + \sqrt{\tfrac{2}{3}}\,\beta_{\mathrm{p}}\,, \qquad \text{with} \quad \widetilde{\varepsilon}^{2}_{\mathrm{e}} = \sum_{i=1}^{3} \left[\varepsilon^{\mathrm{dev}}_{\mathrm{e},i}\right]^2$$
$$\nu_{\mathrm{p},i} = \sum_{j=1}^{3} \left[h(\varepsilon_{\mathrm{e},j})\, f^{-2}(d_{+}) - h(-\varepsilon_{\mathrm{e},j})\, f^{-2}(d_{-})\right] \left[\delta_{ji} - \tfrac{1}{3}\right] \widetilde{\varepsilon}^{-1}_{\mathrm{e}}$$

3. compute damage initiation potential and influence functions

$$\Phi_{\mathrm{d}} = -f(d_{+})\, f'(d_{+}) \left[K\, h^2(\varepsilon^{\mathrm{vol}}_{\mathrm{e}}) + 2\,G\,\widetilde{\varepsilon}^{2}_{\mathrm{e}+}\right] - \sqrt{\tfrac{2}{3}}\, f_{\mathrm{dp}}(\alpha_{\mathrm{p}})\,\beta_{\mathrm{d}}$$
$$\kappa_{+} = \left[1 + f(d_{-}) - f(d_{+})\right] \left[1 + f^{-1}(d_{+}) - f^{-1}(d_{-})\right] \lambda_{\mathrm{d}}$$
$$\kappa^{(1)}_{-} = -\vartheta_{-} \left[f^{-1}(d_{-}) - f(d_{-})\right] \widetilde{\varepsilon}_{\mathrm{e}-}\, \widehat{\varepsilon}^{-2}_{\mathrm{e}}\,, \qquad \text{with} \quad \widehat{\varepsilon}^{2}_{\mathrm{e}} = \widetilde{\varepsilon}^{2}_{\mathrm{e}} + \tfrac{K}{2G}\,|\varepsilon^{\mathrm{vol}}_{\mathrm{e}}|^2$$
$$\kappa^{(2)}_{-} = -\vartheta_{-} \left[f^{-1}(d_{-}) - f(d_{-})\right] \widetilde{\varepsilon}_{\mathrm{e}-}\, \widehat{\varepsilon}^{-1}_{\mathrm{e}}$$

4. evaluate residuum $\boldsymbol{r}^{\mathrm{t}} = [r_{\mathrm{p}},\, r_{\mathrm{d}},\, r_{\varepsilon,1},\, r_{\varepsilon,2},\, r_{\varepsilon,3},\, r_{d_{-}}]$

$$r_{\mathrm{p}} = \sqrt{\Phi^2_{\mathrm{p}} + {\Delta\lambda_{\mathrm{p}}}^2 + \epsilon^{\mathrm{FB}}} + \Phi_{\mathrm{p}} - \Delta\lambda_{\mathrm{p}}$$
$$r_{\mathrm{d}} = \sqrt{\Phi^2_{\mathrm{d}} + {\Delta\lambda_{\mathrm{d}}}^2 + \epsilon^{\mathrm{FB}}} + \Phi_{\mathrm{d}} - \Delta\lambda_{\mathrm{d}}$$
$$r_{\varepsilon,i} = \varepsilon_{\mathrm{e},i} - \varepsilon^{\mathrm{tr}}_{\mathrm{e},i} + \Delta\lambda_{\mathrm{p}}\,\nu_{\mathrm{p},i}\,, \quad \text{with} \quad i = 1, 2, 3$$
$$r_{d_{-}} = d_{-} - d_{-n} - \kappa_{+} - \kappa_{-}$$

Table 5.3: List of material parameters for the homogeneous tension test.

Symbol	Description	Value	Unit
E	Young's modulus	210.0	GPa
ν	Poisson's ratio	0.3	–
$M_{\mathrm{e}}^{\mathrm{max0}}$	yield stress	250.0	MPa
h_{p}	plastic hardening modulus	2500.0	MPa
n_{p}	plastic hardening exponent	0.25	–
$M_{\mathrm{d}}^{\mathrm{max0}}$	damage initiation	2.0	MPa
h_{d}	damage hardening modulus	5.0	MPa
n_{d}	damage hardening exponent	1.0	–
h_{dp}	damage deterioration	0.0	–
$\alpha_{\mathrm{p,max}}$	deterioration offset	3.0	–
ϑ_-	compressive damage recovery	1.0	–

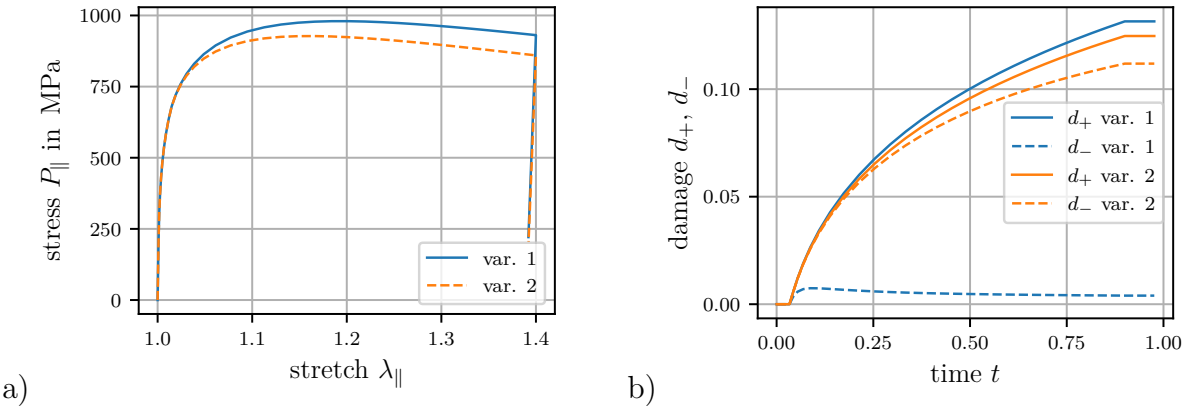

Figure 5.2: Comparison of the model response of variant 1 (blue) with the model response of variant 2 (orange) for uniaxial tension loading. a) depicts the Piola stress $P_\parallel$ in loading direction over the stretch $\lambda_\parallel$ in loading direction. b) shows the evolution of tensile damage d_+ (solid lines) and compressive damage d_- (dashed lines).

the stress state, such that negative strains from the contraction in transverse direction of uniaxial tensile loading are attributed to compression. Furthermore, since $\kappa_-^{(1)}$ is proportional to $\widehat{\varepsilon}_{\mathrm{e}}^{-1}$, very small strains result in a strongly inhibited evolution of d_- — in this case even for a state of uniaxial tension.

For model variant 2 using $\kappa_-^{(2)}$ (orange) evolution of the compressive damage variable d_- is reduced only by about ten percent compared to the tensile damage variable d_+, which is more in line with the expected response — a lower compressive damage variable under pure tension could be caused by zero-volume defects, which are able to contribute to the stiffness immediately upon load reversal. The assumption $\widehat{\varepsilon}_{\mathrm{e}} \leq 1$ — required to fulfil the dissipation inequality for this variant — holds for many typical engineering applications, see Remark 18. Consequently, only model variant 2 is analysed further in the following.

In order to demonstrate the basic properties of the model, the response of the model under triaxial loading is analysed. The deformation is still prescribed according to (5.112), but in primary loading direction the stretch $\lambda_\parallel$ is prescribed such that tension loading is followed by compression loading, see Figure 5.3a). The stretch in lateral direction $\lambda_\perp$ develops so that different levels of Piola stresses in lateral direction are obtained, i.e. $P_\perp = 0\,\mathrm{MPa}$, $-300\,\mathrm{MPa}$, $+100\,\mathrm{MPa}$. These differences are so small, that to the human eye the lines are non-distinguishable in the given figure. Hence, the overall stress state is now given by

$$\boldsymbol{P} = P_\parallel\, \boldsymbol{e} \otimes \boldsymbol{e} + P_\perp\, [\boldsymbol{I} - \boldsymbol{e} \otimes \boldsymbol{e}]\,. \tag{5.113}$$

The stress response of the material in terms of the Kirchhoff stresses $\tau_\parallel$ and $\tau_\perp$ is displayed in Figure 5.3b). During tension loading in direction of $\boldsymbol{e}$ a response typical for ductile material is observed. Under compression, the stress response resembles a response of a purely plastic material. The selected measure of stress increases linearly even though the hardening formulation is non-linear, since the cross-section under compression increases, and both effects together lead to the (seemingly) linear response. The applied lateral stress shifts the level of stress in primary loading direction (slightly) up or down. In contrast to the constantly prescribed lateral Piola stress $P_\perp$, the lateral Kirchhoff stress $\tau_\perp$ is not constant due to the changing cross-section.

Damage evolution, see Figure 5.3c), demonstrates exactly the idea of the proposed formulation: During tensile loading, tensile damage evolves as usual (i.e. as in the model described in Chapter 3) and compressive damage evolves slightly less; identical to before cf. Figure 5.2b). As expected, more damage evolves if a positive (tensile) lateral stress is applied and less damage evolves if a negative (compressive) lateral stress is applied. During compressive loading, tensile damage remains constant while the compressive damage variable is reduced with ongoing plastic deformation.

Evolution of the hardening variables α_p and α_d is shown in Figure 5.3d). One observes damage hardening evolving only during tensile loading and plastic hardening evolution being increased during compressive loading compared to tensile loading.

Remark 18 *The dissipation inequality for variant 2 of the proposed model is fulfilled (especially) if* $\widehat{\varepsilon}_\mathrm{e}^2 \leq 1$. *While the deviatoric contribution* $\widetilde{\varepsilon}_\mathrm{e}^2$ *can safely be assumed to be small if plasticity is active, the volumetric contribution* $\frac{K}{2\,G}\,|\varepsilon^\mathrm{vol}|^2$ *may become large. Assuming a purely volumetric stress/strain state without damage evolution, stress is given by* $\tau = K\,\varepsilon^\mathrm{vol}$. *In the limit case of* $\widehat{\varepsilon}_\mathrm{e}^2 = 1$ *one obtains (with* $\widetilde{\varepsilon}_\mathrm{e}^2 = 0$*)*

$$\varepsilon^\mathrm{vol}_\mathrm{max} = \sqrt{\frac{2\,G}{K}}\,, \tag{5.114}$$

which renders the stress to be

$$\tau_\mathrm{max} = \sqrt{2\,G\,K} \qquad \textit{or in terms of}(E,\,\nu): \quad \tau_\mathrm{max} = E\,\sqrt{3\,[1-2\,\nu]\,[1+\nu]}^{-1}\,. \tag{5.115}$$

For typical metals with $\nu = \frac{1}{3}$ *the maximum stress is* $\tau_\mathrm{max} = \frac{\sqrt{3}}{2}\,E$. *For rather incompressible materials with* $\nu = 0.495$ *one obtains* $\tau_\mathrm{max} \approx 4.72\,E$.

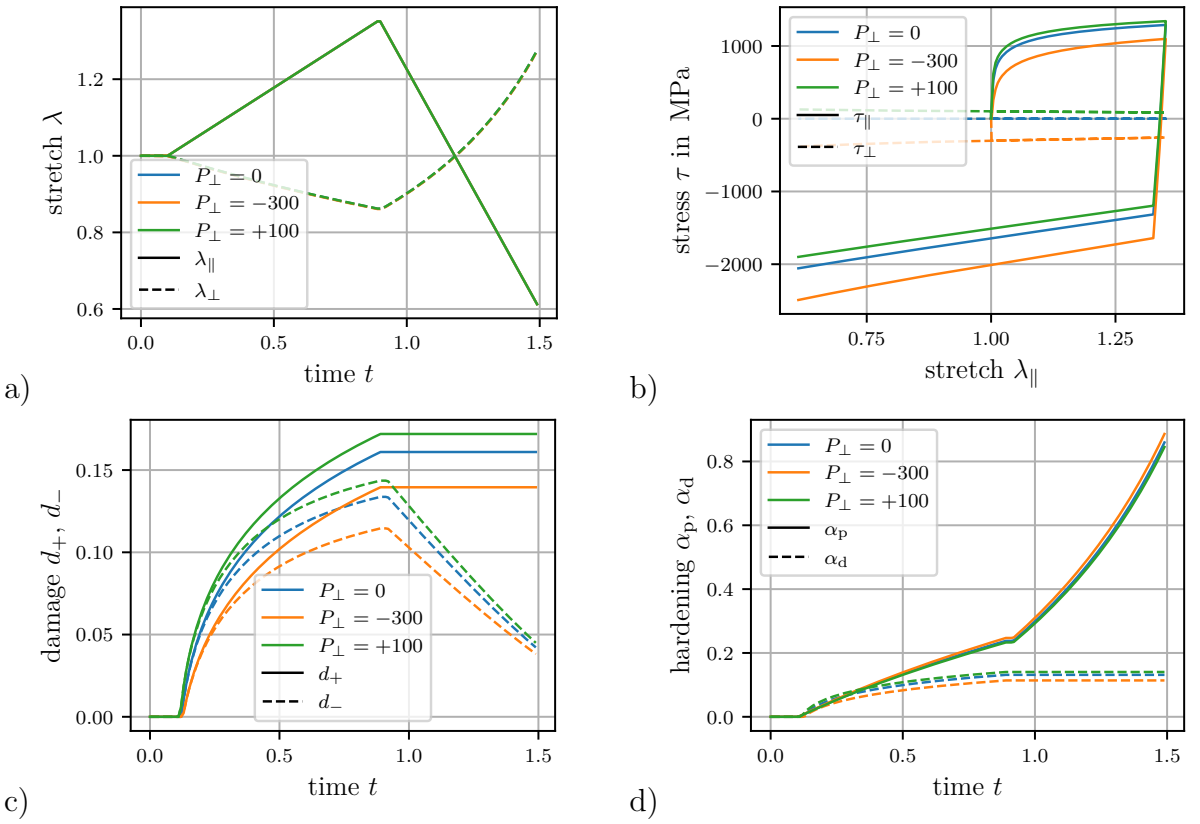

Figure 5.3: Response of the model (variant 2) under tension loading followed by compression loading. Laterally, the constant stresses $P_\perp = 0\,\mathrm{MPa}$ (blue), $P_\perp = -300\,\mathrm{MPa}$ (orange) and $P_\perp = 100\,\mathrm{MPa}$ (green) are applied. a) shows the prescribed stretch $\lambda_\parallel$ and the responses of the lateral stretch $\lambda_\perp$ with barely visible differences. b) shows the stress-stretch response in terms of Kirchhoff stresses with $\tau_\parallel$ in primary loading direction (solid line) and $\tau_\perp$ in lateral direction (dashed line). c) shows the evolution of the damage variables for tension d_+ (solid line) and for compression d_- (dashed line). d) shows the evolution of plastic hardening (solid line) and of damage hardening (dashed line).

6 Summary and outlook

In this thesis, a framework describing regularised ductile damage in metals has been successfully developed. Starting with an isotropic ductile damage model (Chapter 3) which is regularised by means of the micromorphic approach (Chapter 2), the complexity of the developed framework increases in the following chapters by considering anisotropic damage (Chapter 4) and by additionally considering the micro-crack closure and reopening effect (Chapter 5).

Chapter 2 introduces a Finite Element method for regularised damage. After summarising the essential kinematics, the micromorphic approach is formulated. It belongs to the gradient-based regularisation approaches and can be implemented to run numerically efficient simulations. The idea of the micromorphic approach is to introduce an additional global field variable which is coupled to the variable in need of regularisation. Both variables are coupled by penalising their difference in the Helmholtz energy. Regularisation is achieved by considering the gradient of the newly introduced global variable in the Helmholtz energy. The main advantage of this implicit gradient-enhancement — in the context of the Finite Element method — is that one may evaluate the material model on each integration point without taking into account any influence of neighbouring integration points. Thereby, an implementation into standard Finite Element tools is possible by just using a custom element procedure. To this end, the corresponding governing equations are formulated, discretised and linearised.

In contrast to the (implicit) micromorphic approach, a short summary of a direct approach follows thereafter. By considering the gradient of the damage variable directly in the Helmholtz energy, the equations relating to the material model can no longer be solved on each integration point individually and, instead, need to be solved on a global Finite Element level. This makes the implementation into standard Finite Element tools rather difficult, as expansive modifications of the assembly and the global iteration process are necessary. For the described model, partially assembled quantities, i.e. the Lagrange multiplier and the damage initiation criterion, enter the final global system of equations by means of nonlinear complementarity functions of Fischer-Burmeister-type.

The chapter finishes with a formulation of an arc-length method in combination with linear constraints. Simulating boundary value problems with material models which exhibit softening may result in snap-back or snap-through behaviour. In order to accurately follow the load path, employing an arc-length method may become necessary.

Additional consideration of linear constraints helps to accurately simulate loading conditions as present in, e.g., tensile tests for characterisation of the mechanical properties.

Chapter 3 is concerned with the formulation of a gradient-enhanced isotropic ductile damage model. Focus is first set on deriving the fundamental equations of the continuous material model as well as on formulating its algorithmic implementation. In the Helmholtz energy, a typical elasto-plastic ansatz formulated in terms of logarithmic strains is enhanced by the incorporation of damage functions, $f_\bullet : [0, \infty) \rightarrow [1, 0)$, which reduce the elastic stiffness as damage evolves. A multi-surface formulation is pursued, enabling the individual control of evolution of damage and of plasticity. An important concept in this regard is the introduction of effective driving forces for plasticity as well as for damage. The idea of the effective driving forces is to obtain quantities which are independent from other inelastic mechanisms, e.g. the effective driving force for plasticity attains similar values regardless of the state of damage. Evolution equations of the inelastic variables are obtained in associative manner from the postulate of maximum dissipation.

The algorithmic implementation of the defining equations of the material model require a discretisation in time. The evolution equation of the plastic strain is discretised with the exponential map, and the evolution equations for plastic hardening and for isotropic damage are discretised with the backward Euler scheme. In combination with the particular choice of the Helmholtz energy and the yield surface, one obtains a radial return scheme for the update of the plasticity related quantities. Hence, the response of the ductile damage model is obtained by solving two non-linear, strongly coupled equations by means of an active-set algorithm. Further quantities required for the FE-method are determined analytically.

A parameter study is performed to exemplify the behaviour of the ductile damage model. The responses of the model with systematically varied material parameters are analysed with the help of stress over strain diagrams as well as with diagrams depicting the evolution of the Lagrange multipliers over strain. The analysis reveals that stronger plastic hardening leads to faster deterioration and to an overall softer response. Furthermore, the parameters influencing the effective driving forces play a critical role in controlling the character of the response — from rather brittle to very ductile behaviour. It becomes apparent that the model can be flexibly adapted to represent different kinds of material behaviour.

The capability of the ductile damage model to reflect the response of the dual-phase steel DP800 is demonstrated by performing a parameter identification. Tensile tests on two different geometries are performed by using a loading path including multiple unloading points in order to capture changes of the elastic stiffness. During the tests the displacement field is measured by means of DIC. External loading in the simulation is applied by prescribing the displacement in order to be able to capture the softening of the overall response. The accuracy of the response related to a specific parameter set is measured by an objective function which compares relative displacements at each Finite Element node to the measured relative displacements from the tensile tests and

which compares the overall reaction forces of simulation and experiment. The optimal set of parameters is determined by performing a numerical minimisation of the set up objective function by using a simplex algorithm.

Due to the large number of parameters to be determined, parameters are identified sequentially. Firstly, the elastic parameters are determined analytically by using only the first few (elastic) data points. Next, rough estimates of the plastic parameters are identified, followed by identifying estimates of the (most important) damage parameters. Finally, by using a parameter set being in the vicinity of the optimal solution as starting point, two sets of optimal values of all plastic and damage parameters are identified. From the two parameter sets only one set is able to also predict the response of the tensile test using the second geometry.

The applicability of the ductile damage model to production processes is demonstrated by simulating an air bending process. So far, the model is not suitable for use under compression. Hence, a small modification of the model is made to disable damage evolution if the volumetric strain is negative. The developed gradient-enhanced ductile damage model is implemented in a custom user material in the commercial Finite Element tool Abaqus. The simulation of the air bending processes with the gradient-enhanced ductile damage model in Abaqus results in a mesh-independent prediction of damage evolution.

The chapter closes with an update of the model parametrisation. During the parameter identification process it became apparent that the response of the original model cannot be uniquely connected to one parameter set. Consequently, one of the parameters in the damage functions is removed in the updated formulation and the parameter identification process is repeated. With the updated model formulation a single optimal set of parameters is obtained.

The previously proposed isotropic ductile damage model is extended to anisotropic damage in **Chapter 4**. Anisotropic damage is described by means of the fictitious configuration — i.e. damage is described by the mapping between the intermediate (plasticity related) configuration and the fictitious undamaged configuration. The equations of the material model are formulated in the fictitious configuration, where the relation between fictitious strains and fictitious stresses is isotropic — due to the chosen format of the Helmholtz energy dependent on invariants — even though a deformation induced anisotropy of the response in the current configuration develops.

After specification of the modelling framework, the coupling of damage and plasticity is discussed. Similar to the previous chapter, a two-surface approach governs the evolution of damage and plasticity. The coupling of both phenomena is expressed in terms of effective driving forces. The idea behind the concept is that plasticity can continue to develop even though stresses are reduced due to damage and, vice versa, damage can continue to develop even though elastic strains are (nearly) frozen due to evolution of plasticity.

The proposed material model uses an effective stress as driving force for the evolution of plasticity, but instead of an effective damage driving force, the threshold value

determining evolution of damage is reduced dependent on the state of plasticity. This alternate approach is conceptually similar to an effective driving force but numerically and algorithmically much simpler. The algorithmic implementation of the anisotropic ductile damage model results in a system of non-linear equations which need to be solved. Compared to the isotropic model, an additional tensor-valued equation related to the fictitious elastic strains needs to be solved. The system is solved monolithically by making use of non-linear complementarity functions of Fischer-Burmeister type.

Integration of the proposed anisotropic ductile damage model into the micromorphic regularisation framework is achieved by adding two scalar non-local variables coupled to proportional plastic and proportional damage hardening, respectively. The rationale is that the evolution of the inelastic processes is proportional to the Lagrange multipliers and that hence regularisation of the overall response can be achieved by regularisation of quantities directly related to the Lagrange multipliers, i.e. the proportional hardening variables.

The basic (local) model response and the influence of each material parameter is demonstrated for uniaxial tension and for simple shear. A non-proportional loading with uniaxial tension and simple shear in succession — once with tension first and once with shear first — confirms the load-path dependence of the response. Even though the final (deformed) geometry is identical, the damage state is different between both loading scenarios.

Regularisation properties are analysed extensively. Simulations with deactivated and with partially deactivated regularisation (or rather fields which are regularised) show the necessity to regularise damage as well as plasticity. Activating the deterioration function which controls the transition from damage to failure can only partially be regularised — the point of accelerated loss of stiffness can be captured well in the proposed regularisation framework, but the path thereafter shows localising effects.

The final chapter, **Chapter 5**, starts with a micro-mechanical motivation of the introduction of separate damage variables for tension and for compression. By considering a sample of micro-structure first loaded by tensile loading and subsequently by compressive loading, the evolution of micro-cracks and the resulting changes to stiffness, and thus damage, are discussed.

Based on these ideas, a modelling framework in the spirit of the fictitious configuration concept as discussed in Chapter 4 is proposed. Motivated by the introduction of separate damage variables for tension and for compression, a split of the logarithmic strains is employed. Unlike splits of strains discussed in the literature, a four-way split into tensile/compressive contributions and into volumetric/deviatoric contributions is considered. Thereby, the damage driving force is guaranteed to be positive-semi-definite and devoid of compressive contributions. Different to the model in Chapter 4, this material model is formulated in the intermediate configuration, since a mapping between the fictitious and the intermediate configuration cannot (straightforwardly) be given. However, the Helmholtz energy is formulated with the help of invariants with identical

structure as in the previous model and evolution of (tensile) damage and plasticity are, again, governed by a two-surface formulation.

In the prototype model formulation, initiation potentials and hardening contributions are chosen identical to the previous model. The evolution equation for compressive damage is formulated in non-associated manner. It is coupled to the evolution of tensile damage if damage evolves and compressive damage 'heals' as plasticity evolves under compression.

The proposed prototype model is reduced to scalar damage variables and implemented into the framework developed in Chapter 3. Two variants of the non-associated evolution equation for compressive damage are discussed in view of generated dissipation and in view of the response of the model. One variant results in unconditional non-negative dissipation but produces an undesired response of the model. The other variant yields the desired model response, but its dissipation contribution is only non-negative if strains do not exceed a (moderately high) threshold value. The response of the local material model is showcased for uniaxial tension loading combined with transversal compressive loading.

The modelling framework and the corresponding prototype models proposed within this thesis are a mere first step towards the goal of precisely predicting material behaviour during (cold) forming in order to optimise the production process. Many details of the proposed models need to be analysed further, fleshed out or improved upon. Potential future work may be categorised either into an update of the model formulation or into further experimental work in order to verify the features of the model and to identify parameters for a specific material.

Until now, the elasto-plastic description in the proposed models has been kept as simple as possible. Consequently, the von Mises yield criterion may be generalised to an anisotropic yield criterion, e.g. a Hill-type yield criterion [81]. On the downside, this requires a different, more complex, algorithmic structure — similar to additionally considering kinematic hardening, e.g. one of the kinematic hardening formulations discussed in [127]. Increasing the complexity of the plasticity formulation, typically also increasing the number of material parameters, exacerbates the problem of uniquely identifiable parameter sets. Especially in the softening regime of the response, the distinction between decreasing hardening modulus and evolution of damage may only be identified with suitable experimental data, e.g. continuous stiffness measurements.

The material model including the micro-crack closure and reopening effect, proposed in Chapter 5, requires more work to be effectively usable. First of all, it needs to be embedded in the regularisation framework from Chapter 2. Next, the response of the proposed model should be improved in (at least) two aspects:

- Small (but sufficiently large) positive deviatoric strains always lead to the evolution of tensile damage independent of the overall stress state, e.g. even for very high negative stress triaxialities.

- The compressive damage variable evolves less than the tensile damage variable even under uniaxial tension loading. This behaviour of the model cannot be directly controlled via a material parameter but only by reducing recovery of stiffness under compression altogether. A potential remedy may be to formulate the non-associated evolution equation solely in stress-based quantities rather than in strain-based quantities.

Furthermore, the formulation with isotropic damage should be extended by considering tensile and compressive damage as anisotropic (tensorial) quantities — similar to Chapter 4. In this context, special attention should be payed towards 'cross-over' effects, e.g. how evolution of tensile damage in 1-direction is influenced by a compressive load in 2-direction.

Many more extensions of the proposed models are possible. Most prominently, the model formulation may be extended to react to changes in temperature, possibly even by considering healing of damage at higher temperatures.

Regarding future experimental work, an important issue is the analysis of regularisation. To be specific, the identifiability of the gradient parameter — which in reality may not be constant, see e.g. [174, 188] — needs to be analysed, e.g. by considering specimens with an identical shape but different scale ($l = 10\,\text{mm}$, $50\,\text{mm}$, $200\,\text{mm}$). Some research in this regard can be found in, e.g., [115].

The anisotropy related features of the proposed model(s) need to be verified and the corresponding parameters may be identified by means of multiaxial loading and unloading, see e.g. the biaxial experiments reported in [33, 72].

Another open issue, concerned with experimental methodology, is the in-situ determination of elastic stiffness. Several possibilities of measuring elastic stiffness exist, see e.g. [170]. A full field resolution of elastic stiffness, in time and in space, may be obtained by means of DIC. However, this requires modifications to the load path (in the form of additional elastic unloading and reloading) and a high resolution camera in order to be able to accurately capture the small changes in the (small) elastic strains.

Once a suitable method for experimental measurement of the elastic stiffness is determined, the micro-crack closure and reopening effect can be verified experimentally. Of special interest is, on the one hand, to identify the degradation of compressive stiffness under tension loading, and, on the other hand, to identify the recovery of compressive stiffness under compression loading.

At the very end, the developed material model needs to be integrated into some advanced (potentially commercial) simulation tool which is capable of simulating production processes and, finally, enable their optimisation.

A Exponent of a second order tensor

The exponent of a tensor of second order and the derivative thereof may be computed by means of a series representation. Let $\boldsymbol{T}$ be a tensor of second order then $\exp(\boldsymbol{T})$ can be calculated by

$$\exp(\boldsymbol{T}) = \sum_{k=0}^{\infty} \frac{\boldsymbol{T}^k}{k!}\,, \tag{A.1}$$

which is valid for both symmetric and unsymmetric tensors $\boldsymbol{T}$. The derivative with respect to the tensor $\boldsymbol{T}$ itself is straightforwardly obtained as

$$\frac{\partial \exp(\boldsymbol{T})}{\partial \boldsymbol{T}} = \sum_{k=1}^{\infty} \frac{1}{k!} \frac{\partial \boldsymbol{T}^k}{\partial \boldsymbol{T}}\,. \tag{A.2}$$

The derivatives of the powers of the tensor $\boldsymbol{T}^k$ are obtained in the recursively defined representation dependent on the symmetry of $\boldsymbol{T}$ as

$$\frac{\partial \boldsymbol{T}^k}{\partial \boldsymbol{T}} = \begin{cases} [\boldsymbol{I} \mathbin{\overline{\otimes}} \boldsymbol{T}] : \dfrac{\partial \boldsymbol{T}^{k-1}}{\partial \boldsymbol{T}} + \boldsymbol{T}^{k-1} \mathbin{\underline{\overline{\otimes}}} \boldsymbol{I} & \text{if} \quad \boldsymbol{T} = \boldsymbol{T}^{\mathrm{t}} \\ [\boldsymbol{I} \mathbin{\overline{\otimes}} \boldsymbol{T}^{\mathrm{t}}] : \dfrac{\partial \boldsymbol{T}^{k-1}}{\partial \boldsymbol{T}} + \boldsymbol{T}^{k-1} \mathbin{\overline{\otimes}} \boldsymbol{I} & \text{if} \quad \boldsymbol{T} \neq \boldsymbol{T}^{\mathrm{t}} \end{cases}, \tag{A.3}$$

which can be implemented efficiently.

B Some implementation details of abraxas++

B.1 Load curve functionality

Boundary conditions in abraxas++ are applied by means of load-curves. A load-curve conveys information about time of application, type and amplitude of the attached boundary conditions. There are (at the present state) five types of load-curves implemented: a `constant` load-curve, a (piecewise) `linear` load-curve, a `continue` load-curve, an `add` load-curve and a load-curve for the arc-length method (`arccris`). All but the load-curve of type `arccris` are specified identically in the .lod-file, see Table B.1, and can be combined freely. The format for the load-curve of type `arccris` is given in Table B.2. Common to all load-curves is the specification of a unique numeric ID (starting at 1 counting up continuously without gaps), a scale factor α_{lod} and the type (printed in `keyword` within this section).

In order to exemplify how boundary conditions are handled, assume a Dirichlet boundary condition of value v_{drlt} is applied to degree of freedom d_{drlt} and a Neumann boundary condition of value v_{neum} is applied to degree of freedom d_{neum}. Boundary conditions enter the solution procedure through the quantities introduced in Section 2.4.3, namely $\boldsymbol{c}$, $\boldsymbol{c}_\lambda$, $\boldsymbol{f}_{\text{int}}$ and $\boldsymbol{f}_{\text{ext}}$.

The `constant`-load-curve applies the attached boundary conditions in constant manner, starting at time t_0 and ending at time t_1, i.e.

$$\boldsymbol{c}[d_{\text{drlt}}] = \boldsymbol{z}[d_{\text{drlt}}] - v_{\text{drlt}}\,\alpha_{\text{lod}}\,, \qquad \boldsymbol{f}_{\text{int}}[d_{\text{neum}}] = \boldsymbol{f}_{\text{int}}[d_{\text{neum}}] - v_{\text{neum}}\,\alpha_{\text{lod}}\,, \tag{B.1}$$

where the notation $\bullet[i]$ extracts the i-th component of vector $\bullet$. The `constant`-load-curve is the only one which may be combined with the `arccris`-load-curve. Typically, the `constant`-load-curve is used for points which shall remain fixed in space.

The `linear`-load-curve linearly interpolates (by means of function f_{itp}) the values of the attached boundary conditions based on the data points given, i.e.

$$\boldsymbol{c}_\lambda[d_{\mathrm{drlt}}] = \boldsymbol{z}[d_{\mathrm{drlt}}] - v_{\mathrm{drlt}}\,\alpha_{\mathrm{lod}}\,f_{\mathrm{itp}}(t,\,[t_i],\,[v_i])\,, \tag{B.2}$$

$$\boldsymbol{f}_{\mathrm{ext}}[d_{\mathrm{neum}}] = f_{\mathrm{ext}}[d_{\mathrm{neum}}] - v_{\mathrm{neum}}\,\alpha_{\mathrm{lod}}\,f_{\mathrm{itp}}(t,\,[t_i],\,[v_i])\,. \tag{B.3}$$

The `linear`-load-curve is the most common load-curve — it can e.g. be used to ramp up a load in a quasi-static setting.

The `continue`-load-curve continues an applied loading, e.g. in a different direction or at a different location. To this end, the internal reaction forces $\boldsymbol{f}_{\mathrm{cont}}$ and the values of the respective degrees of freedom $\boldsymbol{z}_{\mathrm{cont}}$ at the beginning of the `continue`-load-curve are used to determine the load amplitude. The values of the load amplitudes are computed by

$$\begin{aligned}\boldsymbol{c}_\lambda[d_{\mathrm{drlt}}] = {}& \boldsymbol{z}[d_{\mathrm{drlt}}] - v_{\mathrm{drlt}}\,\alpha_{\mathrm{lod}}\,f_{\mathrm{itp}}(t,\,[t_i],\,[v_i]) \\ & - \boldsymbol{z}_{\mathrm{cont}}[d_{\mathrm{drlt}}]\,\big[1 - f_{\mathrm{itp}}(t,\,[t_i],\,[v_i])\big]\,,\end{aligned} \tag{B.4}$$

$$\begin{aligned}\boldsymbol{f}_{\mathrm{ext}}[d_{\mathrm{neum}}] = {}& \boldsymbol{f}_{\mathrm{ext}}[d_{\mathrm{neum}}] - v_{\mathrm{neum}}\,\alpha_{\mathrm{lod}}\,f_{\mathrm{itp}}(t,\,[t_i],\,[v_i]) \\ & - \boldsymbol{f}_{\mathrm{cont}}[d_{\mathrm{neum}}]\,\big[1 - f_{\mathrm{itp}}(t,\,[t_i],\,[v_i])\big]\,,\end{aligned} \tag{B.5}$$

The values of the `continue`-load-curve should be between zero and one, i.e. $v_i \in [0, 1]$, since $1 - v_i$ is the fraction of the value from which continuation started. The `continue`-load-curve may be used to control unloading — force controlled unloading can e.g. be obtained by setting $v_{\mathrm{neum}} = 0$, $v_0 = 1$ and $v_1 = 0$.

The `add`-load-curve is very similar to the `continue`-load-curve with the difference being that the reaction forces $\boldsymbol{f}_{\mathrm{cont}}$ and/or the degrees of freedom $\boldsymbol{z}_{\mathrm{cont}}$ are applied constantly throughout the load-curve, i.e.

$$\boldsymbol{c}_\lambda[d_{\mathrm{drlt}}] = \boldsymbol{z}[d_{\mathrm{drlt}}] - v_{\mathrm{drlt}}\,\alpha_{\mathrm{lod}}\,f_{\mathrm{itp}}(t,\,[t_i],\,[v_i]) - \boldsymbol{z}_{\mathrm{cont}}[d_{\mathrm{drlt}}]\,, \tag{B.6}$$

$$\boldsymbol{f}_{\mathrm{ext}}[d_{\mathrm{neum}}] = \boldsymbol{f}_{\mathrm{ext}}[d_{\mathrm{neum}}] - v_{\mathrm{neum}}\,\alpha_{\mathrm{lod}}\,f_{\mathrm{itp}}(t,\,[t_i],\,[v_i]) - \boldsymbol{f}_{\mathrm{cont}}[d_{\mathrm{neum}}]\,. \tag{B.7}$$

An example for the application of the `add`-load-curve is switching from force-controlled loading to displacement-controlled loading. Another important difference compared to the `continue`-load-curve is, that values are specified differently. With the `add`-load-curve e.g. the displacement is increased by 2 mm, while with the `continue`-load-curve the displacement is set to change to a value of 10 mm.

The `arccris`-load-curve enables the arc-length method starting at time t_0 and sets the initial loading parameter $\lambda = \lambda_0$. This load-curve continues to be applied until the target value v_{arc} of the specified degree of freedom is reached — given in terms of node number n_{arc} and (node local) degree of freedom number d_{arc}. The radius of the arc Δs is controlled by automatic time-stepping and the load-rate τ_{arc}, i.e.

$$\Delta s = \frac{\Delta t}{\tau_{\mathrm{arc}}}\,. \tag{B.8}$$

Table B.1: Specification of the load-curve in the abraxas++ .lod-file for types `constant`, `linear`, `continue` and `add`. One needs to specify a unique numeric ID l_{ID}, a scale factor α_{lod}, the type in form of `keyword` and $m+1$ pairs of time and value (t_i, v_i).

1	*LODC	l_{ID}	α_{lod}	`type`
2	start time t_0	start value v_0		
i	(end) time t_i	(end) value v_i		

Table B.2: Specification of the `arccris`-load-curve in the abraxas++ .lod-file. One needs to specify a unique numeric ID l_{ID}, a scale factor α_{lod}, the observing node n_{arc} and degree of freedom d_{arc}, the target value v_{arc} a load-rate τ_{arc}, the initial loading parameter λ_0 and start and end times t_0, t_1.

1	*LODC	l_{ID}	α_{lod}	`arccris`	
2	n_{arc}	d_{arc}	v_{arc}	τ_{arc}	λ_0
3	start time t_0	end time t_1			

The values of the displacement controlled loading and the force controlled loading are set as

$$\boldsymbol{c}_\lambda[d_{\text{drlt}}] = -v_{\text{drlt}}\,\alpha_{\text{lod}}\,, \qquad \boldsymbol{f}_{\text{ext}}[d_{\text{neum}}] = v_{\text{neum}}\,\alpha_{\text{lod}}\,, \tag{B.9}$$

i.e. the total amplitudes are set, as the amount of loading is controlled by the load parameter λ.

B.2 Automatic time stepping and convergence control

In abraxas++, the time step size Δt (and thereby the load amplitude) of the current time step is controlled algorithmically in order to be able to efficiently simulate problems which require very small time steps only temporarily, e.g. at the start of necking. To this end, the algorithm may do multiple attempts to find a solution for the current time step, but with different (smaller) time step sizes. If the current attempt a at solving the time step fails, either due to reaching the maximum number of global iterations $R_{\max} \overset{e.g.}{=} 20$ in the Newton-Raphson scheme or due to (convergence) problems at local material point level, a new attempt at solving the current time step is made. The time step size is reduced, the new current time t is computed and all other quantities are reset to their values at the end of the previous time step n, i.e.

$$a = a + 1\,, \quad \Delta t = c_{\text{red}}\,\Delta t\,, \quad t = t_n + \Delta t\,, \quad \{\bullet\} = \{\bullet\}_n\,, \tag{B.10}$$

with cutback factor $c_{\text{red}} \overset{e.g.}{=} 0.5$. If the time step size Δt falls below the lower bound $\Delta t_{\min}$ a final attempt with $\Delta t = \Delta t_{\min}$ is made. In the case of convergence, the time step size Δt is kept identical. In addition, an algorithmically controlled time step size increase is implemented. If the current time step converged in less than R_{low} Newton-Raphson

iterations and the time step size did not need to be reduced twice in the previous $n_{\mathrm{lb}} \overset{e.g.}{=} 7$ time steps (lb = lookback), the time step size may be increased, i.e.

$$\Delta t = c_{\mathrm{inc}}\, \Delta t\,, \tag{B.11}$$

with increase factor $c_{\mathrm{inc}} \overset{e.g.}{=} 1.25$. If the time step size reaches the upper bound Δt_{max}, $\Delta t = \Delta t_{\mathrm{max}}$ is set instead.

A Newton-Raphson iteration j, as presented in Section 2.2.3, is deemed converged if either a norm of the residuum is smaller than some chosen tolerance $r_{\mathrm{tol}} \overset{e.g.}{=} 10^{-8}$ or if a norm of the increments of the degrees of freedom is smaller than some chosen tolerance $w_{\mathrm{tol}} \overset{e.g.}{=} 10^{-8}$. In particular, let the norm of the residuum $\boldsymbol{r}$ and the increments of the degrees of freedom $\Delta \boldsymbol{w}$ be given by

$$r_{\mathrm{norm}} = \max_i |r_i| \qquad \text{and} \qquad w_{\mathrm{norm}} = \max_i |\Delta w_i|\,. \tag{B.12}$$

Convergence of the Newton-Raphson iteration is determined by

$$r_{\mathrm{norm}} < r_{\mathrm{tol}} \quad \text{or if} \quad a > 1 \quad \text{and} \quad s_{\mathrm{alt}} \quad \text{by} \quad w_{\mathrm{norm}} < w_{\mathrm{tol}}\,, \tag{B.13}$$

with s_{alt} being a flag which (alternatively) allows convergence to be determined in terms of the increments of the degrees of freedom. Additionally, starting with the second attempt of solving each time step, the tolerance r_{tol} is increased by factor 10 if the Newton-Raphson iteration j surpasses the threshold value for relaxed convergence R_{relax} (but only once and only for the current time step), i.e.

$$r_{\mathrm{tol}} = 10\, r_{\mathrm{tol}} \quad \text{if} \quad j \geq R_{\mathrm{relax}}\,. \tag{B.14}$$

All parameters which are mentioned in this section can be set in the input file of abraxas++ (the .lod file).

Bibliography

[1] B. Ahmed, G. Z. Voyiadjis, and T. Park. Damaged plasticity model for concrete using scalar damage variables with a novel stress decomposition. *International Journal of Solids and Structures*, 191-192:56–75, 2020. doi:10.1016/j.ijsolstr.2019.11.023.

[2] R. K. A. Al-Rub and G. Z. Voyiadjis. Gradient-enhanced coupled plasticity-anisotropic damage model for concrete fracture: Computational aspects and applications. *International Journal of Damage Mechanics*, 18(2):115–154, 2009. doi:10.1177/1056789508097541.

[3] O. Allix. The bounded rate concept: A framework to deal with objective failure predictions in dynamic within a local constitutive model. *International Journal of Damage Mechanics*, 22(6):808–828, 2012. doi:10.1177/1056789512468355.

[4] D. Anderson, C. Butcher, N. Pathak, and M. J. Worswick. Failure parameter identification and validation for a dual-phase 780 steel sheet. *International Journal of Solids and Structures*, 124:89–107, 2017. doi:10.1016/j.ijsolstr.2017.06.018.

[5] J. Anduquia-Restrepo, C. Narváez-Tovar, and R. Rodríguez-Baracaldo. Computational and numerical analysis of ductile damage evolution under a load-unload tensile test in dual-phase steel. *Strojniski Vestnik / Journal of Mechanical Engineering*, 64(5):339–348, 2018. doi:10.5545/sv-jme.2017.5137.

[6] L. Armijo. Minimization of functions having lipschitz continuous first partial derivatives. *Pacific Journal of Mathematics*, 16(1):1–3, 1966. doi:10.2140/pjm.1966.16.1.

[7] O. Aslan and E. Bayraktar. A large-deformation gradient damage model for single crystals based on microdamage theory. *Applied Sciences*, 10(24):9142, 2020. doi:10.3390/app10249142.

[8] S. Avril, M. Bonnet, A.-S. Bretelle, M. Grédiac, F. Hild, P. Ienny, F. Latourte, D. Lemosse, S. Pagano, E. Pagnacco, and F. Pierron. Overview of identification methods of mechanical parameters based on full-field measurements. *Experimental Mechanics*, 48(4):381, 2008. doi:10.1007/s11340-008-9148-y.

[9] W. Ayadi, L. Laiarinandrasana, and K. Saï. Anisotropic (Continuum Damage Mechanics)-based multi-mechanism model for semi-crystalline polymer. *International Journal of Damage Mechanics*, 27(3):357–386, 2016. doi:10.1177/1056789516679494.

[10] H. Badreddine and K. Saanouni. On the full coupling of plastic anisotropy and anisotropic ductile damage under finite strains. *International Journal of Damage Mechanics*, 26(7):1080–1123, 2016. doi:10.1177/1056789516635729.

[11] Y. Bai and T. Wierzbicki. A new model of metal plasticity and fracture with pressure and Lode dependence. *International Journal of Plasticity*, 24:1071–1096, 2008. doi:10.1016/j.ijplas.2007.09.004.

[12] Y. Bai and T. Wierzbicki. Application of extended Mohr–Coulomb criterion to ductile fracture. *International Journal of Fracture*, 161(1):1–20, 2009. doi:10.1007/s10704-009-9422-8.

[13] S. Balay, S. Abhyankar, M. F. Adams, S. Benson, J. Brown, P. Brune, K. Buschelman, E. Constantinescu, L. Dalcin, A. Dener, V. Eijkhout, J. Faibussowitsch, W. D. Gropp, V. Hapla, T. Isaac, P. Jolivet, D. Karpeev, D. Kaushik, M. G. Knepley, F. Kong, S. Kruger, D. A. May, L. C. McInnes, R. T. Mills, L. Mitchell, T. Munson, J. E. Roman, K. Rupp, P. Sanan, J. Sarich, B. F. Smith, S. Zampini, H. Zhang, H. Zhang, and J. Zhang. PETSc/TAO users manual. Technical Report ANL-21/39 - Revision 3.20, Argonne National Laboratory, 2023. URL `https://www.anl.gov/argonne-scientific-publications/pub/185712`.

[14] R. Balieu and N. Kringos. A new thermodynamical framework for finite strain multiplicative elastoplasticity coupled to anisotropic damage. *International Journal of Plasticity*, 70:126–150, 2015. doi:10.1016/j.ijplas.2015.03.006.

[15] D. Balzani, S. Brinkhues, and G. A. Holzapfel. Constitutive framework for the modeling of damage in collagenous soft tissues with application to arterial walls. *Computer Methods in Applied Mechanics and Engineering*, 213-216:139–151, 2012. doi:10.1016/j.cma.2011.11.015.

[16] E. Baranger. Extension of a fourth-order damage theory to anisotropic history: Application to ceramic matrix compostites under a multi-axial non-proportional loading. *International Journal of Damage Mechanics*, 27(2):238–252, 2016. doi:10.1177/1056789516674766.

[17] O. Barfusz, T. van der Velden, T. Brepols, H. Holthusen, and S. Reese. A reduced integration-based solid-shell finite element formulation for gradient-extended damage. *Computer Methods in Applied Mechanics and Engineering*, 382:113884, 2021. doi:10.1016/j.cma.2021.113884.

[18] O. Barfusz, T. van der Velden, T. Brepols, and S. Reese. Gradient-extended damage analysis with reduced integration-based solid-shells at large deformations. *Computer Methods in Applied Mechanics and Engineering*, 389:114317, 2022. doi:10.1016/j.cma.2021.114317.

[19] I. Barsoum and J. Faleskog. Micromechanical analysis on the influence of the Lode parameter on void growth and coalescence. *International Journal of Solids and Structures*, 48(6):925–938, 2011. doi:10.1016/j.ijsolstr.2010.11.028.

[20] T. Bartel, R. Schulte, A. Menzel, B. Kiefer, and B. Svendsen. Investigations on enhanced Fischer–Burmeister NCP functions: application to a rate-dependent model for ferroelectrics. *Archive of Applied Mechanics*, 89:995–1010, 2019. doi:10.1007/s00419-018-1466-7.

[21] K.-J. Bathe. *Finite Element Procedures*. Prentice Hall, 1996.

[22] Z. P. Bažant and G. Pijaudier-Cabot. Nonlocal continuum damage, localization instability and convergence. *Journal of Applied Mechanics*, 55(2):287–293, 1988. doi:10.1115/1.3173674.

[23] Z. P. Bažant, T. B. Belytschko, and T.-P. Chang. Continuum theory for strain-softening. *Journal of Engineering Mechanics*, 110(12):1666–1692, 1984. doi:10.1061/(ASCE)0733-9399(1984)110:12(1666).

[24] Y. Berthaud, C. La Borderie, and S. Ramtani. Damage modeling and crack closure effect. In J. W. Ju, D. Krajcinovic, and H. L. Schreyer, editors, *Damage Mechanics in Engineering Materials*, volume 109, pages 263–276. American Society of Mechanical Engineers, 1990. URL `https://www.researchgate.net/publication/271699467_Damage_modeling_and_crack_closure_effect`.

[25] J. Besson. Continuum models of ductile fracture: A review. *International Journal of Damage Mechanics*, 19(1):3–52, 2010. doi:10.1177/1056789509103482.

[26] J. Betten. Applications of tensor functions in continuum damage mechanics. *International Journal of Damage Mechanics*, 1(1):47–59, 1992. doi:10.1177/105678959200100103.

[27] J. Betten, S. Sklepus, and A. Zolochevsky. A creep damage model for initially isotropic materials with different properties in tension and compression. *Engineering Fracture Mechanics*, 59(5):623–641, 1998. doi:10.1016/s0013-7944(97)00143-4.

[28] J. Betten. Representation of constitutive equations in creep mechanics of isotropic and anisotropic materials. In A. R. S. Ponter and D. R. Hayhurst, editors, *Creep in Structures*, pages 179–201. Springer Berlin Heidelberg, 1981. doi:10.1007/978-3-642-81598-0_11.

[29] J. P. Boehler, editor. *Applications of Tensor Functions in Solid Mechanics*. Number 292 in CISM International Centre for Mechanical Sciences. Springer Vienna, 1987. doi:10.1007/978-3-7091-2810-7.

[30] J. Bonet and R. D. Wood. *Nonlinear Continuum Mechanics for Finite Element Analysis*. Cambridge University Press (CUP), 1997. doi:10.1017/cbo9780511755446.

[31] T. Brepols, S. Wulfinghoff, and S. Reese. Gradient-extended two-surface damage-plasticity: Micromorphic formulation and numerical aspects. *International Journal of Plasticity*, 97(Supplement C):64–106, 2017. doi:10.1016/j.ijplas.2017.05.010.

[32] T. Brepols, S. Wulfinghoff, and S. Reese. A gradient-extended two-surface damage-

plasticity model for large deformations. *International Journal of Plasticity*, 129: 102635, 2020. doi:10.1016/j.ijplas.2019.11.014.

[33] M. Brünig, S. Koirala, and S. Gerke. Analysis of damage and failure in anisotropic ductile metals based on biaxial experiments with the H-specimen. *Experimental Mechanics*, 62(2):183–197, 2021. doi:10.1007/s11340-021-00774-x.

[34] M. Brünig. An anisotropic ductile damage model based on irreversible thermodynamics. *International Journal of Plasticity*, 19(10):1679–1713, 2003. doi:10.1016/s0749-6419(02)00114-6.

[35] B. Calvo, E. Peña, M. A. Martinez, and M. Doblaré. An uncoupled directional damage model for fibred biological soft tissues. Formulation and computational aspects. *International Journal for Numerical Methods in Engineering*, 69(10): 2036–2057, 2007. doi:10.1002/nme.1825.

[36] T.-S. Cao, M. Mazière, K. Danas, and J. Besson. A model for ductile damage prediction at low stress triaxialities incorporating void shape change and void rotation. *International Journal of Solids and Structures*, 63:240–263, 2015. doi:10.1016/j.ijsolstr.2015.03.003.

[37] M. Cervera and C. Tesei. An energy-equivalent d+/d- damage model with enhanced microcrack closure-reopening capabilities for cohesive-frictional materials. *Materials*, 10(4):433, 2017. doi:10.3390/ma10040433.

[38] M. Cervera, J. Oliver, and R. Faria. Seismic evaluation of concrete dams via continuum damage models. *Earthquake Engineering & Structural Dynamics*, 24 (9):1225–1245, 1995. doi:10.1002/eqe.4290240905.

[39] M. Cervera, C. Tesei, and G. Ventura. Cracking of quasi-brittle structures under monotonic and cyclic loadings: A d+/d- damage model with stiffness recovery in shear. *International Journal of Solids and Structures*, 135:148–171, 2018. doi:10.1016/j.ijsolstr.2017.11.017.

[40] J.-L. Chaboche. Continuum damage mechanics: Present state and future trends. *Nuclear Engineering and Design*, 105(1):19–33, 1987. doi:10.1016/0029-5493(87)90225-1.

[41] J.-L. Chaboche. Damage induced anisotropy: On the difficulties associated with the active/passive unilateral condition. *International Journal of Damage Mechanics*, 1(2):148–171, 1992. doi:10.1177/105678959200100201.

[42] J.-L. Chaboche. Development of continuum damage mechanics for elastic solids sustaining anisotropic and unilateral damage. *International Journal of Damage Mechanics*, 2(4):311–329, 1993. doi:10.1177/105678959300200401.

[43] Y. Chen, E. Lorentz, and J. Besson. Crack initiation and propagation in small-scale yielding using a nonlocal GTN model. *International Journal of Plasticity*, 130:102701, 2020. doi:10.1016/j.ijplas.2020.102701.

[44] J. Clayton and A. Tonge. A nonlinear anisotropic elastic-inelastic constitutive model for polycrystalline ceramics and minerals with application to boron carbide. *International Journal of Solids and Structures*, 64-65:191–207, 2015. doi:10.1016/j.ijsolstr.2015.03.024.

[45] A. Cocks and F. Leckie. Creep constitutive equations for damaged materials. In T. Y. Wu and J. W. Hutchinson, editors, *Advances in Applied Mechanics*, volume 25, pages 239–294. Elsevier, 1987. doi:10.1016/s0065-2156(08)70279-5.

[46] M. A. Crisfield. *Non-linear Finite Element Analysis of Solids and Structures*. Wiley Chichester, 1991. doi:10.1002/9781118375938.

[47] M. Cuomo and M. Fagone. Finite deformation non-isotropic elasto-plasticity with evolving structural tensors. A framework. *Il Nuovo Cimento C*, 32:55–72, 2009. doi:10.1393/ncc/i2009-10352-5.

[48] R. de Borst, L. J. Sluys, H.-B. Muhlhaus, and J. Pamin. Fundamental issues in finite element analyses of localization of deformation. *Engineering Computations*, 10(2):99–121, 1993. doi:10.1108/eb023897.

[49] E. A. de Souza Neto, D. R. J. Owen, and D. Perić. *Computational Methods for Plasticity*. Wiley Chichester, 2008.

[50] J. E. Dennis Jr. and R. B. Schnabel. *Numerical Methods for Unconstrained Optimization and Nonlinear Equations*. Society for Industrial and Applied Mathematics, 1996.

[51] R. Desmorat, F. Gatuingt, and F. Ragueneau. Nonlocal anisotropic damage model and related computational aspects for quasi-brittle materials. *Engineering Fracture Mechanics*, 74(10):1539–1560, 2007. doi:10.1016/j.engfracmech.2006.09.012.

[52] R. Desmorat, F. Gatuingt, and F. Ragueneau. Nonstandard thermodynamics framework for robust computations with induced anisotropic damage. *International Journal of Damage Mechanics*, 19(1):53–73, 2009. doi:10.1177/1056789509104839.

[53] R. Desmorat, M. Chambart, F. Gatuingt, and D. Guilbaud. Delay-active damage versus non-local enhancement for anisotropic damage dynamics computations with alternated loading. *Engineering Fracture Mechanics*, 77(12):2294–2315, 2010. doi:10.1016/j.engfracmech.2010.04.006.

[54] R. Desmorat, F. Gatuingt, and M. Jirasek. Nonlocal models with damage-dependent interactions motivated by internal time. *Engineering Fracture Mechanics*, 142:255–275, 2015. doi:10.1016/j.engfracmech.2015.06.015.

[55] R. Desmorat. Anisotropic damage modeling of concrete materials. *International Journal of Damage Mechanics*, 25(6):818–852, 2016. doi:10.1177/1056789515606509.

[56] B. J. Dimitrijevic and K. Hackl. A method for gradient enhancement of continuum

damage models. *Technische Mechanik*, 28(1):43–52, 2008.

[57] B. J. Dimitrijevic and K. Hackl. A regularization framework for damage-plasticity models via gradient enhancement of the free energy. *International Journal of Numerical Methods in Biomedical Engineering*, 27(8):1199–1210, 2009. doi:10.1002/cnm.1350.

[58] M. Dunand and D. Mohr. Effect of Lode parameter on plastic flow localization after proportional loading at low stress triaxialities. *Journal of the Mechanics and Physics of Solids*, 66:133–153, 2014. doi:10.1016/j.jmps.2014.01.008.

[59] G. Duvaut, J. L. Lions, C. W. John, and S. C. Cowin. *Inequalities in Mechanics and Physics*. Springer, Berlin, 1976.

[60] D. Edelen and N. Laws. On the thermodyanmics of systems with nonlocality. *Archive for Rational Mechanics and Analysis*, 43(1), 1971. doi:10.1007/bf00251543.

[61] M. Ekh, A. Menzel, K. Runesson, and P. Steinmann. Anisotropic damage with the MCR effect coupled to plasticity. *International Journal of Engineering Science*, 41(13-14):1535–1551, 2003. doi:10.1016/s0020-7225(03)00032-6.

[62] M. Ekh and K. Runesson. Bifurcation results for plasticity coupled to damage with MCR-effect. *International Journal of Solids and Structures*, 37(14):1975–1996, 2000. doi:10.1016/S0020-7683(98)00344-8.

[63] M. Fassin, R. Eggersmann, S. Wulfinghoff, and S. Reese. Gradient-extended anisotropic brittle damage modeling using a second order damage tensor — theory, implementation and numerical examples. *International Journal of Solids and Structures*, 167:93–126, 2019. doi:10.1016/j.ijsolstr.2019.02.009.

[64] M. Fassin, R. Eggersmann, S. Wulfinghoff, and S. Reese. Efficient algorithmic incorporation of tension compression asymmetry into an anisotropic damage model. *Computer Methods in Applied Mechanics and Engineering*, 354:932–962, 2019. doi:10.1016/j.cma.2019.03.051.

[65] S. Felder, N. Kopic-Osmanovic, H. Holthusen, T. Brepols, and S. Reese. Thermomechanically coupled gradient-extended damage-plasticity modeling of metallic materials at finite strains. *International Journal of Plasticity*, 148:103142, 2022. doi:10.1016/j.ijplas.2021.103142.

[66] A. Fischer. A special Newton-type optimization method. *Optimization*, 24(3-4): 269–284, 1992. doi:10.1080/02331939208843795.

[67] S. Forest. Micromorphic approach for gradient elasticity, viscoplasticity, and damage. *Journal of Engineering Mechanics*, 135(3):117–131, 2009. doi:10.1061/(ASCE)0733-9399(2009)135:3(117).

[68] S. Forest and E. Lorentz. *Local Approach to Fracture*, chapter 11. Presse des Mines, 2004.

[69] A. Forghani, A. Poursartip, and R. Vaziri. An orthotropic non-local approach to modeling intra-laminar damage progression in laminated composites. *International Journal of Solids and Structures*, 180-181:160–175, 2019. doi:10.1016/j.ijsolstr.2019.07.015.

[70] J. Friedlein, J. Mergheim, and P. Steinmann. Observations on additive plasticity in the logarithmic strain space at excessive strains. *International Journal of Solids and Structures*, 239-240:111416, 2022. doi:10.1016/j.ijsolstr.2021.111416.

[71] J. Friedlein, J. Mergheim, and P. Steinmann. Efficient gradient enhancements for plasticity with ductile damage in the logarithmic strain space. *European Journal of Mechanics - A/Solids*, 99:104946, 2023. doi:10.1016/j.euromechsol.2023.104946.

[72] S. Gerke, M. Zistl, and M. Brünig. Experiments and numerical simulation of damage and fracture of the X0-specimen under non-proportional loading paths. *Engineering Fracture Mechanics*, 224:106795, 2020. doi:10.1016/j.engfracmech.2019.106795.

[73] H. Ghadbeigi, C. Pinna, S. Celotto, and J. Yates. Local plastic strain evolution in a high strength dual-phase steel. *Materials Science and Engineering: A*, 527 (18-19):5026–5032, 2010. doi:10.1016/j.msea.2010.04.052.

[74] C. Goidescu, H. Welemane, O. Pantalé, M. Karama, and D. Kondo. Anisotropic unilateral damage with initial orthotropy: A micromechanics-based approach. *International Journal of Damage Mechanics*, 24(3):313–337, 2014. doi:10.1177/1056789514532299.

[75] A. Gray. *Modern Differential Geometry of Curves and Surfaces with Mathematica*. CRC Press, third edition, 1997.

[76] F. Guhr, L. Sprave, F.-J. Barthold, and A. Menzel. Computational shape optimisation for a gradient-enhanced continuum damage model. *Computational Mechanics*, 65(4):1105–1124, 2020. doi:10.1007/s00466-019-01810-3.

[77] A. L. Gurson. Continuum theory of ductile rupture by void nucleation and growth: Part I—Yield criteria and flow rules for porous ductile media. *Journal of Engineering Materials and Technology*, 99(1):2–15, 1977. doi:10.1115/1.3443401.

[78] B. P. Haigh. The strain-energy function and the elastic limit. *Engineering*, 109: 158–160, 1920.

[79] J. Hancock and A. Mackenzie. On the mechanisms of ductile failure in high-strength steels subjected to multi-axial stress-states. *Journal of the Mechanics and Physics of Solids*, 24(2-3):147–160, 1976. doi:10.1016/0022-5096(76)90024-7.

[80] D. R. Hayhurst. Computational continuum damaged mechanics: Its use in the prediction of creep in structures — past, present and future. In S. Murakami and N. Ohno, editors, *IUTAM Symposium on Creep in Structures*, pages 175–188, Dordrecht, 2001. Springer Netherlands. ISBN 978-94-015-9628-2.

[81] R. Hill. On constitutive inequalities for simple materials—I. *Journal of the Mechanics and Physics of Solids*, 16(4):229–242, 1968. doi:10.1016/0022-5096(68)90031-8.

[82] J. P. M. Hoefnagels, C. C. Tasan, F. Maresca, F. J. Peters, and V. G. Kouznetsova. Retardation of plastic instability via damage-enabled microstrain delocalization. *Journal of Materials Science*, 50(21):6882–6897, 2015. doi:10.1007/s10853-015-9164-0.

[83] H. Holthusen, T. Brepols, S. Reese, and J.-W. Simon. A two-surface gradient-extended anisotropic damage model using a second order damage tensor coupled to additive plasticity in the logarithmic strain space. *Journal of the Mechanics and Physics of Solids*, 163:104833, 2022. doi:10.1016/j.jmps.2022.104833.

[84] G. A. Holzapfel. *Nonlinear Solid Mechanics*. Wiley Chichester, 2000.

[85] J. Hult. Continuum damage mechanics — capabilities, limitations and promises. In K. Easterling, editor, *Mechanisms of Deformation and Fracture*, pages 233–247. Pergamon, 1979. doi:10.1016/B978-0-08-024258-3.50025-4.

[86] M. Itskov. *Tensor Algebra and Tensor Analysis for Engineers*. Springer International Publishing, 2015. doi:10.1007/978-3-319-16342-0.

[87] W. Jin and C. Arson. Anisotropic nonlocal damage model for materials with intrinsic transverse isotropy. *International Journal of Solids and Structures*, 139-140:29–42, 2018. doi:10.1016/j.ijsolstr.2018.01.020.

[88] P. Junker, S. Schwarz, D. R. Jantos, and K. Hackl. A fast and robust numerical treatment of a gradient-enhanced model for brittle damage. *International Journal for Multiscale Computational Engineering*, 17(2):151–180, 2019. doi:10.1615/IntJMultCompEng.2018027813.

[89] L. Kachanov. On time to rupture in creep conditions [in russian], izv. *AN SSSR, OTN*, 8:26–31, 1958.

[90] L. Kachanov. *Introduction to continuum damage mechanics*. Mechanics of Elastic Stability. Springer, second edition, 1986. doi:10.1007/978-94-017-1957-5.

[91] T. Kaiser and A. Menzel. A dislocation density tensor-based crystal plasticity framework. *Journal of the Mechanics and Physics of Solids*, 131:276–302, 2019. doi:10.1016/j.jmps.2019.05.019.

[92] T. Kaiser and A. Menzel. An incompatibility tensor-based gradient plasticity formulation—theory and numerics. *Computer Methods in Applied Mechanics and Engineering*, 345:671–700, 2019. doi:10.1016/j.cma.2018.11.013.

[93] P. I. Kattan and G. Z. Voyiadjis. A coupled theory of damage mechanics and finite strain elasto-plasticity—I. Damage and elastic deformations. *International Journal of Engineering Science*, 28(5):421–435, 1990. doi:10.1016/0020-7225(90)90007-6.

[94] B. Kiefer, T. Waffenschmidt, L. Sprave, and A. Menzel. A gradient-enhanced

damage model coupled to plasticity—multi-surface formulation and algorithmic concepts. *International Journal of Damage Mechanics*, 27(2):253–295, 2018. doi:10.1177/1056789516676306.

[95] D. Krajcinovic. Continuum models. In D. Krajcinovic, editor, *Damage Mechanics*, volume 41 of *North-Holland Series in Applied Mathematics and Mechanics*, chapter 4, pages 415–602. North-Holland, 1996. doi:10.1016/S0167-5931(06)80066-5.

[96] C. Kusche, T. Reclik, M. Freund, T. Al-Samman, U. Kerzel, and S. Korte-Kerzel. Large-area, high-resolution characterisation and classification of damage mechanisms in dual-phase steel using deep learning. *PLOS ONE*, 14(5):e0216493, 2019. doi:10.1371/journal.pone.0216493.

[97] C. F. Kusche, A. Dunlap, F. Pütz, C. Tian, C. Kirchlechner, A. Aretz, A. Schwedt, T. Al-Samman, S. Münstermann, and S. Korte-Kerzel. Efficient characterization tools for deformation-induced damage at different scales. *Production Engineering*, 14(1):95–104, 2019. doi:10.1007/s11740-019-00936-w.

[98] C. F. Kusche, F. Pütz, S. Münstermann, T. Al-Samman, and S. Korte-Kerzel. On the effect of strain and triaxiality on void evolution in a heterogeneous microstructure – a statistical and single void study of damage in DP800 steel. *Materials Science and Engineering: A*, 799:140332, 2021. doi:10.1016/j.msea.2020.140332.

[99] P. Ladevèze and E. LeDantec. Damage modelling of the elementary ply for laminated composites. *Composites Science and Technology*, 43(3):257 – 267, 1992. doi:10.1016/0266-3538(92)90097-M.

[100] P. Ladevèze, O. Allix, J.-F. Deü, and D. Lévêque. A mesomodel for localisation and damage computation in laminates. *Computer Methods in Applied Mechanics and Engineering*, 183(1):105–122, 2000. doi:10.1016/S0045-7825(99)00214-5.

[101] H. Lämmer and C. Tsakmakis. Discussion of coupled elastoplasticity and damage constitutive equations for small and finite deformations. *International Journal of Plasticity*, 16(5):495–523, 2000. doi:10.1016/S0749-6419(99)00074-1.

[102] K. Langenfeld and J. Mosler. A micromorphic approach for gradient-enhanced anisotropic ductile damage. *Computer Methods in Applied Mechanics and Engineering*, 360:112717, 2020. doi:10.1016/j.cma.2019.112717.

[103] K. Langenfeld, P. Junker, and J. Mosler. Quasi-brittle damage modeling based on incremental energy relaxation combined with a viscous-type regularization. *Continuum Mechanics and Thermodynamics*, 30(5):1125–1144, 2018. doi:10.1007/s00161-018-0669-z.

[104] F. A. Leckie and E. T. Onat. Tensorial nature of damage measuring internal variables. In J. Hult and J. Lemaitre, editors, *Physical Non-Linearities in Structural Analysis*, pages 140–155. Springer, 1981. ISBN 978-3-642-81582-9.

[105] J. Lemaitre. A Continuous Damage Mechanics Model for Ductile Frac-

ture. *Journal of Engineering Materials and Technology*, 107(1):83–89, 1985. doi:10.1115/1.3225775.

[106] J. Lemaitre. *A Course on Damage Mechanics*. Springer, 1996. doi:10.1007/978-3-642-18255-6.

[107] J. Lemaitre and R. Desmorat. *Engineering Damage Mechanics*. Springer, 2005. doi:10.1007/b138882.

[108] J. Lemaitre and J. Dufailly. Damage measurements. *Engineering Fracture Mechanics*, 28(5):643 – 661, 1987. doi:10.1016/0013-7944(87)90059-2.

[109] J. Lemaitre and P. Ladevèze. Damage effective stress in quasi-unilateral condition. In F. I. Niordson and N. Olhoff, editors, *16th IUTAM Congress, Lyngby, Denmark*. Elsevier, 1984.

[110] T. Liebe, P. Steinmann, and A. Benallal. Theoretical and computational aspects of a thermodynamically consistent framework for geometrically linear gradient damage. *Computer Methods in Applied Mechanics and Engineering*, 190(49-50): 6555–6576, 2001. doi:10.1016/S0045-7825(01)00250-X.

[111] T. Liebe, A. Menzel, and P. Steinmann. Theory and numerics of geometrically non-linear gradient plasticity. *International Journal of Engineering Science*, 41 (13-14):1603–1629, 2003. doi:10.1016/s0020-7225(03)00030-2.

[112] T. Liebe and P. Steinmann. Theory and numerics of a thermodynamically consistent framework for geometrically linear gradient plasticity. *International Journal for Numerical Methods in Engineering*, 51(12):1437–1467, 2001. doi:10.1002/nme.195.

[113] M. Lindroos, J.-M. Scherer, S. Forest, A. Laukkanen, T. Andersson, J. Vaara, A. Mäntylä, and T. Frondelius. Micromorphic crystal plasticity approach to damage regularization and size effects in martensitic steels. *International Journal of Plasticity*, 151:103187, 2022. doi:10.1016/j.ijplas.2021.103187.

[114] V. A. Lubarda. *Elastoplasticity Theory*. Mechanical Engineering Series. CRC Press, 2002.

[115] R. Mahnken and E. Kuhl. Parameter identification of gradient enhanced damage models with the finite element method. *European Journal of Mechanics - A/Solids*, 18(5):819–835, 1999. doi:10.1016/s0997-7538(99)00127-8.

[116] R. Mahnken and E. Stein. Parameter identification for finite deformation elasto-plasticity in principal directions. *Computer Methods in Applied Mechanics and Engineering*, 147(1):17–39, 1997. doi:10.1016/S0045-7825(97)00008-X.

[117] E. Markiewicz, B. Langrand, and D. Notta-Cuvier. A review of characterisation and parameters identification of materials constitutive and damage models: From normalised direct approach to most advanced inverse problem resolution. *International Journal of Impact Engineering*, 110:371–381, 2017.

doi:10.1016/j.ijimpeng.2017.01.028.

[118] A. Mattiello and R. Desmorat. Lode angle dependency due to anisotropic damage. *International Journal of Damage Mechanics*, 30(2):214–259, 2020. doi:10.1177/1056789520948563.

[119] C. McVeigh, F. Vernerey, W. K. Liu, B. Moran, and G. Olson. An interactive micro-void shear localization mechanism in high strength steels. *Journal of the Mechanics and Physics of Solids*, 55(2):225 – 244, 2007. doi:10.1016/j.jmps.2006.08.002.

[120] S. Medghalchi, C. F. Kusche, E. Karimi, U. Kerzel, and S. Korte-Kerzel. Damage analysis in dual-phase steel using deep learning: Transfer from uniaxial to biaxial straining conditions by image data augmentation. *JOM*, 72(12):4420–4430, 2020. doi:10.1007/s11837-020-04404-0.

[121] A. Menzel. Relations between material, intermediate and spatial generalized strain measures for anisotropic multiplicative inelasticity. *Acta Mechanica*, 182(3-4):231–252, 2006. doi:10.1007/s00707-005-0310-7.

[122] A. Menzel and L. Sprave. Continuum Damage Mechanics — Modelling and Simulation. In J. Merodio and R. Ogden, editors, *Constitutive Modelling of Solid Continua*, pages 231–256. Springer International Publishing, 2020. doi:10.1007/978-3-030-31547-4.

[123] A. Menzel and P. Steinmann. A theoretical and computational framework for anisotropic continuum damage mechanics at large strains. *International Journal of Solids and Structures*, 38(52):9505–9523, 2001. doi:10.1016/S0020-7683(01)00136-6.

[124] A. Menzel and P. Steinmann. On the comparison of two strategies to formulate orthotropic hyperelasticity. *Journal of Elasticity*, 62(3):171–201, 2001. doi:10.1023/A:1012937501411.

[125] A. Menzel and P. Steinmann. Geometrically non-linear anisotropic inelasticity based on fictitious configurations: Application to the coupling of continuum damage and multiplicative elasto-plasticity. *International Journal for Numerical Methods in Engineering*, 56(14):2233–2266, 2003. doi:10.1002/nme.662.

[126] A. Menzel, M. Ekh, P. Steinmann, and K. Runesson. Anisotropic damage coupled to plasticity: Modelling based on the effective configuration concept. *International Journal for Numerical Methods in Engineering*, 54(10):1409–1430, 2002. doi:10.1002/nme.470.

[127] K. A. Meyer, M. Ekh, and J. Ahlström. Modeling of kinematic hardening at large biaxial deformations in pearlitic rail steel. *International Journal of Solids and Structures*, 130–131:122–132, 2018. doi:10.1016/j.ijsolstr.2017.10.007.

[128] C. Miehe and M. Lambrecht. Algorithms for computation of stresses and elasticity

moduli in terms of seth-hill's family of generalized strain tensors. *Communications in Numerical Methods in Engineering*, 17(5):337–353, 2001. doi:10.1002/cnm.404.

[129] G. Mirone and D. Corallo. A local viewpoint for evaluating the influence of stress triaxiality and lode angle on ductile failure and hardening. *International Journal of Plasticity*, 26(3):348–371, 2010. doi:10.1016/j.ijplas.2009.07.006.

[130] S. Murakami. Mechanical modeling of material damage. *Journal of Applied Mechanics*, 55(2):280–286, 1988. doi:doi:10.1115/1.3173673.

[131] S. Murakami. *Continuum Damage Mechanics: A Continuum Mechanics Approach to the Analysis of Damage and Fracture (Solid Mechanics and Its Applications)*. Springer, 2012. doi:10.1007/978-94-007-2666-6.

[132] S. Murakami and K. Kamiya. Constitutive and damage evolution equations of elastic-brittle materials based on irreversible thermodynamics. *International Journal of Mechanical Sciences*, 39(4):473 – 486, 1997. doi:10.1016/S0020-7403(97)87627-8.

[133] A. Needleman. Material rate dependence and mesh sensitivity in localization problems. *Computer Methods in Applied Mechanics and Engineering*, 67(1):69–85, 1988. doi:10.1016/0045-7825(88)90069-2.

[134] J. A. Nelder and R. Mead. A simplex method for function minimization. *The Computer Journal*, 7(4):308–313, 1965. doi:10.1093/comjnl/7.4.308.

[135] T. H. A. Nguyen, T. Q. Bui, and S. Hirose. Smoothing gradient damage model with evolving anisotropic nonlocal interactions tailored to low-order finite elements. *Computer Methods in Applied Mechanics and Engineering*, 328:498–541, 2018. doi:10.1016/j.cma.2017.09.019.

[136] V.-D. Nguyen, F. Lani, T. Pardoen, X. P. Morelle, and L. Noels. A large strain hyperelastic viscoelastic-viscoplastic-damage constitutive model based on a multi-mechanism non-local damage continuum for amorphous glassy polymers. *International Journal of Solids and Structures*, 96:192–216, 2016. doi:10.1016/j.ijsolstr.2016.06.008.

[137] M. Nowak, J. Ostrowska-Maciejewska, R. B. Pęcherski, and P. Szeptyński. Yield criterion accounting for the influence of the third invariant of stress tensor deviator. Part I. Proposition of the yield criterion based on the concept of influence functions. *Engineering Transactions*, 59(4):283–297, 2011.

[138] M. Ortiz. A constitutive theory for the inelastic behavior of concrete. *Mechanics of Materials*, 4(1):67–93, 1985. doi:10.1016/0167-6636(85)90007-9.

[139] R. Ostwald, E. Kuhl, and A. Menzel. On the implementation of finite deformation gradient-enhanced damage models. *Computational Mechanics*, 64(Issue 3):847–877, 2019. doi:10.1007/s00466-019-01684-5.

[140] N. Ottosen and M. Ristinmaa. *The Mechanics of Constitutive Modeling*. Elsevier,

2005.

[141] R. H. J. Peerlings, R. de Borst, W. A. M. Brekelmans, J. H. P. de Vree, and I. Spee. Some observations on localisation in non-local and gradient damage models. *European Journal of Mechanics - A/Solids*, 15:937–953, 1996. URL `https://research.tue.nl/en/publications/some-observations-on-localisation-in-non-local-and-gradient-damag`.

[142] C. Polindara, T. Waffenschmidt, and A. Menzel. A computational framework for modelling damage-induced softening in fibre-reinforced materials — application to balloon angioplasty. *International Journal of Solids and Structures*, 118-119: 235–256, 2017. doi:10.1016/j.ijsolstr.2017.02.010.

[143] C. Polindara, T. Waffenschmidt, and A. Menzel. Simulation of balloon angioplasty in residually stressed blood vessels—application of a gradient-enhanced fibre damage model. *Journal of Biomechanics*, 49(12):2341–2348, 2016. doi:10.1016/j.jbiomech.2016.01.037.

[144] C. Polizzotto and G. Borino. A thermodynamics-based formulation of gradient-dependent plasticity. *European Journal of Mechanics - A/Solids*, 17(5):741–761, 1998. doi:10.1016/s0997-7538(98)80003-x.

[145] H. Qing and L. Mishnaevsky, Jr. 3d constitutive model of anisotropic damage for unidirectional ply based on physical failure mechanisms. *Computational Materials Science*, 50(2):479–486, 2010. doi:10.1016/j.commatsci.2010.09.008.

[146] Y. N. Rabotnov. *Creep problems in structural members*, volume 7 of *North-Holland Series in Applied Mathematics and Mechanics*. North-Holland, Amsterdam, 1969. URL `http://cds.cern.ch/record/103309`. Trans. from the Russian.

[147] G. Rastiello, C. Giry, F. Gatuingt, and R. Desmorat. From diffuse damage to strain localization from an Eikonal Non-Local (ENL) continuum damage model with evolving internal length. *Computer Methods in Applied Mechanics and Engineering*, 331:650–674, 2018. doi:10.1016/j.cma.2017.12.006.

[148] S. Reese, T. Brepols, M. Fassin, L. Poggenpohl, and S. Wulfinghoff. Using structural tensors for inelastic material modeling in the finite strain regime – a novel approach to anisotropic damage. *Journal of the Mechanics and Physics of Solids*, 146:104174, 2021. doi:10.1016/j.jmps.2020.104174.

[149] L. Rose and A. Menzel. Optimisation based material parameter identification using full field displacement and temperature measurements. *Mechanics of Materials*, 145:103292, 2020. doi:10.1016/j.mechmat.2019.103292. Erratum, 151:103630.

[150] L. Rose and A. Menzel. Identification of thermal material parameters for thermo-mechanically coupled material models. *Meccanica*, 56(2):393–416, 2021. doi:10.1007/s11012-020-01267-2.

[151] U. Rotpai, T. Arlai, S. Nusen, and P. Juijerm. Novel flow stress predic-

tion and work hardening behavior of aluminium alloy AA7075 at room and elevated temperatures. *Journal of Alloys and Compounds*, 891:162013, 2022. doi:10.1016/j.jallcom.2021.162013.

[152] G. Rousselier. Ductile fracture models and their potential in local approach of fracture. *Nuclear Engineering and Design*, 105(1):97–111, 1987. doi:10.1016/0029-5493(87)90234-2.

[153] E. Roux and P.-O. Bouchard. On the interest of using full field measurements in ductile damage model calibration. *International Journal of Solids and Structures*, 72:50–62, 2015. doi:10.1016/j.ijsolstr.2015.07.011.

[154] B. R. Seth. Generalized strain measure with application to physical problems. In M. Reiner and D. Abir, editors, *Second-order effects in elasticity, plasticity and fluid dynamics*, pages 162–172. Oxford: Pergamon Press, 1961.

[155] A. Seupel, G. Hütter, and M. Kuna. An efficient FE-implementation of implicit gradient-enhanced damage models to simulate ductile failure. *Engineering Fracture Mechanics*, 199:41–60, 2018. doi:10.1016/j.engfracmech.2018.01.022.

[156] L. Sharma, R. H. J. Peerlings, P. Shanthraj, F. Roters, and M. G. D. Geers. An FFT-based spectral solver for interface decohesion modelling using a gradient damage approach. *Computational Mechanics*, 65(4):925–939, 2019. doi:10.1007/s00466-019-01801-4.

[157] F. Sidoroff. Description of anisotropic damage application to elasticity. In *Physical Non-Linearities in Structural Analysis*, pages 237–244. Springer Berlin Heidelberg, 1981. doi:10.1007/978-3-642-81582-9_35.

[158] M. Šilhavý. *The Mechanics and Thermodynamics of Continuous Media*. Springer Science + Business Media, 1997. doi:10.1007/978-3-662-03389-0.

[159] J. C. Simo. Numerical analysis and simulation of plasticity. In P. G. Ciarlet and J. L. Lions, editors, *Numerical Methods for Solids (Part 3) Numerical Methods for Fluids (Part 1)*, volume VI of *Handbook of Numerical Analysis*, pages 183–499. Elsevier Science B.V., 1998. doi:10.1016/s1570-8659(98)80009-4.

[160] L. Sobisch, T. Kaiser, T. Furlan, and A. Menzel. A user material approach for the solution of multi-field problems in abaqus: Theoretical foundations, gradient-enhanced damage mechanics and thermo-mechanical coupling. *Finite Elements in Analysis and Design*, 232:104105, 2024. doi:10.1016/j.finel.2023.104105.

[161] L. Sprave and A. Menzel. A large strain gradient-enhanced ductile damage model: finite element formulation, experiment and parameter identification. *Acta Mechanica*, 231(12):5159–5192, 2020. doi:10.1007/s00707-020-02786-5.

[162] L. Sprave and A. Menzel. A large strain anisotropic ductile damage model — effective driving forces and gradient-enhancement of damage vs. plasticity. *Computer Methods in Applied Mechanics and Engineering*, 416:116284, 2023.

doi:10.1016/j.cma.2023.116284.

[163] L. Sprave, A. Schowtjak, R. Meya, T. Clausmeyer, A. E. Tekkaya, and A. Menzel. On mesh dependencies in finite-element-based damage prediction: application to sheet metal bending. *Production Engineering*, 14(1):123–134, 2020. doi:10.1007/s11740-019-00937-9.

[164] A. R. Srinivasa and S. M. Srinivasan. *Inelasticity of Materials*, volume 80 of *Series on Advances in Mathematics for Applied Sciences*. WORLD SCIENTIFIC, 2009. doi:10.1142/7131.

[165] P. Steinmann. Formulation and computation of geometrically non-linear gradient damage. *International Journal for Numerical Methods in Engineering*, 46(5):757–779, 1999. doi:10.1002/(SICI)1097-0207(19991020)46:5<757::AID-NME731>3.0.CO;2-N.

[166] P. Steinmann and E. Stein. A unifying treatise of variational principles for two types of micropolar continua. *Acta Mechanica*, 121(1-4):215–232, 1997. doi:10.1007/bf01262533.

[167] H. Swift. Plastic instability under plane stress. *Journal of the Mechanics and Physics of Solids*, 1(1):1–18, 1952. doi:10.1016/0022-5096(52)90002-1.

[168] J. Sylvester. XXXIX. On the equation to the secular inequalities in the planetary theory. *The London, Edinburgh, and Dublin Philosophical Magazine and Journal of Science*, 16(100):267–269, 1883. doi:10.1080/14786448308627430.

[169] P. Szeptyński. Yield criterion accounting for the influence of the third invariant of stress tensor deviator. Part II. Analysis of convexity condition of the yield surface. *Engineering Transactions*, 59(4):283–297, 2011. doi:10.24423/engtrans.139.2011.

[170] C. Tasan, J. Hoefnagels, and M. Geers. Identification of the continuum damage parameter: An experimental challenge in modeling damage evolution. *Acta Materialia*, 60(8):3581–3589, 2012. doi:10.1016/j.actamat.2012.03.017.

[171] F. Thierry, G. Rastiello, C. Giry, and F. Gatuingt. One-dimensional Eikonal Non-Local (ENL) damage models: Influence of the integration rule for computing interaction distances and indirect loading control on damage localization. *Mechanics Research Communications*, 110:103620, 2020. doi:10.1016/j.mechrescom.2020.103620.

[172] N. Triantafyllidis and E. C. Aifantis. A gradient approach to localization of deformation. I. hyperelastic materials. *Journal of Elasticity*, 16(3):225–237, 1986. doi:10.1007/BF00040814.

[173] V. Tvergaard and A. Needleman. Analysis of the cup-cone fracture in a round tensile bar. *Acta Metallurgica*, 32(1):157–169, 1984. doi:10.1016/0001-6160(84)90213-X.

[174] B. Vandoren and A. Simone. Modeling and simulation of quasi-brittle fail-

ure with continuous anisotropic stress-based gradient-enhanced damage models. *Computer Methods in Applied Mechanics and Engineering*, 332:644–685, 2018. doi:10.1016/j.cma.2017.12.027.

[175] A. Vogel and P. Junker. Adaptive and highly accurate numerical treatment for a gradient-enhanced brittle damage model. *International Journal for Numerical Methods in Engineering*, 121(14):3108–3131, 2020. doi:10.1002/nme.6349.

[176] G. Z. Voyiadjis and P. I. Kattan. Local approach to damage in elasto-plastic metal matrix composites. *International Journal of Damage Mechanics*, 2(1):92–114, 1993. doi:10.1177/105678959300200106.

[177] G. Z. Voyiadjis, J.-W. W. Ju, and J.-L. Chaboche, editors. *Damage Mechanics in Engineering*, volume 46 of *Studies in Applied Mechanics*. Elsevier, 1998.

[178] T. Waffenschmidt, C. Polindara, A. Menzel, and S. Blanco. A gradient-enhanced large-deformation continuum damage model for fibre-reinforced materials. *Computer Methods in Applied Mechanics and Engineering*, 268:801–842, 2014. doi:10.1016/j.cma.2013.10.013.

[179] B. Wcisło, J. Pamin, and K. Kowalczyk-Gajewska. Gradient-enhanced damage model for large deformations of elastic-plastic materials. *Archives of Mechanics*, 65 (5):407–428, 2013. URL `http://am.ippt.pan.pl/am/article/view/v65p407/0`.

[180] J. P. Webb. Imposing linear constraints in finite-element analysis. *Communications in Applied Numerical Methods*, 6(6):471–475, 1990. doi:10.1002/cnm.1630060607.

[181] J.-F. Wen, Y. Liu, A. Srivastava, A. A. Benzerga, S.-T. Tu, and A. Needleman. Environmentally enhanced creep crack growth by grain boundary cavitation under cyclic loading. *Acta Materialia*, 153:136 – 146, 2018. doi:10.1016/j.actamat.2018.04.034.

[182] H. Westergaard. On the resistance of ductile materials to combined stresses in two or three directions perpendicular to one another. *Journal of the Franklin Institute*, 189(5):627–640, 1920. doi:10.1016/S0016-0032(20)90373-3.

[183] T. Wierzbicki, Y. Bao, Y.-W. Lee, and Y. Bai. Calibration and evaluation of seven fracture models. *International Journal of Mechanical Sciences*, 47(4-5):719–743, 2005. doi:10.1016/j.ijmecsci.2005.03.003.

[184] J.-Y. Wu and M. Cervera. A novel positive/negative projection in energy norm for the damage modeling of quasi-brittle solids. *International Journal of Solids and Structures*, 139-140:250–269, 2018. doi:10.1016/j.ijsolstr.2018.02.004.

[185] J.-Y. Wu and S.-L. Xu. Reconsideration on the elastic damage/degradation theory for the modeling of microcrack closure-reopening (MCR) effects. *International Journal of Solids and Structures*, 50(5):795–805, 2013. doi:10.1016/j.ijsolstr.2012.11.012.

[186] S. Wulfinghoff, M. Fassin, and S. Reese. A damage growth criterion for anisotropic

damage models motivated from micromechanics. *International Journal of Solids and Structures*, 121:21–32, 2017. doi:10.1016/j.ijsolstr.2017.04.038.

[187] S. Wulfinghoff and T. Böhlke. Gradient crystal plasticity including dislocation-based work-hardening and dislocation transport. *International Journal of Plasticity*, 69:152–169, 2015. doi:10.1016/j.ijplas.2014.12.003.

[188] Y. Xu and L. H. Poh. Localizing gradient-enhanced Rousselier model for ductile fracture. *International Journal for Numerical Methods in Engineering*, 119(9): 826–851, 2019. doi:10.1002/nme.6074.

[189] K. Zhang, H. Badreddine, N. Hfaiedh, K. Saanouni, and J. Liu. Enhanced CDM model accounting of stress triaxiality and Lode angle for ductile damage prediction in metal forming. *International Journal of Damage Mechanics*, 30(2):260–282, 2020. doi:10.1177/1056789520958045.

[190] Y. Zhang, E. Lorentz, and J. Besson. Ductile damage modelling with locking-free regularised GTN model. *International Journal for Numerical Methods in Engineering*, 113(13):1871–1903, 2018. doi:10.1002/nme.5722.

[191] Y. Zhu and M. D. Engelhardt. A nonlocal triaxiality and shear dependent continuum damage model for finite strain elastoplasticity. *European Journal of Mechanics - A/Solids*, 71:16–33, 2018. doi:10.1016/j.euromechsol.2018.03.012.

Publication series of the Institute of Mechanics

published to date:

2010/01 Palnau, V.: Implementierung eines netzfreien Diskretisierungsverfahrens und seine Anwendung auf die Scherbandanalyse.
ISBN 978-3-921823-51-4

2010/02 Klusemann, B.: Application of homogenization methods and crystal plasticity to the modeling of heterogeneous materials of technological interest.
ISBN 978-3-921823-53-8

2011/01 Hortig, C.: Local and non-local thermomechanical modeling and finite-element simulation of high-speed cutting.
ISBN 978-3-921823-54-5

2011/02 Parvizian, F.: Modeling of microstructure evolution in aluminum alloys during hot extrusion.
ISBN 978-3-921823-56-9

2011/03 Noman, M.: Characterization and model identification for the simulation of the forming behavior of ferritic steels.
ISBN 978-3-921823-55-2

2011/04 Kayser, T.: Characterization of microstructure in aluminum alloys based on electron backscatter diffraction.
ISBN 978-3-921823-57-6

2011/05 Bargmann, S.: Computational modeling of material behavior on different scales based on continuum mechanics.
ISBN 978-3-921823-58-3

2013/01 Waffenschmidt, T.: Modelling and simulation of adaptation and degradation in anisotropic biological tissues.
ISBN 978-3-921823-61-3

2015/01 Ostwald, R.: Modelling and simulation of phase-transformations in elastoplastic polycrystals.
ISBN 978-3-921823-66-8

2016/01 Subramanian, M.: Phenomenological modelling and simulation of ferroelectric ceramics.
ISBN 978-3-921823-74-3

2016/02 Clausmeyer, T.: Evolution of plastic anisotropy in metals.
ISBN 978-3-921823-76-7

2017/01 Holtermann, R.: Computational multiscale modelling of grinding processes.
ISBN 978-3-921823-86-6

2017/02 Bartels, A.: Modelling of evolving microstructures at different scales.
ISBN 978-3-921823-93-4

2017/03 Dusthakar Kumar Rao, D. K.: Computational modelling of single and polycrystalline ferroelectric materials.
ISBN 978-3-921823-94-1

2019/01 Buckmann, K.: Microstructure evolution in functional magnetic materials.
ISBN 978-3-947323-09-8

2019/02 Kaiser, T.: Computational modelling of non-simple and anisotropic materials.
ISBN 978-3-947323-14-2

2019/03 Heitbreder, T.: Modelling of material interfaces at different length scales.
ISBN 978-3-947323-18-0

2020/01 Berthelsen, R.: Computational homogenisation of thermomechanical problems.
ISBN 978-3-947323-19-7

2020/02 Sievers, C.: Describing the macroscopic behavior of surfaces based on atomistic models.
ISBN 978-3-947323-24-1

2022/01 Rose, L.: Optimisation based parameter identification using optical field measurements.
ISBN 978-3-947323-31-9

2023/01 Langenfeld, K.: Continuum modeling of brittle and ductile damage: theory and computational frameworks.
ISBN 978-3-947323-41-8

2023/02 Schulte, R.: Parameter identification approaches with application to different classes of materials.
ISBN 978-3-947323-45-6

2023/03 Kaiser, T.: Multiscale multiphysics material modelling.
ISBN 978-3-947323-46-3

2024/01 Noll, I.: Thermomechanical modelling and simulation of laser powder bed fusion processes.
ISBN 978-3-947323-49-4

2024/02 Witt, C.: Isogeometric analysis of anisotropic mechanical and electromechanical higher-gradient continua.
ISBN 978-3-947323-50-0

2025/01 Kurzeja, P.: Modeling, Control and Opportunities of Mechanical Interfaces Across the Scales.
ISBN 978-3-947323-51-7

2025/02 Lammen, H.: Modeling and simulation of general imperfect interfaces using phase-field-theory.
ISBN 978-3-947323-52-4

2025/03 Sprave, L.: Computational Modelling and Simulation of Ductile Damage in Metals.
ISBN 978-3-947323-54-8